



UNIVERSIDADE FEDERAL DE MINAS GERAIS

**DEVELOPMENT PROCEDURE FOR A PROTOTYPE TURBO ENGINE DESIGN
POWERED BY ETHANOL AND ASSISTED BY WATER INJECTION**

THIAGO RODRIGO VIEIRA DA SILVA

Belo Horizonte, MG - Brazil

2022

Thiago Rodrigo Vieira da Silva

**DEVELOPMENT PROCEDURE FOR A PROTOTYPE TURBO
ENGINE DESIGN POWERED BY ETHANOL AND ASSISTED BY
WATER INJECTION**

Thesis presented to the Doctoral Degree Course of the Mechanical Engineering Graduate Program of Universidade Federal de Minas Gerais (UFMG), as partial requirement for obtaining the degree of Doctor Degree in Mechanical Engineering.

Advisor: Prof. Dr. José Guilherme Coelho Baeta

Coadvisor: Prof. Dr.-Ing. Karsten Wittek

Belo Horizonte

2022

S586d Silva, Thiago Rodrigo Vieira da.
Development procedure for a prototype turbo engine design powered by ethanol and assisted by water injection [recurso eletrônico] / Thiago Rodrigo Vieira da Silva. - 2022.
1 recurso online (360 f. : il., color.) : pdf.

Orientador: José Guilherme Coelho Baêta.
Coorientador: Karsten Wittek.

Tese (doutorado) - Universidade Federal de Minas Gerais, Escola de Engenharia.

Inclui bibliografia .
Exigências do sistema: Adobe Acrobat Reader.

1. Engenharia mecânica - Teses. 2. Álcool - Teses. 3. Motores de combustão interna - Teses. 4. Motores a álcool - Teses. I. Baêta, José Guilherme Coelho. II. Wittek, Karsten. III. Universidade Federal de Minas Gerais. Escola de Engenharia.
IV. Título.

CDU: 621 (043)



UNIVERSIDADE FEDERAL DE MINAS GERAIS
ESCOLA DE ENGENHARIA
PROGRAMA DE PÓS-GRADUAÇÃO EM ENGENHARIA MECÂNICA

FOLHA DE APROVAÇÃO

"DEVELOPMENT PROCEDURE FOR A PROTOTYPE TURBO ENGINE DESIGN POWERED BY ETHANOL AND ASSISTED BY WATER INJECTION"

THIAGO RODRIGO VIEIRA DA SILVA

Tese submetida à Banca Examinadora designada pelo Colegiado do Programa de Pós-Graduação em Engenharia Mecânica da Universidade Federal de Minas Gerais, constituída pelos Professores: Dr. José Guilherme Coelho Baêta (Orientador – Departamento de Engenharia Mecânica/UFMG), Dr. Ramon Molina Valle (Professor aposentado da Universidade Federal de Minas Gerais/UFMG), Dr. Fabricio José Pacheco Puja (Departamento de Engenharia Mecânica/UFMG), Dr. Fernando Antonio Rodrigues Filho (CEFET-MG) e Dr. Rogério Jorge Amorim (PUC-Minas), como parte dos requisitos necessários à obtenção do título de "Doutor em Engenharia Mecânica", na área de concentração de "Projeto e Sistemas".

Tese aprovada no dia 31 de agosto de 2022.



Documento assinado eletronicamente por **Jose Guilherme Coelho Baeta, Professor do Magistério Superior**, em 02/09/2022, às 08:57, conforme horário oficial de Brasília, com fundamento no art. 5º do [Decreto nº 10.543, de 13 de novembro de 2020](#).



Documento assinado eletronicamente por **Rogério Jorge Amorim, Usuário Externo**, em 02/09/2022, às 14:30, conforme horário oficial de Brasília, com fundamento no art. 5º do [Decreto nº 10.543, de 13 de novembro de 2020](#).



Documento assinado eletronicamente por **Fabricio Jose Pacheco Puja, Professor do Magistério Superior**, em 08/09/2022, às 15:00, conforme horário oficial de Brasília, com fundamento no art. 5º do [Decreto nº 10.543, de 13 de novembro de 2020](#).



Documento assinado eletronicamente por **Ramon Molina Valle, Professor Magistério Superior - Voluntário**, em 14/09/2022, às 11:08, conforme horário oficial de Brasília, com fundamento no art. 5º do [Decreto nº 10.543, de 13 de novembro de 2020](#).



Documento assinado eletronicamente por **Fernando Antonio Rodrigues Filho, Usuário Externo**, em 20/09/2022, às 21:24, conforme horário oficial de Brasília, com fundamento no art. 5º do [Decreto nº 10.543, de 13 de novembro de 2020](#).



A autenticidade deste documento pode ser conferida no site https://sei.ufmg.br/sei/controlador_externo.php?acao=documento_conferir&id_orgao_acesso_externo=0, informando o código verificador **1727574** e o código CRC **EF15C2D4**.

“Seja você quem for, seja qual for a posição social que você tenha na vida, a mais alta ou a mais baixa, tenha sempre como meta muita força, muita determinação e sempre faça tudo com muito amor e com muita fé em Deus, que um dia você chega lá.

De alguma maneira você chega lá”

Ayrton Senna

ACKNOWLEDGMENTS

Words cannot express my gratitude to God for helping me to overcome this stage, for supporting and guiding my steps, my mind and my heart.

I am extremely grateful to my parents Wantuil Diniz and Maria do Carmo, and my sister Danielle Silva for being comprehensive and encourage me to always pursue my dreams.

I could not have undertaken this journey without my future wife, Jeanine Santos which stayed on my side being patient, helping me with everything and always pushing me further towards my dreams.

I am deeply indebted to my advisor and friend Prof. Dr. Jose G. C. Baeta by always believe in me, for help me to achieve my aiming and teach me vastly about engines. Thank you by being my professional and friend reference since 2012.

I am also grateful to Prof. Dr. Karsten Wittek for received me in his engine laboratory and taught me the basics of engine design. Thank you also for all colleagues in KMH for all kind of help during my days in the laboratory.

Thanks should also go to Thomas Schlee, for all knowledge shared, for believe in me and for helping me to pursue my dream to work on motorsport field.

I would like to acknowledge the CTM colleges for believe in my work and thank you Marina for your constant support on the postgraduate secretary requirements.

Special thanks to my friends Nilton Diniz, Bernardo Hissa, Daniel Schreiner, Felipe Bazzoli, Paulo Netto, Gabriel Mozelli, Victor Pontello, Gabriella Vaz, Augusto Malaquias, Nici Kilian, Diego Golke, Tony and Raphael Meireles, for the partnership, support and advices given throughout my PhD studies.

I would like to express my deepest appreciation to BorgWarner, Hilite, Roltens, and Bosch Motorsport for sharing support technical material which assisted the development of this work.

I would like to acknowledge UFMG and the Graduate Program in Mechanical Engineering for their institutional support to carry out the project. To all the unit's employees for all their patience, dedication and attention.

Thanks should also go to CNPq and CAPES for granting the doctoral scholarship at the beginning and ending of the studies, respectively.

Finally, I would like to acknowledge everyone who has been with me on this incredible journey, my sincere acknowledgment.

ABSTRACT

The management of the global energy resources has stimulated the emergence of various agreements in favor of the environment. Among the most famous are the Conference of Parties (COP) and Rota 2030, which aim to limit global warming to 1.5 °C by reducing the energy consumption and global emission levels. In order to comply with the international standards for energy consumption and pollutant emissions, the Brazilian government has been promoting the expansion of biofuels in the national energy matrix. Considering this scenario, the development of a novel internal combustion engine for the exclusive use of ethanol as a fuel, equipped with state-of-the-art technologies and employing modern design concepts, consists of an innovative and promising pathway for future mobility, from both environmental and technological outlooks. In this sense, this work presents a development procedure for a prototype turbo engine design powered by hydrated ethanol and assisted by water injection. The ethanol was selected due to its physicochemical properties, which allow the engine to achieve loads higher than 30 bar of IMEP, and also due to its availability as a renewable energy. Furthermore, a port water injection system was fitted to the engine in order to assist the combustion process by mitigating the knock tendency. Completely new the engine components were designed on CAD models and evaluated using FEM method for thermal and mechanical loads application. Furthermore, the predicted overall engine performance was obtained by carrying out a GT-Power™ 1D simulation, whose results pointed to a maximum torque of 279 Nm from 2000 to 4000 rpm and an indicated peak power of 135 kW at 5500 rpm. With a maximum water-to-fuel ratio of 19.2%, the engine was able to perform its entire full load curve at full spark authority condition, a fact that makes the WI approach along with the ethanol fuel an attractive solution. As a result of the specific design of each engine component and geometric parameters defined based on modern design approaches, not previously used on an engine running exclusively on ethanol, a maximum indicated fuel conversion efficiency of 45.3% was achieved. Moreover, the engine was capable of achieving over 40% of the indicated fuel conversion efficiency in almost its entire full load curve.

Keywords: Hydrated ethanol; internal combustion engines; engine design; water injection; 1D simulation; high-efficient engine; highly boosted engine

RESUMO

A gestão dos recursos energéticos globais tem estimulado o surgimento de diversos acordos em prol do meio ambiente. Entre os mais conhecidos estão a *Conference of Parties* (COP) e a Rota 2030, que visam limitar o aquecimento global a 1,5°C, reduzindo o consumo de energia e os níveis de emissões globais. Para atender aos padrões internacionais de consumo de energia e emissão de poluentes, o governo brasileiro vem promovendo a expansão dos biocombustíveis na matriz energética nacional. Diante desse cenário, o desenvolvimento de um novo motor de combustão interna para uso exclusivo do etanol como combustível, equipado com tecnologias modernas e empregando conceitos modernos de projeto, consiste em uma alternativa inovadora e promissora para o futuro da mobilidade. Nesse sentido, este trabalho apresenta um procedimento de desenvolvimento de um protótipo de motor turbo alimentado que usa o etanol hidratado como combustível e equipado com injeção indireta de água. O etanol foi selecionado devido às suas propriedades físico-químicas, que permitem ao motor atingir cargas superiores a 30 bar de IMEP, e também devido à sua disponibilidade como energia renovável. Além disso, um sistema de injeção indireta de água foi instalado no motor com o objetivo de auxiliar o processo de combustão, mitigando a tendência de detonação. Completamente novos os componentes do motor foram projetados em modelos CAD e avaliados pelo método FEM para aplicação de cargas térmicas e mecânicas. Além disso, o desempenho geral previsto do motor foi obtido por meio de uma simulação GT-Power™ 1D, cujos resultados apontaram para um torque máximo de 279 Nm de 2000 a 4000 rpm e uma potência de pico indicada de 135 kW a 5500 rpm. Com uma relação *WFR* máxima de 19,2%, o motor foi capaz de realizar toda a sua curva de plena carga na condição de *Full Spark Authority*, fato que torna a abordagem de injeção de água junto com o etanol uma solução atrativa. Como resultado do desenvolvimento de cada componente do motor e dos parâmetros geométricos definidos com base em abordagens de projeto modernas, não utilizadas anteriormente em um motor que funciona exclusivamente com etanol, foi alcançada uma máxima eficiência de conversão de combustível indicada de 45,3%. Além disso, o motor foi capaz de atingir mais de 40% da eficiência de conversão de combustível indicada em quase toda a sua curva de plena carga.

Palavras-chave: Etanol hidratado; motores de combustão interna; projeto do motor; injeção de água; Simulação 1D; motor de alta eficiência; motor altamente sobrealimentado

LIST OF FIGURES

Figure 1 – CO2 emissions between the years 2000 and 2021	34
Figure 2 – The lambda factor value spatially inside a combustion chamber	44
Figure 3 – The water injection effects related to the engine load increase.....	45
Figure 4 – Engine cranktrain kinematic scheme	46
Figure 5 – Engine cranktrain, piston pin offset and crankshaft offset	48
Figure 6 – Piston secondary movement according to piston pin de-axing direction	49
Figure 7 – The TDC and BDC for engines with offset	51
Figure 8 – The forces on the engine cranktrain.....	53
Figure 9 – The piston force of a four-stroke engine over the work cycle.....	54
Figure 10 – The piston force distributed as conrod force and normal force	54
Figure 11 – The connecting rod force of a four-stroke engine over the work cycle	55
Figure 12 – The normal force of a four-stroke engine over the work cycle.....	55
Figure 13 – The connecting rod force distributed as tangential force and radial force	56
Figure 14 – The main journal force	57
Figure 15 – The tangential force over work cycle.....	58
Figure 16 – The tangential force over work cycle according to number of cylinders.....	59
Figure 17 – Torque crank diagram.....	63
Figure 18 – Materials strength – density chart	65
Figure 19 – The piston basic structure.....	66
Figure 20 – Temperature distributions for gasoline (a) and diesel (b) engine pistons	67
Figure 21 – The oil spray target for a Formula 1 engine application	68
Figure 22 – The piston Thermal Coating Barrier (TBC).....	69
Figure 23 – The piston TBC effect on the engine fuel conversion efficiency	70
Figure 24 – Common piston coated regions.....	71
Figure 25 – The main dimensions of light-alloy piston	72
Figure 26 – Piston skirt profiles	74

Figure 27 – Piston barrel profile.....	75
Figure 28 – Piston ovality and superposition, double oval (a) and tri-oval (b) ..	76
Figure 29 – Detailed piston ring belt.....	77
Figure 30 – Piston circular shape (a) and forces on piston (b)	78
Figure 31 – Classification of piston rings per DIN ISO 6621 - Part 1	80
Figure 32 – Piston pin cylindrical inner and outer (a), and conical ends (b).....	82
Figure 33 – Piston pin ovalization behavior related to diametral clearance	83
Figure 34 – Stress on the Piston pin	85
Figure 35 – Connecting rod (a) and piston (b) wear due to pressure peaks in the presence of edges.....	85
Figure 36 – Aspect difference between a DLC coated (a) and an uncoated (b) piston pin	88
Figure 37 – Types of piston pin circlips round without hooks (a), squared with hooks (b) and round with outward hook bended	89
Figure 38 – Connecting rod terminology.....	90
Figure 39 – Connecting rod main motions (a) and connecting rod sweep (b)...	90
Figure 40 – Deformation of the connecting rod big end under tensile load.....	91
Figure 41 – Connecting rod highly stressed sections	92
Figure 42 – Connecting rod buckling modes: side-buckling (a) and front-rear buckling (b).....	93
Figure 43 – Connecting rod shank profiles: I-section (a), H-section (b), Blade-section (c), and Hollow-section (d)	94
Figure 44 – Contact pressure between piston pin and connecting rod pin-eye: (a) von Mises stress distribution and (b) contact pressure distribution	94
Figure 45 – Connecting rod parallel (a), tapered (b) and stepped (c) pin-eye....	95
Figure 46 – Representation of the connecting rod big end blind bore deformation after the bolts tightened.....	95
Figure 47 – Connecting rod with fracture surfaces of the big end bore.....	98
Figure 48 – Connecting rod (a) top-guided and (b) bottom-guided	99
Figure 49 – Crankshaft terminology	100
Figure 50 – Crankshaft deformation due to gas and mass forces	102
Figure 51 – Crankpin section through the oil bore.....	103
Figure 52 – Crank dimensions for stress concentration factor calculation	106

Figure 53 – Crank dimensions relations for stress concentration factor calculation.....	107
Figure 54 – Crank pin acting forces.....	112
Figure 55 – Notch sensitivities for bending and torsion loads	113
Figure 56 – Inertia forces vector diagram for a reciprocating mechanism	115
Figure 57 – Lanchester inertia forces balancing system	116
Figure 58 – Projection of the crankshaft on the xy-plane	116
Figure 59 – Inertia forces and mass couples for a 3-cylinder in-line engine ...	118
Figure 60 – Resultant inertia forces and couples for reciprocating engines ...	118
Figure 61 – Harmonic components of the torsional force four-stroke engine.	119
Figure 62 – Campbell Diagram	119
Figure 63 – Typical bearings used in ICEs.....	121
Figure 64 – Oil bore and oil groove in bearings	123
Figure 65 – Bimetallic (a) and Trimetallic (b) bearings	125
Figure 66 – Forces and loads applied on a crankcase.....	127
Figure 67 – Crankcase thermo-mechanical FEM analysis	127
Figure 68 – Crankcase Open-deck (a) and Closed-deck (b) designs.....	129
Figure 69 – Crankcase individually screwed bearing caps (a), a bearing cap assembly (b), and the bedplate (c).....	130
Figure 70 – Billet machined crankcase	130
Figure 71 – Crankcase major dimensions.....	131
Figure 72 – Magnesium aluminum composite crankcase.....	134
Figure 73 – Magnesium aluminum composite crankcase.....	136
Figure 74 – Cylinder liner FEM deformation analysis due to mechanical and thermal stress.....	136
Figure 75 – Basic designs for water-cooled cylinder liners	137
Figure 76 – Basic initial dimensions for midstop (a) and standard hanging (b) wet cylinder liners used in Formula 1 engines	138
Figure 77 – Cylinder liner tangential (hoop) and longitudinal stresses.....	139
Figure 78 – Cylinder liners in aluminum crankcase	141
Figure 79 – Cylinder liner surface pattern after honing process (a) and FEM deformation analysis (b).....	142
Figure 80 – Influence of total angle between valves on the valve areas	144

Figure 81 – Typical web dimensions or distances for a standard cylinder head	146
Figure 82 – Influence of port and valve angle related to the cylinder center axis on the engine performance	146
Figure 83 – Flame area map (FAM)	148
Figure 84 – Injector sideway mounted (a) and central mounted (b)	149
Figure 85 – Spray target DI injection sideway mounted (a) and centrally mounted (b).....	149
Figure 86 – Typical valve seat insert and counterbore nomenclature.....	150
Figure 87 – Schematic illustration of clad seats and expected effects compared with press-fit type seats	153
Figure 88 – In-cylinder flow pattern swirl (a), tumble (b) and squish (c)	153
Figure 89 – Typical intake and exhaust ports in function of the valve head diameter	154
Figure 90 – Valve flow area stages related to valve lift.....	155
Figure 91 – Integrated exhaust manifold.....	157
Figure 92 – Types of valvetrain systems.....	159
Figure 93 – Cam profile nomenclature	161
Figure 94 – Valve displacement, velocity, acceleration, and jerk curves	161
Figure 95 – The lift-duration envelope ratio	162
Figure 96 – Camshaft nomenclature.....	163
Figure 97 – Different camshaft manufacturing process weight comparison nomenclature.....	164
Figure 98 – Typical valve timing diagram for four-stroke engines	165
Figure 99 – UniAir VVA system applied over the engine operation map	166
Figure 100 – Poppet-valve nomenclature.....	167
Figure 101 – Temperature and stress distribution in the valve under ignition pressure	168
Figure 102 – Bimetallic hollow valve filled with sodium	170
Figure 103 – Valve spring nomenclature.....	171
Figure 104 – Typical valve spring end types.....	172
Figure 105 – Typical valve spring shapes and wire profiles.....	173
Figure 106 – Valve keepers single-bead (a) and three-bead (b)	179

Figure 107 – Valve retainer 7 degrees (a) and 10 degrees (b)	180
Figure 108 – Valve guide smooth bore (a), machined cold end (b) and flanged machined cold end (c).....	181
Figure 109 – Relationship among valve guide length, I.D and wall thickness .	182
Figure 110 – Valve stem seal technical features and nomenclature.....	184
Figure 111 – Lip pressure of different valve stem seal designs.....	184
Figure 112 – Valve stem seal contact pressure profile for the oil metering rate adjustment	185
Figure 113 – Valve stem seal materials applicable temperature ranges and the abrasive wear resistance ranking	186
Figure 114 – Valve lash mechanical (a) and hydraulic (b) adjuster	187
Figure 115 – Rocker arm end-pivot (a) and center-pivot (b).....	187
Figure 116 – Rocker arm end-pivot (a) and center-pivot (b).....	189
Figure 117 – Typical intake manifold for a four-cylinder engine.....	190
Figure 118 – Intake instantaneous pressure signal frequency spectrum (1690 rpm)	191
Figure 119 – Flow contraction associated to a sharp-edge pipe inlet.....	192
Figure 120 – Bellmouth design for a pipe inlet.....	193
Figure 121 – Joint bolted assembly.....	194
Figure 122 – Joint diagram for bolted assembly	196
Figure 123 – Turbocharger assembly.....	197
Figure 124 – Turbo-matching methodology.....	198
Figure 125 – Turbocharger performance maps: (a) Compressor and (b) Turbine	199
Figure 126 – Fatigue fracture surface of a forged connecting rod of AISI 8640 steel.....	200
Figure 127 – Material S-N diagram.....	202
Figure 128 – Equivalent diameter of noncircular cross section for size factor calculation.....	203
Figure 129 – Fatigue strength factor	206
Figure 130 – Types of fluctuation stresses.....	207
Figure 131 – Fatigue Failure criteria	207
Figure 132 – Mesh convergence process	211

Figure 133 – Finite volume element representation	211
Figure 134 – Comparison of the thermal efficiency, the heat and the friction losses of three different S/B ratio normalized by the S/B=0.7 results	225
Figure 135 – LHV breakdown for different S/B ratio at 2000 rpm, $\lambda=1$ and 26 mg/cycle of fuel mass supplied to the engine	226
Figure 136 – Effects of the connecting rod ratio on the FMEP related to engine load and speed	228
Figure 137 – Piston acceleration behavior related to connecting rod ratio	229
Figure 138 – Piston side force related to crankshaft offset.....	230
Figure 139 – Crankshaft offset effect on the power loss of the piston skirt at partial load (a) and full load (b)	231
Figure 140 – Piston acceleration curve of crankshaft with and without 10 mm offset towards the major thrust side	232
Figure 141 – Reference in-cylinder pressure trace for the engine components design.....	235
Figure 142 – Engine component design process flowchart	237
Figure 143 – Base engine piston CAD model	238
Figure 144 – In-cylinder flow pattern comparison between flat piston	240
Figure 145 – Piston Ceramic Thermal Coating Barrier	241
Figure 146 – Piston ring and piston skirt coatings	242
Figure 147 – Asymmetrical piston skirt.....	244
Figure 148 – Thermal circuit resistances model.....	245
Figure 149 – In-cylinder gas temperature trace	248
Figure 150 – Piston CAD geometry (a) and its mesh (b) used for simulation ..	250
Figure 151 – Piston characteristic surfaces used for thermal simulation.....	250
Figure 152 – Piston barrel and ovality shape reference measure planes.....	252
Figure 153 – Piston geometry comparison between a piston applied to a flex-fuel engine (a) and the piston designed for HBS22 (b)	253
Figure 154 – Piston pin geometry	254
Figure 155 – Different piston pin geometries.....	254
Figure 156 – Piston pin CAD geometry (a) and its mesh (b) used for simulation	255
Figure 157 – Connecting rod geometry	257

Figure 158 – Connecting rod tapered small end bore design	258
Figure 159 – Connecting rod CAD geometry (a) and its mesh (b) used for simulation	259
Figure 160 – Connecting rod geometry comparison between a piston applied to a flex-fuel engine (a) and the piston designed for HBS22 (b).....	260
Figure 161 – Crankshaft.....	264
Figure 162 – Torque diagram at engine idle condition.....	265
Figure 163 – Engine flywheel	267
Figure 164 – Cylinder Liner	268
Figure 165 – Cylinder liner CAD geometry (a) and its mesh (b) used for simulation	269
Figure 166 – Cylinder liner thermal boundary conditions	270
Figure 167 – Crankcase bedplate design concept	271
Figure 168 – Connecting rod sweep	272
Figure 169 – Crankcase main characteristics.....	273
Figure 170 – Bedplate fixation.....	274
Figure 171 – Crankcase CAD geometry (a) and its mesh (b) used for simulation	275
Figure 172 – Overall combustion chamber layout and its minimum wed thickness	276
Figure 173 – Valvetrain skeleton.....	276
Figure 174 – Valvetrain basic features positioned	277
Figure 175 – Intake and exhaust camshafts.....	279
Figure 176 – Spark-plug and direct fuel injector position.....	279
Figure 177 – Fuel injection spray target.....	280
Figure 178 – Intake (a) and exhaust (b) valve seats	281
Figure 179 – Cam lobe phases (a) and cam lobe polynomial design (b).....	283
Figure 180 – Intake valve displacement, velocity and acceleration curves	286
Figure 181 – Exhaust valve displacement, velocity and acceleration curves..	286
Figure 182 – Intake and exhaust valve timing diagram.....	287
Figure 183 – Intake (a) and exhaust (b) valve keys and plates assembly	288
Figure 184 – Spring aspect ratio related to ovate wire width	289
Figure 185 – Designed spring for the HBS22.....	293

Figure 186 – Intake (a) and exhaust (b) valve guide	294
Figure 187 – Intake (a) and exhaust (b) valve stem seal	295
Figure 188 – Intake and exhaust valve diagram related to piston displacement	296
Figure 189 – Intake and exhaust valve to piston clearance.....	296
Figure 190 – Combustion chamber main volume and area	297
Figure 191 – Spark-plug to combustion chamber center of gravity position...	297
Figure 192 – Intake and exhaust ports	298
Figure 193 – Engine water-jacket.....	299
Figure 194 – Cylinder head Top view (a) and Bottom view (b).....	301
Figure 195 – Cylinder head and its sub-components assembled.....	301
Figure 196 – Cylinder head, cam-carrier and cam-covers assembly arrangement	302
Figure 197 – Fast sensors bosses for indicated measurements	303
Figure 198 – Intake manifold	308
Figure 199 – Intake manifold runner inlet area	309
Figure 200 – Intake manifold plenum	310
Figure 201 – Water injection system	310
Figure 202 – Water injector spray target	311
Figure 203 – Engine oil lubricant system.....	312
Figure 204 – Timing belt layout.....	314
Figure 205 – Accessories belt layout	315
Figure 206 – Engine starter	315
Figure 207 – (a) Compressor map and (b) turbine map	316
Figure 208 – Engine numerical simulation model	317
Figure 209 – Uncoated piston temperature distribution	321
Figure 210 – Coated piston temperature distribution	322
Figure 211 – Piston profile thermal deformation	322
Figure 212 – Piston, piston pin and connecting rod contacts and mechanical load	323
Figure 213 – Piston safety factor considering fatigue	324
Figure 214 – Piston pin safety factor considering fatigue	324
Figure 215 – Piston pin Von Mises stress distribution	325

Figure 216 – Piston pin ovalization.....	325
Figure 217 – Connecting rod bearing deformation due to bolts preload	326
Figure 218 – Connecting rod cap gap evaluation.....	327
Figure 219 – Connecting rod safety factor considering fatigue.....	328
Figure 220 – Cylinder liner temperature distribution	329
Figure 221 – Cylinder liner distortion due to thermal load	330
Figure 222 – Normal force applied on the crankshaft.....	330
Figure 223 – Tangential force applied on the crankshaft.....	331
Figure 224 – The predicted engine IMEP.....	333
Figure 225 – The predicted engine indicated torque.....	334
Figure 226 – The predicted engine indicated power	334
Figure 227 – In-cylinder pressure trace simulation result at 2500 rpm	335
Figure 228 – In-cylinder pressure trace simulation result related to engine speed	335
Figure 229 – Water fuel ratio throughout the engine running conditions	337
Figure 230 – (a) Exhaust backpressure and (b) exhaust temperature	337
Figure 231 – (a) HC and (b) NO predicted emissions	339
Figure 232 – CO ₂ predicted indicated emissions.	340
Figure 233 – The MFB50% and the combustion duration MFB10-90% achieved at full load engine simulation.	341
Figure 234 – The engine indicated fuel conversion efficiency.	341
Figure 235 – Operating points on (a) compressor and (b) turbine maps	343
Figure 236 – Designed highly boosted prototype engine	344

LIST OF TABLES

Table 1 – The hydrated ethanol fuel properties according to ANP	39
Table 2 – The hydrated ethanol fuel properties to calculate its molar ratio.....	40
Table 3 – The calculated hydrated ethanol fuel properties.....	41
Table 4 – Degree of irregularity according to the type of equipment	61
Table 5 – Typical piston temperature values for passenger car engines.....	67
Table 6 – The main dimensions of light-alloy piston.....	72
Table 7 – Ring gap clearance recommendation guide	78
Table 8 – Typical piston pin dimensions ratios	86
Table 9 – Typical piston pin materials	86
Table 10 – Typical connecting rod materials and their properties.....	97
Table 11 – Typical crankshaft main dimensions	101
Table 12 – Dimensions ranges for valid concentration factors evaluation	108
Table 13 – Typical crankshaft materials	120
Table 14 – Important bearing properties	122
Table 15 – Aluminum alloys for crankcase manufacturing	133
Table 16 – Typical re-boring allowance for ICE cylinder liners	140
Table 17 – Typical mechanical properties of cast iron liners (reference values)	141
Table 18 – Valve head diameter in function of the cylinder bore	144
Table 19 – Typical minimum web widths or distances for a standard cylinder head.....	145
Table 20 – Typical aluminum alloys used for light metal cylinder heads.....	158
Table 21 – Typical valve timing characteristics for the engine performance objectives.....	166
Table 22 – Valve material properties and application fields	170
Table 23 – Some spring wires mechanical properties	175
Table 24 – Constants A and m for the spring ultimate tensile strength estimative	176
Table 25 – Constants values a_0 , a_1 and a_2 for stress concentration factor calculation.....	177
Table 26 – Constants values a and b for surface modification factor.....	203

Table 27 – The temperature modification factor	204
Table 28 – Reliability factor	205
Table 29 – Types of finite elements	209
Table 30 – Brazilian vehicle manufacturing tax	222
Table 31 – Modern 1.0-liter engines bore size	224
Table 32 – Basic engine specification	234
Table 33 – The initial HBS22 piston dimensions relation	238
Table 34 – The M-SP25 aluminum alloy mechanical properties.....	239
Table 35 – The TBC materials properties	241
Table 36 – The HBS22 engine piston rings	243
Table 37 – Woschini-Classic model constants	249
Table 38 – Piston thermal boundary conditions for thermal simulation	251
Table 39 – Piston barrel and ovality shape values	252
Table 40 – Connecting rod bushing material properties (KS S705).....	258
Table 41 – The alternating and midrange bending and torsion moments.....	262
Table 42 – Crankshaft to bearings diameters comparison.....	264
Table 43 – Areas under the torque diagram and the sum of them.....	266
Table 44 – Cylinder liner DIN 1693 GGG70 material properties.....	268
Table 45 – Main bearing caps AISI 1020 carbon steel material properties.....	272
Table 46 – Crankcase main characteristics	274
Table 47 – The intake and exhaust valve seats main dimensions	281
Table 48 – Cam lift curve polynomial coefficients.....	283
Table 49 – The intake and exhaust valve lift calculation input and output	285
Table 50 – The intake and exhaust valvetrain main working values limits	286
Table 51 – Intake and exhaust valve actuation summary	287
Table 52 – Intake and exhaust valve guide	294
Table 53 – Main fuel properties the Brazilian ethanol used in the model.....	318
Table 54 – Combustion and knock model validation	320

LIST OF ABBREVIATIONS AND ACRONYMS

ACAC – Air Charge Air Cooler
ANP – Brazilian National Petroleum Agency
APS – Atmospheric Plasma Spray
BDC – Bottom Dead Center
C - Clearance
CA – Crank Angle [deg]
CAD – Computer-Aided Design
CFD – Computational Fluid Dynamics
CG – Center of Gravity
CHRA – Central Housing and Rotating Assembly
CNC – Computerized Numerical Control
CNG – Natural gas
COP – Conference of Parties
COV – Covariance [%]
CR – Compression Ratio [-]
DI – Direct Injection
DNS – Direct Numerical Simulation
ECR – Effective Compression Ratio [-]
ECU – Engine Control Unit
E-EGR – External Exhaust Gas Recirculation
EGT – Exhaust Gas Temperature
EIVC – Early Intake Valve Closing
ESL – Engine Skeleton Layout
ESDU – Engineering Science Data Unit
ESTEC – Economy with Superior Thermal Efficient Combustion
EVO – Exhaust Valve Open
EVs – Electric Vehicles
E94 – Brazilian ethanol
FCA – Fiat Chrysler Automobiles
FCC – Fuel Conversion Efficiency [-]
FEA – Finite Element Analysis

FEM – Finite Element Method
FFT – Fast Fourier Transform
FMEP – Friction Mean Effective Pressure [kPa]
FVM – Finite Volume Method
FVV - *Forschungsvereinigung Verbrennungskraftmaschinen*
GCR – Geometrical Compression Ratio [-]
GDI – Gasoline Direct Injection
GGG-70 – Cast iron with nodular graphite
GJL – Gray cast iron
GJS – Cast iron with nodular graphite
GJV – Cast iron with vermicular graphite
GM – General Motors
GSE – Global Small Engine
GTS-70 – Black malleable cast iron
HIP – Hot Isostatic Pressing
HLA – Hydraulic Lash Adjuster
HPFP – High Pressure Fuel Pump
HVOF – High Velocity Oxygen Fuel
ICE – Internal Combustion Engines
IEA – International Energy Agency
I-EGR – Internal Exhaust Gas Recirculation
IMEP – Indicated Mean Effective Pressure [kPa]
IPI – Vehicle manufacturing tax, from Portuguese, Imposto sobre Produto Industrializado
LES – Large Eddy Simulation
LHV – Lower Heating Value [kJ/kg]
LPG – Liquefied petroleum gas
MFB – Mass Fraction Burn [-]
MBT – Maximum Brake Torque [N.m]
MEP – Mean Effective Pressure [kPa]
MOFT – Minimum Oil Film Thickness
MON – Motor Octane Number
NA – Naturally Aspirated

NEDC – New European Driving Cycle
NFAM – Normalized Flame Area Map
OECD – Organization for Economic Co-operation and Development
OEM – Original Equipment Manufacturer
PFI – Port Fuel Injection
P_{MAX} – Absolute highest ignition pressure
P_{MEP} – Pumping Mean Effective Pressure [kPa]
PN – Part Number
POFP – Peak Oil Film Pressure
PV – Pressure-Volume
PVD – Physical Vapor Deposition
PWI – Port Water Injection
RANS – Reynolds Averaged Navier-Stokes
RDE – Real Driving Emissions
RON – Research Octane Number
Rpm – Revolutions per minute
S/B – Stroke-to-Bore
SFC – Specific Fuel Consumption [g/kW.h]
SI – Spark Ignited
S-N – Strength to cycles
SUV – Sport Utility Vehicle
S/V – Surface-to-volume
TBCs – Thermal Barrier Coatings
TC – Turbo-Compressor
TDC – Top Dead Center
THC – Total hydrocarbon content
TKE – Turbulent Kinetic Energy [m²/s²]
TS – Temperature-Entropy
VCR – Variable Compression Ratio
VC-T – Variable Compression – Turbo
VDE – Vehicle Demand Energy
VTG – Variable Turbine Geometry
VVA – Variable Valve Actuation

VVL – Variable Valve Lift

VVT – Variable Valve Timing

VW – Volkswagen

WCAC – Water Charge Air Cooler

WI – Water Injection

WFR – Water-to-Fuel Ratio

LIST OF SYMBOLS

CO₂ – Carbon Dioxide

CO – Carbon Monoxide

HC – Hydrocarbon

W_i – Engine indicated work [kJ]

P – Pressure [kPa]

\forall - Volume [m³]

W_{Net} – Net indicated work [kJ]

W_{Gross} – Gross indicated work [kJ]

$W_{Pumping}$ – Pumping work [kJ]

IMEP – Indicated Mean Effective Pressure [kPa]

V_d – Engine displacement [m³]

PMEP - Pumping Mean Effective Pressure [kPa]

$P_{indicated}$ – Indicated power [kW]

n_R – Number of engine revolution for each power stroke [-]

N – Engine operating frequency [Hz]

P_{Brake} – Engine brake power [kW]

T – Engine brake torque [N.m]

P – Engine power [kW]

Z – Number of engine cylinders [-]

A_p – Cylinder bore area [m²]

S_p – Mean piston speed [m/s]

B – Cylinder bore [m]

L – Piston stroke [m]

r_c – Volumetric compression ratio [-]

V_c – Engine combustion chamber [m³]

V_d - Engine displacement volume [m³]

η_t – Otto cycle thermal efficiency [-]

γ – Polytropic exponent or specific heats ratio [-]

Q_t – Heat released by the combustion process [kJ]

η_c – Engine combustion efficiency [-]
 LHV_f – Fuel lower heating value [kJ/kg]
 H_{NO_2} – Enthalpy of formation of NO₂
 NO₂ – Nitrogen dioxide
 $[NO_x]$ – NO₂ mixture concentration
 H_{CO} – Enthalpy of formation of CO
 $[CO]$ – Mixture concentration of CO
 $[THC]$ – Mixture concentration of THC
 η_f – Fuel conversion efficiency [-]
 m_c – Fuel mass supplied to the engine [kg]
 \dot{m}_c – Fuel mass flow supplied to the engine [kg/s]
 sfc - Specific fuel consumption [g/kW.h]
 $P_{friction}$ – Friction power [kW]
 η_m – Engine mechanical efficiency [-]
 η_v – Volumetric efficiency [-]
 m_a – Air mass supplied to the engine [kg]
 \dot{m}_a – Air mass flow consumed by the engine [kg/s]
 ρ_a – Air density [kg/m³]
 u' - Instantaneous flow velocity [m/s]
 \bar{U} – Mean flow velocity [m/s]
 U_T – Turbulent burning velocity
 f_T – Turbulence factor
 U_L – Laminar burning velocity
 $\Delta\theta_d$ – Combustion duration
 C₂H₅OH – Anhydrous ethanol
 $(A/F)_{stoich.}$ – Stoichiometric air-fuel ratio [-]
 M_a – Molecular weight of air [kg/kmol]
 M_{eth} - Molecular weight of anhydrous ethanol [kg/kmol]
 m_f – Fuel mass [kg]
 N_a – Air number of mols
 N_{eth} - Ethanol number of mols

$(A/F)_{real}$ – Real mixture air-fuel ratio [-]
 λ_{exh} - Lambda factor [-]
 NO_x – Nitrogen oxide
 r – Crank radius [m]
 l – Connecting rod length [m]
 S_0 – Higher piston position related to crankshaft center [m]
 S_x – Instantaneous piston position throughout the engine stroke [m]
 S – Difference between S_0 and S_x [m]
 φ – Rotational crank angle
 ψ – Connecting rod pivot angle
 λ_{rod} – Connecting rod ratio [-]
 v – Instantaneous piston speed
 a – Instantaneous piston acceleration
 ω – Crankshaft angular speed [rad/s]
 L – Engine stroke [m]
 V_d – Engine displacement volume [m³]
 SB_{ratio} – Stroke to bore ratio
 y – Total engine offset
 F_{Gas} – Gas force
 $F_{Mass\ Osc.}$ – Mass oscillating force
 $p(\varphi)$ – In-cylinder pressure as function of crankshaft angle [kPa]
 A_p – Cylinder area
 $m_{osc.}$ – Oscillating mass [kg]
 F_{Conrod} – Conrod force
 F_N – Normal force
 $F_{Conrod\ rot.}$ – Rotating connecting rod inertia force
 $F_{Crank\ Pin}$ – Crank pin force
 $F_{Conrod\ Bear.}$ – Connecting rod bearing force
 $F_{Crank\ Pin\ rot.}$ – Rotating inertia force of the crank pin
 $F_{Counterweight}$ – Force of the counterweight
 $F_{Main\ Journal}$ – Main journal force
 F_{Tm} – Mean tangential force

W_S – Rotational kinetic energy

I – Moment of inertia [kg.m²]

ω_{max} – Maximum crankshaft rotational speed

ω_{min} – Minimum crankshaft rotational speed

δ – Degree of irregularity

ω_m – Mean rotational speed

$T_a(\varphi)$ – Net torque applied to the shaft in function of the shaft position

$\dot{\omega}$ – Angular acceleration about the axis of rotation

$T(\varphi)$ - Instantaneous torque applied to the shaft [Nm]

T_m , - Mean Torque [Nm]

R_{gyr} – Radius of gyration [m]

m – Flywheel mass [kg]

D_{fly} – Inertia diameter [m]

WG_{fly} – Flywheel weight calculation [N]

σ_{max} – Hoop stress [MPa]

ν – Poisson's ratio

σ_f – Failure stress

Gap – Ring gap clearance

δ - Piston pin ovalization

σ_N – Normal stress

σ_a – Bending stress

σ_o – Ovalizing stress

τ – Shear stress

Si₃N₄ – Silicon Nitride

$\omega_{max_circlip}$ – Maximum engine speed allowable for a round circlip without hooks [rad/s]

E – Young's module [GPa]

K_e – Empirical factor considering the influence of adjacent crank and bearing restraint

τ_N – Nominal alternating torsional stress referred to crankpin or journal [N/mm²]

M_{TN} – Maximum alternating torque [Nm]

W_P – Polar section modulus related to cross-section of crankpin or journal [mm³]

L_b/D_b – Length to diameter ratio

p_b – Pressure on bearing

L_b – Bearing length [mm]
 D_b – Bearing diameter [mm]
 P_i – Cylinder liner internal pressure [MPa]
 t – Cylinder liner thickness [mm]
 R_{all} – Additional metal thickness [mm]
 MI – Mach index
 A_v – Valve curtain area [m²]
 C_d – Discharge coefficient
 a – Speed of sound [m/s]
 w_{seat} – Valve seat width [m]
 L_v – Valve lift [m²]
 D_v – Valve head diameter [m²]
 K_m – Manifold-port area ratio
 n_v – Number of valves
 K_{LD} – Lift-duration envelope ratio
 τ_{max} – Maximum shear stress [MPa]
 K_B – Stress concentration factor
 C – Spring index
 ξ – Parameter fractional overrun to closure
 k – Valve spring rate [N/mm]
 G – Shear modulus [GPa]
 N_a – Number of active coils
 N_t – Spring total number of coils
 N_i – Number of inactive coils
 L_s – Spring solid length
 L_f – Valve spring free length
 S_{ut} – Ultimate tensile strength [MPa]
 E – Material Young's module
 α – End-condition constant
 f – Valve spring natural frequency [Hz]
 g – Gravity [m/s²]
 γ – Specific weight [N/m³]

RR – Rocker arm ratio
 ϕ – Pressure angle
 β – Angle of the centerlines of cam/roller and roller/pivot
 f_{run} – Resonant frequency [Hz]
 n_{modes} – Odd numbers of quarter wavelengths
 f_{Hel} – Helmholtz frequency [Hz]
 N_c – Number of cycles
 S_e – Corrected endurance limit [MPa]
 S'_e – Uncorrected endurance limit [MPa]
 k_{sur} – Surface condition modification factor
 k_{siz} – Size modification factor
 k_{load} – Load modification factor
 k_{temp} – Temperature modification factor
 k_{rel} – Reliability factor
 k_{mis} – Miscellaneous factor
 S_f – Fatigue strength [MPa]
 f – Fatigue strength factor
 E_{conv} – The convergence error
 t – Fluid density [kg/m³]
 τ_{ij} – Viscous stress tensor [N/m²]
 μ – Dynamic viscosity [Pa.s]
 δ_{ij} – Kronecker delta
 e – Internal energy [kJ/kg]
 K_t – Thermal conductivity [W/m.K]
 D – Mass diffusion coefficient [m²/s]
 h_k – Specific enthalpy of k [kJ/kg]
 T – Temperature [K]
 Y_k – Mass fraction of k
 S – Source of specific energy gain or loss
 B_{pitch} – Cylinder bore pitch [mm]
 R – Resistance [m².K/W]
 h_{eff} – Effective heat transfer coefficient [W/m².K]

N_{rpm} – Engine operating frequency [rpm]

h_c – Instantaneous convective transfer coefficient

C – Clearance [μm]

C_d – Discharge coefficient

CONTENTS

1.	INTRODUCTION.....	34
1.1.	GENERAL ASPECTS.....	34
1.2.	RESEARCH OBJECTIVES	37
1.2.1.	<i>General Objective</i>	38
1.2.2.	<i>Specific Objectives.....</i>	38
2.	LITERATURE REVIEW	38
2.1.	FUEL.....	38
2.1.1.	<i>Ethanol.....</i>	39
2.1.2.	<i>Air-Fuel Mixture Formation.....</i>	42
2.2.	WATER INJECTION.....	44
2.3.	ENGINE KINEMATIC AND ENGINE COMPONENTS ENGINEERING	46
2.3.1.	<i>Geometrical Relationships for Reciprocal Engines</i>	46
2.3.2.	<i>Forces in Reciprocating Mechanism</i>	52
2.3.3.	<i>Flywheel.....</i>	61
2.3.4.	<i>Piston and Piston Rings.....</i>	65
2.3.5.	<i>Piston Pin.....</i>	82
2.3.6.	<i>Piston Circlip</i>	88
2.3.7.	<i>Connecting Rod</i>	89
2.3.8.	<i>Crankshaft.....</i>	99
2.3.9.	<i>Bearings.....</i>	121
2.3.10.	<i>Crankcase.....</i>	126
2.3.11.	<i>Cylinder Liner (Sleeves).....</i>	135
2.3.12.	<i>Cylinder Head</i>	143
2.3.13.	<i>Valvetrain.....</i>	159
2.3.14.	<i>Intake Manifold.....</i>	189
2.3.15.	<i>Bolts and Clamping Force.....</i>	194
2.4.	TURBOCHARGER	197
2.5.	FATIGUE ANALYSIS	200
2.5.1.	<i>S-N Diagrams</i>	201
2.5.2.	<i>Endurance Limit and Fatigue Strength.....</i>	202
2.5.3.	<i>Characterizing Fluctuating Stresses and Failure Criteria</i>	206
2.6.	NUMERICAL SIMULATION	208

2.6.1.	<i>Finite Element Method</i>	208
2.6.2.	<i>CFD Simulation</i>	211
2.7.	STATE OF ART	213
2.7.1.	<i>Ethanol used as fuel</i>	213
2.7.2.	<i>Volumetric compression ratio</i>	214
2.7.3.	<i>Direct injection System</i>	215
2.7.4.	<i>Variable valve timing system</i>	216
2.7.5.	<i>Water injection</i>	217
2.7.6.	<i>Turbocharger</i>	219
3.	METHODOLOGY	220
3.1.	ENGINE DEVELOPMENT PLAN	221
3.2.	ENGINE SPECIFICATION AND BASIC DATA	222
3.2.1.	<i>Engine Displacement Limit and Number of Cylinders</i>	222
3.2.2.	<i>Volumetric Compression Ratio</i>	223
3.2.3.	<i>Cylinder Bore and Bore Pitch</i>	223
3.2.4.	<i>Stroke-to-Bore Ratio</i>	224
3.2.5.	<i>Engine Crank-Stroke and Crank-Radius</i>	226
3.2.6.	<i>Connecting Rod Ratio</i>	227
3.2.7.	<i>Piston Pin and Crankshaft Offset</i>	230
3.2.8.	<i>Engine Stroke (Piston True Stroke)</i>	233
3.2.9.	<i>Effective Engine Displacement</i>	233
3.2.10.	<i>IMEP, Torque and Power Target</i>	233
3.2.11.	<i>Engine Specification Summary</i>	234
3.3.	ENGINE COMPONENTS DESIGN	235
3.3.1.	<i>Engine Skeleton Layout</i>	237
3.3.2.	<i>Engine Piston and Piston Rings</i>	237
3.3.3.	<i>Piston Pin</i>	253
3.3.4.	<i>Piston Circlip</i>	255
3.3.5.	<i>Connecting rod</i>	256
3.3.6.	<i>Crankshaft and Bearings</i>	261
3.3.7.	<i>Flywheel</i>	265
3.3.8.	<i>Cylinder liner (sleeve)</i>	267
3.3.9.	<i>Crankcase</i>	271

3.3.10.	<i>Cylinder Head, Valvetrain System and Fuel injection System</i>	275
3.3.11.	<i>Clamping forces</i>	304
3.3.12.	<i>Intake manifold and Water injection System</i>	308
3.3.13.	<i>Lubricant oil circuit</i>	312
3.3.14.	<i>Engine timing belt</i>	313
3.3.15.	<i>Engine Accessories and Starter</i>	314
3.3.16.	<i>Turbocharger</i>	316
3.4.	1D NUMERICAL SIMULATION MODEL	317
4.	RESULTS	320
4.1.	FEM NUMERICAL SIMULATION	321
4.1.1.	<i>Piston</i>	321
4.1.2.	<i>Piston Pin</i>	324
4.1.3.	<i>Connecting rod</i>	326
4.1.4.	<i>Liner</i>	328
4.1.5.	<i>Crankshaft</i>	330
4.1.6.	<i>Crankcase</i>	332
4.2.	1D NUMERICAL SIMULATION	332
4.3.	HIGHLY BOOSTED PROTOTYPE ENGINE	344
5.	CONCLUSION	344
5.1.	SUGGESTIONS FOR FUTURE RESEARCH	346
	REFERENCE	347

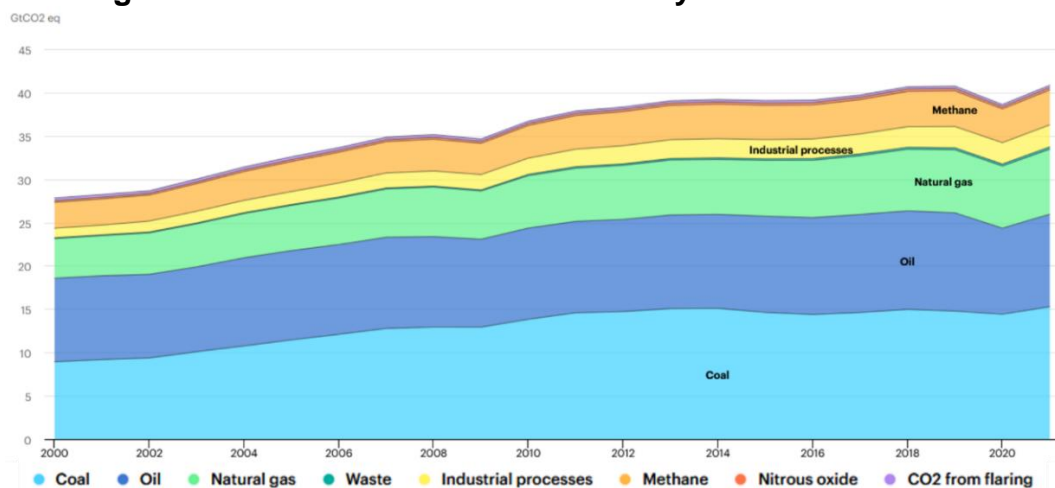
1. INTRODUCTION

The general aspects on which this work is based, as well as the general and specific objectives that guide it, are addressed in this introduction.

1.1.General Aspects

Managing world energy production and consumption is the key to human longevity. Thus, international agreements such as the RIO+20 and the Glasgow Climate Pact (COP-26) have established strategies and goals to reduce energy consumption and global emission levels. In an attempt to limit global warming to 1.5°C, the COP-26 signatory countries are committed to drastically reducing the levels of CO₂ emissions, 70% of which are caused by the burning of fossil fuels (United Nations Climate Change 2021). However, after a period of stability in CO₂ emission levels between 2014 and 2016, recent data (Figure 1) show a regrowth tendency over the last couple of years, even though the COVID-19 pandemic scenario caused the levels of CO₂ emissions to reduce between 2019 and 2020. The production resumption and consumption of goods recovery have raised the levels of CO₂ emissions to values higher than those reached before the pandemic (BP 2018; IEA 2021).

Figure 1 – CO₂ emissions between the years 2000 and 2021



Source: (IEA 2021)

Globally, the road transport sector is one of the main CO₂ emission sources. Among the OEDC (Organization for Economic Co-operation and Development) countries, the road transportation achieved an average of 26.6% of total CO₂ emissions

in 2016 (WARNECKE W. 2018). Nevertheless, even in countries in which initiatives to increase energy efficiency and use renewable energy sources are well advanced, the road traffic sector has not contributed significantly to reducing CO₂ emissions. For instance, the overall emissions from Germany, converted into CO₂ equivalents, were reduced by 27% between 1990 and 2015, and the main sectors responsible for these reductions were the construction sector (34%) and industry (32%). The road traffic sector, on the other hand, achieved a reduction of only 2%, which even decreased to 0% at the end of 2016. According to (SCHAEFFLER 2018), the increase in CO₂ emissions levels, despite the reduction in fuel consumption per distance traveled, is attributed to the growing vehicular fleet. Globally, it is estimated that the number of cars worldwide will be around 2 billion by 2050.

Given the necessity to reduce carbon dioxide emissions by road transport sector, automotive companies have been researching and developing new technologies for internal combustion engines (ICE) over the last few years. The evolution of the engine design might be verified by the technologies applied to modern propulsion systems, such as fuel direct injection (DI), turbochargers, variable valve actuation (VVA) systems, internal or external exhaust gas recirculation (I-EGR /E-EGR), variable compression ratio (VCR) systems, water injection (WI), among others (Rocha et al. 2021; SILVA et al. 2016; SILVA et al. 2017a, 2017b). Furthermore, these technologies have been used along with engine design concepts such as downsizing, down-speeding, and the most recent approach, rightsizing. While the engine downsizing and down-speeding concepts are currently well known by the engineering community, the rightsizing concept is not so widespread. In an overview, it can be defined as the engine displaced volume adequacy in relation to the vehicle weight in order to achieve the required results by the homologation cycles and a better vehicle drivability (SILVA 2017; AUDI 2018; BAËTA, Pontoppidan, and Silva 2015).

Besides the aforementioned technologies and engine concepts, the use of alternative fuels, such as ethanol, has shown to be a promising way to reach the established levels of fuel consumption and pollutant emissions defined by international agencies. The physicochemical properties of ethanol, such as the high octane rating and the high latent heat of vaporization, allows the engine to operate at high load conditions with a lower knock tendency, which in turn makes possible the development of a turbocharged engine with a high volumetric compression ratio. As a result, there

would be both an increase in the thermal efficiency of the engine and a reduction in CO₂ emission levels (HEYWOOD 2018; BAËTA, Pontoppidan, and Silva 2015).

In Brazil, ethanol is known as hydrated ethanol or hydrated ethyl alcohol. It is mainly extracted from sugar cane and is composed by 94% of ethanol and 6% of water, on a volumetric basis (Agência Nacional de Petróleo ANP 2015). As an alternative to hydrated ethanol produced from sugar cane, other sources for hydrated ethanol production such as corn, sweet sorghum and biomass have been presented, aiming at competitive fuel prices and production stability during the sugarcane off-season (EMBRAPA 2012). In order to comply with the international standards for energy consumption and pollutant emissions, the Brazilian government created two main programs called *RenovaBio* and *Rota-2030*. *RenovaBio* aims to promote the expansion of biofuels in the Brazilian energy matrix and ensure fuel market predictability. *Rota-2030* aims to develop the automobile industry by reducing taxes, increasing energy efficiency and reducing vehicle pollutant emissions (Agência Nacional do Petróleo ANP 2018; BrazilGovNews 2018).

Nowadays, despite the strong appeal for the use of electric vehicles (EVs), the spread of the growing technological development of ICEs remains very important for the sustainable future of mobility. This happens because in order to evaluate the environmental impact of EVs, it is essential to analyze their entire life cycle, from their production to battery recycling, rare metals and their extraction techniques and the power generation sources. Only 5% of the lithium-ion batteries are recycled and the mining activity needed to extract their rare minerals is still a concern, since the contamination of water and soil with heavy metals constitutes large-scale pollution and security issues. Beyond that, 65% of global electricity still comes from the burning of non-renewable fossil fuels. In addition, electric vehicles are only CO₂-free if their electric power comes from renewable sources, which is also true for ICE vehicles fueled by biofuels, such as ethanol (A.C.T. Malaquias et al. 2019). Hence, it is clear that the association between electric vehicles and sustainability is not necessarily correct. For instance, when addressing a holistic and cognitive approach to vehicle sustainability, Zoldy et al. (2022) report that, beyond the use phase, the precepts of sustainable development should be deemed during design, production, and waste management. As the literature shows, the sustainability concept has different dimensions, such as environmental, economic, social, and cultural, and its analysis should not be simplified or limited to a certain type of vehicle propulsion system.

According to Andersson et al. (2020), the transition to a more sustainable transportation should not disregard the consumer's cost perception, which is preponderant in the decision-making process. This is one of the factors that lead Gonçalves et al. (2022) to state that, for future Brazilian mobility, the use of ethanol in flex-fuel vehicles is still the best solution when managing economic, environmental, social, and infrastructure aspects.

In Brazil, the first ethanol-fueled engines were launched in the market in the 1970s as a result of the Proalcool government program. However, at that time, these engines were basically gasoline engines with a higher volumetric compression ratio and a colder spark plug, without any further updates for the proper use of the ethanol as a fuel option. It is worth to point out that most of development studies in that time had to be declined due to fast response to make available an engine running on ethanol required from the automotive market. In 2004, 34 years later, the flex-fuel engine technology was created. A flex-fuel engine is able to run using gasoline, ethanol or any proportion of them. Despite the advantages of a flex-fuel ICE, the engine could not be optimized for each kind of fuel, which in turn lead to an engine which is not capable to exploit completely the benefits of each fuel and maximize the fuel conversion efficiency of them (BAËTA, Pontoppidan, and Silva 2015; A. Malaquias et al. 2020).

In this context, the development of a novel internal combustion engine employing modern design concepts, equipped with state-of-the-art technologies and conceived to operate with the exclusive use of ethanol as a fuel, is understood as an innovative and promising pathway for Brazilian future mobility, from both technological and sustainability perspectives. Therefore, this work presents a development procedure of a prototype turbo engine from geometrical main dimensions to 3D-CAD design and FEM simulation of each engine component. This new engine aims to use Brazilian ethanol as fuel, assisted by water injection in order to achieve the full spark authority condition which means that the engine is capable to run with MFB50 at the MBT regardless its load and speed. Furthermore, a 1D model was developed and calibrated based on experimental results in order to obtain the predicted indicated engine performance and evaluate the influence of the water injection approach on it.

1.2. Research Objectives

The general and specific objectives of this work is presented in this topic.

1.2.1. General Objective

This work aims to develop a novel downsizing prototype internal combustion engine entirely designed to run specifically on hydrated ethanol assisted by a port water injection able to achieve higher fuel conversion efficiency by operating at loads higher than 30 bar of Indicated Mean Effective Pressure (IMEP) on full spark authority condition.

1.2.2. Specific Objectives

In order to achieve the general objectives, the following specific objectives are established:

- Assess both modern technologies and the main design characteristics applied on internal combustion engines;
- Define the engine basic geometrical data based on modern design approaches not previously used on an engine running exclusively on ethanol as fuel;
- Design completely new the engine components in Computer-Aided Design (CAD) software and subject them to thermal and mechanical loading using a Finite Element Method (FEM) for performance evaluation;
- Create a 1D computational model able to predict the performance of the novel engine designed.

2. LITERATURE REVIEW

2.1. Fuel

The fuel is responsible for providing energy to the engine for its operation. Consecutively, the fuel properties have a significant influence on the engine performance and emissions. As the hydrated ethanol was used in this work, it is discussed only about it. Information about another fuel may be found on the available literature.

2.1.1. Ethanol

The ethanol is a chemical compound belonging to the family of alcohols containing in its chemical formula, C_2H_5OH , two carbon atoms and an OH radical, which characterizes it as alcohol. It can be obtained through vegetables rich in sugars such as sugar cane in Brazil and corn in the United States of America, (BAËTA 2006).

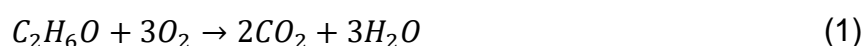
In Brazil, the ethanol as fuel is used in two ways: in the form of anhydrous ethanol, as a blending component in the formation of type C gasoline, or as hydrated ethanol, sold throughout the country as a finished product (ANP 2016). The Brazilian ethanol is also called E94 due to its 94% ethanol content and 6% of water. The Table 1 presents some of the E94 limit properties established by the National Petroleum Agency, ANP, in Brazil. The fuel LHV, used in this work was 24.76 MJ/kg, according to the results of tests carried out by (MELO 2012).

Table 1 – The hydrated ethanol fuel properties according to ANP

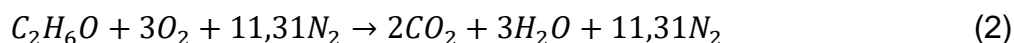
Characteristic	Unit	Value
Fuel density at 20°C	kg/m ³	805,2 - 811,2
Ethanol content	% Mass	92,5 - 96,5
Water maximum content	% Mass	7,5

Source: (Agência Nacional de Petróleo ANP 2015)

The anhydrous ethanol combustion reaction may be described as follow:



However, considering the fuel burning reaction with atmospheric air (20.95% of oxygen and 79.05% of nitrogen on volumetric base), a new combustion equation is obtained.



In order to calculate the anhydrous ethanol stoichiometric air-fuel ratio, $(A/F)_{stoich.}$, it was considered the molecular weight of 29 kg/kmol and 46 kg/kmol for air, M_a , and anhydrous ethanol, M_{eth} , respectively. Thus, the anhydrous ethanol stoichiometric air-fuel ratio is calculated as follow:

$$(A/F)_{stoich.} = \frac{m_a}{m_f} = \frac{N_a \cdot M_a}{N_{eth} M_{eth}} = \frac{(14,31) \cdot (29)}{(1) \cdot (46)} \approx 9,0 \text{ kg}_{ar}/\text{kg}_{et} \quad (3)$$

Where, the fuel mass is m_f [kg] and N_a and N_{eth} are the air and ethanol number of mols, respectively.

As aforementioned, the Brazilian ethanol has 6% of water on it, which in turn it changes the fuel stoichiometric air-fuel ratio. In order to calculate a new chemical formula for the hydrated ethanol, it is required to calculate the new mixture molar ratio. The Table 2 shows the hydrated ethanol fuel properties to calculate its molar ratio. (PERRY and Green 2008)

Based on the fuel properties shown in Table 2 the hydrated ethanol properties may be obtained. Such properties presented in the Table 3 are in accordance with the fuel characteristics established by the ANP in Table 1.

Table 2 – The hydrated ethanol fuel properties to calculate its molar ratio

Component	Anhydrous Ethanol	Water
Volumetric content ratio [%]	94	6
Density a 20°C [kg/m ³]	789,7	997,2

Weighted mass [kg]	742,3	59,8
Total mass [kg]	802,2	
Mass content ratio [%]	92,5	7,5
Molecular weight [kg/kmol]	46	18
Number of mols	2,01	0,41
Total number of mols	2,42	
Molar content ratio [%]	83,1	16,9

Source: (PERRY and Green 2008) and (SILVA 2017)

Table 3 – The calculated hydrated ethanol fuel properties

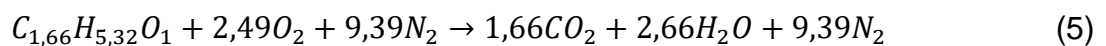
Characteristic	Unit	Value
Fuel density at 20°C	kg/m ³	805,2
Ethanol content	% Mass	92,5
Water maximum content	% Mass	7,5
Mixture molecular weight	Kg/kmol	41.2

Source: (SILVA, 2017)

The chemical formula found, based on the molar fraction of the mixture, which represents hydrated ethanol is:



The combustion reaction of the proposed hydrated ethanol with atmospheric air can be described as:



In order to calculate the hydrated ethanol stoichiometric air-fuel ratio, $(A/F)_{stoich.}$, it was considered the molecular weight of 29 kg/kmol and 41.2 kg/kmol for air, M_a , and hydrated ethanol, M_{eth} , respectively. Thus, the hydrated ethanol stoichiometric air-fuel ratio is calculated as follow:

$$(A/F)_{stoich.} = \frac{m_a}{m_c} = \frac{N_a \cdot M_a}{N_{eth} M_{eth}} = \frac{(11,88) \cdot (29)}{(1) \cdot (41,2)} \approx 8,36 \text{ kg}_{ar} / \text{kg}_{et} \quad (6)$$

According to (PULKRABEK 1997), the advantages of ethanol as fuel are:

- It can be obtained from numerous sources, both natural and manufactured;
- Contains high octane with high resistance to abnormal combustion;
- It presents lower levels of pollutant emissions when compared to gasoline;
- High latent heat of vaporization, which results in a higher charge cooling effect, compared to gasoline;
- Low sulfur content.

On the other hand, the ethanol as fuel disadvantages are, (PULKRABEK 1997):

- Lower energy content;
- Greater amount of aldehydes in the exhaust gases, which for emissions would be a problem;
- Ethanol as fuel is much more corrosive than gasoline to copper, bronze, aluminum, rubber and plastic, imposing some restrictions on engine designs that use this fuel;
- Engine start cranking issues at lower temperatures due to low vapor pressure and vaporization.

2.1.2. Air-Fuel Mixture Formation

In the current internal combustion engines, the fuel supply comes from an electronic fuel injection system. The function of this system is to provide the adequate amount of fuel for the formation of the air-fuel mixture that can be efficiently burned, thus improving the engine performance and emissions for the entire range of engine operation. The air-fuel mixture formation may be called external mixture formation

when a Port Fuel Injection (PFI) system is used or internal mixture formation when Direct Injection (DI) system is used, (F. SCHÄFER 2017).

The air-fuel mixture can be stoichiometric, rich, or lean. A stoichiometric mixture is called when the amount of fuel supplied to the engine is proportional to the amount of air present in the cylinder for a complete burn. On the other hand, the air-fuel mixture is rich if the amount of fuel supplied to the engine is greater than the amount of air present in the cylinder. Conversely, the air-fuel mixture is considered lean when the amount of fuel supplied to the engine is less than the amount of air present in the cylinder, (HEYWOOD 2018).

A common approach to identify if the air-fuel mixture is stoichiometric, rich, or lean, is comparing the real mixture air-fuel ratio $(A/F)_{real}$ to the stoichiometric mixture air-fuel ratio. The factor that expresses this relationship between air-fuel ratios is called the lambda factor, λ_{exh} , and it can be calculated according to Equation 7, (HEYWOOD 2018).

$$\lambda_{exh} = \frac{(A/F)_{real}}{(A/F)_{stoich.}} \quad (7)$$

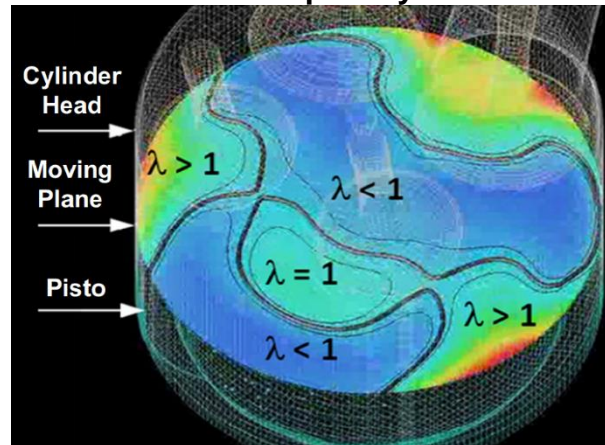
The lambda factor value is equal to 1, $\lambda_{exh} = 1$, indicates that the air-fuel mixture is stoichiometric. If the lambda factor value is lower than 1, $\lambda_{exh} < 1$, indicates that the air-fuel mixture is rich. On the other hand, If the lambda factor value is higher than 1, $\lambda_{exh} > 1$, indicates that the air-fuel mixture is lean, (BAËTA 2006).

The lambda factor is measured by means of an oxygen sensor fitted on the engine exhaust pipe just after exhaust branches joint. However, due to the cylinder-to-cylinder supplied air mass difference, it has been used a lambda sensor fitted individually on each cylinder exhaust branch in order to supply each cylinder with the corrected amount of fuel which leads to a smooth engine operation. Further improvement on the engine operation, related to the ignition timing, may be achieved by fitting individually Exhaust Gas Temperature (EGT) sensors on each cylinder exhaust branch, (di Giacomo A. Pignone 2003).

It is worth to point out that, even if the oxygen sensor fitted on the engine exhaust pipe indicates, for instance, a stoichiometric mixture, it does not mean that inside the engine combustion chamber the air-fuel mixture is evenly stoichiometric.

The lambda factor value may vary spatially inside the combustion chamber as shown by Figure 2. Lambda factor value spatially different inside the combustion chamber is a result of the combination among the in-cylinder flow pattern, the type of the fuel system used, the engine operating condition and parameters, and combustion chamber design, (BAËTA, Pontoppidan, and Silva 2015).

Figure 2 – The lambda factor value spatially inside a combustion chamber



Source: (BAËTA, Pontoppidan, and Silva 2015)

2.2. Water Injection

Recent searches have been investigating the WI approach for automotive internal combustion engines although its use is not new. The WI technology was firstly used in aircraft engines during 40`s and later in Formula One engines during 80`s as an option to increase the engine power output. Due to its high enthalpy of vaporization, the WI into engine results in a higher charge cooling effect, which in turn, increases the air density and increase the air mass flow into the engine, (BORETTI 2013; ROHIT et al. 2017).

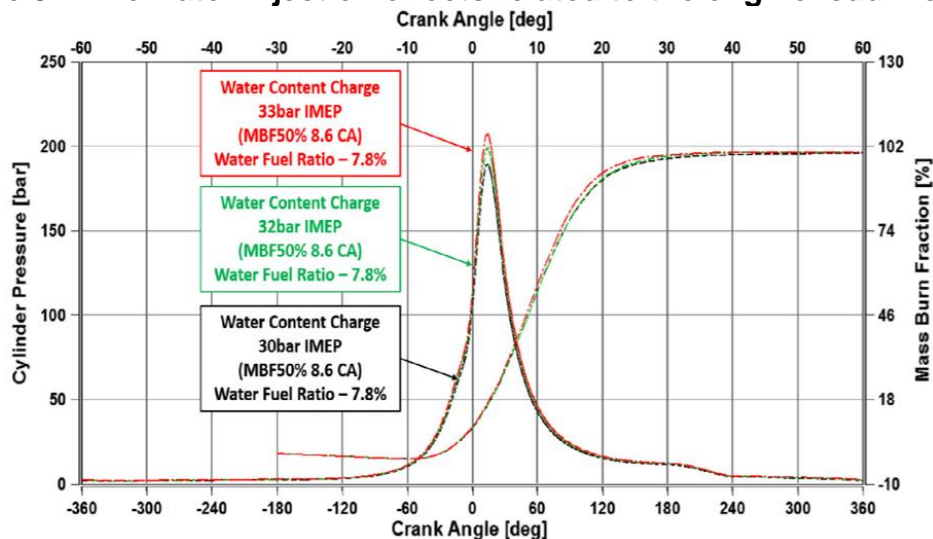
The water molecule is a triatomic molecule and hence it has a higher specific heat than air. The presence of water vapor in the combustion chamber increases specific heat capacity, assuming the same equivalence ratio, which results in lower combustion temperature and lower nitrogen oxide (NOx) emissions, (MINGRUI et al. 2017; NICHOLLS 1969). Furthermore, the presence of water vapor can lead to an increase of the specific heat capacity of air charge as compared to carbon dioxide (CO₂) on a mass basis, which in turn could become a potential replacement of cooled EGR system, (Bozza, De Bellis, and Teodosio 2016; JEREMY et al. 2017).

Additionally, the water molecules may dissociate into H and OH radicals due to the peak temperatures during the combustion process. According to experimental investigation, the formation of NO is suppressed in the presence of OH radicals. In general, studies have suggested that WI in gasoline DI engines reduces NO_x, increases the unburned hydrocarbons (HC) and it has minimal effects on carbon monoxide (CO) and CO₂, (ROHIT et al. 2017; J.-K. WANG et al. 2009).

Despite of WI the benefits to the engine performance and emissions, the WI has drawbacks in the combustion process. The WI into the engine reduces the flame propagation speed, which in turn, it requires an optimum amount of water injected for a given engine running condition as well as a carefully spark timing adjustment in order to maximize the benefits of it, (HARRINGTON 1982).

Figure 3 illustrates the water injection effects on the engine running condition related to the engine load increase. As shown in Figure 3, the WI allows the engine to achieve a highly boosted load at the MBT condition, (BAËTA et al. 2018).

Figure 3 – The water injection effects related to the engine load increase



Source: (BAËTA et al. 2018)

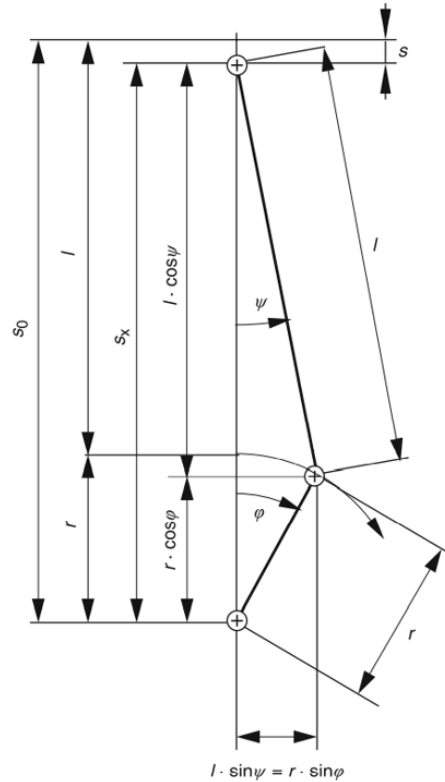
2.3. Engine Kinematic and Engine Components Engineering

In this topic is presented the firstly about the engine kinematic, forces and balancing. Then, it is presented the main engine elements design engineering such as piston, piston pin, connecting rod, crankshaft, crankcase, cylinder head and valvetrain. In addition, the concepts of thermal and mechanical fatigue are introduced.

2.3.1. Geometrical Relationships for Reciprocal Engines

The pressure forces from combustion process are transmitted directly to the crankshaft via piston pin and connecting rod. Therefore, a proper setting of the engine kinematics parameters according to its application establishes the engine basic operation behavior (Pischinger 2012; F. SCHÄFER 2017). Figure 4 shows a scheme of the main geometrical engine dimensions that defines its cranktrain kinematic.

Figure 4 – Engine cranktrain kinematic scheme



Source: (F. SCHÄFER 2017)

On Figure 4, r is the crank radius [m], l is the connecting rod length [m], S_0 is the higher piston position related to crankshaft center [m], S_x is the instantaneous piston position throughout the engine stroke [m], S is difference between S_0 and S_x [m], φ is the rotational crank angle and ψ is the connecting rod pivot angle.

The crankshaft radius and the connecting rod length ratio is called connecting rod ratio [-], as shown by Equation 8.

$$\lambda_{rod} = \frac{r}{l} \quad (8)$$

The instantaneous piston position (Equation 9), as function of the engine crank angle, can be obtained by rearranging the terms in Equation and replacing the related terms for the connecting rod ratio, (F. SCHÄFER 2017; Pischinger 2012).

$$S = r \cdot \left[1 - \cos \varphi + \frac{1}{\lambda_{rod}} \cdot \left(1 - \sqrt{1 - \lambda_{rod}^2 \cdot \sin^2 \varphi} \right) \right] \quad (9)$$

The instantaneous piston speed v and the instantaneous piston acceleration a equations as function of engine crank angle are obtained by Equation 9 derivation once and twice, respectively, (Pischinger 2012; F. SCHÄFER 2017).

$$v = r \cdot \omega \cdot \left(\sin \varphi + \frac{1}{2} \cdot \lambda_{rod} \cdot \sin 2\varphi \right) \quad (10)$$

$$a = r \cdot \omega^2 \cdot (\cos \varphi + \lambda_{rod} \cdot \cos 2\varphi) \quad (11)$$

Where, ω is the crankshaft angular speed [rad/s].

The engine stroke L [m] is twice the crank radius:

$$L = 2 \cdot r \quad (12)$$

The cylinder displacement volume V_d [m³] is calculated as function of cylinder bore B [m] and piston stroke L [m], according to Equation 13.

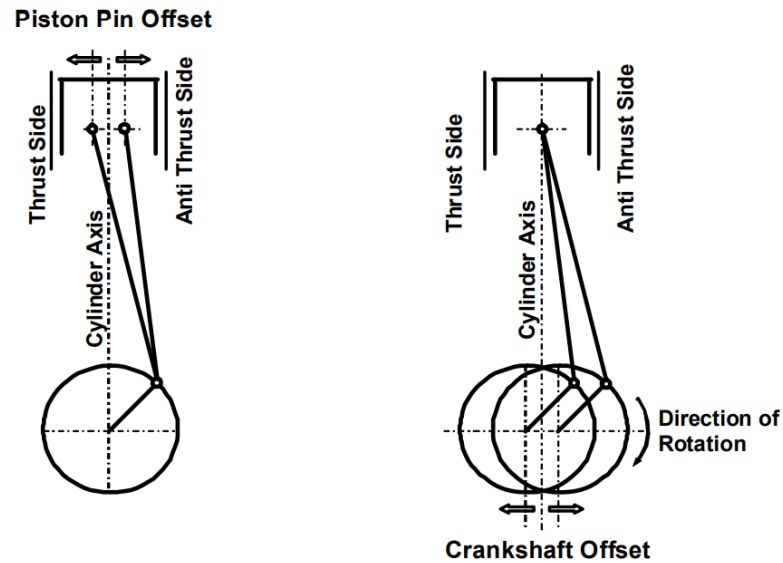
$$V_{dcyl} = \frac{\pi \cdot B^2}{4} \cdot L \quad (13)$$

A further engine parameter is the stroke to bore ratio SB_{ratio} . The bore to stroke ratio affects the enables a correlation among engine combustion chamber size, thermal efficiency, and engine rated speed, (BAËTA 2006). An engine with $SB_{ratio} = 1$ is commonly called square engine whereas if the $SB_{ratio} < 1$ the engine is called over-square and finally, whereas if the $SB_{ratio} > 1$ the engine is called under-square. Typical SB_{ratio} values, for small engines, are between 0.8 and 1.2, (PULKRABEK 1997). The stroke to bore ratio is given by Equation 14.

$$SB_{ratio} = \frac{L}{B} \quad (14)$$

As shown by Figure 5, the engine cranktrain can be implemented with a piston pin offset and/or a crankshaft offset also called piston or crankshaft de-axing. The reasons for these offset implementations may be the engine acoustics, friction, mechanical load and geometric arrangement, (F. SCHÄFER 2017; Pischinger 2012).

Figure 5 – Engine cranktrain, piston pin offset and crankshaft offset



Source: (Pischinger 2012)

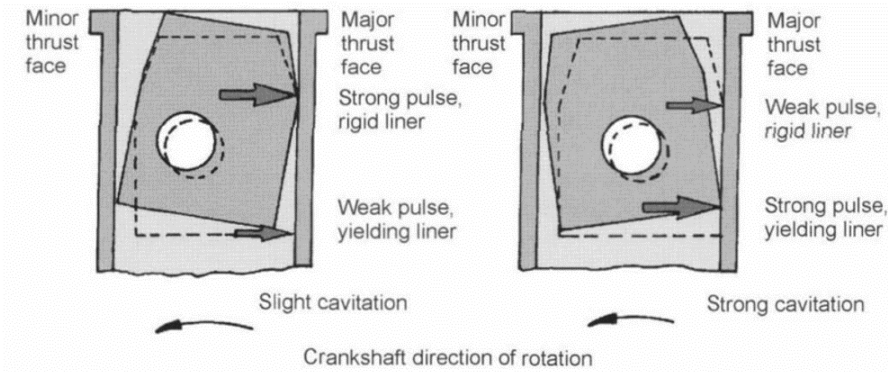
The total engine offset y [m] is given by the difference between the crankshaft offset and the piston pin offset. Nevertheless, the engine total offset is expressed as function of the connecting rod length as shown by Equation 15.

$$\pm e = \frac{y}{l} \quad (15)$$

The parameter $\pm e$ should be positive in case of an offset towards the anti-thrust side and negative in case of an offset towards the thrust side, (Eduard Köhler 2011).

The piston pin de-axing in the thrust direction causes the piston to change its position, also called piston secondary movement, earlier during its upward stroke. As a result of its tilting movement, the piston first rest against the cylinder wall with the piston skirt softening its impact. That is the reason why commonly the piston offset is also known as “noise desaxation”. On the other hand, the piston pin offset in the anti-thrust direction, as commonly used on diesel engines, is called “thermal de-axing”. In this case, the piston remains more in the middle of the cylinder which has a positive effect on the sealing effect of the piston rings and counteracts the build-up of carbon on the piston top land, (F. SCHÄFER 2017). Figure 6 shows the piston secondary movement according to the direction of piston pin de-axing.

Figure 6 – Piston secondary movement according to piston pin de-axing direction



Source: (Pischinger 2012)

The crankshaft offset reduces the sideways force that piston exerts on the cylinder liner during the expansion stroke and thus reduces engine friction. Furthermore, it reduces the piston speed during the earlier part of the expansion stroke improving engine efficiency by completing the combustion process sooner, (HEYWOOD 2018).

According to HEYWOOD (2018), piston pin offset and crankshaft offset may be about 1.5% and 15% of the cylinder bore.

For an engine with crankshaft and or piston pin offset, the piston instantaneous displacement, velocity and acceleration equations may be rearranged to take it to account. According to (F. SCHÄFER 2017) the piston instantaneous displacement, velocity and acceleration for center displaced engine is given by Equation 16, Equation 17 and Equation 18, respectively.

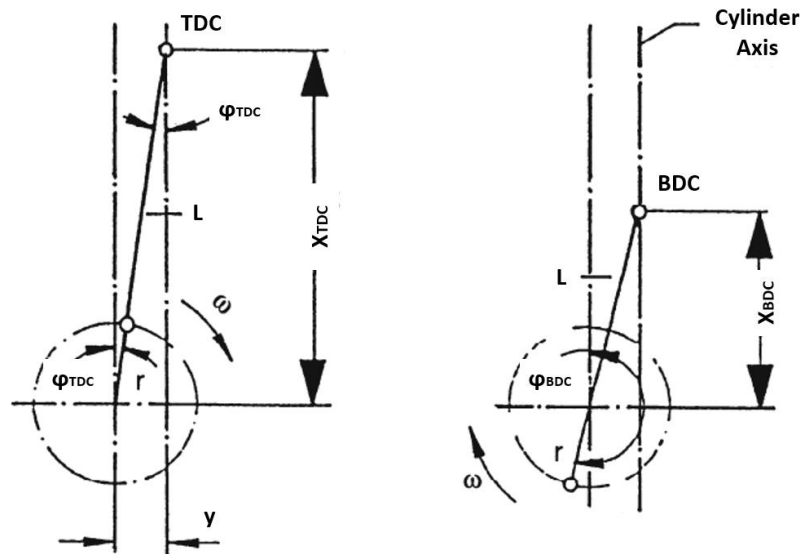
$$S_{off} = r \cdot \left[\cos \varphi + \frac{1}{\lambda_{rod}} \cdot \left(1 - \sqrt{1 - (\lambda_{rod} \cdot \sin \varphi + e)^2} \right) \right] \quad (16)$$

$$v_{off} = -r \cdot \omega \cdot \left(\sin \varphi + \frac{\cos \varphi \cdot (\lambda_{rod} \cdot \sin \varphi + e)}{\sqrt{1 - (\lambda_{rod} \cdot \sin \varphi + e)^2}} \right) \quad (17)$$

$$\begin{aligned}
a_{off} = -r \cdot \omega \cdot & \left[\cos \varphi + \frac{\lambda_{rod} \cdot \cos^2 \varphi \cdot (\lambda_{rod} \cdot \sin \varphi + e)^2}{[1 - (\lambda_{rod} \cdot \sin \varphi + e)^2]^{\frac{3}{2}}} \right. \\
& \left. + \frac{\lambda_{rod} \cdot \cos^2 \varphi - \sin \varphi \cdot (\lambda_{rod} \cdot \sin \varphi + e)}{\sqrt{1 - (\lambda_{rod} \cdot \sin \varphi + e)^2}} \right] \\
& - r \cdot \omega^2 \cdot \left[\sin \varphi + \frac{\cos \varphi \cdot (\lambda_{rod} \cdot \sin \varphi + e)}{\sqrt{1 - (\lambda_{rod} \cdot \sin \varphi + e)^2}} \right]
\end{aligned} \tag{18}$$

The engine stroke must be calculated differently than Equation 12 for an engine with offset implemented. As shown by Figure 7, the offset implementation leads to an asymmetrical piston stroke and a higher engine stroke than twice the crankshaft radius, (Eduard Köhler 2011). Thus, the piston stroke for an engine with offset implemented can be calculated according to Equation 19.

Figure 7 – The TDC and BDC for engines with offset



Source: Adapted from (EDUARD KÖHLER, 2011)

$$\begin{aligned}
L_{off} &= X_{TDC} - X_{BDC} \\
&= \frac{r}{\lambda_{rod}} \cdot \left(\sqrt{(1 + \lambda_{rod})^2 - e^2} - \sqrt{(1 - \lambda_{rod})^2 - e^2} \right)
\end{aligned} \tag{19}$$

Furthermore, the engine geometrical parameters that depends on piston stroke such as the engine volume displacement and the volumetric compression ratio are calculated considering Equation 19. Equation 20 and Equation 21 can be used to

calculate the engine volume displacement and the volumetric compression ratio, respectively.

$$V_{dcyl_off} = \frac{\pi \cdot B^2}{4} \cdot L_{off} \quad (20)$$

$$r_{c_off} = \frac{V_c + V_{dcyl_off}}{V_c} \quad (21)$$

Further effects from the crankshaft offset and the piston pin offset on the engine performance will be discussed in the following chapters of this work.

2.3.2. Forces in Reciprocating Mechanism

The forces in the engine cranktrain of an ICE result from the gas pressure in the combustion chamber and from the inertia forces. As a result of the non-uniform work and motion sequences of the reciprocating engine, the forces in the engine change their size and direction during a work cycle. The forces on the engine are effectively the gas force, oscillating inertia force and rotating inertia force. Figure 8 illustrates the forces that acting on the engine cranktrain.

The forces acting on piston in [N] are gas force F_{Gas} and the mass oscillating force $F_{Mass\ Osc.}$. The mass oscillating force is the combination of piston and connecting rod oscillating force and its acts in the opposite direction to the gas force. Equation may be used for forces on piston calculation, (F. SCHÄFER 2017).

$$F_{piston} = F_{Gas} + F_{Piston\ Osc.} + F_{Conrod\ Osc.} = F_{Gas} + F_{Mass\ Osc.} \quad (22)$$

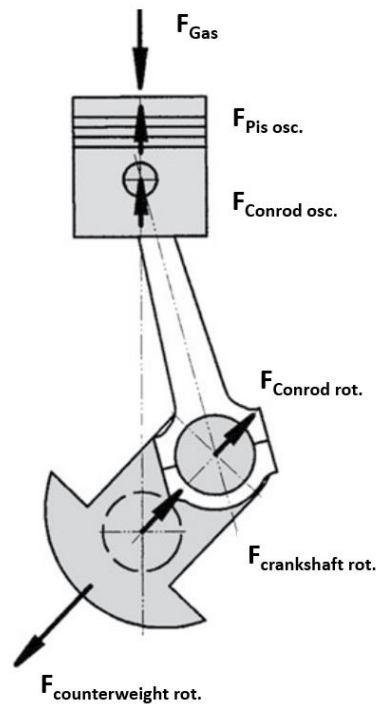
The piston gas force may be calculated from Equation .

$$F_{Gas} = p(\varphi) \cdot A_p \quad (23)$$

Where, the $p(\varphi)$ is the in-cylinder pressure as function of crankshaft angle [kPa] and A_p is the cylinder area calculated according to Equation .

$$A_p = \frac{\pi \cdot B^2}{4} \quad (24)$$

Figure 8 – The forces on the engine cranktrain



Source: Adapted from (SCHÄFER, 2017)

The mass oscillating force or inertia force may be calculated using Equation 25 in case of engines without de-axing and Equation 26 in case of engines with offset implemented.

$$F_{Mass\ Osc.} = -m_{osc.} \cdot a \quad (25)$$

$$F_{Mass\ Osc.\ Off} = -m_{osc.} \cdot a_{off} \quad (26)$$

Where, $m_{osc.}$ is the oscillating mass [kg].

The oscillating mass is calculated by Equation 27.

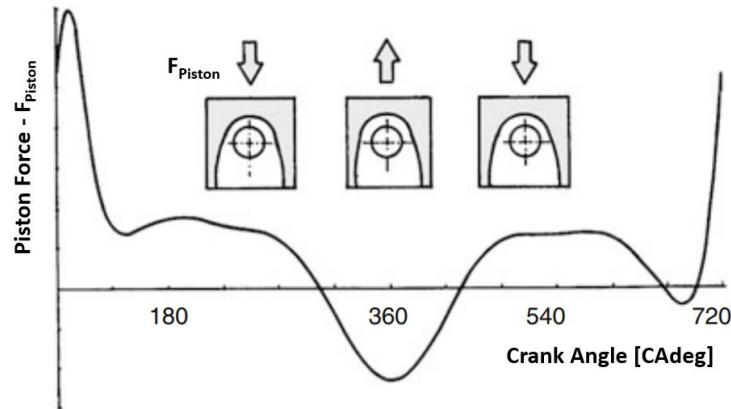
$$m_{osc.} = m_{piston\ Osc.} + m_{Conrod\ Osc.} \quad (27)$$

Replacing Equation 38 and Equation 40 in Equation 37, the Equation 28 is obtained for the force on piston calculation.

$$F_{piston} = p(\varphi) \cdot A_p - m_{osc.} \cdot a \quad (28)$$

Figure 9 illustrates the piston force of a four-stroke engine over the work cycle.

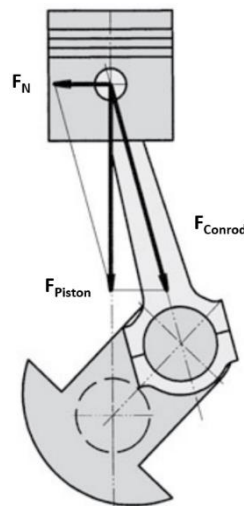
Figure 9 – The piston force of a four-stroke engine over the work cycle



Source: Adapted from (SCHÄFER, 2017)

Since the connecting rod, apart from the dead centers, assumes a position deviating from the cylinder axis direction, the piston force must be redirected accordingly. This results in the conrod force F_{Conrod} and the normal force F_N that is perpendicular to cylinder barrel.

Figure 10 – The piston force distributed as conrod force and normal force



Source: Adapted from (SCHÄFER, 2017)

The conrod force and the normal force may be calculated using Equation 29 and Equation 30, respectively, (F. SCHÄFER 2017).

$$F_{Conrod} = \frac{F_{piston}}{\cos \psi} \quad (29)$$

$$F_N = -F_{piston} \cdot \tan \psi \quad (30)$$

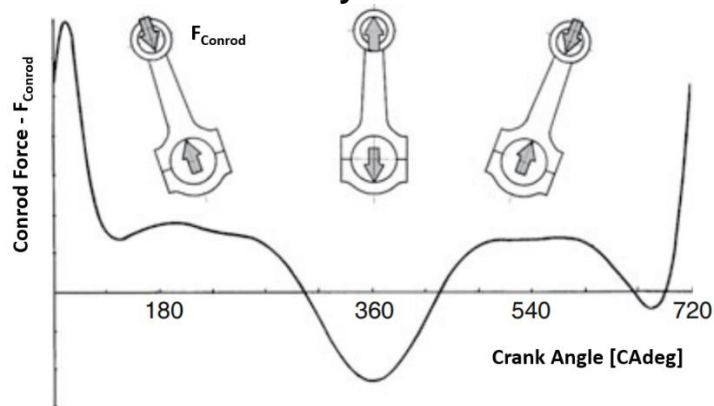
The connecting rod pivot angle ψ may be calculated according to Equation 31 for non-de-axing engine and according to Equation 32 for a de-axed one, (F. SCHÄFER 2017)(Shafer, 2017).

$$\psi = \arctan \frac{\lambda_{rod} \cdot \sin \varphi}{\sqrt{1 - \lambda_{rod}^2 \cdot \sin^2 \varphi}} \quad (31)$$

$$\psi_{off} = \arcsin(\lambda_{rod} \cdot \sin \varphi - e) \quad (32)$$

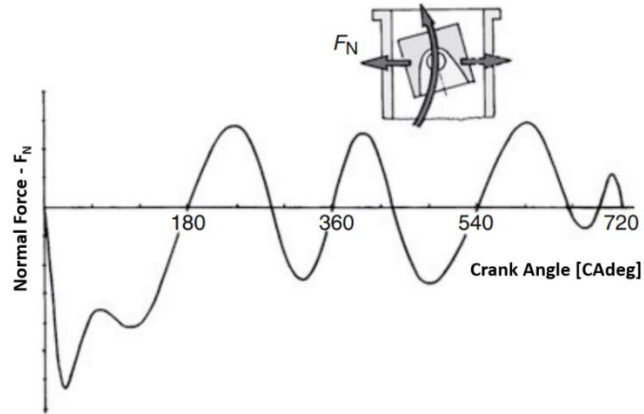
Figure 11 and Figure 12 illustrate the connecting rod force and normal force of a four-stroke engine over the work cycle, respectively.

Figure 11 – The connecting rod force of a four-stroke engine over the work cycle



Source: Adapted from (SCHÄFER, 2017)

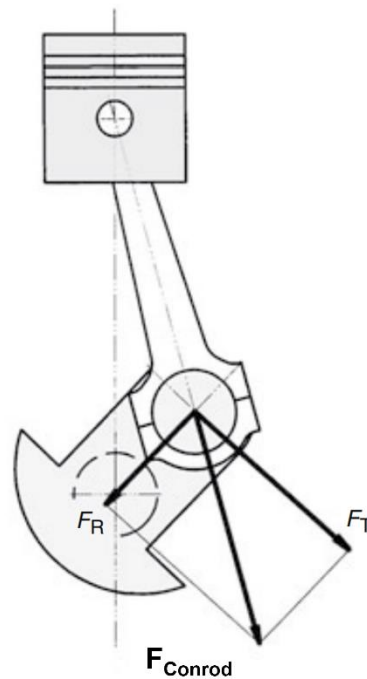
Figure 12 – The normal force of a four-stroke engine over the work cycle



Source: Adapted from (SCHÄFER, 2017)

The crank pin rotates under the action of the connecting rod force on the turning circle of the crankshaft radius, whereby the tangential component F_T of the rod force with the crank radius results in the torque. The radial component F_R makes no contribution to the engine torque. It only loads the crank throw in bending, (F. SCHÄFER 2017). Figure 13 shows the connecting rod force distributed as tangential force and radial force.

Figure 13 – The connecting rod force distributed as tangential force and radial force



Source: Adapted from (SCHÄFER, 2017)

The tangential force and the radial force may be calculated using Equation 33 and Equation 34, respectively.

$$F_T = F_{Conrod} \cdot \sin(\varphi + \psi) = F_{piston} \cdot \frac{\sin(\varphi + \psi)}{\cos \psi} \quad (33)$$

$$F_R = F_{Conrod} \cdot \cos(\varphi + \psi) = F_{piston} \cdot \frac{\cos(\varphi + \psi)}{\cos \psi} \quad (34)$$

The engine crank pin withstands the connecting rod force F_{Conrod} and the rotating connecting rod inertia force $F_{Conrod\ rot.}$, Equation 35. When added geometrically, these forces result in the crank pin force $F_{Crank\ Pin}$, Equation 36.

$$F_{Conrod\ rot.} = m_{Conrod\ rot.} \cdot r \cdot \omega^2 \quad (35)$$

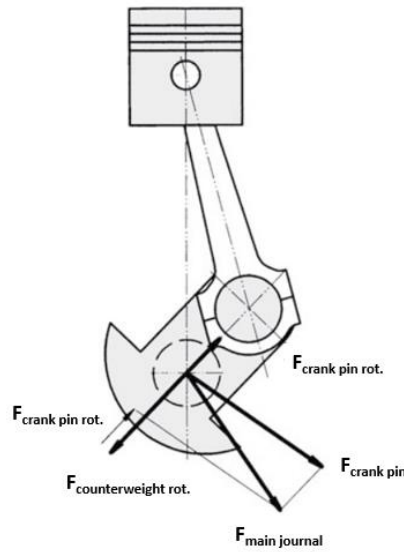
$$F_{Crank\ Pin} = \sqrt{F_{Conrod}^2 + F_{Conrod\ rot.}^2 - 2 \cdot F_{Conrod} \cdot F_{Conrod\ rot.} \cdot \cos(\varphi + \psi)} \quad (36)$$

The connecting rod bearing force $F_{Conrod\ Bear.}$ is the reaction force related to the crank pin force and it may be calculated according to Equation 37.

$$F_{Conrod\ Bear.} = -F_{Crank\ Pin} \quad (37)$$

As illustrated by Figure 14, the engine forces are transmitted to the crankcase via the crankshaft main journals and main bearing journals. The rotating inertia force of the crank pin $F_{Crank\ Pin\ rot.}$, the crank pin force $F_{Crank\ Pin}$ or their components, and the force of the counterweight $F_{Counterweight}$ together result in the main journal force $F_{Main\ Journal}$.

Figure 14 – The main journal force



Source: Adapted from (SCHÄFER, 2017)

The rotating inertia force of the crank pin and the force of the counterweight may be calculated by Equation 38 and Equation 39, respectively, (F. SCHÄFER 2017).

$$F_{Crank\ Pin\ rot.} = m_{Crank\ Pin\ rot.} \cdot r \cdot \omega^2 \quad (38)$$

$$F_{Counterweight} = m_{Counterweight} \cdot r \cdot \omega^2 \quad (39)$$

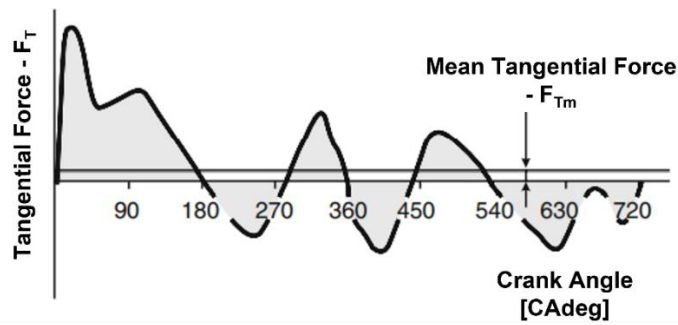
The main journal force may be calculated according to Equation 40.

$$F_{Main\ Journal} = \sqrt{(F_{Crank\ Pin\ rot.} + F_R + F_{Conrod\ rot.} - F_{Counterweight})^2 + F_T^2} \quad (40)$$

The periodical change of the gas force and inertial force inside the engine leads to the tangential force fluctuation and hence, the engine torque also fluctuates. The mean tangential force F_{Tm} is calculated from the integral of the tangential force curve over a work cycle φ_P according to Equation 41, (F. SCHÄFER 2017).

$$F_{Tm} = \frac{1}{\varphi_P} \int_0^{\varphi_P} F_T(\varphi) \cdot d\varphi \quad (41)$$

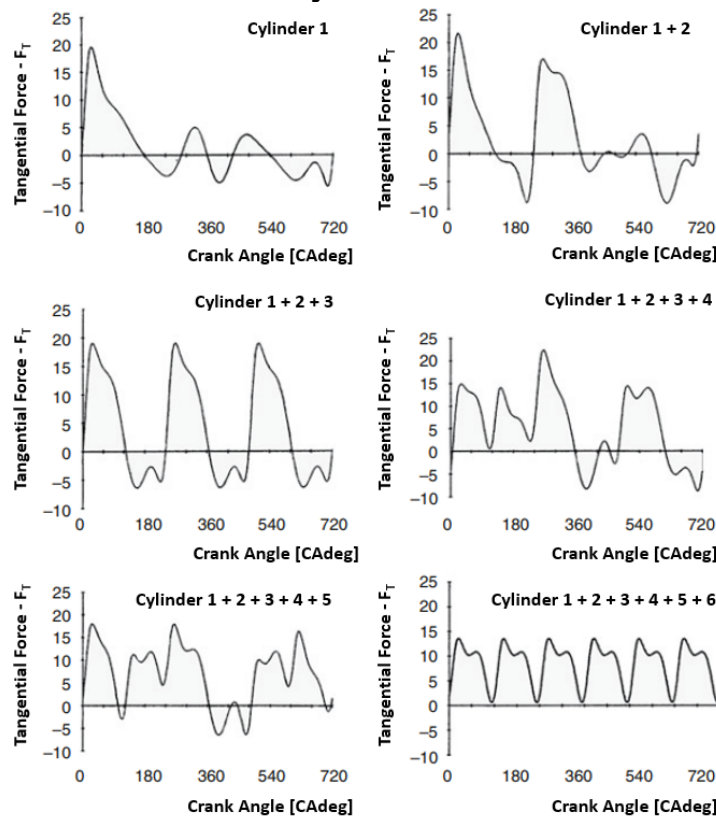
Figure 15 – The tangential force over work cycle



Source: Adapted from (SCHÄFER, 2017)

In order to even out the tangential force curve and to increase the power, the engines are built, with a few exceptions, with multiple cylinders. The tangential force of the individual cylinders is added up phase-shifted according to the ignition intervals over the crankshaft to the total torsional force on the clutch side of the engine. As a result, the tangential force is evened out and hence the tangential force fluctuation has dropped to a fraction of that of a single-cylinder engine, (F. SCHÄFER 2017).

Figure 16 – The tangential force over work cycle according to number of cylinders



Source: Adapted from (SCHÄFER, 2017)

The crankshaft rotational speed varies over work cycle due to the torque fluctuation. Thus, if the tangential force value is higher than the mean tangential force, the engine is accelerated. On the other hand, if the tangential force value is lower than the mean tangential force, the engine is decelerated. Therefore, the engine rotational speed fluctuation may be considered as rotational kinetic energy variation, (F. SCHÄFER 2017). The rotational kinetic energy W_S may be calculated by Equation 42.

$$W_S = \frac{1}{2} \cdot I \cdot (\omega_{max}^2 - \omega_{min}^2) \quad (42)$$

Where, the I is the moment of inertia [$\text{kg}\cdot\text{m}^2$], the ω_{max} and the ω_{min} are the maximum and the minimum crankshaft rotational speed, respectively.

The engine rotational speed fluctuation may be reduced by using a flywheel. The flywheel acts as an energy store device, which stores kinetic energy then there is excess tangential force and releases it again in the opposite case. Depending on the engine type and application, different requirements are placed on the engine rotational speed fluctuation. Thus, the speed fluctuation is indicated by the degree of irregularity δ . The degree of irregularity may be calculated according to Equation 43, (F. SCHÄFER 2017).

$$\delta = \frac{(\omega_{max} - \omega_{min})}{\omega_m} \quad (43)$$

Where, ω_m is the mean rotational speed which may be calculated the using Equation 44.

$$\omega_m = 2 \cdot \pi \cdot N \approx \frac{1}{2} \cdot (\omega_{max} + \omega_{min}) \quad (44)$$

Therefore, the rotational kinetic energy W_S may be calculated as function of the mean rotational speed and the degree of irregularity according to Equation 45.

$$W_S \approx I \cdot \delta \cdot \omega_m^2 \quad (45)$$

Table 4 presents some values of the degree of irregularity according to the type of equipment.

Table 4 – Degree of irregularity according to the type of equipment

Type of Equipment	δ
Punching, shearing and forming presses	0.200
Compressor (belt drive)	0.120
Compressor (gear drive)	0.020
Machine tools	0.025
Reciprocating pumps	0.040
Geared drives	0.020
Internal Combustion Engines	0.030
D.C. generators (direct drive)	0.010
A.C. generators (direct drive)	0.005

Source: (BHANDARI, 2010) and (BUDYNAS; NISBETT, 2011)

2.3.3. Flywheel

A flywheel is a mechanical filtering element in a system through which energy is flowing. In ICE application, the mechanical energy is supplied by the engine at a variable rate due to the interval between ignition events, and it is taken from the engine at a constant rate. Which in turn, it causes the shaft to vary speed during one cycle. The flywheel reduces this speed fluctuation and even out the ripples of the torque crank angle diagram by absorbing energy when it is delivered by the engine. Therefore, the flywheel acts as a smoothing or equalizing element in any mechanical transmission system in which has a back-and-forth energy flow, (Patel 1965).

2.3.3.1. Flywheel Design

The Euler equation of motion is presented in Equation 46.

$$T_a(\varphi) = I \cdot \dot{\omega} \quad (46)$$

Where, $T_a(\varphi)$ is the net torque applied to the shaft in function of the shaft position and $\dot{\omega}$ is the angular acceleration about the axis of rotation.

Equation 46 can be reconsidered as the instantaneous torque, $T(\varphi)$, applied to the shaft in [Nm] related to the mean torque, T_m , in [Nm], according Equation 47, (Patel 1965).

$$T_a(\varphi) = T(\varphi) - T_m = I \cdot \dot{\omega} \quad (47)$$

The work done by the net torque applied to the shaft in [joule] related to a defined angular interval from φ_i to φ_f can be calculated using Equation 48.

$$W_S = \int_{\varphi_i}^{\varphi_f} T_a(\varphi) \cdot d\varphi = \int_{\varphi_i}^{\varphi_f} (T(\varphi) - T_m) \cdot d\varphi = \int_{\varphi_i}^{\varphi_f} I \cdot \dot{\omega} \cdot d\varphi \quad (48)$$

Since the angular acceleration is the angular speed rate related to time, Equation 48 can be rearranged to Equation 49.

$$W_S = \int_{\varphi_i}^{\varphi_f} (T(\varphi) - T_m) \cdot d\varphi = I \cdot \int_{\omega_i}^{\omega_f} \omega \cdot d\omega = \frac{1}{2} \cdot I \cdot (\omega_f^2 - \omega_i^2) \quad (49)$$

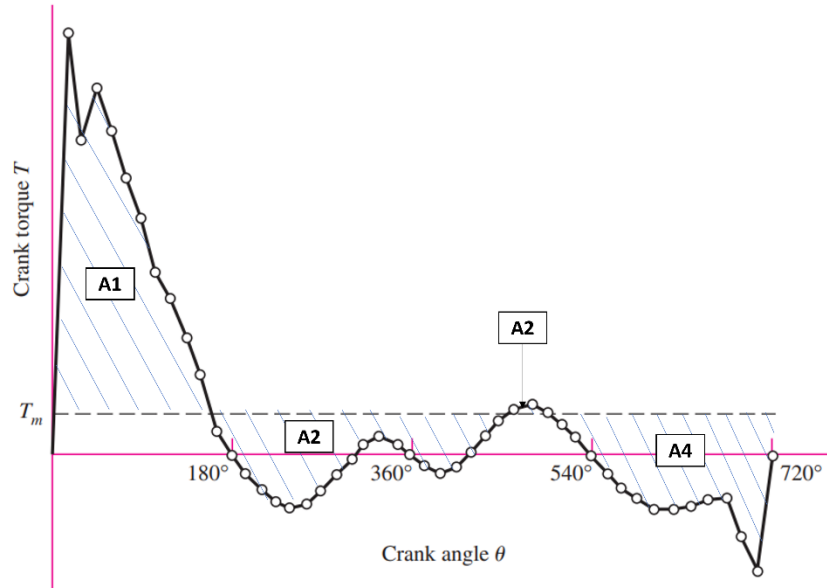
The maximum work done by the torque on a shaft occurs between the minimum angular speed and maximum angular speed. This means that the torque fluctuation on a shaft in the torque angle diagram occurs between ω_{max} and ω_{min} . Thus, the last term of Equation 49 became equal to Equation 50 and the work done during a cycle equals to the rotational kinetic energy, (Patel 1965; Budynas and Nisbett 2011).

$$W_S = \frac{1}{2} \cdot I \cdot (\omega_{max}^2 - \omega_{min}^2) \quad (50)$$

The first term of Equation 50 represents the areas sum of the instantaneous torque applied to a shaft throughout a cycle related to the mean torque as shown in Equation 51 and the torque crank diagram (Figure 17), (Patel 1965; Schrön 1947).

$$W_S = A_{Total} = \int_{\varphi_i}^{\varphi_f} (T(\varphi) - T_m) \cdot d\varphi = \sum_1^n A_n \quad (51)$$

Figure 17 – Torque crank diagram



Source: Adapted from (BUDYNAS; NISBETT, 2011)

Finally, by rearranging Equation 50, calculating the rotational kinetic energy using Equation 49, and considering an appropriate degree of irregularity, it is possible to calculate the flywheel moment of inertia using Equation 52, (F. SCHÄFER 2017).

$$I \approx \frac{W_S}{\delta \cdot \omega_m^2} \quad (52)$$

Considering Equation 53 for the radius of gyration, R_{gyr} , in [m].

$$R_{gyr} = \sqrt{\frac{I}{m}} \therefore I = R_{gyr}^2 \cdot m = \left(\frac{D_{fly}}{2}\right)^2 \cdot m \quad (53)$$

Where m is the flywheel mass in [kg] and D_{fly} is the inertia diameter in [m]. Combining Equation 76 in Equation 75, the Equation 54 is created for the flywheel weight calculation, WG_{fly} , in [N], (Schrön 1947).

$$WG_{fly} \approx \frac{W_S \cdot 4 \cdot g}{\delta \cdot \omega_m^2 \cdot D_{fly}^2} \quad (54)$$

Rewriting Equation 54 in function of the engine operating frequency and simplifying it, Equation 55 for the flywheel weight calculation, WG_{fly} , in [N] is obtained, (Schrön 1947).

$$WG_{fly} \approx \frac{3580 \cdot W_s}{\delta \cdot N \cdot D_{fly}^2} \quad (55)$$

2.3.3.2. Flywheel materials

An efficient flywheel stores as much energy per unit mass as possible without failing. As the flywheel is spun up, it stores more kinetic energy. The rotational velocity limit is set by failure caused by the centrifugal loading and a factor of safety. Thus, if the centrifugal stress exceeds the tensile strength or fatigue strength, the flywheel flies apart, (Ashby and Jones 2005).

The flywheel kinetic energy per unit of mass, U/m , in [kJ/kg], can be calculated using Equation 56.

$$\frac{U}{m} = \frac{1}{4} \cdot R_{gyr}^2 \cdot \omega_m^2 \quad (56)$$

As the flywheel is spun up, the energy stored in it increases, but so does the centrifugal stress. The maximal principal stress, hoop stress, σ_{max} in [MPa], in a spinning disk of uniform disk thickness is calculated using Equation 57, for a Poisson ratio of $\nu \approx 1/3$, (Ashby and Jones 2005).

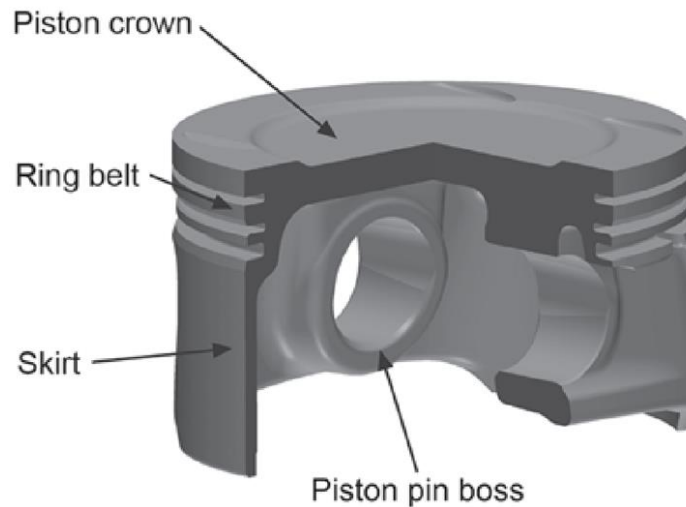
$$\sigma_{max} = \left(\frac{3 + \nu}{8}\right) \cdot \rho \cdot R_{gyr}^2 \cdot \omega_m^2 \approx \frac{1}{2} \cdot \rho \cdot R_{gyr}^2 \cdot \omega_m^2 \quad (57)$$

This stress must not exceed the failure stress σ_f which is the maximal principal stress related to a factor of safety.

Replacing Equation 57 in Equation 56, Equation 58 is obtained establishing the upper flywheel angular velocity limit, (Ashby and Jones 2005).

$$\frac{U}{m} = \frac{1}{2} \cdot \left(\frac{\sigma_f}{\rho}\right) \quad (58)$$

Figure 19 – The piston basic structure



Source: (MAHLE, 2016)

The piston together with the piston rings must reliably seal the combustion chamber against gas passage and oil lubricant penetration. Thus, the materials, geometries, and surfaces must carefully match. Long piston service life requires good wear behavior, which in turn requires that the moving parts are correctly supplied with lubricating oil. The surfaces oil retaining capacity, particularly of the cylinder liner, plays a decisive role. This is particularly challenging near of the engine TDC and BDC due to the mixed friction behavior predominates over hydrodynamic friction condition, (Mahle 2016).

Further than the sealing task, the piston also has to assist the air-fuel mixture formation and to dissipate heat. For the air-fuel mixture formation, the piston crown has a partially jagged shape like a bowl or a dome in order to interact with the in-cylinder flow pattern and achieve the required charge homogeneity. The heat on pistons is primarily dissipated through the oil jetted underneath piston, by the piston rings but also by the piston skirt, (Mahle 2016; F. SCHÄFER 2017).

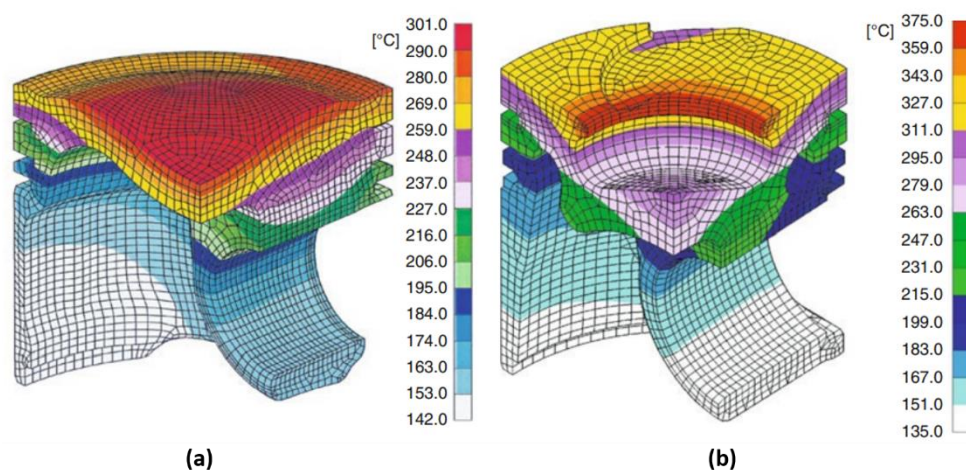
2.3.4.1. Piston Mechanical and Thermal Load

As aforementioned, the piston is subjected to an equilibrium of gas, inertia and lateral force. The maximum gas force during the expansion stroke has critical significance on the mechanical loads. The maximum gas force magnitude is related to the combustion process and the intake charge (NA or TC). Currently, modern NA and TC four-stroke gasoline engines could achieve 6.0 – 9.0 MPa and 9.0 – 13.0 MPa of

mechanical load, respectively. On the other hand, modern NA and TC four-stroke diesel engines could achieve 8.0 – 10.0 MPa and 14.0 – 24.0 MPa of mechanical load, respectively. Further than the maximum gas force, the combustion pressure increase rate also affects the stress on the piston. The values for diesel engines are about 6 to 12 bar/CAdeg and for gasoline engines 3 to 6 bar/CAdeg. However, the pressure increase rate could achieve up to 30 bar/CAdeg in case of knock or pre-ignition combustion process (Mahle 2016).

Further than the piston mechanical load, the piston working temperature is another important parameter for its operational safety and service life. The piston crown absorbs different amounts of heat, due to its exposure to the hot combustion gases, depending on the engine running point (RPM, load). An example of the piston temperature distributions for gasoline and diesel engine pistons are shown in Figure 20. The piston temperature magnitude and distribution essentially determine the mechanical stress that it can withstand. Thus, a high thermal load leads to a drastic reduction in the fatigue resistance of the piston material. The piston critical temperature location for gasoline engines is the transition area from the pin boss connection to the piston crown and the skirt. The Table 5 presents typical temperature values for passenger car engines, (Mahle 2016).

Figure 20 – Temperature distributions for gasoline (a) and diesel (b) engine pistons



Source: (SCHÄFER, 2017)

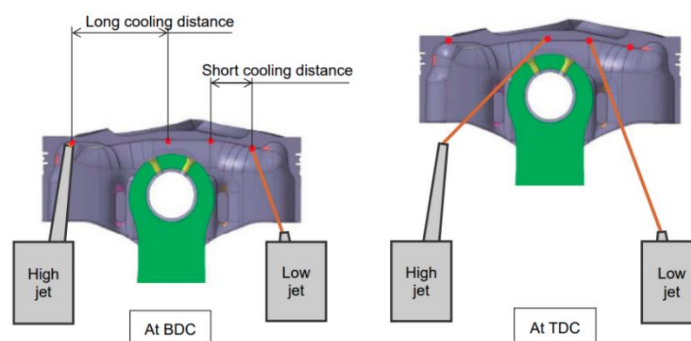
Table 5 – Typical piston temperature values for passenger car engines

Piston region	Temperature C
Center of piston crown (gasoline engine, PFI)	270 – 310

Piston crown bowl (gasoline engine, DI)	270 – 350
Bowl rim (Diesel engine, DI)	350 – 400
Support area	200 – 250
Pin bore	200 – 250
Top ring groove (jet cooled, salt-core cooling gallery)	200 – 280
Top ring groove (cooled ring carrier)	180 – 230
Cooling gallery	250 – 300

Nowadays, the oil jets implementation is a common approach used in engines in order to reduce the piston temperature. The oil jet spread out oil directly underneath the piston crown or supply it to an oil channel designed underneath the piston crown. According to (Agarwal and Varghese 2006), a temperature difference of approximately 40°C could be achieved between oil jet cooled and non-cooled pistons. Aiming an effective piston temperature reduction, the oil jet spray is designed to face as large as possible area throughout the piston stroke. Due to oil spray target limitations, it is common to apply more than one oil jet per cylinder. In severe engine application such as racing engines, the number of oil jets holes could achieve values about 24 holes, (Gotou and Yanagisawa 2009). Figure 21 illustrates the oil spray target for a Formula 1 piston engine application throughout its stroke.

Figure 21 – The oil spray target for a Formula 1 engine application



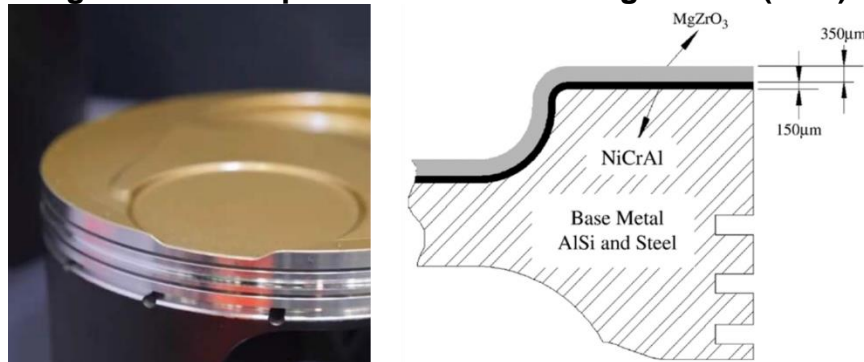
Source: (GOTOU; YANAGISAWA, 2009)

2.3.4.2. Piston Coating

Currently, another way to reduce the piston temperature is the application of Thermal Barrier Coatings (TBCs) on it. The TBCs have been used on the piston crown in order to reduce the in-cylinder heat rejection and improve its thermal fatigue

property. The TBC consist of a bond layer and a top coating, Figure 22. The bond layer is used to improve coating adhesion between TBC and the piston. Typically, the NiCrAl is used as bond material for piston coating application. The top coating layer is built up typically using ceramic material which has to be selected taking to account some factors such as high melting point, no phase transformation, low thermal conductivity, chemical inertness, thermal expansion match with the metallic substrate, good adherence to the metallic substrate and low sintering rate of the porous microstructure. Nowadays, the most ceramic materials used for IC engines piston TBC are Ytria Stabilized Zirconia (YSZ), Mullite, Magnesia-Stabilized Zirconia ($MgZrO_3$), Alumina (Al_3O_2) and AlSi, (Chan and Khor 2000; Dhomne and Mahalle 2018).

Figure 22 – The piston Thermal Coating Barrier (TBC)

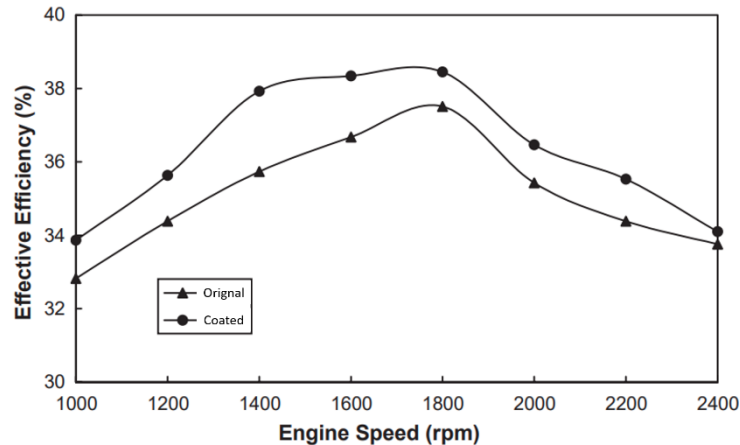


Source: (Buyukkaya and Cerit 2007; Calico 2021)

Further than the coating material, the coating thickness is also an important parameter to determine. According to the (Reghu et al. 2020) research, an YSZ coating thickness about 100 and 125µm could lead to a piston temperature drop of 40 to 48C°and adding more 25µm it could drop the piston temperature further 40%. As a result, the piston temperature in function of the coating thickness presented a non-linear relationship. In conclusion, the combustion chamber insulation using a TBC influences the combustion process and hence the engine performance and its exhaust emissions, (Chan and Khor 2000). Figure 23 illustrates the effect of the TBC on the fuel conversion efficiency of a diesel engine, at full load, compared to the same engine

without the TBC applied on it. The increase of the combustion temperature causes the engine fuel conversion efficiency to rise about 3% throughout engine rpm conditions, (Taymaz, Çakır, and Mimaroglu 2005).

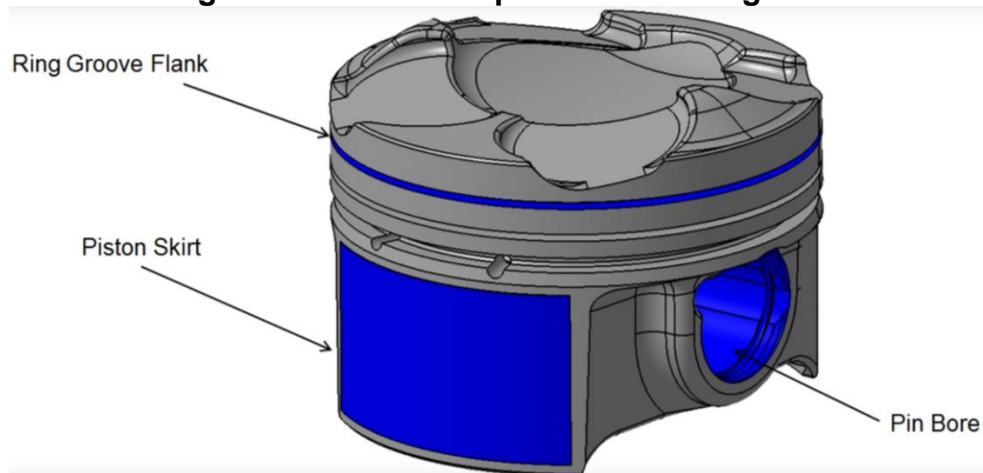
Figure 23 – The piston TBC effect on the engine fuel conversion efficiency



Source: (TAYMAZ; ÇAKIR; MIMAROGLU, 2005)

Further than TBC, another types of coating are applied on piston surface in order to prevent local micro-welding between the piston and piston ring (mainly at the first ring groove due to the higher temperature achieved), or piston seizing. The protection against micro-welding is localized hard-anodizing of the groove with a coating thickness about 15 μ m. The quasi-ceramic structure of the hard oxide layer eliminates the metallic contact between parts. Although the hard oxide layer is rougher than the machined groove, there is no problem on the piston ring sealing because the groove surface is quickly smoothed by the piston ring motion. A piston does not require a coating on the piston skirt if it is correctly dimensioned and works under normal, moderate operating conditions. However, the risk of piston seizing under extreme operating conditions exist. A coating on the piston skirt provides protection to the piston in such extreme situations. It is worth to point out that the skirt coating must be tribologically matched to the cylinder wall material. The piston pin boss is another location where is coated depending on the engine application. The pin boss coating is mainly performed in order to reduce the friction and increase the fatigue strength in this region. Alternatively, the pin boss could be bushed using copper-based materials to achieve the same goals related to friction and strength, (F. SCHÄFER 2017; Mahle 2016). Figure 24 illustrates the piston coated region.

Figure 24 – Common piston coated regions



Source: (MOTORSPORT, 2018)

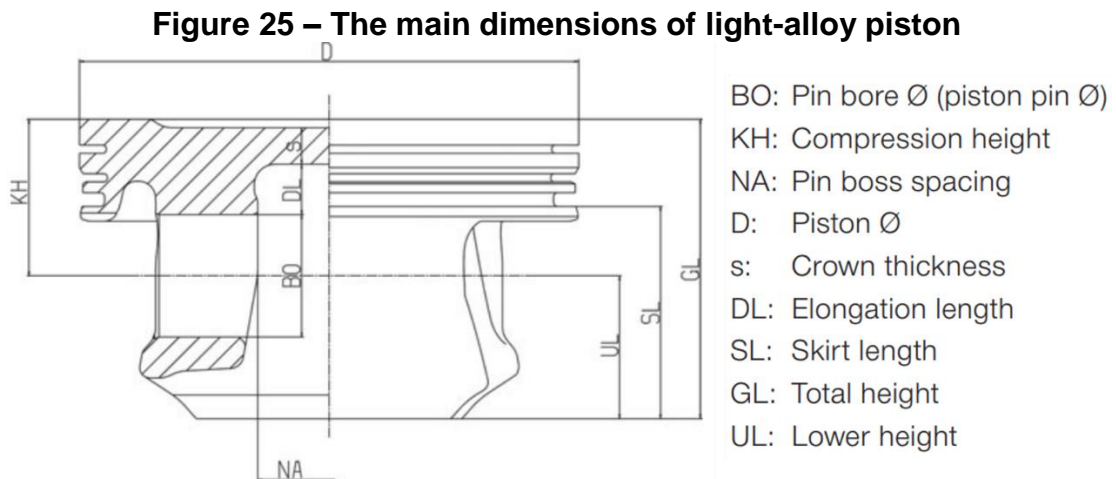
2.3.4.3. Piston Design

Modern engines employ lightweight piston design with symmetrical or asymmetrical skirt profiles and potentially different wall thickness for the thrust and anti-thrust sides in order to achieve as much as possible a good balance between piston mass, flexibility and strength. Considering the operational requirements of a typical internal combustion engine (two-stroke, four-stroke, gasoline, and diesel), aluminum-silicon alloys are commonly the most appropriate piston material. On the other hand, the large-bore pistons and commercial vehicle piston have often or their crowns or their upper parts made of steel, (Mahle 2016).

The aluminum-silicon is a light alloy with high thermal conductivity which is ideal for engine piston application. A high thermal conductivity is advantageous because it leads to a uniform temperature distribution within the piston. The silicon content in the aluminum-silicon alloy is one of the major parameters that determine the piston seizure under thermal load. Alloys with silicon content $<12.5\%$ are called hypoeutectic and allows the piston to expand more than hypereutectic alloys with silicon content $>12.5\%$. Despite of the piston seizure issue when the lower silicon content alloy is used, the piston strength improvement is greater than the higher silicon content alloy. Therefore, the aluminum-silicon alloy should be chosen according to the piston application. For severe applications such as racing engine application, there is an aluminum alloy called "Silicon Free" due to its lower silicon content ($<0.25\%$) that presents high

strength which is suitable for this application. In addition to the piston material choose, the piston manufacturing process also influence the piston strength properties. The aluminum-silicon piston alloys are employed mainly for cast piston. However, they can also be forged for high loads applications which leads to a different microstructures and mechanical properties, (Mahle 2016).

In order to design a piston with as low as possible mass, good piston cooling, strength and flexibility, the authors MAHLE (2016b) and TRZESNIOWSKI (2010), suggest typical piston design dimensions as a guideline, Figure 25 and Table 6.



Source: (MAHLE, 2016; TRZESNIOWSKI, 2010)

Table 6 – The main dimensions of light-alloy piston

	Gasoline engines		Diesel engines
	Two-stroke	Four-stroke	Four-stroke
Diameter D [mm]	30 – 70	65 – 105	65 – 95
Total height GL/D	0.8 – 1.0	0.6 – 0.7	0.8 – 0.95
Compression height KH/D	0.4 – 0.55	0.30 – 0.45	0.5 – 0.6
Pin diameter BO/D	0.20 – 0.25	0.20 – 0.26	0.3 – 0.4
Top land height [mm]	2.5 – 3.5	2 – 8	6 – 12
1 st ring land height St/D*	0.045 – 0.06	0.040 – 0.055	0.055 – 0.1
Groove height for 1 st piston ring [mm]	1.2 – 1.5	1.0 – 1.75	1.75 – 3.5
Skirt length SL/D	0.55 – 0.7	0.4 – 0.5	0.5 – 0.65

Pin boss spacing NA/D	0.25 – 0.35	0.20 – 0.35	0.25 – 0.35
Crown thickness s/D or s/DMu, max**	0.055 – 0.07	0.06 – 0.10	0.14 – 0.23

*Values for diesel engines apply to ring carrier pistons, **Diesel

Source: (MAHLE, 2016; TRZESNIOWSKI, 2010)

Starting from the piston top, firstly it is the piston crown that forms part of the combustion chamber. The piston crown for a gasoline internal combustion engine could be flat, raised or sunken and, as it is exposed to the hot gases, it has to withstand the greatest thermal stress. The number and size of the engine valves also affects the shape of the piston crown. The piston crown thickness is determined based on the maximum gas pressure and the amount of the heat should be dissipated, (Mahle 2016).

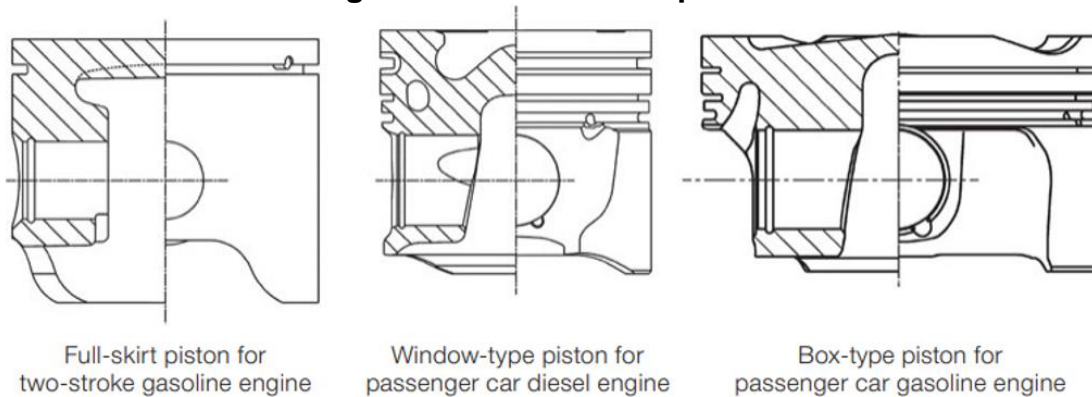
Following the piston crown there is the first ring zone which is called top land. The top land dimensions are a compromise between low piston mass and minimum crevice volume for reducing fuel consumption and exhaust gas emissions, in one side, whereas it should withstand higher mechanical and thermal loads, and provide a suitable temperature for the first ring work properly. For gasoline engines, it is advisable to design the top land width about 4 to 10% of the piston diameter. On the other hand, this value should be between 8 to 15% of the piston diameter for passenger car diesel engines, (Mahle 2016).

Another important piston parameter of a piston design is the piston compression height. The piston compression height is the distance between the piston pin center and the upper edge of the piston top land. The minimum piston compression height is determined by the number and height of piston rings, the required ring lands, the piston pin diameter, and the top land width. The main goal is to have as low a compression height as possible to keep the piston mass and the engine height lower. As 80% of the piston mass is in the upper region of the piston from the center of the piston pin to the piston crown, it accounts for the greatest proportion of the oscillating masses, (Mahle 2016).

At the lower part of the piston is the piston skirt. The piston skirt tasks are to guide the piston in the cylinder and keep the tipping of the piston low during contact alteration from the thrust side to the anti-thrust side. The gasoline engine pistons have a wide range of profile designs as showed on Figure 26. In order to keep the piston passive losses as lower as possible, the piston skirt have been designed commonly

with relative narrow skirt surfaces, which led to the box-type piston type. In contrast to narrow skirt design, the piston skirt must meet a few requirements related to its strength such as bear lateral forces without major deformations and elastically adapt to the deformations of the cylinder, (Mahle 2016).

Figure 26 – Piston skirt profiles

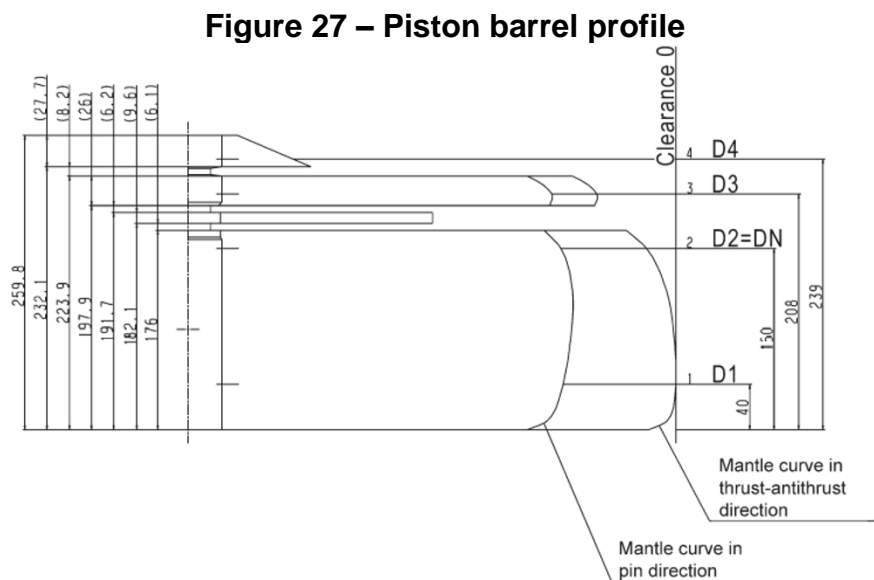


Source: (MAHLE, 2016)

The piston crown deflects under the mechanical and thermal load hence, it deforms the piston skirt to an oval shape in the thrust and anti-thrust direction. Thus, the piston diameter increases in the piston pin direction and reduces it along the thrust to anti-thrust direction. This change on the piston shape must be taken into consideration when design a new piston in order to ensure that it runs without seizure issue at working temperature. To this end, the piston is designed to have some clearance to cylinder wall and this piston shape is known as piston profile. The piston profile deviates from an ideal circular cylinder in the axial direction (barrel shape), and in the circumferential section (ovality), (Mahle 2016).

The piston is tapered at upper and lower skirt ends (barrel shape) in order to promote a lubricating oil wedge formation that acts as a support element. Furthermore, the ring belt has a greater taper to compensate the higher thermal and mechanical load deformation in this area. Figure 27 illustrates a piston barrel profile. The reference

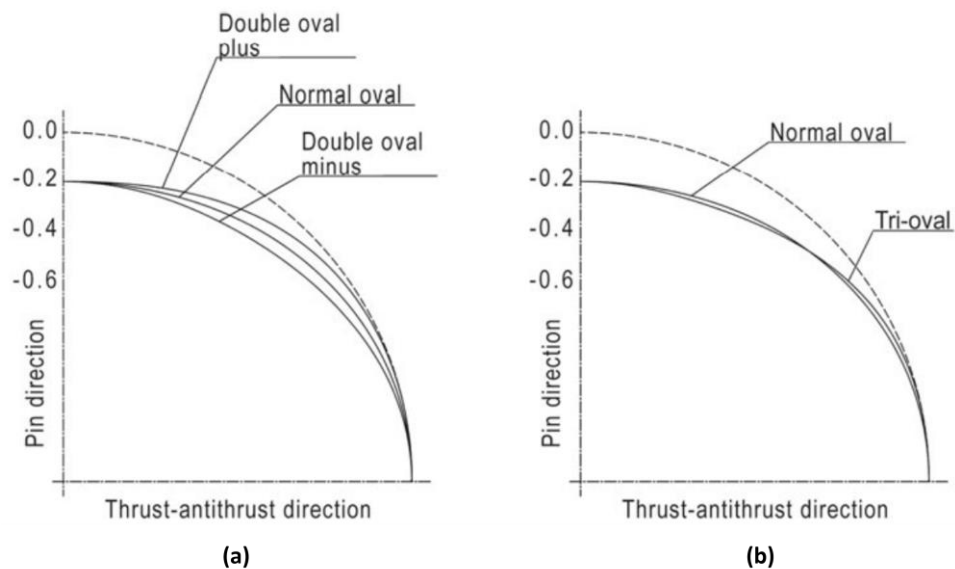
measuring plane is designated as DN. Preferably, the DN is located at the point with tightest clearance between piston and cylinder wall ($DN=D1$) or in an area with a stable shape ($DN=D2$). Typically, the dimensional tolerance is 8 to $18\mu\text{m}$ (diametric), depending on the piston diameter. Deviations from the nominal form are called form tolerances. The form tolerances for passenger car and commercial vehicles are, typically, about $7\mu\text{m}$ in the skirt area (diametric) relative to DN, and 10 to $15\mu\text{m}$ in the ring belt area (diametric), (Mahle 2016).



Source: (MAHLE, 2016)

The piston ovality design is used to further compensate the piston deformation under thermal and mechanical load on its circumferential section. The piston ovality is typically about 0.3 to 0.8% of the piston diameter. A piston could be designed with a normal ovality or with multiple superposition ovalities to achieve an even piston wear pattern, as shown in Figure 28. The positive superposition widens the wear pattern relative to the normal ovality, whereas the negative superposition makes it narrower. The piston designed running surfaces in the thrust and anti-thrust direction should not be too narrow. Otherwise, the specific pressures between piston and cylinder would not remain low. In order to prevent hard contact between the piston and the cylinder, and the risk of galling, the piston support area should not extend out to the piston box walls, (Mahle 2016).

Figure 28 – Piston ovality and superposition, double oval (a) and tri-oval (b)

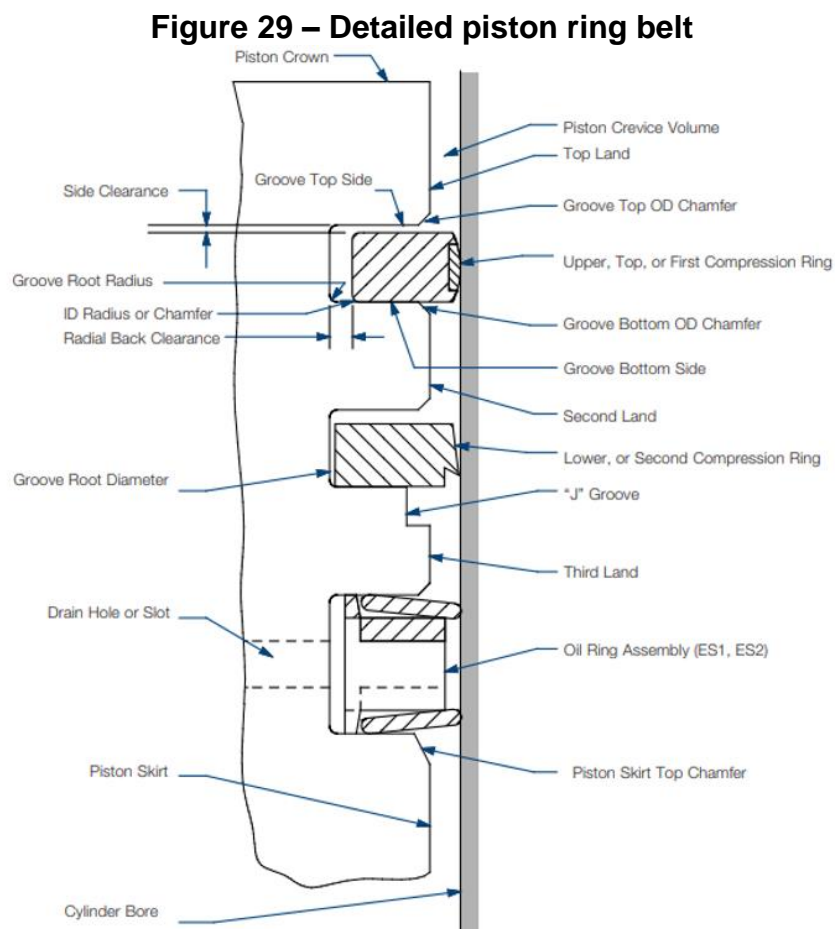


Source: (MAHLE, 2016)

2.3.4.4. Piston Rings

Following the piston top land is the ring belt or ring pack. The ring belt usually consists of three piston rings: two compression rings (also known as the first and the second piston rings) and an oil control ring (third piston ring). The first piston ring task is mainly sealing the combustion chamber by supporting the gas pressure throughout the engine operating cycle, dissipate heat to cylinder surface and scrap residual oil from cylinder wall. The piston second ring on the other hand, support the remaining gas pressure due blow-by past the first piston ring, control the pressure ratios in the ring belt, scrap oil from cylinder surface and dissipate heat. Finally, the third piston ring is responsible to promote a homogeneous oil lubricating distribution of the piston and

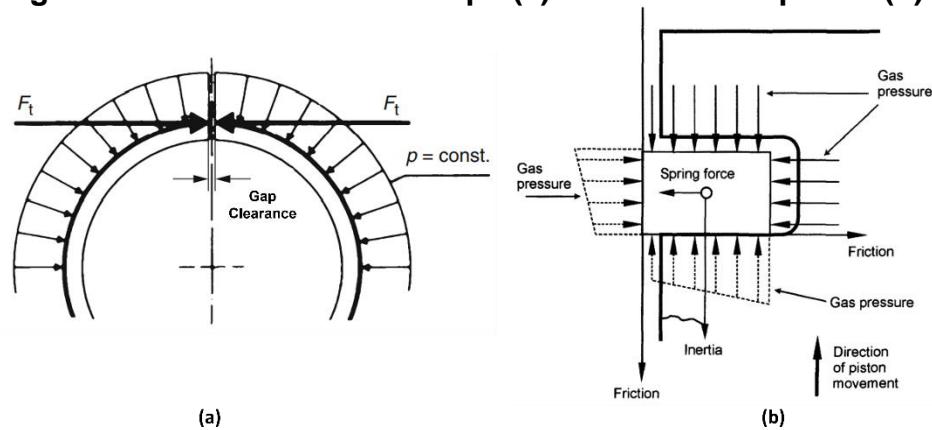
cylinder, and scrap the excess of oil, (MAHLE 2016). Figure 29 illustrates a ring belt in detail, (Mahle 2014).



The compression rings are mostly single piece with a spring force. In order to generate the contact pressure against the cylinder wall, the piston rings are in the shape of an open circular spring, Figure 30a. Furthermore, this radial force in the installed state is greatly amplified by the gas pressure behind the piston ring, Figure 30b. The drawback of higher piston ring pressure against the cylinder wall for

combustion sealing is the higher friction produced from it. The piston rings can contribute to over than 50% of the piston friction, (Eduard Köhler 2011).

Figure 30 – Piston circular shape (a) and forces on piston (b)



Source: (MAHLE, 2014)

On the piston axial direction, the piston ring contact with the piston groove flank is substantially affected by the gas pressure dynamics in the ring belt. When the piston is installed in the cylinder, the piston rings are compressed at their ends to their gap clearance generating radial and tangential force. The rings gap clearance must be carefully determined according to the engine application. If the gap clearance is too tight for a specific engine application, the rings tend to close the gap and lock in the piston, which in turn it could lead to an engine failure. On the other hand, if the gap clearance is too loose, the blow-by rate tends to increase and the cylinder compression capability decreases, (Mahle 2014). According to (Motorsport 2020), the gap clearance value could be estimated in function of bore diameter using a Gap Factor presented in Table 7.

Table 7 – Ring gap clearance recommendation guide

Engine Application	Gap Factor
--------------------	------------

	First Ring (Min.)	Second Ring (Min.)	Oil Ring (Min.)
High performance street – NA	0.0045"	0.0050"	0.015"
Circle track, Drag racing – NA	0.0050"	0.0060"	0.015"
Nitrous up to 200 hp	0.0060"	0.0060"	0.015"
Nitrous race 200+ hp	0.0070"	0.0070"	0.015"
Turbo / Supercharger	0.0060"	0.0060"	0.015"
Turbo / Supercharger Race	0.0070"	0.0070"	0.015"
Diesel - Turbocharged	0.0060"	0.0055"	0.015"

Source: (MOTORSPORT, 2020)

The ring gap clearance can be calculated using Equation 59.

$$Gap = gap_{factor} \cdot B \quad (59)$$

It is worth to point out that most of the second ring gap recommendations in the Table 7 are larger than the top rings. Recent tests have been proven that a larger second ring gap leads to a higher stability of the top ring by preventing an inter-ring pressure building up and lifting it off the piston groove flank. Hence, the top ring seal performance is improved, (Motorsport 2020).

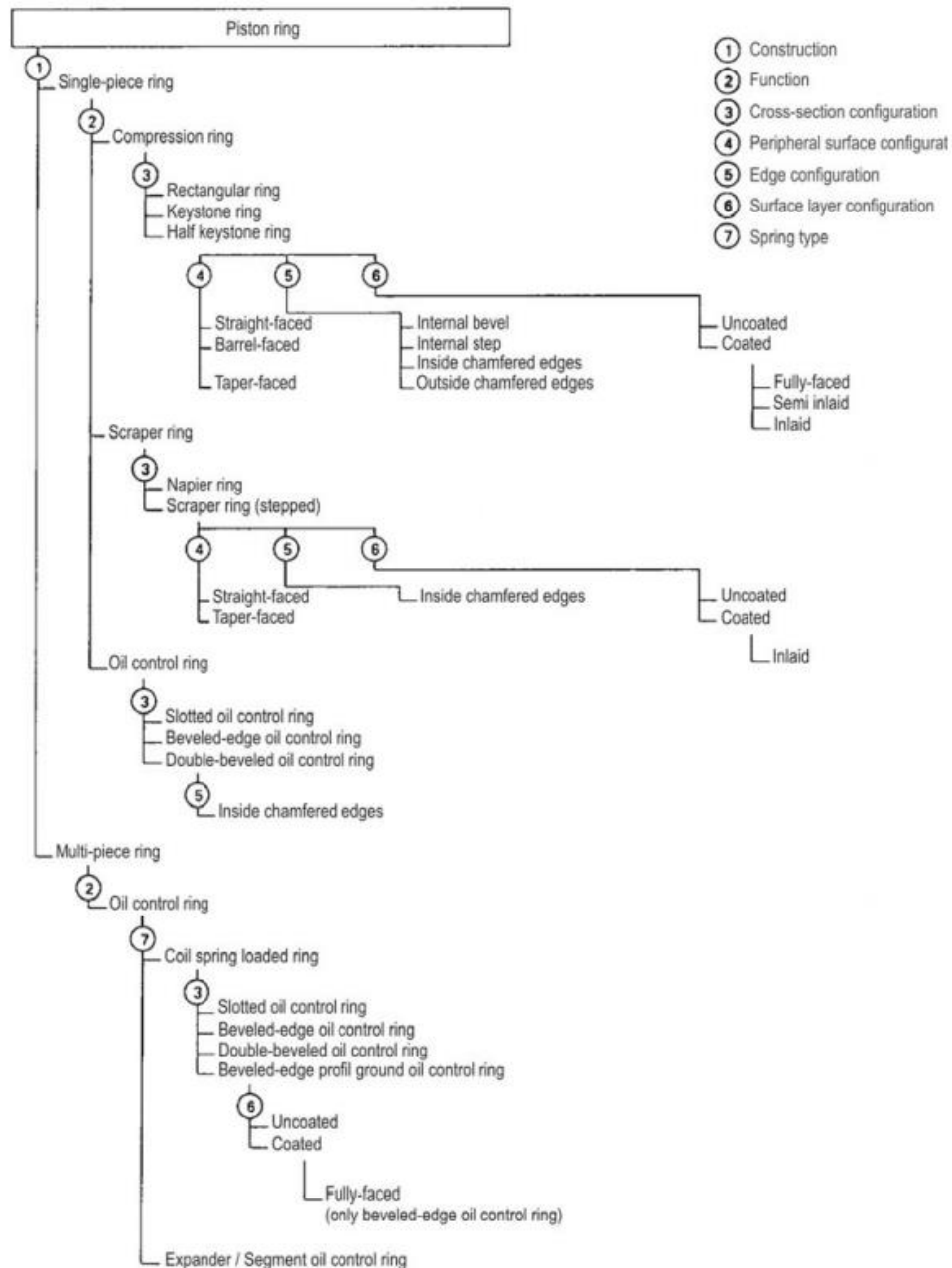
There are various types of piston rings that were developed in order to properly perform its required tasks depending on the engine application. For the purpose of sort, the piston rings types out, they were classified in the standard DIN 6621-Part 1 as shown on Figure 31, (MAHLE 2016).

The requirements for a good piston ring running, wear properties, elastic behavior, thermal conductivity, thermal expansion properties as well as high corrosion resistance are decisive for the piston ring materials choice. Furthermore, high strength is required when the engine is subjected to extreme conditions such as high speeds or high combustion pressure gradients. Typically, the following materials are used for piston ring materials:

- **Cast iron with lamellar graphite:** untempered “standard material” for piston rings with good running properties as well as satisfactory wear behavior. The flexural strength values are relatively low with at least 350 N/mm². It is also used for of the second groove and oil scraper rings;

- **Cast iron with nodular graphite (spheroidal graphite iron), low-alloyed and tempered:** this cast iron is characterized by a high flexural strength of at least 1300 N/mm². Due to this high flexural strength, nodular cast iron is preferably used for rings in the first groove;
- **Steel:** due to its high resistance to breakage, steel is used, for example, with low ring heights (~1.2mm) for petrol engines and in diesel engines with high rates of pressure increase; as well as for oil scraper rings for steel lamellae, spacer springs and as profile steel oil rings. Preferred steel materials are spring steels, to wear protection through subsequent nitriding, high chromium alloyed martensitic materials are also used, (F. SCHÄFER 2017).

Figure 31 – Classification of piston rings per DIN ISO 6621 - Part 1



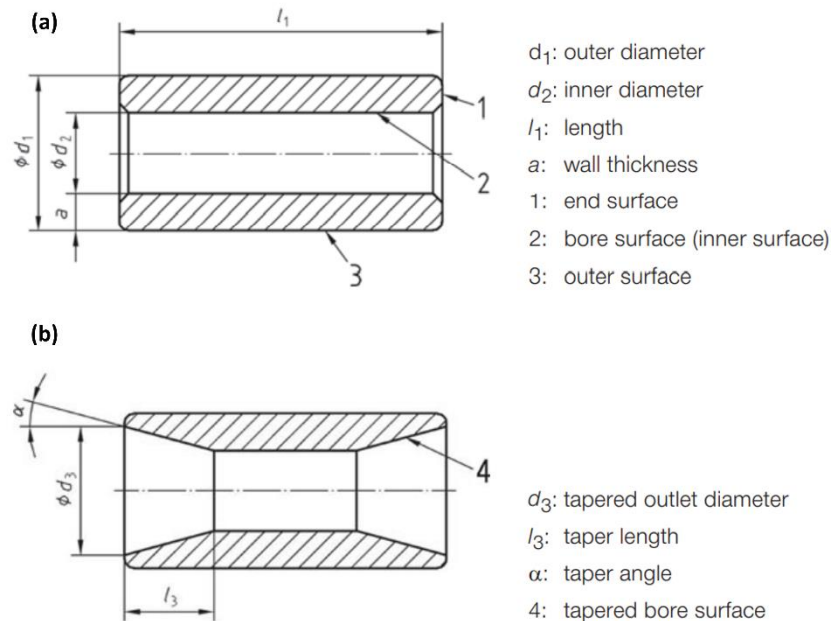
Source: (MAHLE, 2014)

In addition to the piston ring materials, the ring coatings and surface treatment provide wear resistance and seizure resistance, along with low cylinder wear favorable lubrication properties. Nitrided steel and cast iron, coatings based on chromium such as hard chrome and chromium-ceramic, plasma-sprayed molybdenum, plasma-sprayed cermet, and coatings using high-speed flame spraying (High Velocity Oxygen Fuel, HVOF) and Physical Vapor Deposition (PVD) meet the most demanding service life and run requirements. The selection of suitable piston ring coating depends on the engine technology, application, tribological requirements, and cost, (MAHLE 2016).

2.3.5. Piston Pin

The mechanical connection between the piston and the connecting rod is made by the piston pin also called wrist pin. The piston pin bear high loads from gas pressure and inertia forces. Furthermore, due to small relative movements (rotary movements) between the piston and the pin or between the pin and connecting rod, there are also unfavorable lubrication conditions. Commonly, the piston pin is a cylindrical inner and outer contour. However, in order to reduce its weight and thus the inertia forces, the less stressed ends of the inner pin are often designed conically, (F. SCHÄFER 2017). Figure 32 illustrates the most common piston pin profile used nowadays.

Figure 32 – Piston pin cylindrical inner and outer (a), and conical ends (b)



Source: (MAHLE, 2016a)

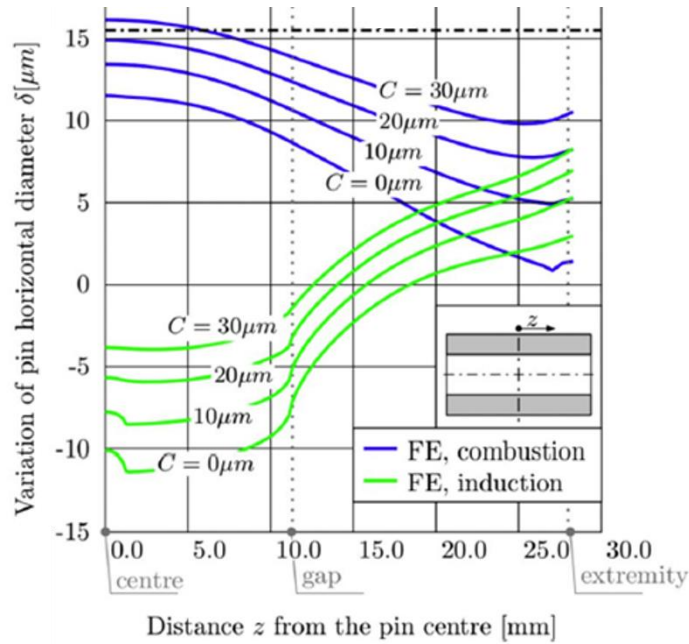
The piston pin assembly on the connecting rod and piston can be done via interference fit or using a circlip to hold the piston pin on place. There are three types of piston pin assembly known as:

- **Stationary or fixed pin:** The piston pin has an interference fit in the piston bosses and is free to rotate in the connecting rod;
- **Semi-floating pin:** The piston pin is secured to the connecting rod and free to move in the piston;
- **Fully floating pin:** The piston pin is free to rotate in both the piston bosses and the connecting rod, (F. SCHÄFER 2017; Bohn 2016).

For pistons in engines with moderate specific power output, the piston pin can be fixed in the small end bore with shrinkage stresses. This approach allows savings due to elimination of piston circlips and the bushing in the small end bore and makes the automatic assembly of the piston pin easier for large-scale engine production. However, for high stressed engines applications, the fully-floating approach is used and requires circlips to hold the piston pin in place. The fully-floating assembly is used on higher loads engines in order to avoid the component remained stress after the interference press-fit process, (MAHLE 2016).

In case of piston pin floating approach is used, an initial clearance (C) must be provided between the pin outer surface on one side, and the small end bore and piston boss bores on the other side. This clearance must fall within a certain interval. Otherwise, if the clearance at the operating temperature is too small, seizure might occur, whereas, if it is too high, an initial play may cause lubrication regime deterioration, (Strozzi et al. 2018). According to (Strozzi et al. 2018) literature review, the diametral clearance between eye and pin is suggested to fall within the interval 0.0008 to 0.003 times the piston pin radius. Furthermore, tests of piston pin ovalization (δ) in function of the diametral clearance presented an increase of piston pin ovalization as the clearance increase, Figure 33. Thus, the piston pin diametral clearance has to be carefully defined.

Figure 33 – Piston pin ovalization behavior related to diametral clearance



Source: (STROZZI; BALDINI; GIACOPINI; BERTOCCHI et al., 2018)

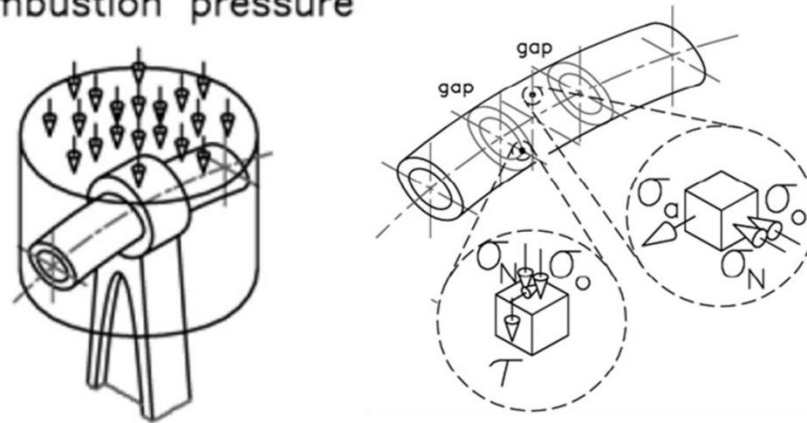
Under the effect of the forces described above, there is a very complex stress on the piston pin, which is also influenced by the deformation of the piston and the connecting rod. The essential aspects for the design of the piston pin are: sufficient strength, reaction to the piston stress, weight, surface quality/dimensional accuracy and surface hardness, (F. SCHÄFER 2017).

2.3.5.1. Piston Pin Design

The piston pin is subjected to normal stress σ_N , bending stress σ_a , ovalizing stress σ_o and shear stress τ during its usage. Figure 34 illustrates the stresses on the piston pin under gas pressure actuation. The main deformation modes of the piston pin are the bending mode and the ovalizing mode. Usually, a check on the ovalization is carried out in the pin design phase. An excessive piston pin cross section ovalization produces high frictional forces which, heating the pin, may cause seizure. On the other hand, the bending mode is less detrimental once that piston is made of relatively deformable aluminum alloy, and it deflects accompanying the steel pin bending. However, the realistic pressure distribution exhibits pressure peaks typical of elastic contact problems in the presence of edges. Which in turn, it makes the gap between connecting rod and piston the one of the most critical for piston pin. Figure 35 illustrates connecting rod and piston wear due to pressure peaks in the presence of edges. Nowadays, some pistons bosses, connecting rods and piston pins have they outer

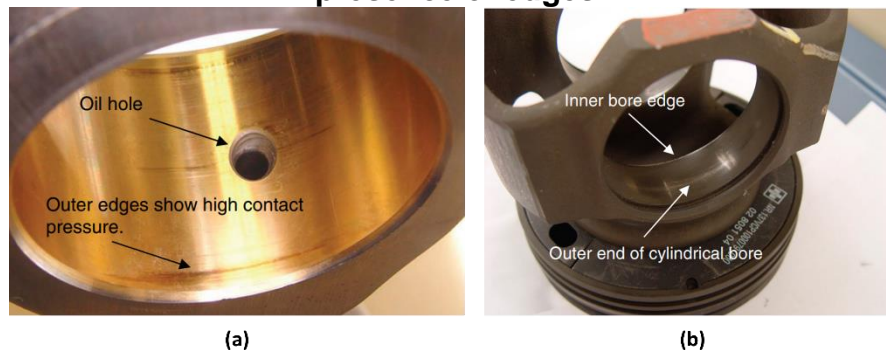
edges radiused or chamfered to limit the presence of pressure spikes at those extremities, (Strozzi et al. 2018).

Figure 34 – Stress on the Piston pin combustion pressure



Source: (STROZZI; BALDINI; GIACOPINI; BERTOCCHI et al., 2018)

Figure 35 – Connecting rod (a) and piston (b) wear due to pressure peaks in the presence of edges



Source: (CLARK; ANTONEVICH; KEMPPAINEN; BARNA, 2009)

The piston pin ovalization is defined as the difference between the deformed horizontal diameter and its vertical counterpart. The allowable piston pin ovalization has been investigated by several authors that defined functions of it related to piston pin outer diameter. According to (Lawton and Crutcher 1966) the allowable pin ovalization should be $1.0\mu\text{m}/\text{mm}$ of outer pin diameter for pins equal or less than 63.5mm diameter. On the other hand, according to (Rothmann 1963), the admissible increase of the pin horizontal diameter is $25\mu\text{m}$.

The piston pin is usually dimensioned with the help of 3D-FEM (Finite Element Method) and sometimes taking to account the formation of a lubricating film (pressure distribution) in the hub and connecting rod. The piston and connecting rod geometry, and the maximum pressure during the engine the expansion stroke must be considered

when dimensioning the piston pin. The Table 8 presents the typical piston pin dimension according to the application, (F. SCHÄFER 2017).

Table 8 – Typical piston pin dimensions ratios

Application		Piston	Piston Pin		
		B [mm]	d1/B	d2/d1	l1/B
Gasoline engines	2 – Stroke	35 – 70	0.20-0.30	0.40-0.73	0.65-0.80
	Passenger car	65-100	0.20-0.30	0.47-0.60	0.60-0.75
Diesel engines	Passenger car	65-95	0.30-0.40	0.43-0.53	0.65-0.80
	Commercial car (Al)	100-160	0.40-0.45	0.40-0.47	0.78-0.82
	Commercial car (St)			0.31-0.47	0.60-0.85
Large-bore engines	-	< 250	0.30-0.45	0.34-0.56	0.70-0.86
	-	> 250	0.35-0.45	0.38-0.45	0.65-0.86

Source: (MAHLE, 2016a; SCHÄFER, 2017)

2.3.5.2. Piston Pin Materials

The piston pins are, usually, manufactured from case-hardened or nitride steels. Case or nitride hardening promote a good toughness in the core and surface hardness with a good wear behavior of the piston pin. However, the piston pins made of case-hardened steel bear the problem of lack volume stability due increased residual austenite content. The Table 9 presents the typical piston pin materials currently used in internal combustion engines, (MAHLE 2016).

Table 9 – Typical piston pin materials

Chemical composition by weight %	Case-hardened steels			Nitrided steel
	17Cr3	16MnCr5	17CrNi6	31CrMoV9

C	0.13-0.20	0.14–0.19	0.14–0.20	0.27–0.34
Si	0.15–0.40	0.15–0.40	0.40 max	0.40 max.
Mn	0.60–0.90	1.00–1.30	0.50–0.90	0.40–0.70
P	≤ 0.035	≤ 0.035	≤ 0.035	≤ 0.025
S	≤ 0.040	≤ 0.035	≤ 0.035	≤ 0.035
Cr	0.70–1.00	0.80–1.10	1.40–1.70	2.30–2.70
Ni	-	-	1.40–1.70	-
Mo	-	-	-	0.15–0.25
V	-	-	-	0.10–0.20
Young's modulus [MPa]	210.000	210.000	210.000	214.000
Thermal expansion [10 ⁻⁶ 1/K] 20–200°C	13.1	13.1	12.8	13.0
Thermal conductivity [W/m*K]	36	36	37	39
Density [g/cm ³]	7.82	7.84	7.84	7.83
Poisson ratio μ	0.27	0.27	0.27	0.27
Application	Gasoline and passenger car diesel engines	High- performance passenger car engines and commercial vehicle and mediumspeed diesel engines	Large bore engines	Highly loaded gasoline and diesel engines

Source: (MAHLE, 2016a)

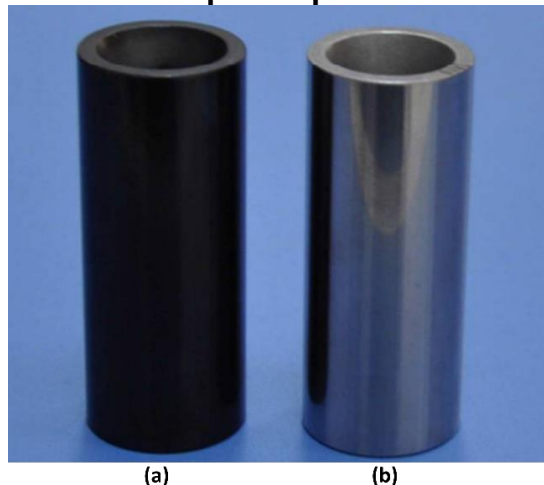
2.3.5.3. Piston Pin Coating

In addition to harder materials, some coatings have been studied for the piston pin application. The silicon nitride (Si₃N₄) based ceramic is one of the most coatings studied for piston pin application due to its high-temperature thermal and mechanical properties. The silicon nitride ceramics increase the piston pin load bear capability

making possible weight savings up to 25%. Furthermore, the ceramics had significant advantages in terms of the tribological properties in regions with lubrication deficit. However, regarding its mass production use, economic factors play a crucial role. Which in turn, the silicon nitride coating became expensive for a spread-out application, (May et al. 2008; Bocanegra-Bernal and Matovic 2010).

Alternatively, to the ceramic coating, several amorphous DLC coatings that contain hydrogen (a-C:H) have been used for low-friction and secure piston pin operation. The DLC coatings are built up to three layers and the layer hardness is adapted to the contact loads and materials contact with the piston pin. The total coating thicknesses are about 2 and 3.5 μm . The results from (KONG, 2016) work presented a reduction of 11% of piston pin friction and it showed capable to withstand durability tests. As well as (Morgenstern, Kießling, and Reichstein 2008) research result suggest that the specific engine output and fuel consumption can be positively influenced if DLC coatings are applied to the piston pins. The

Figure 36 – Aspect difference between a DLC coated (a) and an uncoated (b) piston pin



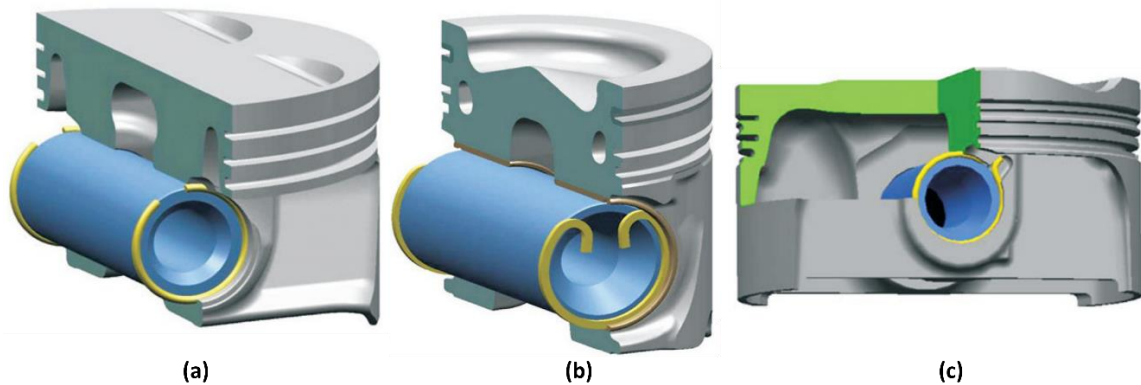
Source: (MORGENSTERN; KIEßLING; REICHSTEIN, 2008)

2.3.6. Piston Circlip

As aforementioned, if the piston pin is not assembled by a shrink-fit connection, then it must be secured to prevent sideways movement out of the piston boss and contacting the cylinder wall. This held in place requirement is addressed with circlips mounted on the outside the piston pin on the piston boss. Usually, the circlips are made of round or square drawn spring wire (DIN EN 10270-1) or oil-tempered spring steel

wire (DIN EN 10270-2). For an easier assembly, the ends of the circlips can be drawn in to form hooks. However, these hooks increase the mass at the ends of the rings and thus lead to lower engine speed to the point where the snap rings are lifted out of the circlip groove. Thus, the circlips with the hooks design are used almost exclusively in diesel engines. For high-speed engines, the circlips ends can be fixed in the groove by a hook that is bent outward, so that the opening is oriented in the direction of the stroke and the ring cannot rotate in the pin boss groove, (MAHLE 2016). Figure 37 illustrates the types of circlips described in this section.

Figure 37 – Types of piston pin circlips round without hooks (a), squared with hooks (b) and round with outward hook bended



Source: (MAHLE, 2016a)

The maximum engine speed allowable for a round circlip without hooks, $\omega_{\max_circlip}$ in [rad/s], may be calculated using Equation 60, (Eduard Köhler 2011).

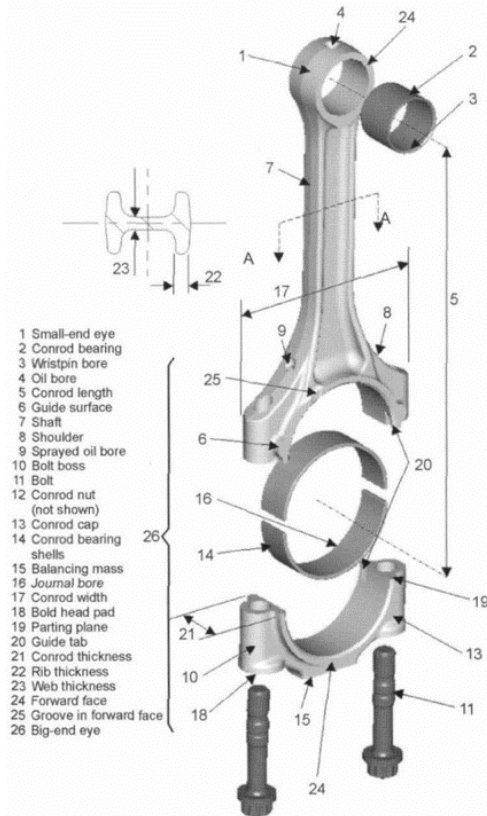
$$\omega_{\max_circlip} = \frac{0.3162 \cdot d_2 \cdot \left(\frac{E}{\rho}\right)^{\frac{1}{2}}}{d_4 - d_2} \cdot \left(\frac{\frac{1}{(d_4 - d_2)} - \frac{1}{(d_3 - d_2)}}{r \cdot (1 + \lambda)}\right)^{\frac{1}{2}} \quad (60)$$

Where, the E is the Youngs module in [GPa], the ρ is the density in [kg/m³], the d_2 is the circlip wire diameter [m], the d_3 is the circlip diameter in the unclamped state in [m], the d_4 is the circlip diameter in the clamped state in [m], the r is the crank radius in [m] and the λ is the connecting rod ratio.

2.3.7. Connecting Rod

The connecting rod, as its name implies, connects the piston to the crankshaft and consist of a small end and bid end bores, as well as the shank. Figure 38 presents the usual connecting rod terminology.

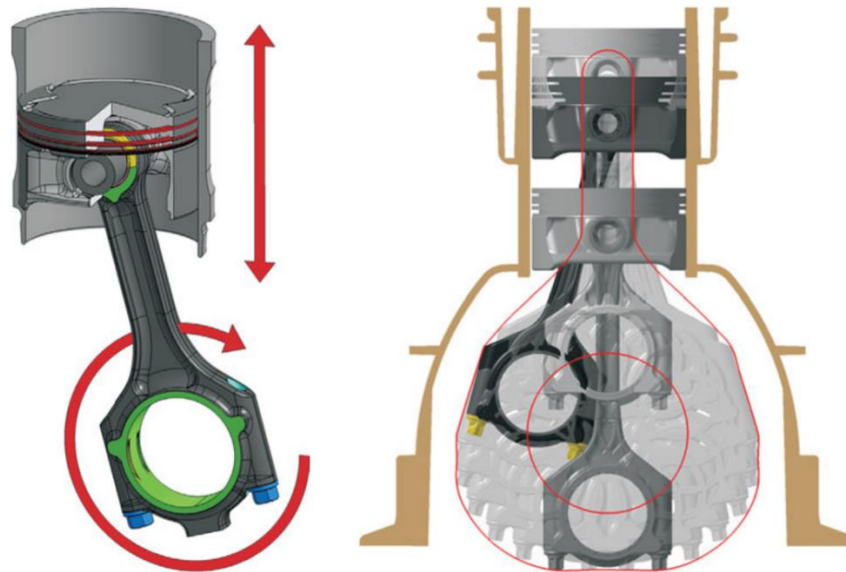
Figure 38 – Connecting rod terminology



Source: (SCHÄFER, 2017)

The connecting rod combines the axial movement of the piston and the rotational movement of the crankshaft. The space covered by the connecting rod during one crankshaft revolution is called connecting rod sweep and it must be considered in collision analysis for the engine crankcase and oil pan. While the connecting rod small end bore is always closed, the big end bore is usually designed to come apart for assembly, (MAHLE 2016). Figure 39 illustrates the connection rod main motions and the connecting rod sweep.

Figure 39 – Connecting rod main motions (a) and connecting rod sweep (b)

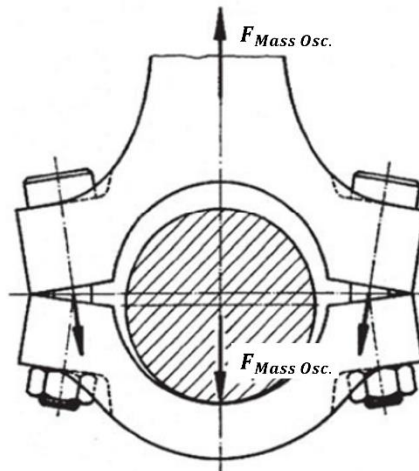


Source: (MAHLE, 2016a)

2.3.7.1. Mechanical Load

As a transfer forces and motions, the connecting rod is subjected to large alternating loads. The connecting rod is loaded in compression by the gas force, in tension by inertia forces and in bending because of its pivoting motion. A connecting rod design should achieve the engine application requirements with a good balance between weight and stiffness. Under compression load the connecting rod shank bear the higher loads. On the other hand, under tensile load the connecting rod bolts are responsible to hold the connecting rod attached to the crankshaft. At the latest condition, the connecting rod deforms with ovality in the vertical direction and the bolts are bent outward. Which in turn, if the bolt force is insufficient, the connecting rod joint will gape on the inside, (Eduard Köhler 2011; Pischinger 2012). Figure 40 illustrates the connecting rod big end deformation under tensile load.

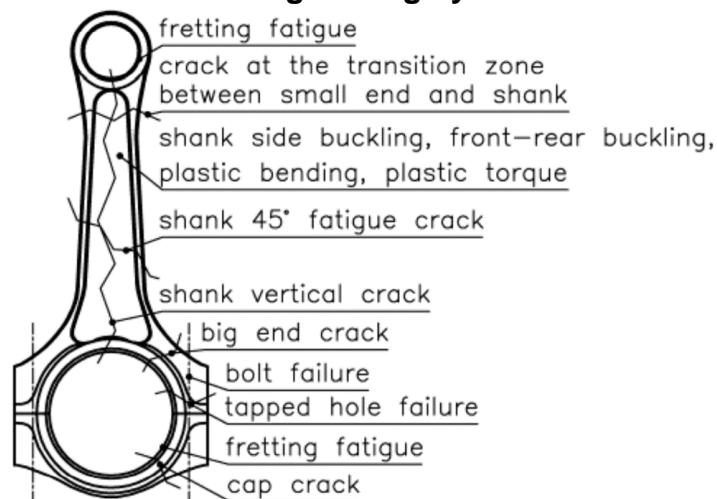
Figure 40 – Deformation of the connecting rod big end under tensile load



Source: (MAHLE, 2016a)

As a result of these applied loads the connecting rod will deform. The most highly stressed areas in connecting rods, in addition to the connecting rod bolt threads, are the fillets on the transition from the shank to the big end bore and to the small bore, (MAHLE 2016). Further highly stressed areas in the connecting rod are investigated in detail by (Strozzi et al. 2018), and it is highlighted in Figure 41.

Figure 41 – Connecting rod highly stressed sections

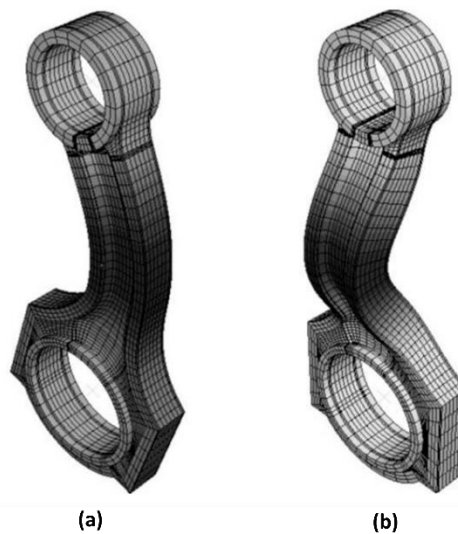


Source: (MAHLE, 2016a)

The connecting rod is a slender engine component that has considerable length in proportion to its width and breadth. Therefore, the connecting rod may be designed and analyzed as a column or a strut. One of the most critical stresses on a column is called buckling stress. Buckling may be defined as a sudden change in shape of a structural component under load and it is also called elastic instability. As shown in

Figure 42, the connecting rods may present two buckling modes: side-buckling (on-plane buckling) and front-rear buckling (out of plane buckling). Nowadays, the connecting rod buckling stress analyses are performed via FEM method, (Strozzi et al. 2018; BHANDARI 2010; M.K. Lee et al. 2010).

Figure 42 – Connecting rod buckling modes: side-buckling (a) and front-rear buckling (b)



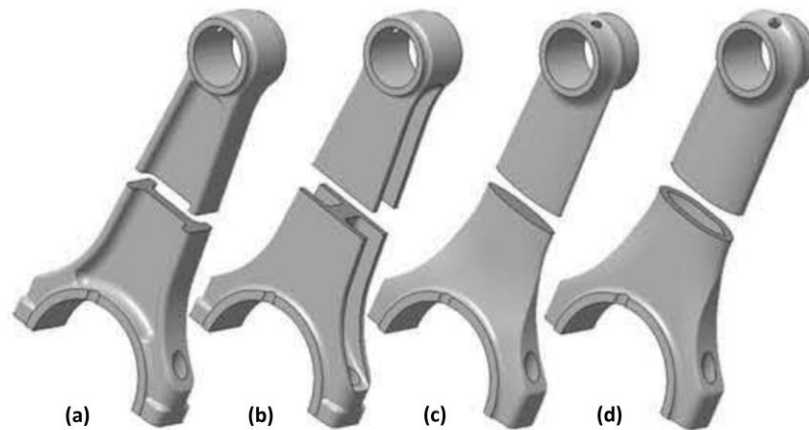
Source: (LEE; JANG, 2010)

2.3.7.2. Connecting Rod Design

The connecting rod, as shown in Figure 43, may be designed with different shank profiles, such as I-section, H-section, Blade-section, and Hollow-section. However, the two most common profiles are the H-section and I-section. It is worth to point out that the shank profile may affect the connecting rod buckling tendency towards one of the two modes due to its section radius of gyration changes. For instance, the H-section is commonly used for racing engines in order to avoid side-buckling due to high bending moment generate by high engine speeds combined to high gas forces. On the other hand, I-section is easier to manufacture, and it reduces the contact stresses at the connecting rod pin-eye ends. The piston pin is deflected by the gas forces and this bending promotes high contact stresses at the pin-eye ends. If the shank profile is I-shaped, the presence of the pockets increases the deformability of the shank projecting zones sustaining the piston pin and the contact pressure remains reasonably constant. On the other hand, if the shank profile is H-shaped, the shank zones supporting the piston pin are less flexible leading to a higher non-uniform

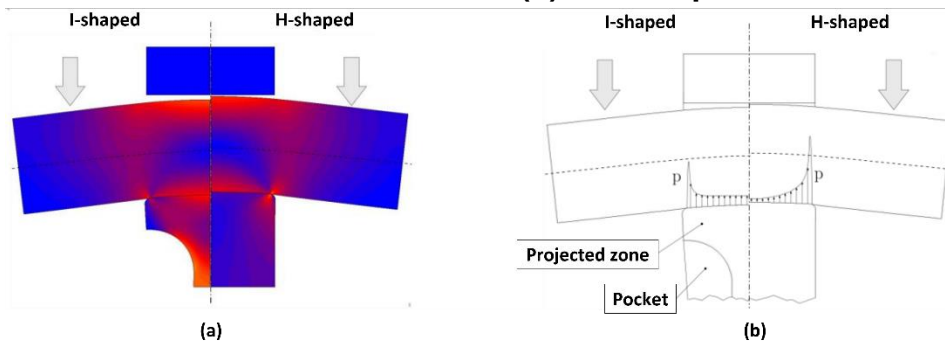
contact pressure, as shown in Figure 44. Hence, in some high-performance H-section connecting rods, a small frontal pocket is added to increase the deformability of the shank zones supporting the piston pin, (Strozzi et al. 2018; Gotou and Yanagisawa 2009; Eduard Köhler 2011).

Figure 43 – Connecting rod shank profiles: I-section (a), H-section (b), Blade-section (c), and Hollow-section (d)



Source: (TRZESNIOWSKI, 2010)

Figure 44 – Contact pressure between piston pin and connecting rod pin-eye: (a) von Mises stress distribution and (b) contact pressure distribution

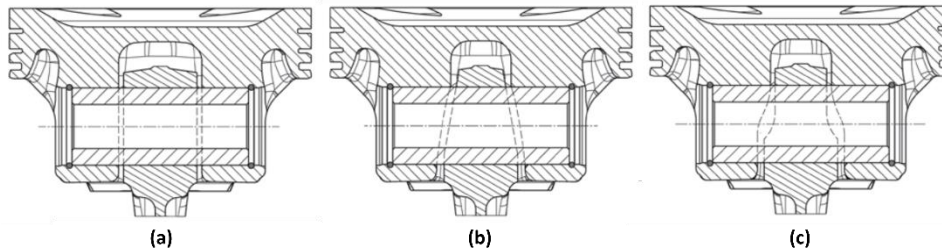


Source: (STROZZI; BALDINI; GIACOPINI; BERTOCCHI et al., 2018)

The small end bore (pin-eye bore) accepts the piston pin, and together with the piston pin boss, forms the joint about which the connecting rod pivots. The contact pressure is derived from the gas force, the piston pin diameter and the bearing length, and its values generally is greater than 100 MPa. The gas force is the highest magnitude load and acts only in the direction of the big end bore, which has led to the development of various types of support in the small end bore to meet load carrying capacity, weight, and cost requirements. The parallel connecting rod is the basic version and the easiest to use and most economical to manufacture especially when

it has the same width of the big end bore. On the other hand, the tapered connecting rod is slanted at the small end bore and thus gets wider in the direction of the connecting shank. The piston pin boss is adapted in order to reduce the contact pressure as well. The third pin-eye type the stepped connecting rod is the harder to manufacture. However, it best combines load carrying capacity and shape. The lubrication of the connecting rod small end usually is made by a small oil channel internally in the connecting rod shank or by the oil from the piston jet cooling. In last case, the oil drips onto the small end bore and move laterally or through oil bores into the gap between the piston pin and the small end bore, (Bertocchi, Giacopini, and Dini 2012; MAHLE 2016). Figure 45 illustrates the typical connecting rod small end designs.

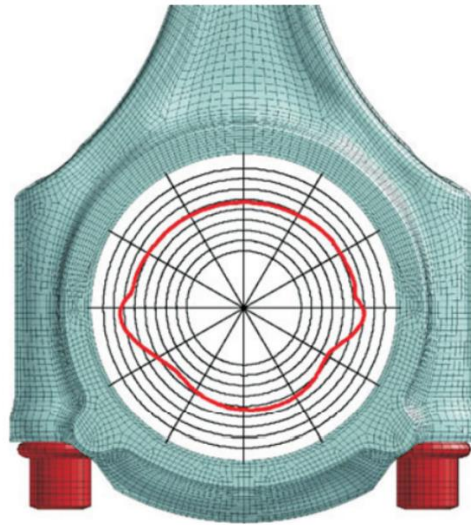
Figure 45 – Connecting rod parallel (a), tapered (b) and stepped (c) pin-eye



Source: (MAHLE, 2016a)

The big end bore dimensions is defined from the crankshaft journal diameter and the bearing wall thickness. As aforementioned, the critical stress on the big end bore results from inertia forces and it is important that the parting line remains closed under closed under all operating conditions. For that, the connecting rod bolts are tightened at the specified pre-load. However, as a reaction to the bolt force, the big end bore deforms into an out-of-round blind bore as shown in Figure 46. Thus, it is necessary to recreate the bolt tightening procedure in order to prevent any over stresses and over deformations, (MAHLE 2016).

Figure 46 – Representation of the connecting rod big end blind bore deformation after the bolts tightened



Source: (MAHLE, 2016a)

2.3.7.3. Connecting Rod Materials

Depending on the engine application different materials are used for connecting rods. Cast iron with nodular graphite (GGG-70) and black malleable cast iron (GTS-70) are primarily used as material for casted connecting rod. The GGG-70 has both technical and economic advantages over malleable iron. In particular, the specific fatigue strength, which is important for connecting rods, is significantly higher with GGG-70. In the case of malleable cast iron, which is also an iron-carbon casting material, the microstructure is adjusted by means of a heat treatment carried out after the casting. Nowadays, most of the connecting rods are made of steel manufactured using the drop forging process. In most cases, micro-alloyed steels such as 27MnVS6 BY or carbon-manganese steels such as C40 mod BY are used. Usually, a steel with a high carbon content (C70 S6 BY) is used for fracture-separated forged connecting rods (cracking). For highly stressed connecting rods, the 34CrNiMo6 V (or 42CrMo4) steel with a tensile strength of 1200 MPa is available. However, an additional heat treatment (hardening) is required. In case of powder metal for connecting rods, the P/F-11C50 material is currently the most used. The strength-increasing elements, 2% Cu and 0.5% C, allow a tensile strength of up to 950 MPa to be achieved after sintering and forging. Further developments of this sintered material by increasing the Cu content from 2 to 3% show an improvement in tensile strength of 10% and an improvement in fatigue strength of 22%, (F. SCHÄFER 2017).

In addition to these connecting rod materials for large-scale production, the use of alternative materials such as, carbon fiber reinforced aluminum or carbon fiber reinforced plastic, primarily aims to reduce the weight of the connecting rod while maintaining the same load capacity. The titanium connecting rods, with which a considerable weight reduction can be achieved, are widespread used in racing engines. The disadvantage of the titanium connecting rods is the enlargement of the connecting rod bores during operation, which has a negative effect on the press fit of the bearing shells. The titanium is also not a good friction partner for steel, which means that anti-friction coatings are required on the end faces to prevent friction welding (scuffing) or on the bearing steel back to prevent fretting. Thus, the connecting rods made of these alternative materials have in common the high production costs, which are justified for individual engines, although prevent them from being used widely in mass-produced engines, (F. SCHÄFER 2017). The Table 10 presents typical connecting rod materials and their properties.

Table 10 – Typical connecting rod materials and their properties

Material Name	NCI	P/F-11C50 Cu2C5	HS150 Cu3C6	C70S6 / C70+	36MnVS4	C38	42Cr	Al	TiAl4V4
Young Modulus [GPa]	170	199	200	213	210	210	210	68.9	128
Fatigue strength (pull) [MPa]	200	320	390	300/365	430	420	480	50	225
Fatigue strength (push) [MPa]	200	330	395	300/365	430	420	480	50	309
Rp 0.2% Yield strength [MPa]	410	550	700	550/650	750	550	>800	130	1000
Compressive Yield strength [MPa]	-	620	-	550/650	700	620	850	150	-
Rm: Tensile strength [MPa]	750	860	950	900/1050	950/1100	900	1050	200	1080
Density [g/cm ³]	7.2	7.6	7.8	7.85	7.85	7.85	7.85	2.71	4.51

Source: (SCHÄFER, 2017)

Cracking, or fracture splitting, of connecting rods has become common practice in recent years. The big end bore is notched inside the bore with a laser beam or

reamer. The resulting joint face (fracture surface) is not machined, and dowel sleeves or fitting screws are not needed. Therefore, the fit is provided solely by the engagement of the uneven surfaces. In cracking, the fracture splitting ability of the connecting rod material is critical. Special steel materials with a yield point/tensile strength ratio of up to 0.75 are used, (MAHLE 2016). Figure 47 illustrates a connecting rod with fracture surfaces of the big end bore.

Figure 47 – Connecting rod with fracture surfaces of the big end bore

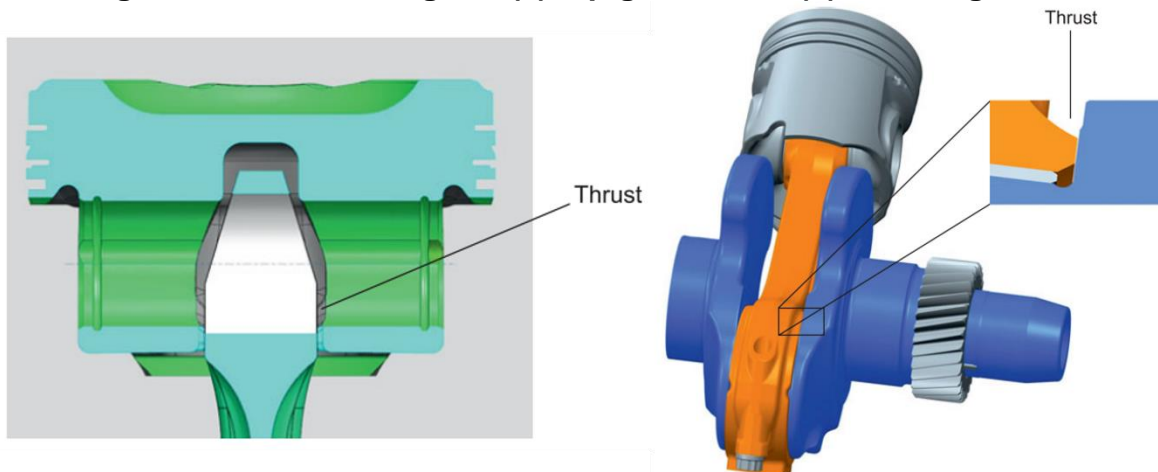


Source: (MAHLE, 2016a)

2.3.7.4. Connecting Rod Assembly

The connecting rod assembly is typically guided axially, in the crankshaft direction, by the big end bore on the crankshaft crank web also called bottom-guided connecting rod. Conversely, if the connecting guidance is provided by the piston and the small end bore it is called top-guided. In case of top-guided is applied the need or thrust washers on the crankshaft is eliminated and the length of the piston pin can be reduced. However, the motions and vibrations from the crankshaft are transmitted directly into the piston. Furthermore, lubrication conditions in the small bore are also worsened, because less oil travels through the narrow gap between the connecting rod and the piston, (MAHLE 2016).

Figure 48 – Connecting rod (a) top-guided and (b) bottom-guided



Source: (MAHLE, 2016a)

2.3.8. Crankshaft

The crankshaft is one of the key components of an internal combustion engine and must be designed carefully. It is also one of the most critical components due to high loads, cyclically variable in modulus and direction applied on it. The crankshaft has a complex geometry, and its dimensions vary according to the type of application. Despite of its type of application, it is required from a crankshaft to convert the linear piston motion to a rotary movement, to absorb the connecting rod forces, to convert tangential force into a torque, to mass balance the crank mechanism and to drive engine subsystems, (Baragetti 2015; Eduard Köhler 2011).

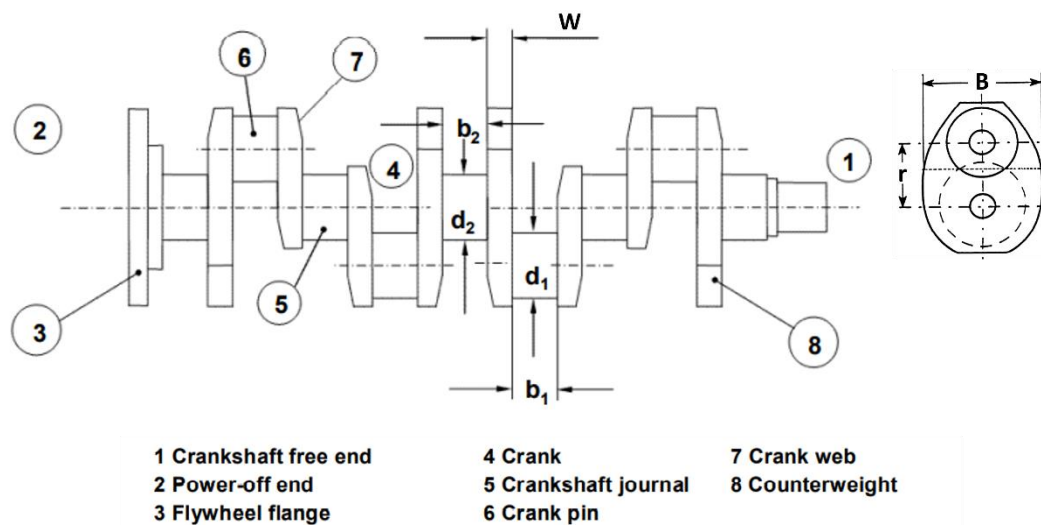
In order to the crankshaft fulfill all the aforementioned requirements, it must meet the following criteria:

- Sufficient fatigue strength with regard to torsion and bending loads;
- Main and connecting rod bearing journals for sufficient bearing dimensioning;
- Low friction losses;
- Higher quality bearing lubrication;
- Favorable arrangement, correct dimensioning of the counterweights;
- Secure connection with flywheel and belt pulley as well as vibration dampers; (Eduard Köhler 2011).

2.3.8.1. Crankshaft Design

The design of a crankshaft and outer dimensions are determined, mainly, by the crank spacing or bore spacing (distance between cylinder bore center lines), the piston stroke, the number of crankshaft throws and the throw angle between them, and the number, size and arrangement of counterweights. A crankshaft throw dimensions are the main pin width (b_2) and crank pin width (b_1), the related journal diameters (d_2) and (d_1), and the crankshaft web thickness (C). The flywheel flange is located on the engine output end. On the other side, the crankshaft free end is constructed as a shaft journal for the attachment of the belt pulley, vibration damper and engine auxiliary systems. Powered by the crankshaft, the camshaft drive may be mounted on the front end or, frequently in diesel engines, on the flywheel end for reasons of vibrations, (Mollenhauer and Tschoeke 2010). Figure 49 presents the crankshaft terminology.

Figure 49 – Crankshaft terminology



Source: (PISCHINGER, 2012)

The crankshaft running smoothness is a universally important criterion for its design. For gasoline engines a high speed has priority, which in turn it makes a minimum of moving masses the main target. On the other hand, the emphasis shifts somewhat for diesel engines. In diesel engines, the firing pressures can be twice as high as in gasoline engines and the engine speed is relatively low compared to gasoline engines. Thus, to bear the effects of the gas force became the primary challenge, (Mollenhauer and Tschoeke 2010). The Table 11 presents the typical crankshaft main dimensions relative to the cylinder bore for passenger car engines.

Table 11 – Typical crankshaft main dimensions

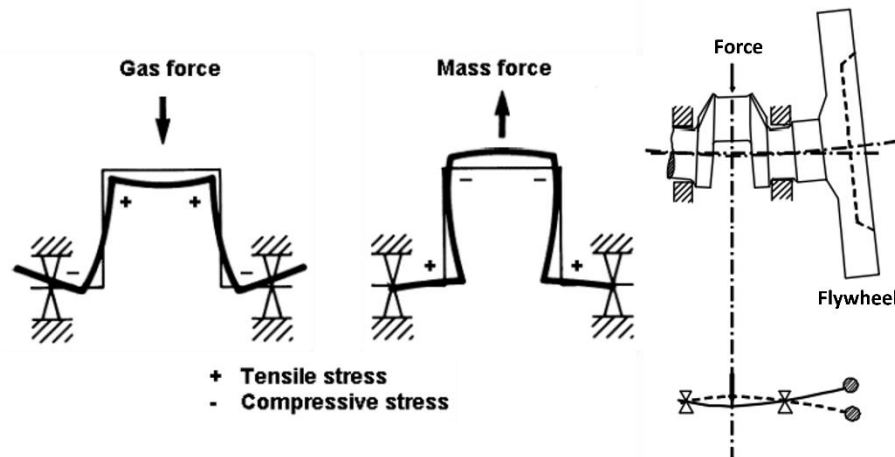
Engine type	Shaft pin		Crank pin		Web thickness	Bore spacing
	d2	b2	d1	b1	C	a
Gasoline in-line engine	0.55 – 0.75	0.20 – 0.35	0.45 – 0.65	0.15 – 0.35	0.20 – 0.35	1.06 – 1.20
Gasoline V-engine	0.68 – 0.80	0.24 – 0.36	0.48 – 0.67	0.22 – 0.53	0.14 – 0.21	1.06 – 1.30
Diesel in-line engine	0.65 – 0.80	0.24 – 0.33	0.53 – 0.64	0.24 – 0.31	0.22 – 0.31	1.08 – 1.12
Diesel V-engine	0.80 – 0.85	0.25 – 0.35	0.64 – 0.74	0.25 – 0.52	0.15 – 0.2	1.10 – 2.00

Values shown as a fraction of the bore diameter

Source: (EDUARD KÖHLER, 2011; PISCHINGER, 2012)

The main loads on the crankshaft are the bending load and the torsional load caused by the gas and the mass forces. The bending load is caused by gas and mass forces with stress peaks occurring mainly near of the TDC. A compression stress in the crankshaft throw transitional radius of journal and web is caused by the gas pressure throughout the engine expansion stroke. Conversely, at gas exchange TDC and BDC the mass forces cause tensile stress resulting in a reversed bending stress. Furthermore, an additional bending load on the throws at the crankshaft power end may be caused by vibration of the flywheel due to crankshaft deformations. Figure 50 illustrates the crankshaft deformation due to gas and mass forces. The torsional vibrations and the fluctuating torque that is transmitted by the crankshaft cause crankshaft torsional stress. However, the torsional load caused by the tangential force fluctuations is typically low when compared to the alternating torsional stress due to torsional vibrations, (Pischinger 2012).

Figure 50 – Crankshaft deformation due to gas and mass forces



Source: (PISCHINGER, 2012)

The stress of a crankshaft is supported by multiple bearings, which in turn, it is difficult to calculate. As a solution, an approximation is performed on a single section between two bearings which are assumed as flexible joints. With this approach, the bending stress can be calculated for the center of the crankshaft web. The calculation of crankshaft strength consists initially in determining the nominal alternating bending and nominal alternating torsional stresses which, multiplied by the appropriate stress concentration factors, result in an equivalent alternating stress. This equivalent alternating stress is then compared with the fatigue strength of the selected crankshaft material. This comparison will show whether the crankshaft concerned is dimensioned adequately, (M53 2017).

The alternating values are calculated according to Equation 61:

$$X_A = \pm \frac{1}{2} \cdot (X_{max} - X_{min}) \quad (61)$$

Where, the X_A is considered as alternating force, moment, or stress, X_{max} is the maximum value within one working cycle and X_{min} is the minimum value within one working cycle, (M53 2017).

The nominal alternating bending and compressive stresses in the crankshaft web are calculated using Equation 62 and Equation 63, respectively.

$$\sigma_{NBW} = \pm \frac{M_{bend}}{W_{eqw}} \cdot 10^3 \cdot K_e = \pm \frac{6 \cdot M_{bend}}{Ba \cdot W^2} \cdot 10^3 \cdot K_e \quad (62)$$

$$\sigma_{QFN} = \pm \frac{F_{RadAlt}}{A_{web}} \cdot K_e \quad (63)$$

Where, the σ_{NBW} is the nominal alternating bending stress related to the web in [N/mm²], the M_{bend} is the alternating bending moment to the center of the web in [Nm], the K_e is an empirical factor considering to some extent the influence of adjacent crank and bearing restraint ($K_e=0.8$ for 2-stroke engines and $K_e=1.0$ for 4-stroke engines), the σ_{QFN} is the nominal alternating compressive stress due to radial force related to the crank web, the F_{RadAlt} is the alternating radial force related to the crank web and the A_{web} is the area to cross section of the crank web, (M53 2017).

The nominal alternating bending stress in the outlet of the crankpin oil bore is calculated using Equation 64, Equation 65 and Equation 66.

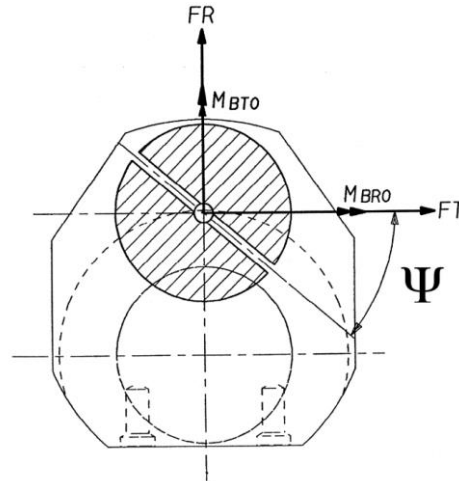
$$\sigma_{BON} = \pm \frac{M_{BON}}{W_e} \cdot 10^3 = \pm \frac{M_{BON} \cdot 32}{\pi \cdot d_1} \cdot 10^3 \quad (64)$$

$$M_{BON} = \pm \frac{1}{2} \cdot (M_{BOmax} - M_{BOmin}) \quad (65)$$

$$M_{BO} = (M_{BTO} \cdot \cos \psi + M_{BRO} \cdot \sin \psi) \quad (66)$$

Where, the σ_{BON} is the nominal alternating bending stress related to the crank pin diameter in [N/mm²], the M_{BON} is the alternating moment calculated at outlet of the crankpin oil bore as in [Nm], the M_{BO} is the moment calculated at outlet of the crankpin oil bore as in [Nm] in function of the bending moment of the radial component of the connecting rod M_{BRO} and the bending moment of the tangential component of the connecting-rod force M_{BTO} , the W_e is the section modulus related to cross section of crankpin in [mm³] and, the ψ is crankshaft oil bore angular position as shown in Figure 51, (M53 2017).

Figure 51 – Crankpin section through the oil bore



Source: (M53, 2017)

The alternating stresses in fillets for crankpin as well as journal fillets is to be carried out according to Equation 67 and Equation 68, respectively.

$$\sigma_{BCP} = \pm(\alpha_B \cdot \sigma_{NBW}) \quad (67)$$

$$\sigma_{BJO} = \pm(\beta_B \cdot \sigma_{NBW} + \beta_Q \cdot \sigma_{QFN}) \quad (68)$$

Where, the σ_{BCP} is the bending stress in the crankpin fillet in [N/mm²], the α_B is the dimensionless stress concentration factor for bending in crankpin fillet, the σ_{BJO} is the bending stress in the journal fillet in [N/mm²], the β_B is the dimensionless stress concentration factor for bending pin in journal fillet and the β_C is the dimensionless stress concentration factor for compression due to radial force in journal fillet, (M53 2017).

For the alternating bending stresses in crankpin oil bore outlet calculation, Equation 69 is used.

$$\sigma_{BO} = \pm(\gamma_B \cdot \sigma_{BON}) \quad (69)$$

Where, the σ_{BO} is the bending stress in the crankpin oil bore outlet in [N/mm²], the γ_B is the dimensionless stress concentration factor for bending in the crankpin oil bore outlet, (M53 2017).

The nominal alternating torsional stress calculation is made using Equation 70.

$$\tau_N = \pm \frac{M_{TN}}{W_P} \cdot 10^3 = \pm \frac{M_{TN} \cdot 16}{\pi \cdot d_*} \cdot 10^3 \quad (70)$$

$$M_{TN} = \pm \frac{1}{2} \cdot (M_{Tmax} - M_{Tmin}) \quad (71)$$

Where, the τ_N is the nominal alternating torsional stress referred to crankpin or journal in [N/mm²], the M_{TN} is the maximum alternating torque in [Nm], the W_P is polar section modulus related to cross-section of crankpin or journal in [mm³], the d_* is the diameter of the crankpin (d_1) or the journal diameter (d_2), and the M_{Tmax} and M_{Tmin} are the maximum and minimum torque value respectively, (M53 2017).

The alternating torsional stresses in fillets and in crankpin oil bore outlet calculation is made using the following equations.

For the crankpin fillet, Equation 72:

$$\tau_H = \pm(\alpha_T \cdot \tau_N) \quad (72)$$

Where, the τ_H is the alternating torsional stress in the crankpin fillet in [N/mm²] and the α_T is the dimensionless stress concentration factor for torsion in the crankpin fillet.

For the journal fillet, Equation 73:

$$\tau_G = \pm(\beta_T \cdot \tau_N) \quad (73)$$

Where, the τ_G is the alternating torsional stress in the journal fillet in [N/mm²] and the β_T is the dimensionless stress concentration factor for torsion in the journal fillet.

For the outlet of crankpin oil bore, Equation 75:

$$\tau_{TO} = \pm(\gamma_T \cdot \tau_N) \quad (74)$$

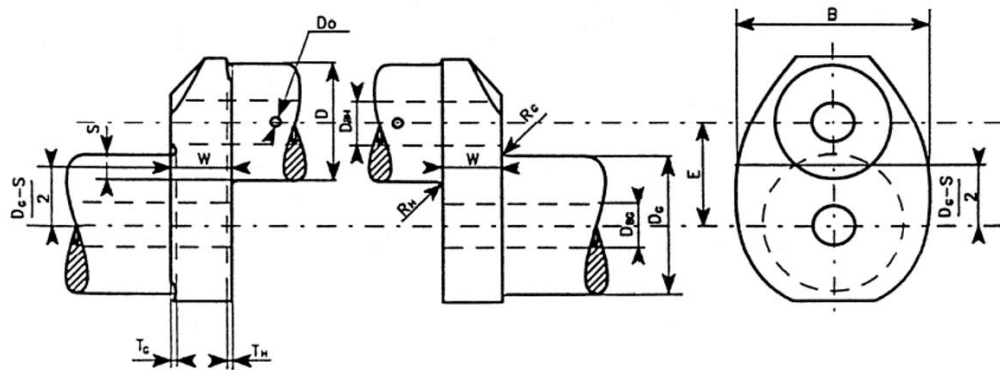
Where, the τ_{TO} is the alternating stress in in outlet of crankpin oil bore due to torsion in [N/mm²] and the γ_T is the dimensionless stress concentration factor for torsion outlet of crankpin oil bore, (M53 2017).

The stress concentration factor for bending (α_B , β_B) is defined as the ratio of the maximum equivalent stress (Von Mises) occurring in the fillets under bending load to

the nominal bending stress related to the web cross-section. On the other hand, the stress concentration factor for compression (β_Q) in the journal fillet is defined as the ratio of the maximum equivalent stress (Von Mises) occurring in the fillet due to the radial force to the nominal compressive stress related to the web cross-section. The stress concentration factor for torsion (α_T, β_T) is defined as the ratio of the maximum equivalent shear stress occurring in the fillets under torsional load to the nominal torsional stress related to the Crankpin or journal cross-section. The stress concentration factors for bending (γ_B) and torsion (γ_T) are defined as the ratio of the maximum principal stress occurring at the outlet of the crankpin oil-hole under bending and torsional loads to the corresponding nominal stress related to the crankpin cross section, (M53 2017).

The stress concentration factors are evaluated by means of the formulae applicable to the fillets and crankpin oil bore of solid forged web-type crankshafts and to the crankpin fillets of semi-built crankshafts. All formulae are based on investigations of FVV (*Forschungsvereinigung Verbrennungskraftmaschinen*) for fillets and on investigations of ESDU (Engineering Science Data Unit) for oil holes. Figure 52 and the presented the applied dimensions used for the calculation of the stress concentration factors in the following equations, (M53 2017).

Figure 52 – Crank dimensions for stress concentration factor calculation



D	[mm]	crankpin diameter
D _{BH}	[mm]	diameter of axial bore in crankpin
D _o	[mm]	diameter of oil bore in crankpin
R _H	[mm]	fillet radius of crankpin
T _H	[mm]	recess of crankpin fillet
D _G	[mm]	journal diameter
D _{BG}	[mm]	diameter of axial bore in journal
R _G	[mm]	fillet radius of journal
T _G	[mm]	recess of journal fillet
E	[mm]	pin eccentricity
S	[mm]	pin overlap
		$S = \frac{D + D_G}{2} - E$
W (*)	[mm]	web thickness
B (*)	[mm]	web width

Source: (M53, 2017)

Figure 53 – Crank dimensions relations for stress concentration factor calculation

Crankpin fillet	Journal fillet
$r = R_H / D$	$r = R_G / D$
$s = S/D$	
$w = W/D$ crankshafts with overlap	
W_{red}/D crankshafts without overlap	
$b = B/D$	
$d_o = D_o/D$	
$d_G = D_{BG}/D$	
$d_H = D_{BH}/D$	
$t_H = T_H/D$	
$t_G = T_G/D$	

Source: (M53, 2017)

According to (M53 2017), the stress concentration factors are valid for the ranges of related dimensions for which the investigations have been carried out. The ranges are presented in the Table 12.

Table 12 – Dimensions ranges for valid concentration factors evaluation

$s \leq 0.5$
$0.2 \leq w \leq 0.8$
$1.1 \leq b \leq 2.2$
$0.03 \leq r \leq 0.13$
$0 \leq d_G \leq 0.8$
$0 \leq d_H \leq 0.8$
$0 \leq d_o \leq 0.2$

Source: (M53, 2017)

The stress concentration factor for bending in the crankpin fillet is calculated using Equation 75.

$$\alpha_B = 2.6914 \cdot f(s, w) \cdot f(w) \cdot f(b) \cdot f(r) \cdot f(d_G) \cdot f(d_H) \cdot f(recess) \quad (75)$$

Where:

$$\begin{aligned} f(s, w) = & -4.1883 + 29.2004 \cdot w - 77.5925 \cdot w^2 + 91.9454 \cdot w^3 \\ & - 40.0416 \cdot w^4 \\ & + (1 - s) \cdot (9.5440 - 58.3480 \cdot w + 159.3415 \cdot w^2 \\ & - 192.5846 \cdot w^3 + 85.2916 \cdot w^4) + (1 - s)^2 \cdot (-3.8399 \\ & + 25.0444 \cdot w - 70.5571 \cdot w^2 + 87.0328 \cdot w^3 \\ & - 39.1832 \cdot w^3) \end{aligned} \quad (76)$$

$$f(w) = 2.1790 \cdot w^{0.7171} \quad (77)$$

$$f(b) = 0.6840 - 0.0077 \cdot b + 0.1473 \cdot b^2 \quad (78)$$

$$f(r) = 0.2081 \cdot r^{(-0.5231)} \quad (79)$$

$$f(d_G) = 0.9993 + 0.27 \cdot d_G - 1.0211 \cdot d_G^2 + 0.5306 \cdot d_G^3 \quad (80)$$

$$f(d_H) = 0.9978 + 0.3145 \cdot d_H - 1.5241 \cdot d_H^2 + 2.4147 \cdot d_H^3 \quad (81)$$

$$f(recess) = 1 + (t_H + t_G) \cdot (1.8 + 3.2 \cdot s) \quad (82)$$

The stress concentration factor for torsion in the crankpin fillet is calculated using Equation 83.

$$\alpha_T = 0.8 \cdot f(r, s) \cdot f(b) \cdot f(w) \quad (83)$$

Where:

$$f(r, s) = r^{(-0.322+0.1015 \cdot (1-s))} \quad (84)$$

$$f(b) = 7.8955 - 10.654 \cdot b + 5.3482 \cdot b^2 - 0.857 \cdot b^3 \quad (85)$$

$$f(w) = w^{(-0.145)} \quad (86)$$

The stress concentration factor for bending in the journal fillet is calculated using Equation 87.

$$\beta_B = 2.7146 \cdot f_B(s, w) \cdot f_B(w) \cdot f_B(b) \cdot f_B(r) \cdot f_B(d_G) \cdot f_B(d_H) \cdot f_B(recess) \quad (87)$$

Where:

$$\begin{aligned} f_B(s, w) = & -1.7625 + 2.9821 \cdot w - 1.5276 \cdot w^2 \\ & + (1 - s) \cdot (5.1169 - 5.8089 \cdot w + 3.1391 \cdot w^2) \\ & + (1 - s)^2 \cdot (-2.1567 + 2.3297 \cdot w - 1.2952 \cdot w^2) \end{aligned} \quad (88)$$

$$f_B(w) = 2.2422 \cdot w^{0.7548} \quad (89)$$

$$f_B(b) = 0.5616 - 0.1197 \cdot b + 0.1176 \cdot b^2 \quad (90)$$

$$f_B(r) = 0.1908 \cdot r^{(-0.5568)} \quad (91)$$

$$f_B(d_G) = 1.0012 - 0.6441 \cdot d_G + 1.2265 \cdot d_G^2 \quad (92)$$

$$f_B(d_H) = 1.0022 + 0.1903 \cdot d_H + 0.0073 \cdot d_H^2 \quad (93)$$

$$f(recess) = 1 + (t_H + t_G) \cdot (1.8 + 3.2 \cdot s) \quad (94)$$

The stress concentration factor for compression in the journal fillet due to the radial force is calculated using Equation 95.

$$\beta_Q = 2.7146 \cdot f_Q(s) \cdot f_Q(w) \cdot f_Q(b) \cdot f_Q(r) \cdot f_Q(d_H) \cdot f_Q(recess) \quad (95)$$

Where:

$$f_B(s, w) = 0.4368 + 2.1630 \cdot (1 - s) - 1.5212 \cdot (1 - s)^2 \quad (96)$$

$$f_B(w) = \frac{w}{0.0637 + 0.9369 \cdot w} \quad (97)$$

$$f_B(b) = -0.5 + b \quad (98)$$

$$f_B(r) = 0.5331 \cdot r^{(-0.2038)} \quad (99)$$

$$f_B(d_H) = 0.9937 - 1.1949 \cdot d_H + 1.7373 \cdot d_H^2 \quad (100)$$

$$f(recess) = 1 + (t_H + t_G) \cdot (1.8 + 3.2 \cdot s) \quad (101)$$

The stress concentration factor for torsion in the journal fillet is calculated using Equation 102 if the diameters and fillet radii of crankpin and journal are the same. On the other hand, if crankpin and journal diameters and/or radii are of different sizes Equation 103 should be used, (M53 2017).

$$\beta_T = \alpha_T \quad (102)$$

$$\beta_T = 0.8 \cdot f(r, s) \cdot f(b) \cdot f(w) \quad (103)$$

The stress concentration factor for bending and torsion in the crankpin oil bore outlet is calculated using Equation 104 and Equation 105, respectively.

$$\gamma_B = 3 - 5.88 \cdot d_o + 34.6 \cdot d_o^2 \quad (104)$$

$$\gamma_T = 4 - 6 \cdot d_o + 30 \cdot d_o^2 \quad (105)$$

Finally, the equivalent alternating stress is calculated in accordance with Equation 106, Equation 107 and Equation 108 for the crankpin fillet, the journal fillet and crankpin oil bore outlet, in [N/mm²], respectively, (M53 2017).

$$\sigma_{V_{CP}} = ((\sigma_{BH} + \sigma_{add})^2 + 3 \cdot \tau_H^2)^{\frac{1}{2}} \quad (106)$$

$$\sigma_{V_J} = ((\sigma_{BG} + \sigma_{add})^2 + 3 \cdot \tau_G^2)^{\frac{1}{2}} \quad (107)$$

$$\sigma_{V_{Oil}} = \pm \frac{1}{3} \cdot \sigma_{BO} \cdot \left[1 + 2 \cdot \sqrt{1 + \frac{9}{4} \cdot \left(\frac{\sigma_{TO}}{\sigma_{BO}} \right)^2} \right] \quad (108)$$

Where, the σ_{add} is an additional alternating bending stress due to misalignment and bedplate deformation as well as due to axial and bending vibrations in [N/mm²]. For crosshead engines is recommended an additional ± 30 N/mm² and for trunk piston engines is recommended ± 10 N/mm², (M53 2017).

The sufficient dimensioning of a crankshaft is confirmed by a comparison of the equivalent alternating stress and the crankshaft material fatigue strength. This comparison must be carried out for the crankpin fillet, the journal fillet, the outlet of crankpin oil bore. An adequate dimensioning of the crankshaft is ensured if the smallest of all acceptability factors satisfies the criteria $Q \geq 1.15$, (M53 2017).

Although Equations for a crankshaft analytical stress evaluation are available, nowadays this analysis is performed using FEM. The FEM methodology is described in the 2.8.1 of this work. However, it is still required to calculate and design a base crankshaft geometry for FEM analysis.

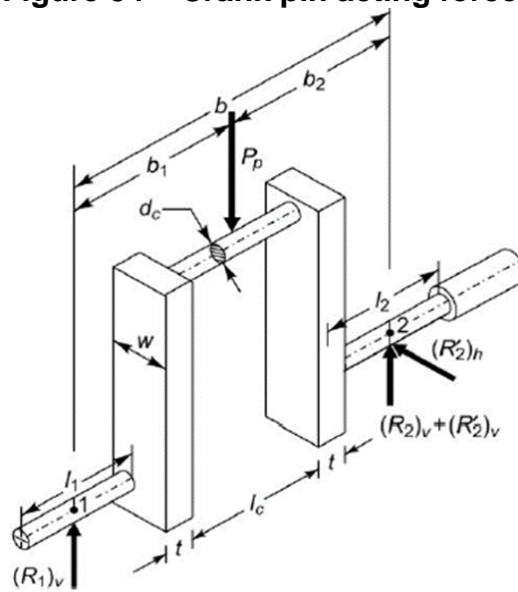
The crank pin diameter, D_h in mm, can be calculated using Equation 109 based on the bending moment at the crankshaft central plane.

$$d_c = \sqrt[3]{\frac{32 \cdot M_b}{\sigma_{all} \cdot \pi}} \quad (109)$$

Where σ_{all} is the allowable bending stress and M_b is the bend moment. According to Figure 54, the bend moment can be calculated using Equation 110. Furthermore, according to crankshaft design guide lines from engine manufactures, it is suggested to use a safety factor of 2 for forged and machined.

$$M_b = P_p \cdot b_1 = \frac{F_{gas}}{2} \cdot b_1 \quad (110)$$

Figure 54 – Crank pin acting forces



Source: (BHANDARI 2010)

For the crankshaft journal diameter calculation it is required to combine the bending moment and the torsion moment. According to (Budynas and Nisbett 2011), the crankshaft journal diameter, d_{CJ} in mm, can be calculated using Equation 111 based on ASME Elliptic method.

$$d_{CJ} = \left\{ \frac{16 \cdot n}{\pi} \cdot \left[4 \cdot \left(\frac{K_f \cdot M_a}{S_e} \right)^2 + 3 \cdot \left(\frac{K_{fs} \cdot T_a}{S_e} \right)^2 + 4 \cdot \left(\frac{K_f \cdot M_m}{S_y} \right)^2 + 3 \cdot \left(\frac{K_{fs} \cdot T_m}{S_y} \right)^2 \right]^{1/2} \right\}^{1/3} \quad (111)$$

Where M_a and M_m are the alternating and midrange bending moments in N.mm, T_a and T_m are the alternating and midrange torques in N.mm, and K_f and K_{fs} are the fatigue stress-concentration factors for bending and torsion, respectively. The S_e and S_y are the corrected endurance limit and material Yield strength in MPa. The corrected endurance limit calculation is presented in the topic 2.7.2 of this work.

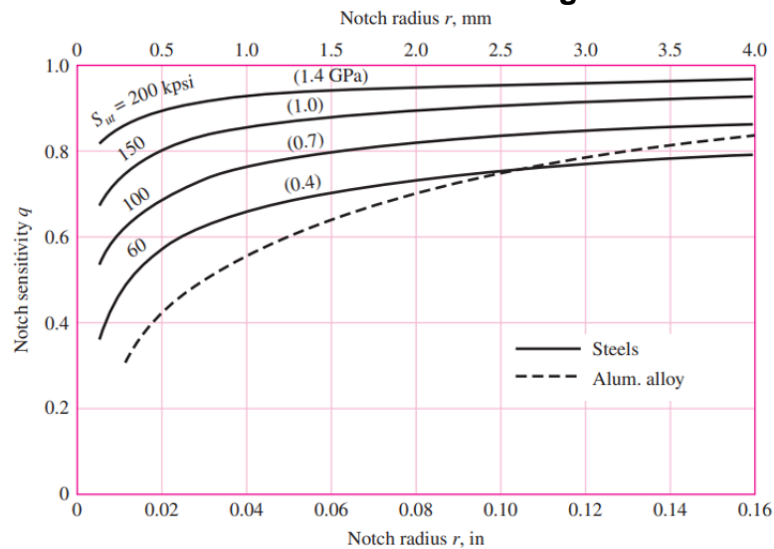
The K_f and K_{fs} can be calculated using Equation 112 and Equation 113 respectively.

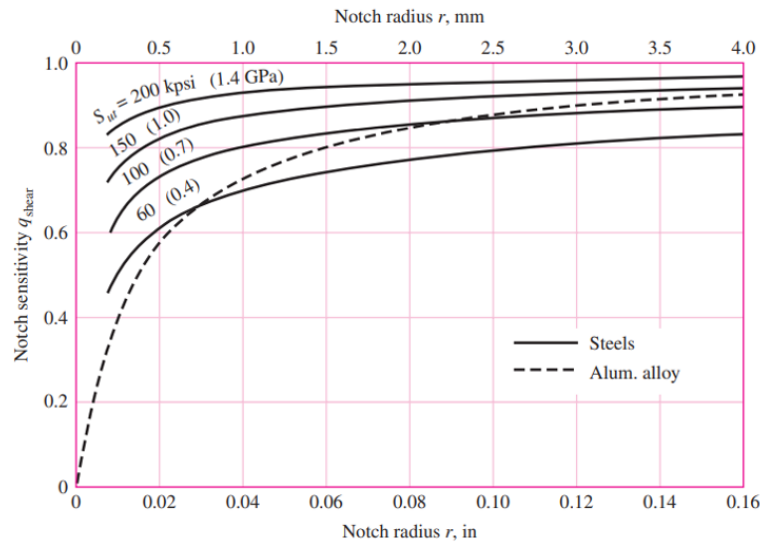
$$K_f = 1 + q \cdot (K_t - 1) \quad (112)$$

$$K_{fS} = 1 + q_{shear} \cdot (K_{ts} - 1) \tag{113}$$

Where q and q_{shear} are the notch sensitivity for bending and torsion loads, respectively. The notch sensitivities can be defined base on the notch radius using Figure 55. The K_t and K_{ts} are the theoretical, or geometric, stress-concentration factors related to normal and shear stress, respectively. The theoretical, or geometric, stress-concentration factors can be obtained using the tables A-15 available in (Budynas and Nisbett 2011).

Figure 55 – Notch sensitivities for bending and torsion loads





Source: (BHANDARI 2010)

2.3.8.2. Crankshaft Balancing

The forces acting on the reciprocating mechanism is presented in the 2.5.2 topic of this work. It was presented that an engine has free inertial forces divided into oscillating and rotational forces. The crankshaft counterweights may be designed to balance the rotational forces and partially balance the oscillating forces. However, sometimes secondary shafts are used to balance the oscillating inertial forces. As previously presented, the oscillating force is calculated by Equation 25 for a non-offset mechanism. Combining Equation 27 with Equation 11, the oscillating force is calculated using Equation 114, (Pischinger 2012).

$$F_{Mass\ Osc.} = m_{osc.} \cdot r \cdot \omega^2 \cos \varphi + m_{osc.} \cdot r \cdot \omega^2 \lambda \cdot \cos 2\varphi \quad (114)$$

Equation 114 can be divided into forces of 1st order, F_1 , and force of 2nd order, F_2 , as presented by Equation 115 and Equation 116, respectively.

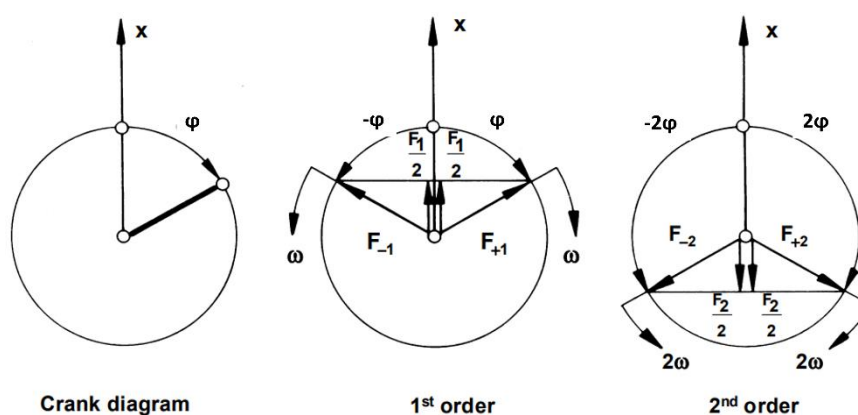
$$F_1 = m_{osc.} \cdot r \cdot \omega^2 \cos \varphi = F_{01} \cdot \cos \varphi \quad (115)$$

$$F_2 = m_{osc.} \cdot r \cdot \omega^2 \lambda \cdot \cos 2\varphi = F_{02} \cdot \cos 2\varphi \quad (116)$$

Where, the F_{01} and F_{02} are the amplitude of the inertia force of 1st order and force of 2nd order.

It is worth to point out that the force of 2nd order is always smaller than the force of 1st order. For passenger cars engines, the inertia forces higher than the 2nd order can be neglected. Furthermore, the inertia forces are harmonic and act in the direction of the cylinder center line and thus, they can be represented by two force vectors that are rotating in opposite direction (\vec{F}_{+1} and \vec{F}_{-1} for the inertia force of the 1st order, \vec{F}_{+2} and \vec{F}_{-2} for the inertia force of the 2nd order), as presented in Figure 56, (Pischinger 2012).

Figure 56 – Inertia forces vector diagram for a reciprocating mechanism

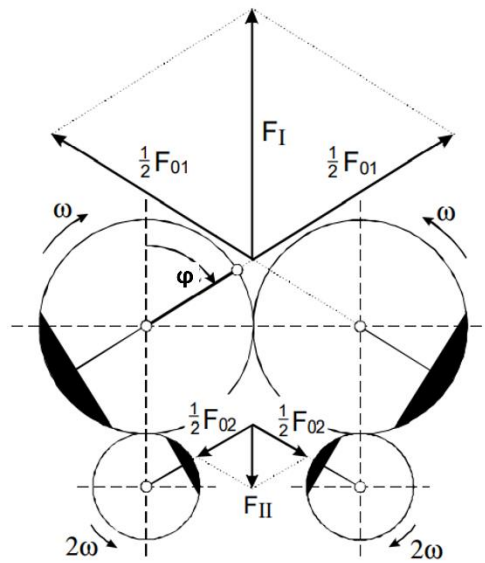


Source: (PISCHINGER, 2012)

The force vectors of 1st order \vec{F}_{+1} rotates synchronously in the crankshaft direction. However, the \vec{F}_{-1} rotates in opposite direction of it but symmetrically to \vec{F}_{+1} related to cylinder center axis. On the other hand, the force vectors of 2nd order \vec{F}_{+2} rotates with the twice of the crankshaft speed and synchronously in its direction. The \vec{F}_{-2} also rotates with the twice of the crankshaft speed but in opposite direction of the \vec{F}_{+2} , (Pischinger 2012).

The actions that compensate for the effect of inertia forces are called balancing of reciprocating masses. In case of single cylinder cranktrain, a complete compensation of the mass forces is possible using two pairs of rotating masses in system called Lanchester balancing system. These compensating masses are arranged such that the resulting alternating harmonic forces act in the center of the cylinder and are opposite to inertia forces of 1st order and 2nd order. The Lanchester balancing system is expensive and rarely applied, (Schrön 1947). Figure 57 illustrates the Lanchester inertia forces balancing system.

Figure 57 – Lanchester inertia forces balancing system



Source: (PISCHINGER, 2012)

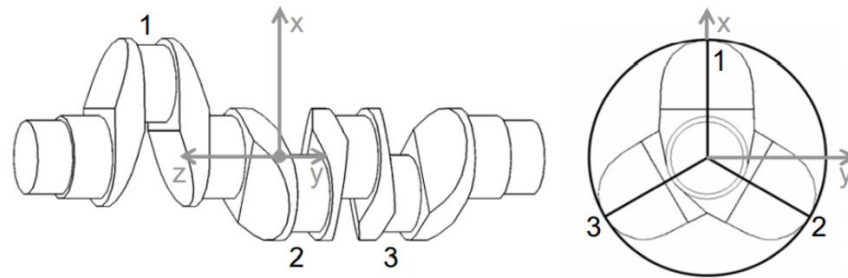
In case of multi-cylinder cranktrain the inertia forces of 1st order and 2nd order are the sum of the inertia forces of the individual cylinders. However, as the inertia forces of the individual cylinders act in its own cylinder, mass couples are generated. In this work going to be developed an in-line engine arrangement, thus only the balancing for in-line engine approach will be described.

For in-line engines, a schematic calculation is used to determine the inertia forces due to a parallel cylinder arrangement. The force vectors of the individual cylinder \vec{F}_{+1K} (where K is the number of cylinder), which rotate for the same direction, are added up according with its order creating a resultant force vector, Equation 117 and Equation 118. For each order, the projection of this resultant force vector on the cylinder direction represent half the mass forces. Furthermore, the projection of these resultant force vectors onto crankshaft xy-plane creates what is called a crank star, (Pischinger 2012). Figure 58 illustrates a crankshaft xy-plane for a crank star creation.

$$\vec{F}_{+1} = \sum_{K=1}^z \vec{F}_{+1K} \quad (117)$$

$$\vec{F}_{+2} = \sum_{K=1}^z \vec{F}_{+2K} \quad (118)$$

Figure 58 – Projection of the crankshaft on the xy-plane



Source: (PISCHINGER, 2012)

The crank star diagram of the 1st order inertia forces corresponds to the actual crank star. On the other hand, the 2nd order inertia forces result of doubling the angles of the crank.

The individual cylinder mass couple vectors of 1st order, \vec{M}_{+1K} , and 2nd order \vec{M}_{+2K} , are determined considering each force vector at a distance \vec{a}_K of the crankshaft center of gravity, Equation 119 and Equation 120, (Pischinger 2012).

$$\vec{M}_{+1K} = \vec{F}_{+1K} \times \vec{a}_K \quad (119)$$

$$\vec{M}_{+2K} = \vec{F}_{+2K} \times \vec{a}_K \quad (120)$$





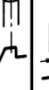
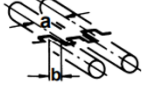

Summing all rotating vectors of the same order generate the resultant couple vector, Equation 121 and Equation 122.

$$\vec{M}_{+1} = \sum_{K=1}^z \vec{M}_{+1K} \quad (121)$$

$$\vec{M}_{+2} = \sum_{K=1}^z \vec{M}_{+2K} \quad (122)$$

Figure 59 illustrates an example of inertia forces and couples determination for a 3-cylinder in-line engine. In a 3-cylinder in-line engine, the inertia forces of both orders are inherently balanced (no resulting vectors \vec{F}_{+1} and \vec{F}_{+2}) due to crankshaft arrangement, however this does not apply for the inertia couples. These inertia couples stress the crankcase through the crankshaft bearings due to a bent crankshaft. It is worth to point out that symmetrical crank star diagrams do not have resulting inertia forces of 1st order, (Pischinger 2012).

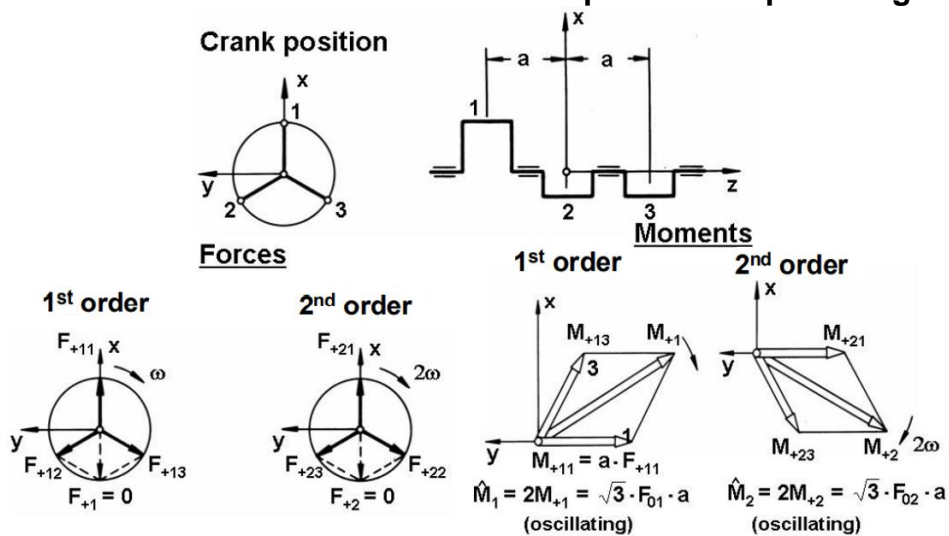
Figure 59 – Inertia forces and mass couples for a 3-cylinder in-line engine

Type							
Free forces	1 st order	F_{01}					
	2 nd order	F_{02}	$2 \cdot F_{02}$		$4 \cdot F_{02}$		
Free moments	1 st order		$F_{01} \cdot a$	$\sqrt{3} \cdot F_{01} \cdot a$			$\sqrt{10} \cdot F_{01} \cdot a$
	2 nd order			$\sqrt{3} \cdot F_{02} \cdot a$		$2 \cdot F_{02} \cdot b$	

Source: (PISCHINGER, 2012)

Figure 60 presents typical crankshaft arrangements and their associated inertia forces and couples. The 6-cylinder in-line engine is inherently balanced, while a complete compensation of the unbalanced of the 8-cylinder V-90 engine is possible through counterweights arrangement, (Pischinger 2012).

Figure 60 – Resultant inertia forces and couples for reciprocating engines

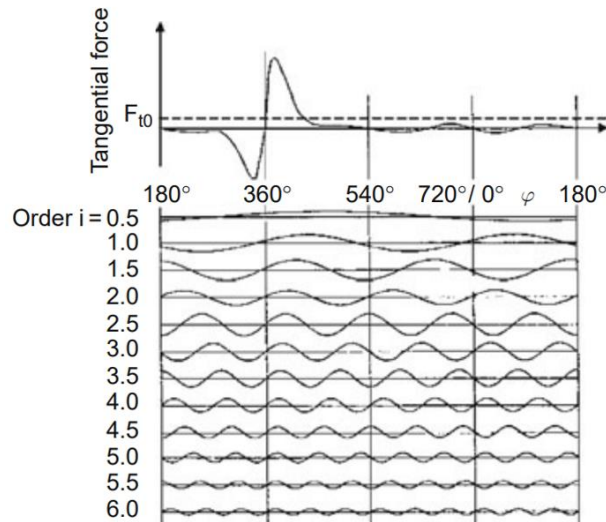


Source: (PISCHINGER, 2012)

The torsional forces variation leads to torsional oscillations on the crankshaft assembly. However, as the cylinder pressure is periodic event, the gas torque can be

broken down into its harmonic components. It is worth to point out that four-stroke engines have 0.5 as the lower harmonic order. Figure 61 illustrates the harmonic components of the torsional force four-stroke engine.

Figure 61 – Harmonic components of the torsional force four-stroke engine

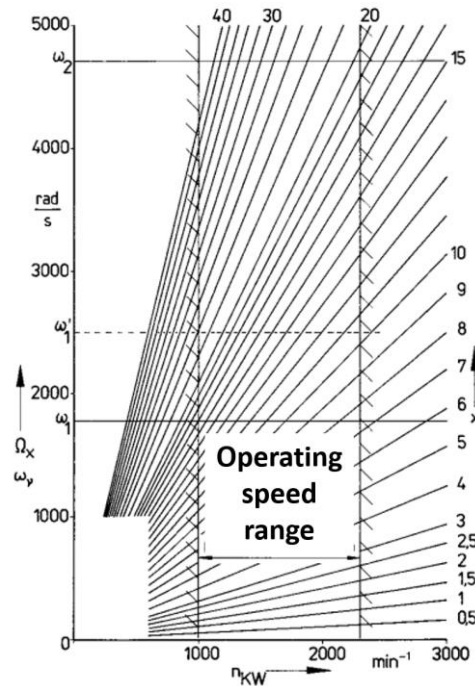


Source: (PISCHINGER, 2012)

At constant engine operating speed, a proper balanced cranktrain system is able to operate free of resonance. However, rotational vibration resonances must be run through during transient engine operation conditions. Therefore, torsional vibration dampers and absorbers are usually mounted on a crankshaft nose end where large vibration amplitudes occur. A torsional vibration damper is able to reduce vibration amplitudes within a frequency range, which in turn reduces the engine wear and improve the vehicle comfort, (F. SCHÄFER 2017).

The torsional vibration damper frequency is defined by means of a Campbell diagram. A Campbell diagram correlated the frequency of each harmonic versus engine speed. Various frequency points for the crankshaft system for different modes, and for each vibration mode the system can have different critical speeds depending on the harmonic order. However, some critical speeds of higher modes may occur outside the range of engine operation. The intersection between harmonics and engine speed define the damper characteristics for an engine application, (Küntscher and Hoffmann 2015).

Figure 62 – Campbell Diagram



Source: (KÜNTSCHER; HOFFMANN, 2015)

2.3.8.3. Crankshaft material

Forged crankshafts made of heat-treated steel such as 30Mn5, 41Cr4V80, 25CrMo5 and 42CrMo4, meet high demands on strength and rigidity. In addition, less expensive micro-alloyed steels with tempering by controlled cooling from the forging heat are increasingly being used. In the case of lower-loaded crankshafts, primarily in naturally aspirated engines, more cost-effective in terms of blank production and machinability nodular cast iron (EN-GJS-600-3 and EN-GJS-800-2) is often used. Nowadays, further than forging and casting manufacturing process billet crankshafts have been used in engines subjected to higher mechanical loads. Table 13 presents typical steel materials used for crankshaft manufacture.

Table 13 – Typical crankshaft materials

Steel	Tensile strength [N/mm ²]	Yield strength [N/mm ²]	Elongation at break A [%]
C38+N2	580	>340	>12

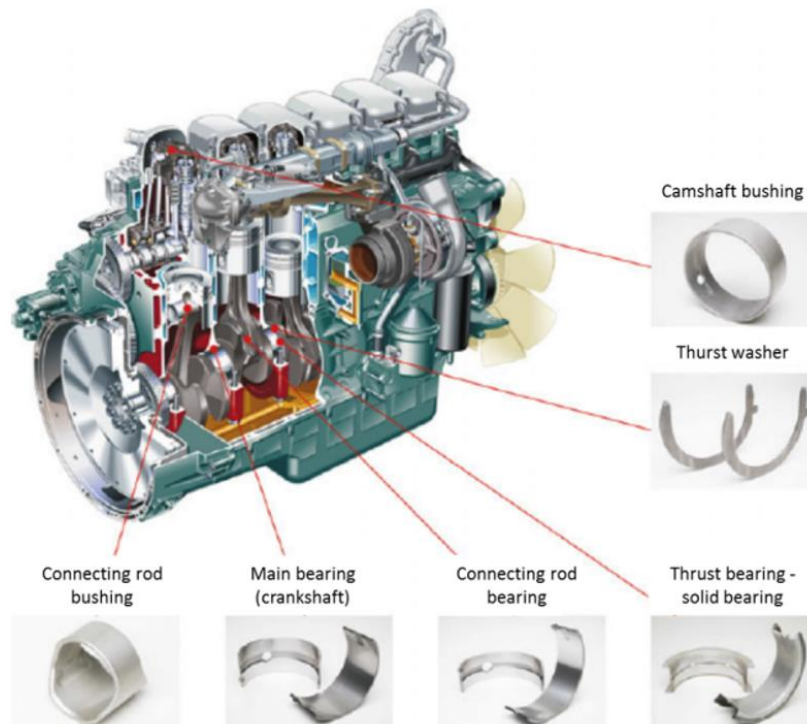
38MnVS6	610	>350	>12
46MnVS6	610	>360	>10
16MnCr5	595	>360	>10
37Cr4	600	>375	>11
37Cr4V	620	>380	>14
42CrMo4V	655	>415	>12

Source: (F. SCHÄFER 2017)

2.3.9. Bearings

Lubricated bearings are used aiming a correct function between movable components. The bearings separate surfaces that move relative to each other creating a tiny space between them which might withstand external loads by a pressurized lubricating film. There are different types of bearings including roller, plain, air liquid and magnetic bearings. In automotive ICEs, the bearings are typically used on the connecting rods big and small bore, on the crankshaft journals, on crankshaft as axial thrust washer as illustrated by Figure 63, (MAHLE 2016).

Figure 63 – Typical bearings used in ICEs



Source: (SANTOS, 2019)

Generally, a distinction made between bearings are the bimetal and trimetal bearings. The bimetal bearings typically consist of a steel support shell with an aluminum or bronze alloy coating. On the other hand, the trimetal bearings consist of a steel support shell coated with an aluminum or bronze alloy, with a thin bearing layer (galvanic, polymer, or sputter layer) referred to as an overlay, (M. Clevite 2016).

2.3.9.1. Bearing Properties

The correct bearing selection is based on the engine application and bearing material properties. The mechanical and tribological requirements for a bearing are established based on the bearing loads occurring in the engine. Material selection is always the result of a compromise among all the properties, which are often contradictory in nature, (Santos 2019). The Table 14 presents the main properties desired in a bearing.

Table 14 – Important bearing properties

Property	Description
Load carrying capacity	Ability to bear mechanical loads on a sustained basis
Wear resistance	Resistance of the material to sliding wear
Seizure resistance	Ability of the material to run at the lubrication limit without welding to the journal; it depends on whether soft phases are present in the material composition
Embeddability	Ability of the material to tolerate and absorb hard particles on the sliding surface
Conformability	The ability to compensate for geometric deviations that cause local contacts
Corrosion resistance	Ability to resist corrosion by organic and mineral acids from combustion and oxidation of lubricants

Source: (MAHLE, 2016a)

2.3.9.2. Bearing Design

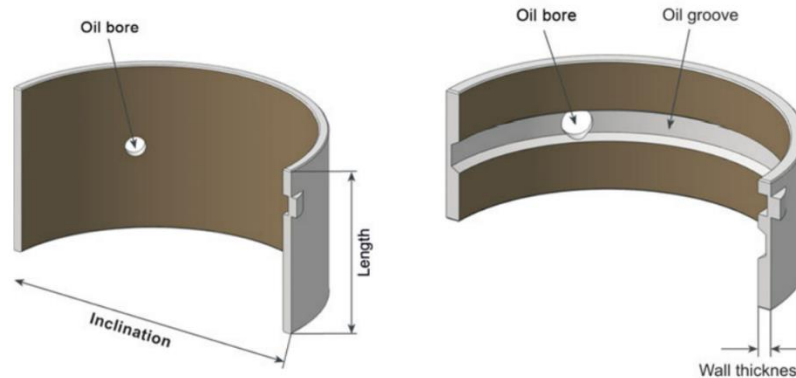
The parameters POFP (Peak Oil Film Pressure) and MOFT (Minimum Oil Film Thickness) are strongly related to the bearing length and bearing diameter. The length to diameter ratio (L_b/D_b) influences the operating characteristics of the bearing. For a given bearing surface, the bearing with the higher L_b/D_b ratio experiences lower oil film pressures, greater minimum oil film thicknesses, and thus more advantageous load conditions. However, higher L_b/D_b presents higher hydrodynamic friction losses, (MAHLE 2016; F. SCHÄFER 2017).

The bearings can be divided into two main categories related to its width:

- **Thick-walled bushes and shells:** This type of bearing is used when the housing has a low stiffness. Which in turn, it is possible to maintain the bearing functionality without a strain in a house;
- **Thin-walled bushes and shells:** This type of bearing reaches its desired end position only when installed in the housing. Hence, on installed condition, the bearing is tensioned high enough to prevent the bearings from turning. When not installed, thin-walled bearings are neither dimensionally stable nor round, (Santos 2019).

The bearings contain oil supply holes and grooves at the journal and bearing surfaces to make lubrication possible as shown in Figure 64. The hole and groove are pressurized and thus influence the oil flow rate, the journal orbit and also the load from the journal on the bearing shell. These holes and grooves are undesirable in loaded areas because they reduce the usable contact surface of the bearing and thus increase the POFP and reduce the MOFT. There is an increased risk of surface contact between the sliding partners or cavitation damage to the bearing mate if the grooves and bores are poorly located. Thereby, oil hole and grooves are placed only in the upper main and lower con rod bearings, (Santos 2019).

Figure 64 – Oil bore and oil groove in bearings



Source: (MAHLE 2016).

Another important aspect for a bearing design it is the bearing clearance. The bearing clearance has a conflicting effect on the oil film properties. Bearings with less clearance presents a better load distribution due to the elastic journal deformation occurs during operation be nearly identical to the bearing curvature. Which in turn, it generates a lower POFP. However, the lower clearance generates more heat, which reduces the oil viscosity. Thus, the POFP increases proportionally to greater clearance whereas the MOFT decreases, (Bonneau, Fatu, and Souchet 2014).

The bearing load capacity is determined using a test bench suitable for it. The test bench consists of a motor-driven eccentric test shaft that exerts an impulse load on the bearing every revolution while the counterforce is applied by a hydraulic cylinder. The test is run under controlled lubricated and the temperature conditions. The pressure on bearing, p_b , in function the gas load and the bearing dimensions may be calculated using Equation 123, (MAHLE 2016; BHANDARI 2010).

$$p_b = \frac{F_{Gas}}{L_b \cdot D_b} \quad (123)$$

Where L_b is the bearing length in [mm] and D_b is the bearing diameter in [mm].

2.3.9.3. Bearing Materials

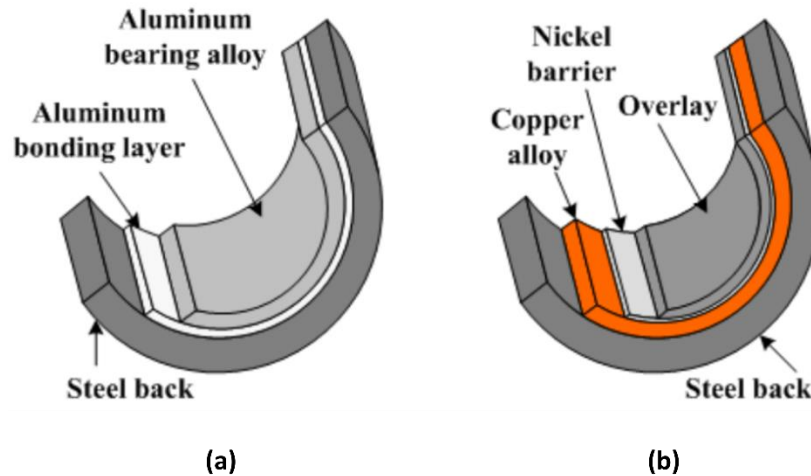
The bearing material selection considers factors like mechanical properties, tribology aspects, corrosion resistance and costs. Usually, the metals have been used for this application once their composition and microstructure are well known and its properties are easily predicted. Nonmetallic materials are also used although it is not common. Regardless of if metallic or nonmetallic material, the tribological properties

are difficult to be expressed by number and quantities. Thus, for bearings components in which the tribology plays an important role, the materials and surfaces selection is more dependent on generalized rules and previous experiments, (Santos 2019).

The modern bearing design considers different materials and alloys, and their respective load limits obtained via simulation, test bench and engine tests. Normally, the main and connecting rod bearings have overestimated limits for safety reasons due to possible misalignments. Based on the test results for each bearing material and bearing application, it is defined if the bearing with one coated layer is capable to bear the given operation condition or it would be required other material layers. Thus, the bearings can be distinguished into bimetallic and trimetallic bearings as follow, (Santos 2019):

- **Bimetallic bearings:** They usually consist of a steel supporting shell coated with a lining of aluminum, bronze alloy, or white metal. Normally, they are used for bushings and thrust washers. As a bimetallic bearing, its tribological performance is determined by the bearing lining itself. Figure 65 – (a) illustrates a bimetallic bearing structure;
- **Trimetallic bearings:** They also have a steel supporting shell coated with an aluminum or bronze alloy. However, an intermediate layer, from 1 - 4 μ m thickness, is deposited over the lining as a diffusion barrier. Furthermore, an overlay is electroplated or sputtered on top of it improving the bearing tribological properties. Due to optimal combination several materials, the trimetallic bearing presents a higher load capacity compared to bimetallic bearings. Figure 65 – (b) illustrates a trimetallic bearing structure.

Figure 65 – Bimetallic (a) and Trimetallic (b) bearings



Source: (Kopeliovich 2019)

2.3.10. Crankcase

The engine crankcase may be considered as the central component of an ICE. It contains and connect the crank mechanism and forms a system boundary that seals off the combustion engine externally. Furthermore, it prevents the working medium, coolant and lubricant to leakage, and the entry of moisture and dirt in it. In addition, the crankcase must have sufficient structural stiffness, ensure shape accuracy of the bearing and cylinder bores as well as cylinder sleeves, and keep its mass as lower as possible, (MAHLE 2016).

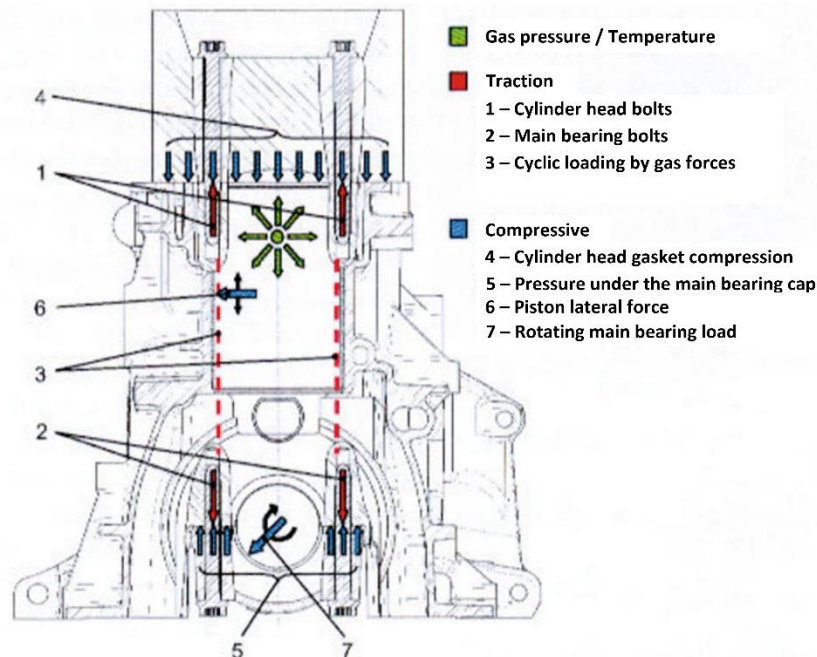
2.3.10.1. Crankcase Forces and Stresses

Due to the diverse functions to be fulfilled, the crankcase is exposed to different and overlapping stresses. It is subjected to tension, compression, bending and torsion by mass and gas forces as shown in Figure 66. In detail these are:

- Gas forces to be absorbed by the cylinder head screw connection and the crankshaft bearing;
- Internal mass moments (bending moments), resulting from rotating and oscillating mass forces;
- Internal torsional moments (tilting moments) between individual cylinders;

- Crankshaft torque and the resulting reaction forces in the engine bearings;
- Free inertial forces and moments of inertia resulting from oscillating inertial forces that are of the engine mounting are to be included, (F. SCHÄFER 2017).

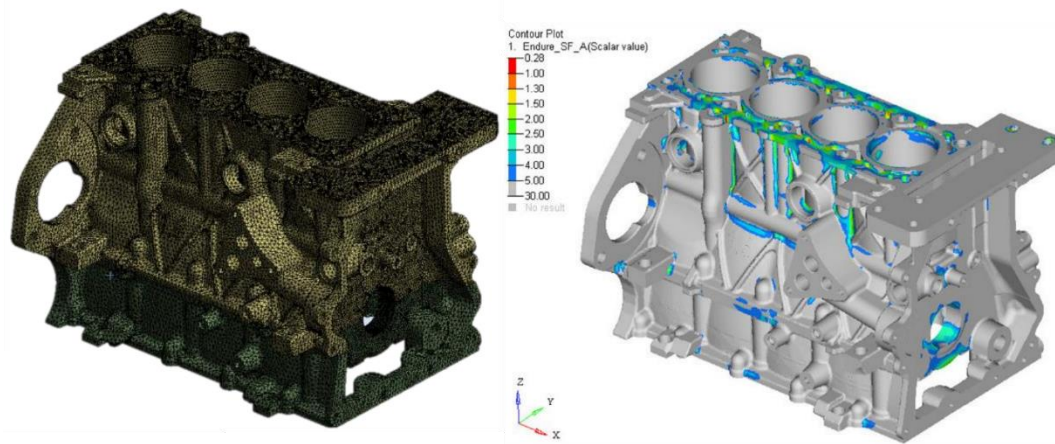
Figure 66 – Forces and loads applied on a crankcase



Source: Adapted from (Eduard Köhler 2011)

Nowadays, the crankcase development is supported by a detailed FEM analysis called thermo-mechanical analyses which in turn helps both to predict the crankcase behavior under working conditions and minimize possible problems that may occur, (MAHLE 2016). Figure 67 illustrates a crankcase thermo-mechanical FEM analysis.

Figure 67 – Crankcase thermo-mechanical FEM analysis



Source: Adapted from (Vasconcelos 2018)

2.3.10.2. Crankcase Design

One of the main goals of the crankcase design is its weight reduction. The lightweight concept is not focused on the cost factor, but also aims the fuel consumption and engine emissions reduction. By comparing the cast iron density at about 7.3 g/cm³ and aluminum alloy density at about 2.7g/cm³ a potential mass reduction of about 45-55% for aluminum crankcases could be achieved. However, an aluminum crankcase requires an adapted design due to lower aluminum stiffness. Which in turn, it significantly reduces the mass savings advantage, (MAHLE 2016).

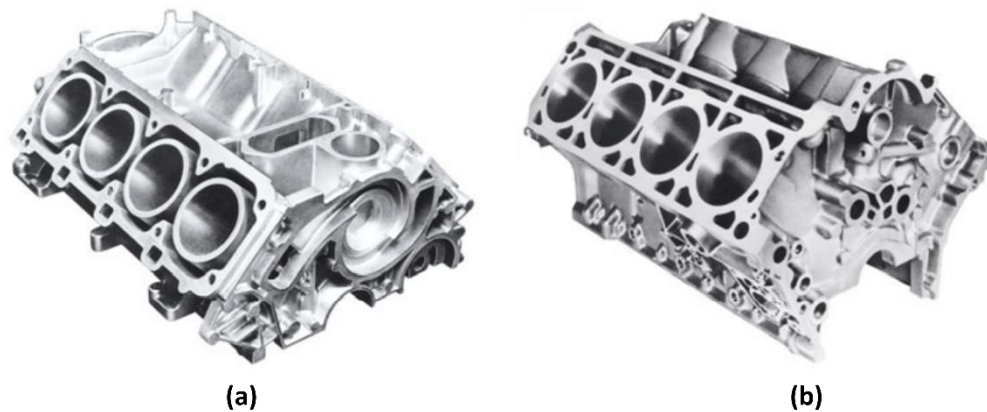
The crankcase types can be structured according to the structural design related to the cover plate, crankshaft bearing blocks and cylinder liner. The cylinder liner will be discussed in the section 2.5.11 of this work.

A key design feature that limits the casting process choice is the crankcase cover plate. A distinction can be made between closed-deck and open-deck designs.

For a closed-deck design, the crankcase cover plate is largely closed in the area around the cylinders. Irrespective of their design, the cover plate always has openings for the cylinders, openings for threaded holes for screwing on the cylinder head and, as a rule, holes and channels for pressure oil, cooling water, oil return and crankcase ventilation. The advantage of the closed-deck design compared to the open-deck design is the higher rigidity of the cover plate. This has a positive effect on cover plate deformation, cylinder distortion and acoustics. However, this design has disadvantages in terms of cylinder cooling in the TDC area and higher complexity manufacturing process, (F. SCHÄFER 2017).

In the open-deck design, the water jacket surrounding the cylinders is open at the top. From the manufacturing point of view, this means that no sand core and therefore no core bearings are required to create the water jacket. The rigidity of the top plate is lower with the open deck design than with the closed deck construction. The cover plate deformation and cylinder distortion can be minimized by using a metal cylinder head gasket. Due to its lower setting behavior compared to conventional soft material cylinder head gaskets, this enables a lower preload force on the cylinder head bolting, which reduces cover plate deformation and cylinder distortion, (F. SCHÄFER 2017).

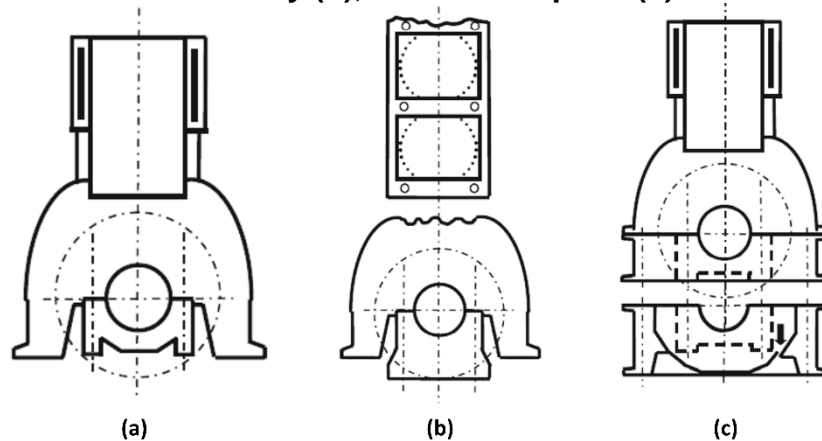
Figure 68 – Crankcase Open-deck (a) and Closed-deck (b) designs



Source: (MAHLE 2016)

In addition to these designs, many other design options are distinguished according to the crankshaft bearing blocks area. The crankshaft can be mounted in bearing caps screwed individually to the crankcase, or in a bearing cap assembly, or even in a separate component called bedplate. With the bedplate construction, the crankcase is practically divided in the middle of the crankshaft. The alternative to the two-piece bedplate construction is the deep-skirt construction with side walls pulled down far. Furthermore, the oil pan can be also used as a structural component of the crankcase assembly, (Eduard Köhler 2011). Figure 69 illustrates the individually screwed bearing caps (a), a bearing cap assembly (b), and the bedplate (c), design concepts.

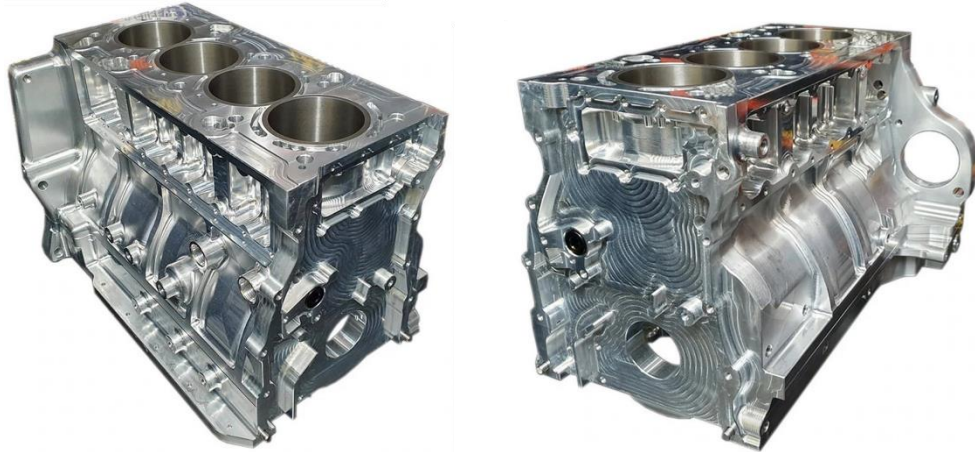
Figure 69 – Crankcase individually screwed bearing caps (a), a bearing cap assembly (b), and the bedplate (c)



Source: Adapted from (Eduard Köhler 2011)

Currently, the crankcases are mostly manufactured using casting process. Casting can cater for lower quantities with processes such as sand casting, or incredibly high volumes with processes such as high-pressure die casting. Casting is a 'near-net-shape' forming method, so very little material is wasted, and very little post-processing is required to form the geometry of the component. The materials can be versatile, and a wide variety of surface finishes can be applied. In case of lower volume produced parts, the tooling costs could become an issue. However, at the last few years, the billet CNC (Computerized Numerical Control) machined crankcase has been showed an attractive for engine crankcase manufacturing. A billet material is not a manufacturing process, it is simply a form of material used for CNC machining products and produces high quality, high accuracy parts without the need for expensive tooling. This makes it exceptional for low quantity or non-mass-produced part. A billet machined crankcase presents a higher rigidity, and a lower distortion of both cylinder bores and crank tunnel. A drawback of a billet machined crankcase is its weight compared to a casted crankcase, (Castings 2019). Figure 70 illustrates a billet machined crankcase.

Figure 70 – Billet machined crankcase

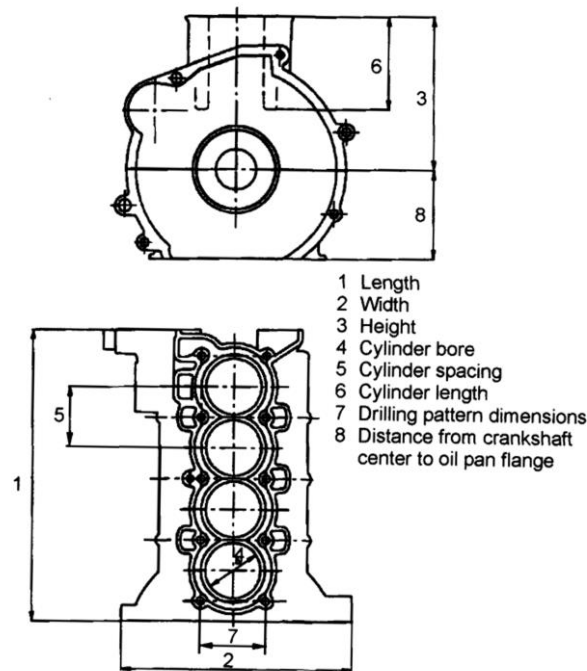


Source: (Maxworx 2020)

The crankcases may be characterized according to main dimensions presented in Figure 71 depending on the engine type, such as in-line, V and boxer engines:

1. Length is the measure from the front edge of the crankcase to the engine-gearbox flange;
2. width, is the maximum overall crankcase width;
3. Height is the dimension from the center of the crankshaft in the direction of the cylinder axis to the cover plate level;
4. Cylinder bore is the nominal inner diameter of the cylinder;
5. Cylinder spacing or bore pitch, is the measure between the centers of two adjacent cylinders;
6. Cylinder length is the distance from the cover plate to the lower end of the cylinder;
7. The hole pattern indicates the position of the cylinder head screw connection: depending on its design, for example 4 or 6 points per cylinder;
8. Vertical distance from the center of the crankshaft to the oil pan flange, (F. SCHÄFER 2017).

Figure 71 – Crankcase major dimensions



Source: Adapted from (F. SCHÄFER 2017)

The cylinder bore pitch depends on the arrangement of cylinder head studs, crankcase sleeves upper support dimensions and its cooling gallery design, and sufficient crankshaft fatigue strength. According to (Xi-Hou Fu 1994), the bore pitch, BP in mm, can be calculated in function of the cylinder bore using Equation 124, and large values are recommended for engines operating with higher combustion pressure, in order to promote adequate cooling between the engine cylinders. For a 4-valve engine fitted with a single piece cylinder head, a bore pitch factor, bp_f , from 1.21 to 1.25 is recommended (Xi-Hou Fu 1994).

$$B_{pitch} = bp_f \times B = 87.95 \text{ mm} \quad (124)$$

2.3.10.3. Crankcase Materials

The crankcases are typically made of cast iron, aluminum, or magnesium materials.

The most important cast iron materials commonly used for crankcase production are the GJL (gray cast iron), GJV (cast iron with vermicular graphite), and GJS (cast iron with nodular graphite). The GJL presents advantages in terms of cost, machineability, and stability regarding the deformation in both the main bearings and the cylinder surfaces. As disadvantages, the GJL presents a higher density value,

lower thermal conductivity relative to aluminum, and lower load carrying capacity compared to GJS and GJV. The GJV has a higher load carrying capacity compared to GJL, although it is significantly less machinable than the GJL. It allows thinner walls to be used however it has a higher cost. Finally, the GJS has a greater load carrying capacity than GJV. However, it has a reduced castability, poor thermal conductivity and higher cost, (MAHLE 2016).

The aluminum alloys are commonly used in crankcase production due to a good thermal conductivity, low weight, easy machinability, and acceptable mechanical properties. These advantages are countered by lower stiffness, higher costs, and reduced strength values especially at high temperatures (> 200 °C). The most alloying elements for the use of aluminum in crankcase are magnesium, manganese, copper, and silicon. The magnesium, manganese, and copper are used for improving the aluminum mechanical properties. On the other hand, the silicon improves the casting properties and the wear behavior, (MAHLE 2016). The Table 15 presents the main aluminum alloys used for crankcases manufacturing.

The magnesium, owing to its density 35% lower than that of aluminum and its low Young's modulus, is mainly used in non-structural engine components in order to reduce weight. In crankcase, one possible approach for reducing component weight is to produce highly stressed locations in a hypereutectic aluminum alloy, which are then encapsulated with magnesium (Figure 72). With a hybridized combination of magnesium and aluminum, weight savings in such a component can be up to 25%, (MAHLE 2016).

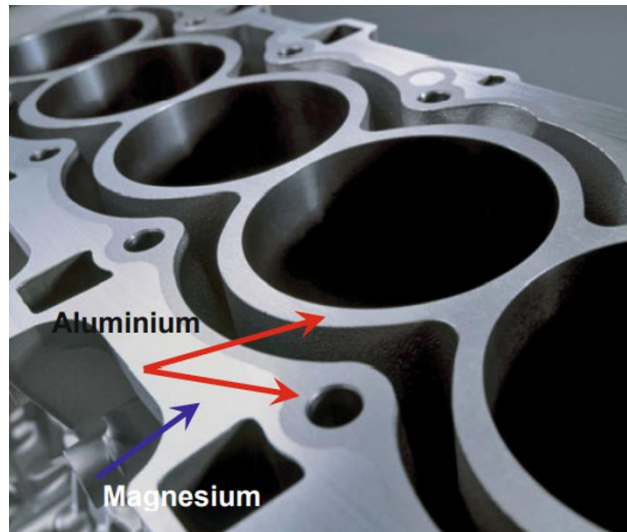
Table 15 – Aluminum alloys for crankcase manufacturing

Properties	AlSi17Cu4Mg	AlSi10MgCu	AlSi12MgCuNi	6061-T6
Hardness HB10	90–120	85–110	90–125	85-95

Tensile strength [MPa]	20°C	180–220	190–250	210–230	310
	150°C	160–210	180–220	180–200	
Yield point $R_{p0.2}$ [MPa]	20°C	160–210	160–210	190–210	276
	150°C	150–190	150–200	170–180	
Fatigue strength under reversed bending stress [MPa]	20°C	70	80	90–100	96
	150°C	60	70	75–80	
Young's modulus [MPa]	20°C	84.000	78.000	80.000	68.900
	150°C	79.000	76.000	77.000	
Thermal conductivity λ [W/m.K]	20°C	152	155	155	167
	150°C	153	156	156	
Thermal expansion [10^{-6} m/m.K]	20-100°C	19.4	22	19.6	23
	20-100°C	20.4	22.4	20.6	
Density ρ [g/cm ³]	20°C	2.7	2.7	2.68	2.7

Source: (MAHLE 2016; Metals 2018)

Figure 72 – Magnesium aluminum composite crankcase



Source: (Eduard Köhler 2011)

2.3.11. Cylinder Liner (Sleeves)

The cylinder liners are used to accommodate the piston group and, with their surface and the material used, fulfill sliding and sealing functions in conjunction with the piston rings. Depending on the design, they also contribute to heat dissipation via the crankcase or directly into the cooling water, (F. SCHÄFER 2017).

A cylinder liner has as basic functions to limit the working chamber, to guide the piston and to seal sideways along with the piston rings. These basic functions are performed with the cylinder liner under operation which it is subjected to mechanical loads, thermal loads, wear, and corrosion, (Pischinger 2012).

2.3.11.1. Cylinder Liner Design

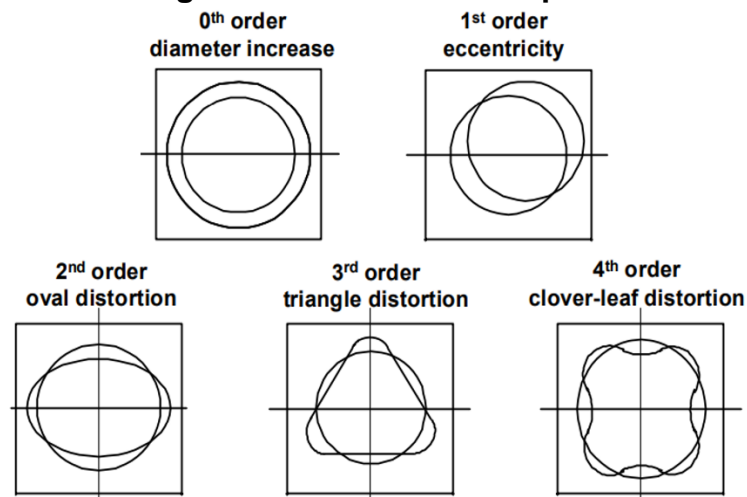
The cylinder liner design, coolant flow and liner arrangement must guarantee an as lower as possible deformation caused by the thermal and mechanical stress ensuring a good sealing performance, the temperatures in the ring operation zone remain below 220°C to guarantee lubrication and to not exceed the resistance to breakings, (Pischinger 2012).

Even with a proper cooling design, the cylinder liner deformation is inevitable due to the uneven thermal expansion. Furthermore, the mechanical stress due to cylinder pressure and cylinder head bolting forces also contribute to the cylinder liner deformation. The cylinder liner deformation can be categorized by orders by means of a Fourier analysis. The individual orders correspond as follows:

- **0 order** – enlargement of the cylinder liner diameter;
- **1st order** – displacement of the center of the cylinder liner;
- **2nd order** – deformation with two maximum values, corresponds to the tendency of the cylinder liner to take an oval shape;
- **3rd order** – deformation with three maximum values;
- **4th order** – deformation with four maximum values called “cloverleaf deformation, (Pischinger 2012).

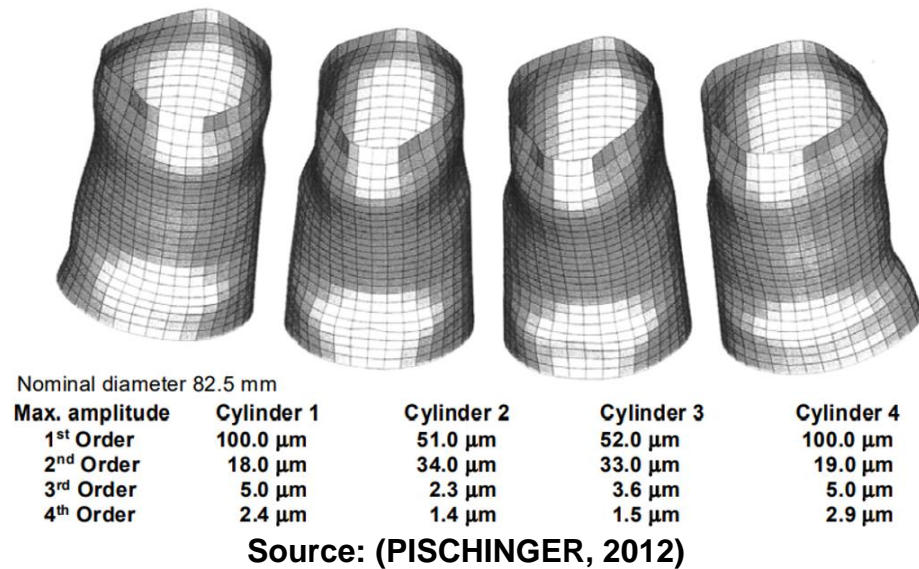
In a case of a 4th order deformation, the combustion chamber sealing can become critical since the piston rings can only follow the liner shape to a limited extent. The capability of the piston rings to adjust to the cylinder liner shape is called form-matching. Figure 73 illustrates the cylinder liner deformation orders, whereas Figure 74 illustrates a cylinder liner FEM deformation analysis which a 4th order deformation is present in the TDC area of the cylinders 1 and 4, and a 2nd order deformation is shown in the cylinders 2 and 3, (Pischinger 2012).

Figure 73 – Magnesium aluminum composite crankcase



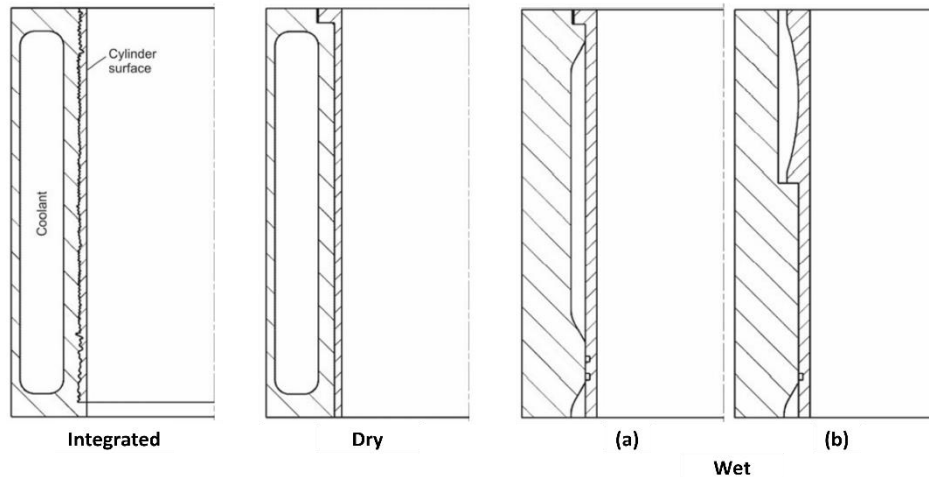
Source: (PISCHINGER, 2012)

Figure 74 – Cylinder liner FEM deformation analysis due to mechanical and thermal stress



The cylinder liner shape design for water cooled engines are divided into three main groups: the integrated cylinder liners, the dry cylinder liners and the wet cylinder liners as shown in Figure 75. In the integrated cylinder liners, the cylinder liner and the crankcase are made of one piece. The advantages of this design are economical high-volume production, high crankcase rigidity and compact design. On the other hand, the disadvantages include difficult to material selection, a higher casting complexity and repair difficulty. With a dry cylinder liner, a thin-walled cylinder wall is pressed into the cylinder bore of the crankcase. As advantages can be considered an ease cylinder liner repair and freedom to material selection. However, as disadvantages can be considered the higher production costs and relatively poor heat transfer. In case of the wet cylinder liner which the coolant fluid is directly in contact on it, the advantages include ease exchange, low mechanical crankcase deformation, freedom to material selection, higher heat exchange, and a simpler crankcase design. Conversely, the disadvantages are the liner damage by the cavitation of the coolant fluid, lower heat transfer at the TDC, and risk of material crack on the cylinder liner collar region, (Pischinger 2012).

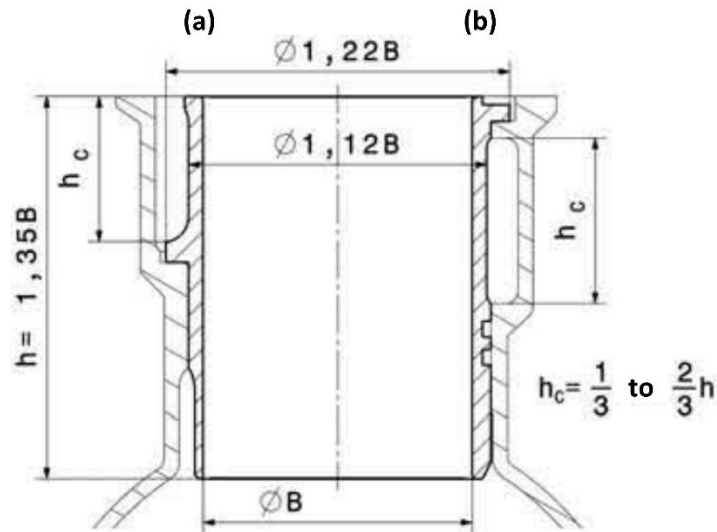
Figure 75 – Basic designs for water-cooled cylinder liners



Source: (MAHLE 2016)

The wet cylinder liners are divided into standard hanging and mid-stop liners. The standard hanging cylinder liners design cooling over the entire running surface area. On the other hand, the mid-stop design there is a flange within the running surface which in turn leads to a cooling only at the upper part of the cylinder liner. Thus, the mid-stop design cooled more efficiently. In both cases, the combustion chamber is sealed by the cylinder head gasket at top and radially by O-rings at bottom. Currently, the wet cylinder liners have been used as a structural component in high-performance engines which an open-deck crankcase design is turned to a close-deck design. Attention must be paid at the cylinder liner collar regarding mechanical and thermal stress, (MAHLE 2016; Trzesniowski 2010). Figure 76 presents some suggested initial basic dimensions for mid-stop and standard hanging wet cylinder liners used in Formula 1 engines in function of the cylinder bore.

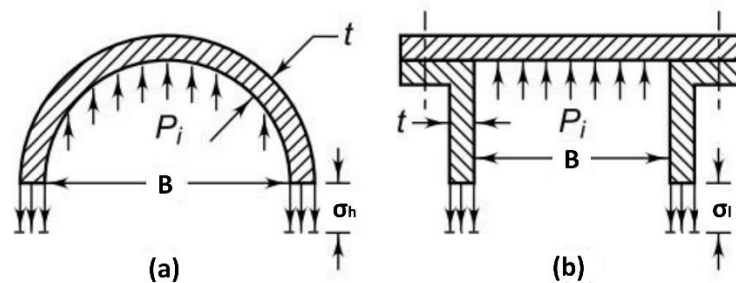
Figure 76 – Basic initial dimensions for midstop (a) and standard hanging (b) wet cylinder liners used in Formula 1 engines



Source: (Trzesniowski 2010)

An engine cylinder liner can be modeled as a pressure vessel with a thin wall thickness. As shown in Figure 77, the cylinder liner is subjected to tangential (hoop) and longitudinal stress. Considering an equilibrium of forces acting uniformly on the half portion of the cylinder liner of one unit length, the hoop, σ_h , and longitudinal, σ_l , stresses in [MPa] can be calculated using Equation 125 and Equation 126 respectively. From Equation 125 and Equation 126, it is seen that the hoop stress is twice the longitudinal stress. Therefore, the hoop stress should be the criterion for determining the cylinder liner thickness. Furthermore, a thin cylinder liner subjected to an internal pressure, the tendency to burst lengthwise is twice as great as at transversal section, (BHANDARI 2010).

Figure 77 – Cylinder liner tangential (hoop) and longitudinal stresses



Source: (BHANDARI 2010)

$$\sigma_h = \frac{P_i \cdot B}{2 \cdot t} \quad (125)$$

$$\sigma_l = \frac{P_i \cdot B}{4 \cdot t} \quad (126)$$

Where the P_i is the cylinder liner internal pressure in [MPa] and the t is the cylinder liner thickness in [mm]. In case of an engine cylinder liner design, the maximum gas pressure should be considered as the internal pressure and the hoop stress replaced to an allowable stress, σ_{all} , in [MPa], related to a factor of safety. Thus, the cylinder liner wall thickness can be calculated using Equation 127, (BHANDARI 2010).

$$t = \frac{P_{max} \cdot B}{2 \cdot \sigma_{all}} + R_{all} \quad (127)$$

Where R_{all} is the additional metal thickness, in [mm], called reboring allowance, over the required cylinder liner wall thickness to withstand the maximum internal cylinder pressure in case of any reboring process throughout the engine lifetime. Typical re-boring allowance values in function of the cylinder bore are presented in the Table 16, (BHANDARI 2010).

Table 16 – Typical re-boring allowance for ICE cylinder liners

B [mm]	75	100	150	200	250	300	350	400	450	500
R_{all} [mm]	1.5	2.4	4.0	6.3	8.0	9.5	11.0	12.5	12.5	12.5

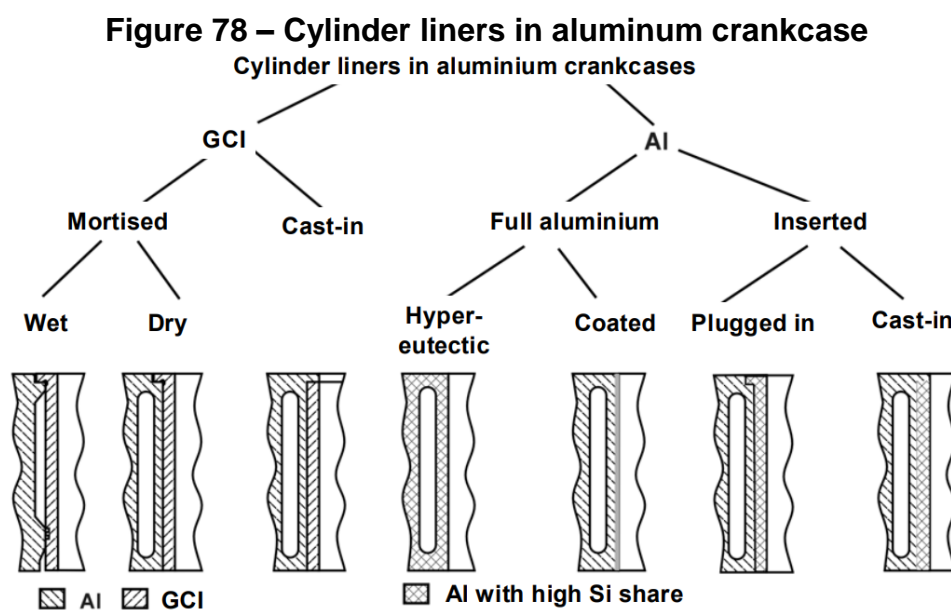
Source: (BHANDARI 2010)

2.3.11.2. Cylinder Liner Materials and Coatings

The cylinder liners are made of cast iron, coated or uncoated aluminum alloys, or steels. Furthermore, the aluminum liners are typically coated with Nikasil, and steel liners can be hardened, reinforced, or coated with Cromal, (MAHLE 2016).

The engine application requirements such as the installation space, the operating conditions and cost determine the cylinder liner material choice and their properties. Some important material properties to be considered are the specific weight, microstructure, hardness, tensile strength and fatigue strength under vibration, thermal conductivity, thermal expansion coefficient, stiffness, and Young's modulus. As an overall, cast iron is preferred for diesel engines, whereas cylinder liners made of aluminum provide significant advantages in thermal conductivity and specific weight.

On the other hand, the steel cylinder liners stand out for its high strength and stiffness, (MAHLE 2016). Figure 78 presents a summary of the possible combination of the cylinder liners materials and fit in process into aluminum crankcases proposed by (Pischinger 2012). The Table 17 presents the typical mechanical properties for cast iron cylinder liners as reference values.



Source: (Pischinger 2012)

Table 17 – Typical mechanical properties of cast iron liners (reference values)

Properties	Gray cast iron (GJL)		Cast iron with nodular graphite (GSJ)
Basic microstructure	Pearlite	Bainite and very fine pearlite	Pearlite
Hardness [HB]	180–300	270–330	260–330
Tensile strength [MPa]	200–350	400–600	≥600
Young's modulus [GPa]	100–120	120–140	≥150

Source: (MAHLE 2016)

According to the required service life and operational reliability, various running surface coatings are available to the user of light-alloy cylinder liners. As aforementioned, two common coatings used on the cylinder liner are Nikasil and Cromal.

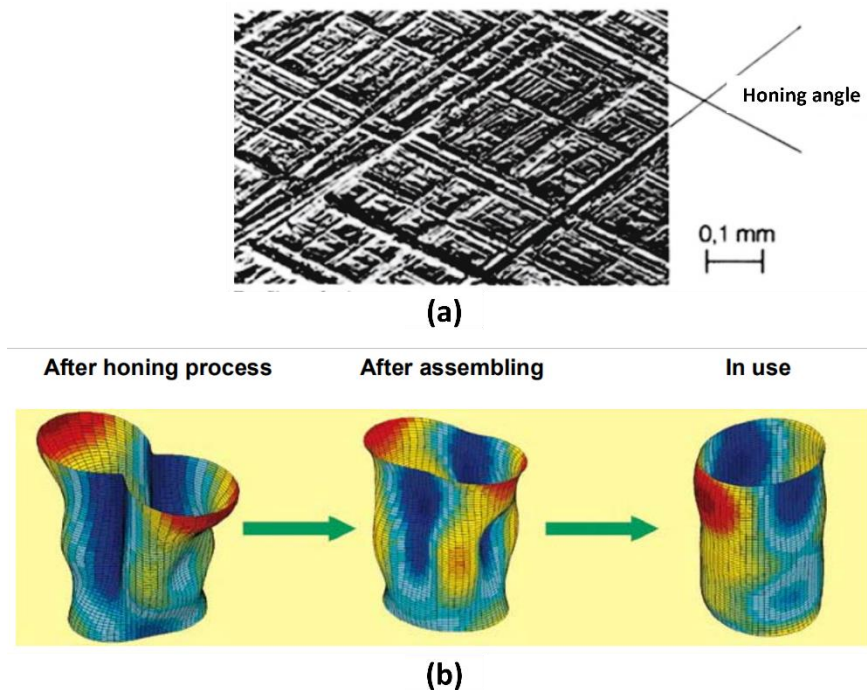
The Nikasil consists of a nickel dispersed layer, about 0.05 mm thick in its finished state, on the cylinder liner surface providing a relatively smooth cylinder liner

surface after honing. Which in turn, it leads to a fast run-in and good sealing of the piston rings. Furthermore, the low friction power loss provided by Nikasil, improves the engine output, the blow-by quantity, the oil consumption, and the cylinder wear, (MAHLE 2016).

The Cromal is a galvanically applied hard chrome layer of about 0.06 to 0.08 mm in thickness. The chrome running surface and the piston rings wear is significantly affects the by providing as even a distribution and adhesion of the lubricating oil to the cylinder surface as possible. Furthermore, the hardness and chemical resistance of the chrome coating leads to low wear values for the cylinder and piston rings and to a long service life, (MAHLE 2016).

The engine operating conditions, the running-in characteristics of the piston rings, and the wear pattern of the sliding components are greatly affected by the cylinder liner surface structure achieved by the honing process. The honing process consists of a cylindrical tool equipped with honing stones that perform a rotational and a vertical motion simultaneously creating a cross scored structure in the cylinder in pre-defined angles that varies between 30 to 60 degrees. The honing stones could be made by diamond (diamond honing) or silicon carbide (ceramic honing). The honed surface can be characterized by its roughness, fax-film, white light interferometry, and metallographic. In order to evaluate the cylinder liner surface roughness, the standardized values in DIN EN ISO 13565-2 should be used. Furthermore, it is advisable to use a torque plate during the honing process in order to create the cylinder running surface as similar as possible of the engine running condition, (MAHLE 2016; Eduard Köhler 2011). Figure 79 illustrates the cylinder liner surface after honing as well as its honing angle (a) and a FEM simulation of the cylinder liner deformation after the honing process to usage condition (b).

Figure 79 – Cylinder liner surface pattern after honing process (a) and FEM deformation analysis (b)



Source: (EDUARD KÖHLER, 2011; MAHLE, 2016a)

2.3.12. Cylinder Head

The cylinder head is the performance-determining component of an engine. It accommodates essential parts of the gas exchange and the cooling. Furthermore, the ignition system is also fitted in it. In case of DI engines, the injection valve is also housed in the cylinder head. Additionally, the cylinder head must seal the cylinder head. A cylinder head therefore consists of a support plate, cover, side walls, gas channels, water core channels, bores for valve guides, direct injection valves, spark plugs and tensioning bolts, (Pischinger 2012).

The cylinder head during operation is subjected to higher thermal load due to the heat flow from the combustion chamber, the valve seats, the valve guides, as well as from the exhaust port. At the same time, the cylinder head is subjected to mechanical loads from gas and clamping forces, (Pischinger 2012).

2.3.12.1. Cylinder Head Design

The Cylinder bore and distance between cylinders determine the basic geometry of the cylinder head. As a rule, the number of valves per cylinder is also fixed

for the new design. The minimum wall thicknesses required from the manufacturing process results in narrowed space available for accommodating the valvetrain components. Thus, the first step in the cylinder head design is to define the arrangement and size of the valvetrain components and to take into account the geometry of the gas exchange ports and combustion chamber, (F. SCHÄFER 2017).

The engine power increases as the amount of air supplied to it increase. Therefore, the largest possible valve opening area should be aimed, (Trzesniowski 2010). The Table 18 presents typical valve head diameter in function of the cylinder bore which attempts to fit the largest possible valves.

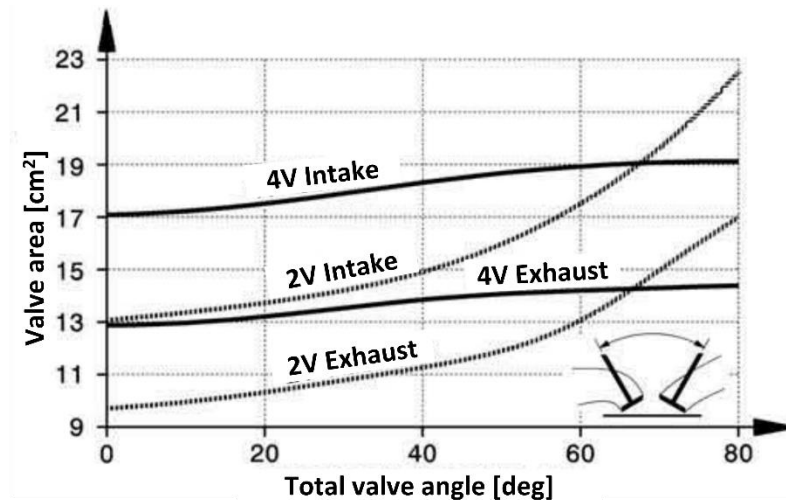
Table 18 – Valve head diameter in function of the cylinder bore

Combustion chamber shape	Inlet valve	Exhaust valve	Approx. Mean piston speed at max power [m/s]
Two-valve wedge or bathtub	0.43-0.46B	0.35-0.37B	15-16
Two-valve hemispherical	0.48-0.50B	0.41-0.43B	17
Three-valve open	0.38-0.40B	0.41-0.43B	19
Four-valve pent-roof	0.38-0.41B	0.31-0.35B	20

Source: (HEYWOOD 2018)

Several studies have been carried out to investigate the best number of valves and combustion chamber form aiming to increase the engine efficiency. Figure 80 presents the influence of total angle between valves on the valve areas. It can be seen that the valve areas for a two-valve engine increase significantly with the total valve angle. Over a total valve angle of about 68° , a two-valve engine has a larger valve area than a four-valve engine. However, for total valve angle between 0° to 40° , a four-valve engine has about 25 to 30% more valve area than a two-valve engine. In addition, there is a favorable shape of the combustion chamber with small total valve angles, (Trzesniowski 2010).

Figure 80 – Influence of total angle between valves on the valve areas



Source: Adapted from (Trzesniowski 2010)

The largest possible valve opening area is limited by manufacturing requirements and flow restriction issues. A minimum web must remain in the cylinder head between the valve seat insert bores so that the valve seat inserts do not come loose after being pressed in. For the same reason, there must also be a minimum web to the spark plug hole and fuel injector in case of DI engines. Furthermore, the valve openings must also be at a certain distance from the cylinder liner, otherwise the flow resistance between the valve head and the cylinder liner will reduce the valve circumference area available for gas exchange, (Trzesniowski 2010). The Table 19 presents the typical minimum web widths or distances for a standard cylinder head as shown in Figure 81.

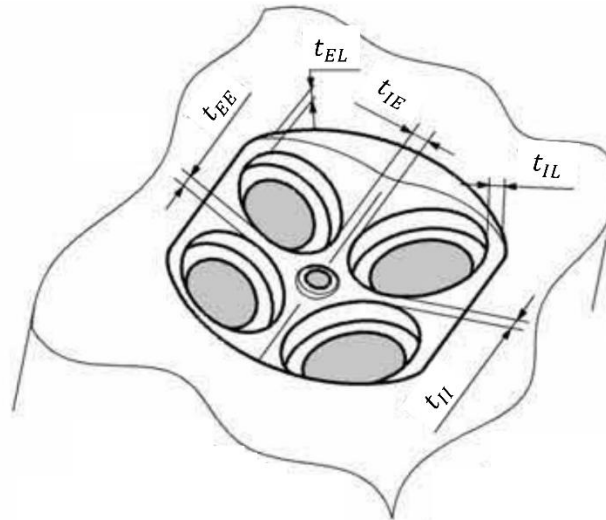
Table 19 – Typical minimum web widths or distances for a standard cylinder head

Dimensions	t_{II}	t_{EE}	t_{IE}	t_{IL}	t_{EL}	t_{IS}	t_{ES}
Values [mm]	2.5	2.5	3	1.5	1	3	3

I – Intake, E – Exhaust, L – Liner, S – Sparkplug

Source: (Trzesniowski 2010)

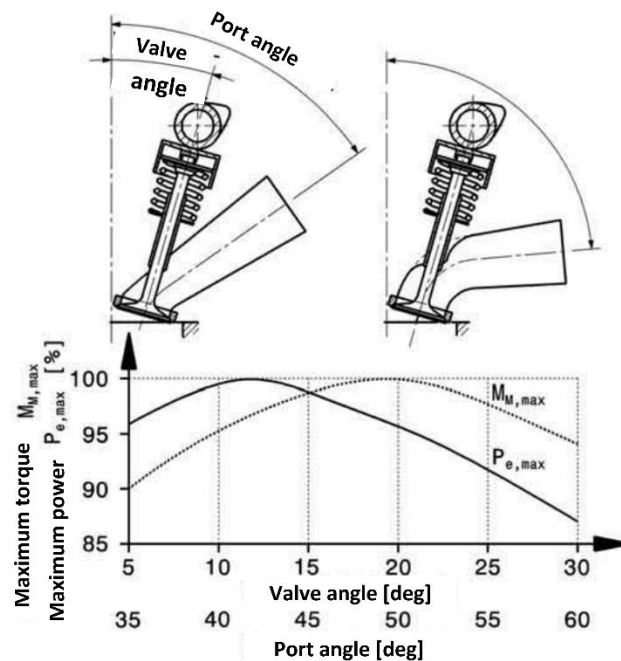
Figure 81 – Typical web dimensions or distances for a standard cylinder head



Source: Adapted from (Trzesniowski 2010)

The position of the valve and the ports in relation to the cylinder axis affect the gas flow, the turbulence in the combustion chamber and the shape of the combustion chamber. A steeper port (smaller port angle related to cylinder center axis) leads to a greater fluid flow and thus a higher maximum engine output. On the other hand, a larger valve angles results in a combustion chamber shape that is more favorable for high engine torque. Figure 82 illustrates how the two variables ultimately affect the engine performance. As a reference rule, the smaller the cylinder unit - or the larger the number of cylinders for a given cubic capacity - the smaller the valve angle. In addition, the cylinder head with narrow valve angle is smaller and, hence smaller and lighter. As presented by Figure 82, the highest torque is achieved with the intake port angle about 50° degrees. On the other hand, the valve angle about 20° to 22° leads to the higher power output. A good compromise is provided by valves that are at an angle of 15° to 18° and intake ports with a port angle of around 45°, (Trzesniowski 2010).

Figure 82 – Influence of port and valve angle related to the cylinder center axis on the engine performance

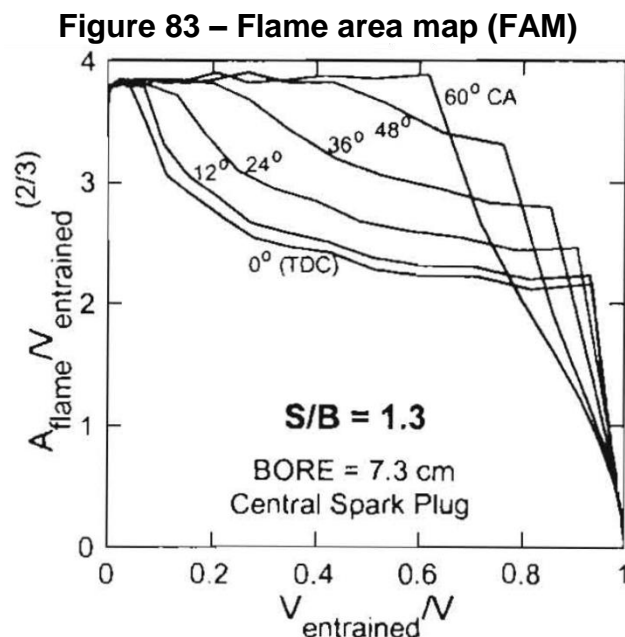


Source: Adapted from (Trzesniowski 2010)

The shape of the combustion chamber in the cylinder head is determined by the arrangement of the valves and the position of the spark plugs. The main goal for the combustion chamber design is to reduce as much as possible the combustion duration. The combustion path is the greatest distance that the combustion flame front has to cover from the spark plug to the edge of the combustion chamber. A short combustion paths results in a quicker combustion event, which in turn reduces the thermal losses and enable to place the MFB50 at the MBT condition. Furthermore, a short combustion chamber reduces the risk of knocking. Thus, the location of the spark plug should be as close as possible to the center of gravity of the combustion chamber. The knocking tendency is also reduced if the charge is in a relatively cool area of the combustion chamber at the end of combustion. This can be achieved by placing the spark plug close to the exhaust valves leading to a flame front that spreads in the direction of cooler intake valves. In addition, the sparkplug placed near of the exhaust valves help to cooling them down, (Trzesniowski 2010; Bizjan 1999).

A small combustion chamber surface-to-volume (S/V) ratio is advantageous for low wall heat losses, which leads to a higher cycle thermal efficiency as presented by the authors, (Poulos and Heywood 1983; Siewert 1978; Novak and Blumberg 1978). However, in case of SI engines, the combustion chamber S/V ratio offers somewhat limited insight about the heat transfer process. As there are a burned and an unburned

zones in the cylinder during the flame-propagation, the gas temperature in the burned zone is much higher than in the unburned one. Which in turn, it leads to a higher heat flux to wall surfaces in contact with burned zone than the surfaces in contact with the unburned zone. In order to better evaluate the potential of heat loss throughout the combustion process, it can be used a Normalized Flame Area Map (NFAM) approach based on the flame front area, the flame front entrained volume and the combustion chamber volume. In this NFAM approach, the flame front area is normalized by the flame front entrained volume and compared to the flame front entrained volume normalized by the combustion chamber volume as shown in Figure 83. Figure 83 presents the NFAM for several piston positions and it can be seen that the normalized flame front areas start to decline after the flame contacts the piston top and at the end of the combustion process it declines sharply to zero as the flame contacts the cylinder walls. Thus, a physical meaning for the flame propagation is a higher mass burn rate for a higher normalized flame front area, (Z. S. Filipi 2000).

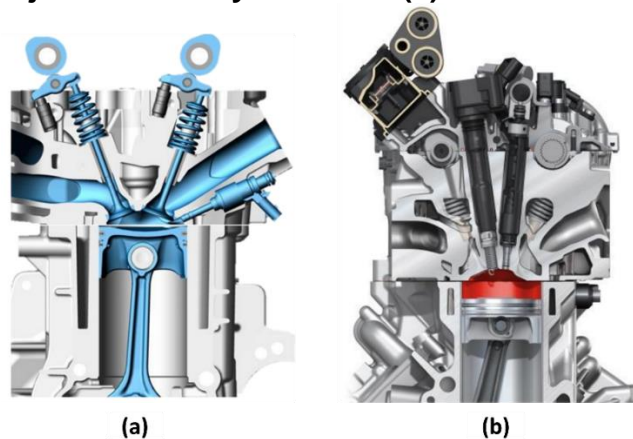


Source: Adapted from (Trzesniowski 2010)

For DI engines, the fuel injector position is also defined at initial steps of the cylinder head design. The two main challenges faced to determine the DI fuel injector position is its required space to fit it in the cylinder head and the fuel injection pattern related to the combustion chamber geometry and the charge motion. Usually, the DI fuel injector are fitted to cylinder head in central position or sideways depending on

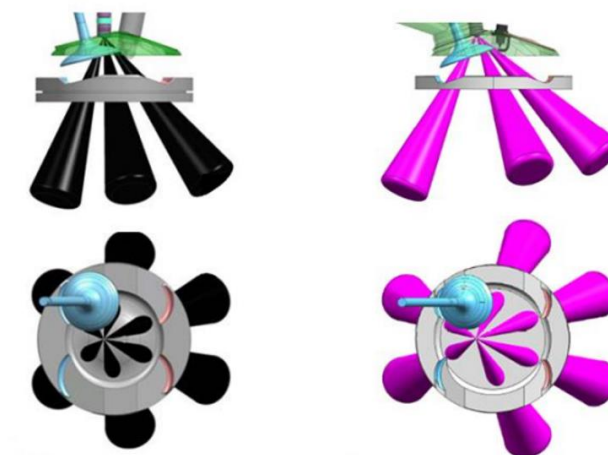
package requirements of the project. Figure 84 illustrates the injector sideway and central mounted designs. The fuel injection pattern and its interaction with the charge motion is usually carried out by CFD (Computational Fluid Dynamics) analysis. However, it can be initially evaluated by creating an injection spray target in the CAD (Computer-Aided Design) model, as shown in Figure 85. Studies have been shown that centrally mounted fuel injectors provide a better interaction with charge motion and requires a simpler piston crown geometry, (ZHAO 2010).

Figure 84 – Injector sideway mounted (a) and central mounted (b)



Source: (J. Kim et al. 2018; Königstedt et al. 2016)

Figure 85 – Spray target DI injection sideway mounted (a) and centrally mounted (b)

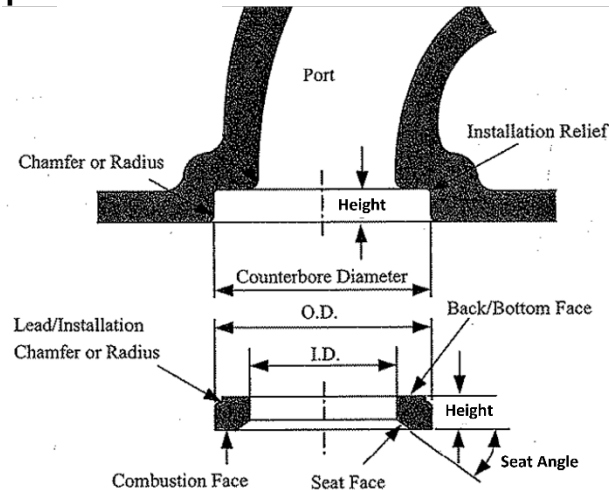


Source:(DE MARINO et al. 2018)

In order to provide a seating surface for the valves, the valve seat inserts are installed in the cylinder head. The valve seat insert surface must bear high contact stresses and temperatures, as well as corrosive gases under working conditions. The valve seats are mainly used to provide a more wear and heat resistant material to

support the valves than the cylinder head material. In addition, the valve seat inserts permit easier engine repair or rebuild, (Y. WANG 2007). Figure 86 presents the typical valve seat insert and counterbore nomenclature.

Figure 86 – Typical valve seat insert and counterbore nomenclature



Source: (Y. WANG 2007)

The valve seat insert is a cylindrical, ring-shaped component that is usually installed on the cylinder head through an interference fit. The typical tolerance for interference fit between a valve seat insert and its mating counterbore is about 0.05-0.13mm. The valve seat insert dimensions must be rigid enough to absorb the continuous hammering and to provide a sufficiently large mass to dissipate the heat from the valves to the cylinder head coolant system. Typical valve seat insert dimension can be defined as a function of the port throat diameter as follows:

- **Radial thickness (T)** – 0.10 to 0.14 times the throat diameter;
- **External diameter (O.D.)** – 1.2 to 1.3 times the throat diameter;
- **Height (H)** – 0.15 to 0.25 times the throat diameter;
- **Aspect ratio (H/T)** – 1.7 to 2.5, (Y. WANG 2007).

The valve seating angle, β_{seat} , is an important parameter for the air flow. Typically, the basic seat angles are in the range from 15 to 45°. A shallower seat angle allows effective flow area to increase more rapidly as the valve initially lifts from the seat and it reduces wear due to impact loads. On the other hand, a shallower seat angle typically increases flow separation as lift is increased, and it makes the valve

sealing more difficult. The valve seat angle higher than 45° is not used as this result in the valve sticking in the closed position and increase the required opening force. Usually, an angle difference between the valve and the valve insert seat about 0.5 to 2.0° is applied to aid in sealing. The valve seat width is typically about 1.25 to 2.0mm for intake seats and 1.5 to 2.5mm for exhaust seats. The air flow breakaway from the port wall can be reduced and the discharge coefficient increased by machining on the valve seat three or more angles. Usually, the valve seat angle is 45° , and it is added to the valve seat a shallower angle of 30° and a steeper 60° as approach angles from the cylinder and port, respectively. The valve seat angle should not be higher than 15° increase the air flow breakaway tendency. The number of valve seat angles higher than three is not frequently used in mass production engines as it is hard to control the valve seat width on the production line and in the field. On the other hand, for the high-performance engine applications, which are less cost sensitive, a radius and up to a seven-angle valve seat geometry are sometimes applied, (Kevin L. Hoag 2016; Carley 2008).

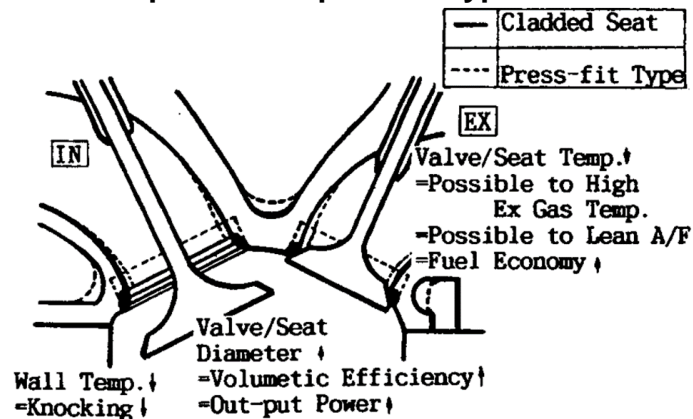
The valve seat materials must meet the requirements of the modern engines application providing a reliable function for the valvetrain system. The valve seat materials properties should be chosen based on the engine running conditions. The following materials are the range of valve seats materials available on market from (Mahle 2015).

- **ST** – Cobalt-based material with high chromium and tungsten content. Valve seat inserts made of these extremely wear and corrosion resistant alloys are mostly used in engines powered by alternative energies, such as natural gas (CNG), biogas, and landfill gas;
- **GG1** – Good machinable gray cast iron alloys with a high carbon content. These stand out because of their high resistance and compressive strength, and are used in the intake area of petrol, turbo, and diesel engines;
- **SG1** – High-temperature cast steel with high chrome content ($> 10\%$) and molybdenum. Along with their high resistance to heat, these valve seat inserts are characterized by their strong resistance to creep and outstanding resistance to corrosion. They are used in diesel and petrol engines;

- **SG2** – High-performance cast steel with very high chrome content (> 30%), which, together with molybdenum, is extremely resistant to corrosion and heat, and is mainly used in diesel and petrol engines;
- **SG3** – Highly alloyed cast steel material with high molybdenum and vanadium content, which is used for highly wear-resistant valve seat inserts in supercharged diesel and petrol engines, and also in combination with alternative energies such as natural gas (CNG) and liquefied petroleum gas (LPG);
- **SM1** – Extremely high-quality and high-performance sintered material for intake and exhaust valve seat inserts with outstanding resistance to wear. Developed for high-performance naturally aspirated and turbocharged engines using petrol, diesel, and gas.

The current valve seat insert press-fit method presents some drawbacks for the combustion chamber design as well as for the engine performance. Firstly, the press-fit method creates residual mechanical stresses on the cylinder head counterbore, which lead to a higher crack formation tendency. Furthermore, a thermal insulation is created between the valve seat and the cylinder head due to layers of air between them. In addition, there is a limitation for the engine performance improvement by the valve seat diameter and the minimum web thickness required for the cylinder head casting manufacturing. As an alternative, it has been used the laser cladding technology for manufacturing valve seats. The laser cladding technology creates the valve seat by depositing a copper-based alloy directly onto aluminum alloy and establishing a stable bead. After adding the cladding alloy onto the cylinder head, the valve seat angles are machined. The advantages of the laser cladding compared to the conventional press-fit method are the valve seat enlargement which enables more air flow capacity, the valve temperature reduction due to a better cooling design around the valve seats, the cost reduction mainly due to material usage decreasing, and furthermore the reduction of the knocking tendency due to a cooler valve. For a mass-production use, the laser clad technology has been developing new clad materials suitable for several applications, (Kawasaki et al. 1992; Imai and Nishida 2009). Figure 87 presents a Schematic illustration of clad seats and expected effects compared with press-fit type seats.

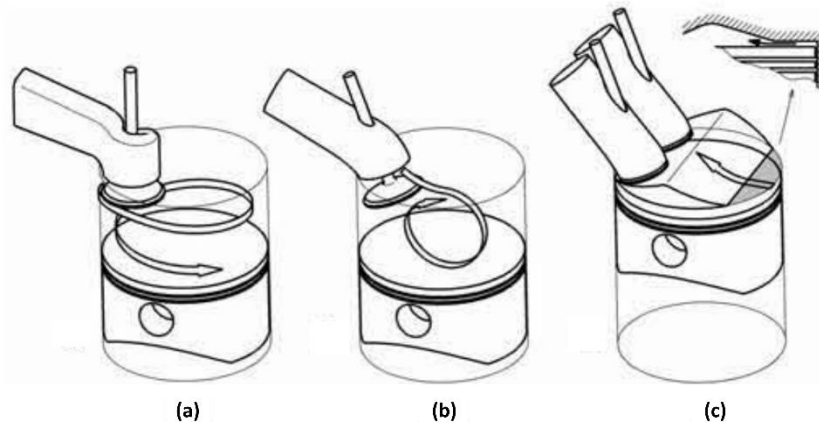
Figure 87 – Schematic illustration of cladded seats and expected effects compared with press-fit type seats



Source: (Kawasaki et al. 1992)

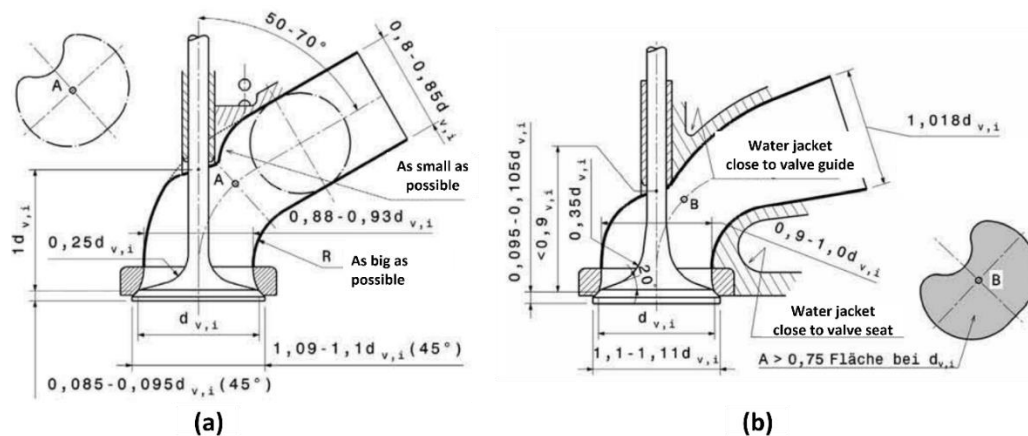
As aforementioned, the initial in-cylinder flow pattern such as tumble, swirl, and squish (Figure 88), is generated by the intake air flow combined with intake port and combustion chamber design during the engine intake stroke. Furthermore, the volumetric efficiency depends heavily on the design of the intake ports. The port layout in the cylinder head, the cross-section area and the actual local flow velocities are just as important as the flow losses in the valve seat area. The intake ports are used as pure charge ports generating the swirl or the tumble. However, the generation of swirl and tumble is at the expense of the mass flow. The limiting criterion for the smallest port angle is the machining for the valve spring seat. In addition, a minimum wall thickness must remain in this area. The intake port is generally circular, or nearly so, and the cross-sectional area is no larger than is required to achieve the desired power output. For the exhaust port, the importance of good valve seat and guide cooling, along with the shortest length of exposed valve stem, (HEYWOOD 2018; Trzesniowski 2010). Figure 89 shows the proportions of typical intake and exhaust ports in function of the valve head diameter.

Figure 88 – In-cylinder flow pattern swirl (a), tumble (b) and squish (c)



Source: (Kawasaki et al. 1992)

Figure 89 – Typical intake and exhaust ports in function of the valve head diameter



Source: Adapted from (Trzesniowski 2010)

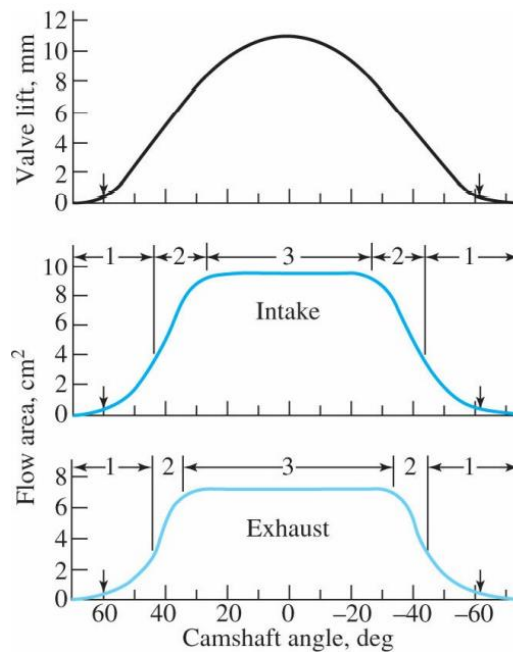
At high engine speeds, unless the intake valve is of sufficient size, the inlet flow during part of the intake process can become choked, achieving a sonic velocity at the minimum valve flow area. A choked flow reduces substantially the engine volumetric efficiency. The Mach number have been used to identify the onset of choking behavior. Correlation between the engine volumetric efficiency and an inlet Mach Index, MI , were performed on a range of engines and the results presented a rapidly decrease of the engine volumetric efficiency for $MI \geq 0.5$, (HEYWOOD 2018). The inlet Mach Index can be calculated using Equation 128.

$$MI = \frac{A_p \cdot S_p}{A_v \cdot C_d \cdot a} \quad (128)$$

Where the A_v is the valve curtain area in [m²], the C_d is the discharge coefficient and the a is the speed of sound in [m/s].

The valve curtain area, A_v , is the instantaneous valve flow area defined based on the valve lift and geometrical details of the valve seat and the valve stem, which corresponds to the side surface area of a frustrum cone between the valve and the valve seat, (HEYWOOD 2018). The flow through the valves can be divided into three main stages as shown in Figure 90.

Figure 90 – Valve flow area stages related to valve lift



Source: (HEYWOOD 2018)

For the first stage the valve lift range is evaluated according to Equation 129.

$$\frac{w_{seat}}{\sin \beta_{seat} \cdot \cos \beta_{seat}} > L_v > 0 \quad (129)$$

Where the w_{seat} is the valve seat width in [m] and the L_v is the valve lift in [m²]. The flow area related to this stage is calculated using Equation 130.

$$A_v = \pi \cdot L_v \cdot \cos \beta_{seat} \cdot D_v - 2 \cdot w_{seat} + \frac{L_v}{2} \cdot \sin 2 \cdot \beta_{seat} \quad (130)$$

Where the D_v is the valve head diameter in [m²].

In the second stage, the instantaneous valve flow area is still the frustrum cone side area, however its surface is no longer perpendicular to the valve seat. For the first stage the valve lift range is evaluated according to Equation 131, and the instantaneous valve flow area is calculated using Equation 132.

$$\left[\frac{D_P^2 - D_S^2}{4 \cdot D_m} - w_{seat}^2 \right]^{1/2} + w_{seat} \cdot \tan \beta_{seat} \geq L_v \cdot \frac{w_{seat}}{\sin \beta_{seat} \cdot \cos \beta_{seat}} \quad (131)$$

$$A_v = \pi \cdot D_m \cdot [(L_v - w_{seat} \cdot \tan \beta_{seat})^2 + w_{seat}^2]^{1/2} \quad (132)$$

Where the D_P is the port diameter in [m], the D_S is the valve stem diameter, and the D_m is the mean seat diameter in [m].

At the final stage, when the valve lift is sufficiently large, the instantaneous valve flow area is no longer between the valve head and the valve seat, it is the port flow area minus the valve stem area. Thus, the final range is defined by a lift according to Equation 133 and the instantaneous valve flow area is calculated using Equation 134.

$$L_v > \left[\frac{D_P^2 - D_S^2}{4 \cdot D_m} - w_{seat}^2 \right]^{1/2} + w_{seat} \cdot \tan \beta_{seat} \quad (133)$$

$$A_v = \frac{\pi}{4} \cdot (D_P^2 - D_S^2) \quad (134)$$

In summary, the valve lift and valve duration should be defined taking to account the valve discharge coefficient in order to achieve the required flow area to supply air into cylinder and remove burned gas from it. For the intake valves, the typical maximum instantaneous flow area is achieved at L_v/D_v about 0.25. On the other hand, for the exhaust valves the maximum instantaneous flow area is achieved at L_v/D_v about 0.2 due to higher pressure difference, (HEYWOOD 2018; Blair 1999).

In order to keep the flow velocity through the valves lower enough to not overcome $MI = 0.5$, a parameter called manifold-port area ratio, K_m , proposed by (Blair 1999). Based on tests results from a range of engines, it was concluded that the manifold-port area ratio should be $0.9 < K_{im} < 1.0$ for intake, K_{im} , ports and $1.2 < K_{im} < 1.4$ for exhaust ports, K_{em} . As standard reference values could be considered

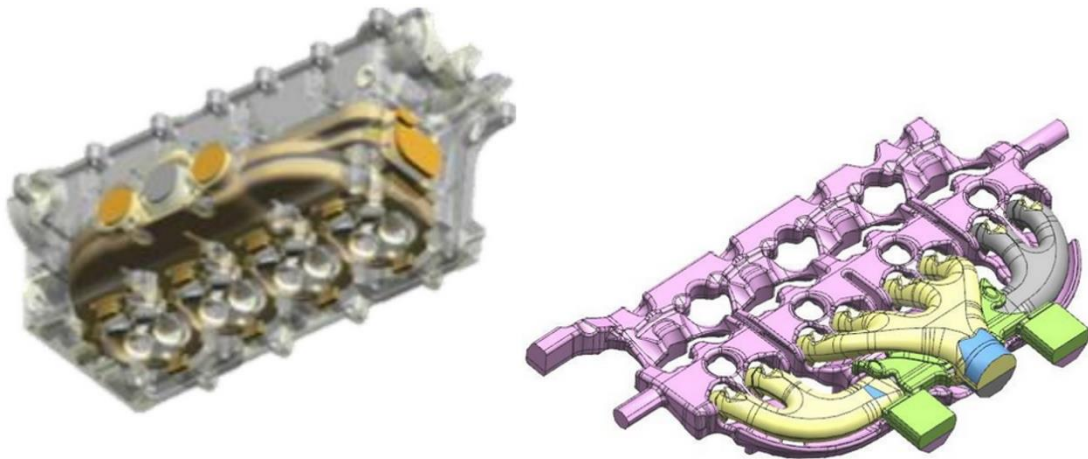
$K_{im} = 0.95$ and $K_{em} = 1.3$. The manifold-port area ratio can be calculated using Equation 135.

$$K_m = \frac{A_{manifold}}{A_{port}} = \frac{A_{manifold}}{n_v \cdot A_e} \quad (135)$$

Where the $A_{manifold}$, in [m²], is the inlet and outlet area of intake and exhaust port, respectively, the n_v is the number of valves and the A_e is the product of $A_v \cdot C_d$ called the effective valve area, in [m²].

Nowadays, the exhaust manifold has become an integrated part in the cylinder head. The exhaust manifold in a conventional engine is an independent component, commonly made of cast iron. In case of a turbo-charged engine application, expensive alloys are combined with the cast iron aiming to enhance its thermal resistance. Furthermore, the cast iron exhaust manifold could require a rich air-fuel mixture in order to protect the component. The exhaust manifold integrated to the cylinder head have been used as an alternative to overcome the limits established by the conventional exhaust manifolds. The integrated exhaust manifold presents advantages of weight reduction, lower manufacture cost, fuel consumption reduction, lower temperatures of the exhaust gases and inner walls and faster engine warm-up. However, the integrated exhaust manifold approach required a cooled exhaust manifold which increase the ware jacket complexity, an improved water pump along with a larger radiator and fan and a lower thermal energy available to the turbocharger, (Neshan 2013; Xiangwang Li et al. 2017; Neshan et al. 2012). Figure 91 illustrates an integrated exhaust manifold.

Figure 91 – Integrated exhaust manifold



Source: (DE MARINO et al. 2018)

2.3.12.2. Cylinder head material

Currently, there are two main alloy groups in competition for aluminum cylinder heads. The first are called heat-hardening AlSiMg alloys (additional designation "wa" stands for "artificial aging") with a significant Mg content and the second are the cold-hardening AlSiCu alloys with a larger Cu content. A trend can be seen throughout the past few years to switch from more temperature stable AlSiCu alloys to more ductile AlSiMg alloys aiming to be able to better prevent thermal fatigue cracks. The heat treatment initially serves to set the desired initial hardness or strength as a function of parameters such as the artificial aging time and temperature, and at the same time, it reduces internal stresses. However, the influence of the alloy tolerances on the achievable material properties must also be considered. A subsequent improvement in the quality of the material is given by a relatively expensive pressure-time-temperature treatment (HIP = "Hot Isostatic Pressing") which pores in the material can be largely closed, (Eduard Köhler 2011). The Table 20 presents the properties of the Typical aluminum alloys used for light metal cylinder heads.

Table 20 – Typical aluminum alloys used for light metal cylinder heads

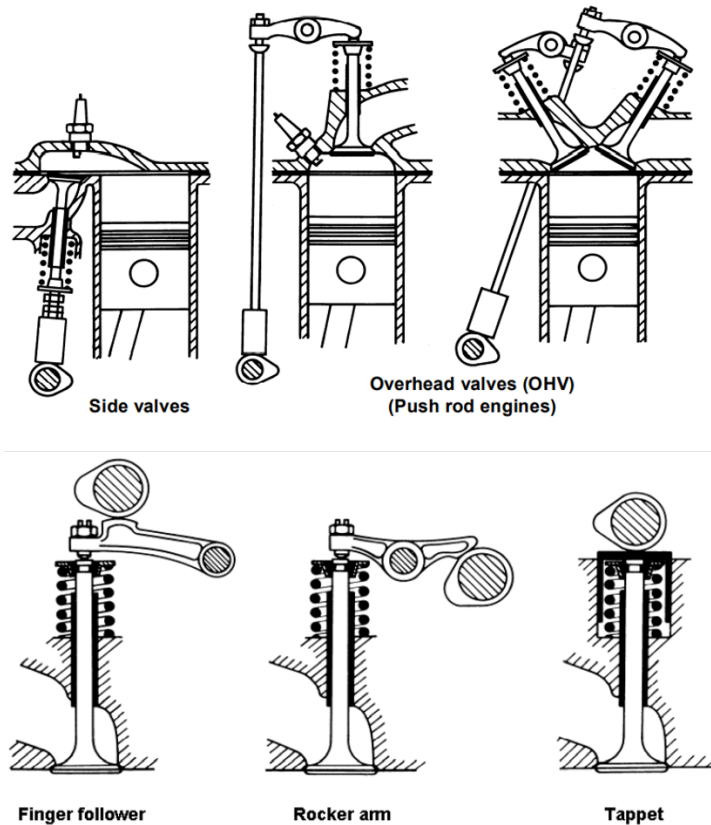
Properties	R _{p0.2} Yield Strength [MPa]		HB		Density [g/cm ³]	Young's Module [GPa]	Thermal expansion [10 ⁻⁶ m/m.K]	Thermal conductivity [W/m*K]
AlSi7Mg wa	180	200	75	80	2.66	69-75	22	143-172
AlSi10Mg	80 wh	100	50	60	2.65	75	22	140-170
	180	200	75	85				
AlSi10Mg (Cu)	100 wh	130	55	60	2.65	75	22	140-170
	190	210	75	85				
AlSi7Mg0.6 wh	-	220	-	90	2.67	69-75	22	143-172
AlSi6Cu4	140 wh	-	75	-	2.75	75	22	110-130
	200							
AlSi9Cu3	140	140	65	70	2.75	75	22	110-130
AlCu5Ni1.5Ni CoSbZr	140	210	85	-	2.84	70	22.5	150

Source: (Pischinger 2012)

2.3.13. Valvetrain

The valvetrain is a mechanism which use the intake and exhaust valves to control the inlet and outlet charge in each individual cylinder following each cycle of the engine operation. The valves must bear the combustion pressures and temperatures, as well as respond quickly to the valvetrain actions. Commonly, the poppet valve has been used in four-stroke engines due to its low lubrication requirement, low friction, simplified sealing, easy adjustment, and low cost. Basically, the valvetrain system consists of one or more camshafts, one or more transfer elements between the camshaft and valve, valve springs, valve guide, keepers, valve stem seals, and the valves themselves. There are several types of valvetrain system as shown in Figure 92. The definition of the suitable valvetrain type in a project is based on the engine application, package and cost, (Y. WANG 2007).

Figure 92 – Types of valvetrain systems



Source: (Pischinger 2012)

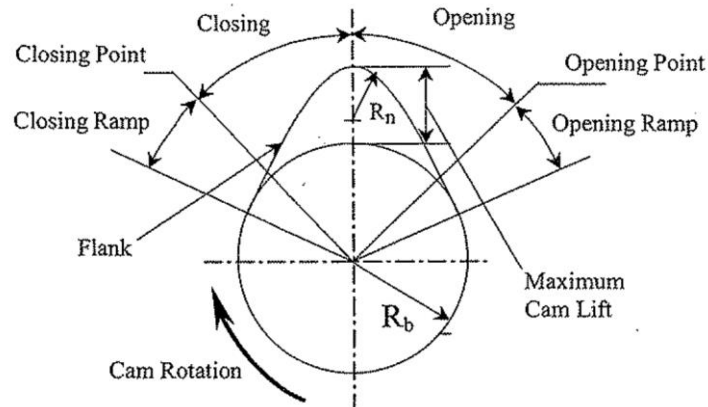
2.3.13.1. Cams and camshaft

The cam is the component responsible to open and close the valves within an overall valve event duration. The cam profile has a huge impact on the engine performance. Thus, the cam profile must be designed to obtain the most effective valve lift diagram possible considering valvetrain system and according to practical limits imposed on the design. These limits include maximum allowable stresses, valvetrain resonant frequency and cam manufacturing limits. The cam profile is composed of following parts and illustrated in Figure 93:

- **Ramp** – The portion of the cam profile event from (or to zero lift) to defined valve opening or valve closing point;
- **Base circle radius (R_b)** – The portion of the cam contour at zero lift;
- **Flank** – The portion of the cam profile between the ramp and the nose radius;
- **Nose radius (R_n)** – The at the maximum lift point of the nose of the cam which is tangent to the flank radius and the maximum lift point. It is worth

to point out that some cam profiles have a dwell time in which the valve remains at full lift during few degrees, thus those cam lobes have dual nose radius, (Y. WANG 2007).

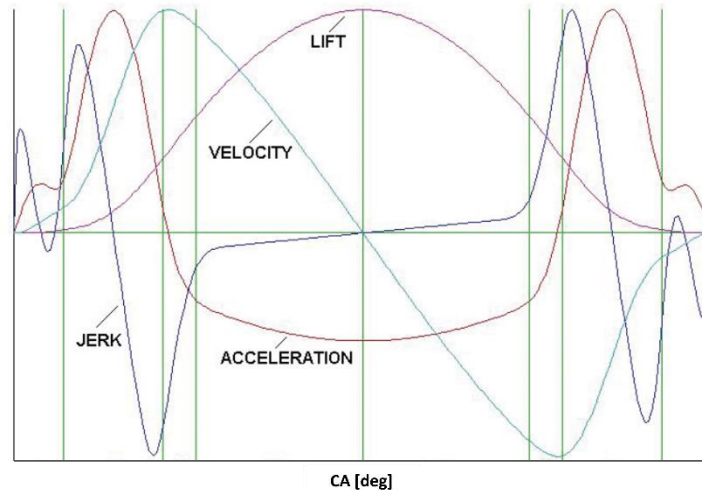
Figure 93 – Cam profile nomenclature



Source: (Y. WANG 2007)

The distance that the valve travels off its seat is called valve lift. The valve lift is directly developed in the cam lobe in case of direct valve actuation layout. If the valvetrain system uses rocker arm, the valve lift is the cam lift multiplied by the instantaneous rocker arm ratio. The rate of valve lift is the speed in which the valve operates. Therefore, the valve velocity is the first derivative of the lift contour with respect to the cam angle. The valve opening velocity should remain constant in order to take up any clearances or slack before the load is applied to the valvetrain system. Similarly, the closing ramp should be constant and low in order to prevent a hammering noise as the valve approaches its valve seat. As a reference, the faster the valve opening, the higher will be the engine volumetric efficiency. The valve acceleration is the second derivative of the valve lift contour. Aiming at a proper valvetrain action, the acceleration curve should be as smooth as possible and have the smallest maximum values. In addition to the valve displacement, velocity, and acceleration, the cam profile is also evaluated with regard to its pulse or jerk behavior. The jerk is the acceleration rate in respect to time or the acceleration curve slope at an instantaneous angle. The jerk curve is used to evaluate the force change of direction as well as the valvetrain system vibration, (Y. WANG 2007). Figure 94 illustrates the valve displacement, velocity, acceleration, and jerk curves.

Figure 94 – Valve displacement, velocity, acceleration, and jerk curves

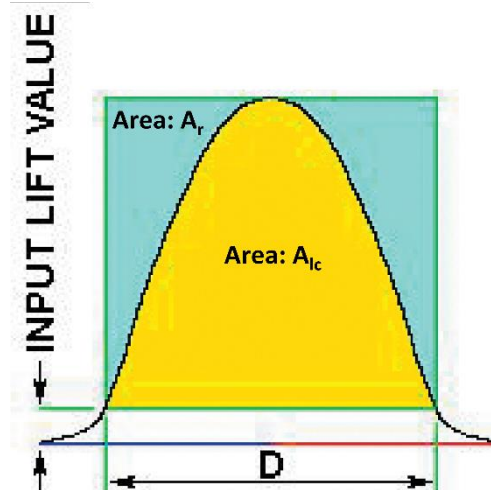


Source: (Blair 2003)

The cam profile for high-speed operation, like in engines application, must be designed in a way that the cam profile be continuous through the first and second derivatives of the displacement across the entire valve event duration. In case of the jerk, it must be finite across the entire valve event duration. Therefore, in order to accomplish this requirement, the valve displacement curve must be constructed with at least a fifth-degree polynomial, (Norton 2012).

The engine breathing capacity is increased by maximizing the area under the valve lift curve. In order to evaluate the area under the valve lift curve and compare it with other valve lift curves, the lift-duration envelope ratio, K_{LD} , can be used. The lift-duration envelope ratio is the area under the valve lift curve, A_{lc} , divided by the rectangle area, A_r , in which it sits as shown by Figure 95 and Equation 136. Therefore, the higher is the lift-duration envelope ratio higher is the engine breathing capacity for a given valvetrain system, (Blair 2003).

Figure 95 – The lift-duration envelope ratio



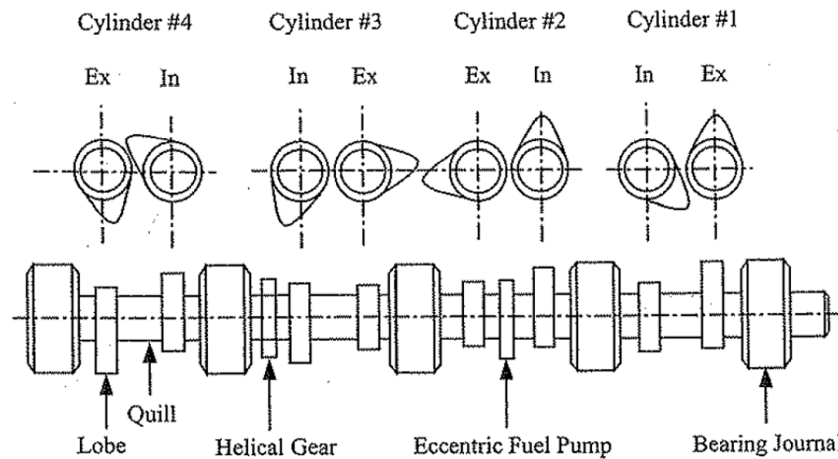
Source: Adapted from (Blair 2003)

$$K_{LD} = \frac{A_{lc}}{A_r} \quad (136)$$

During the valve lift curve design, it is advisable to develop a cam profile with maximum positive acceleration is numerically about three times the absolute value of the maximum negative value and the duration of the positive acceleration about 35 – 40% of the negative acceleration period. Furthermore, the spring natural frequency must be designed to match the valvetrain harmonic of lowest amplitude. Commonly, the valvetrain is designed to have a low amplitude at the 7th harmonic, (Blair 2003).

The camshaft consists of the quill, the bearing journals, the thrust faces, and the cam lobes as shown in Figure 96. The camshaft must be stiffer enough to minimize the deflections under load which may affect the valvetrain dynamic behavior. The quill size is dependent on the sum of individual camshaft lobes load and the transmitted load by the camshaft drive due to crankshaft torsions. The number of bearing journals is determined by the configuration of the cylinder head. The cam lobes should be positioned at an equal distance throughout the quill length in order to equalize the camshaft stiffness, (Y. WANG 2007).

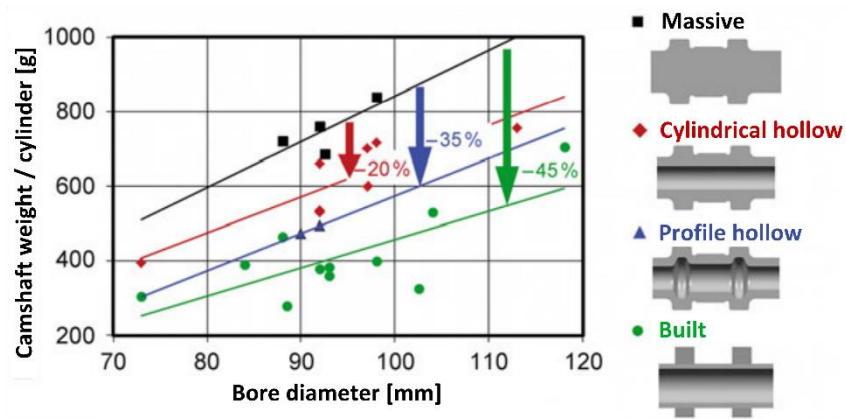
Figure 96 – Camshaft nomenclature



Source: (Y. WANG 2007)

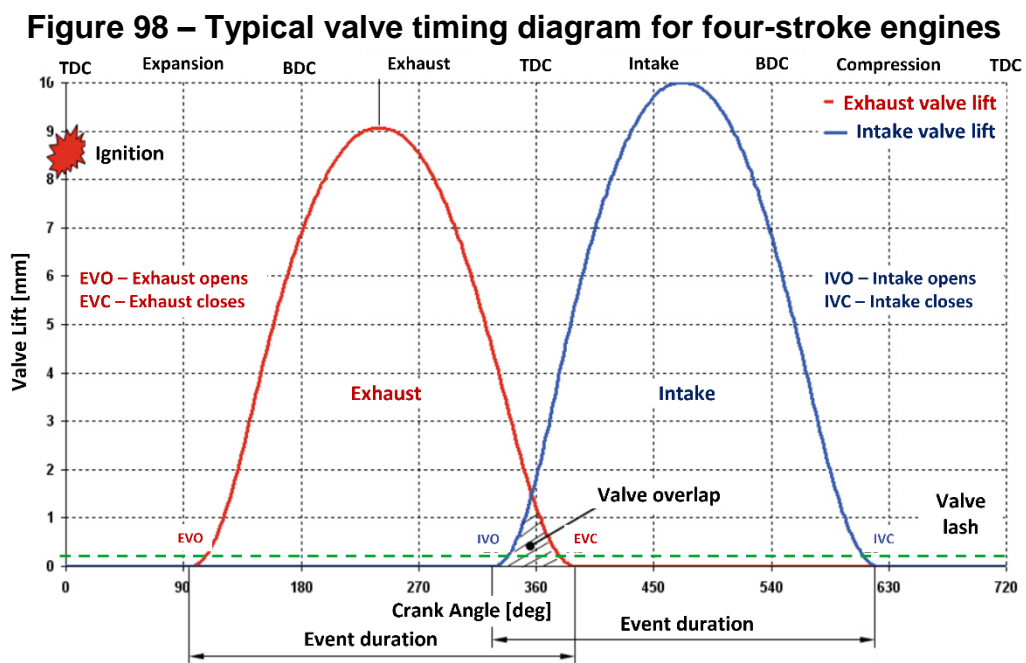
The camshafts are commonly manufacture by casting, forging, and assembling. The cast camshaft requires a heat treatment after casting process to achieve the necessary strength and qualification for the application. In case centrifugal casting, the metal flows into a rotating casting die and solidifies under the influence of a centrifugal force. In order to reduce weight, the camshafts are typically manufactured hollow. In case of assembled camshafts, the shaft and the cams are manufactured separately and then assembled. Due to independent component manufacturing, it is possible to select an appropriate material to matches function, production, and stress. Usually, the cold-drawn structural steels (e.g., St 52K) or alloyed steels (e.g., 100Cr6) are used for the shaft, and case or inductive hardened steels (e.g., 16MnCr5) are utilized for the cams. The assembled camshaft has a disadvantage to limited torque transmission by the joint components. However, it presents advantages that include a small possible cam distance, a lower mechanical stress in the transitional shaft to cam area, and mainly a weight reduction. Figure 97 presents a weight comparison among different manufacturing process and the assembled camshaft approach can reach up to 45% of weight reduction, (Pischinger 2012; F. SCHÄFER 2017).

Figure 97 – Different camshaft manufacturing process weight comparison nomenclature



Source: Adapted from (F. SCHÄFER 2017)

The matching of a camshaft related to the crankshaft angle is performed by the engine synchronization. One way to represent the valve timing related to the crankshaft is called valve timing diagram. The valve timing diagram provides a complete information about the intake and exhaust valve opening and closing timing, the valve events duration, the valves maximum lift and the valve overlap related to the crankshaft angle, (MAHLE 2013). Figure 98 illustrates a typical valve timing diagram for four-stroke engines.

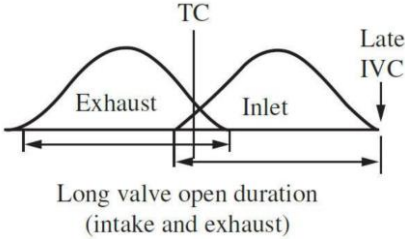
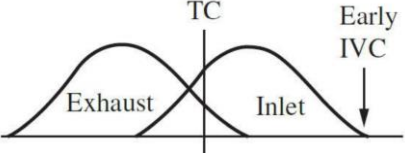
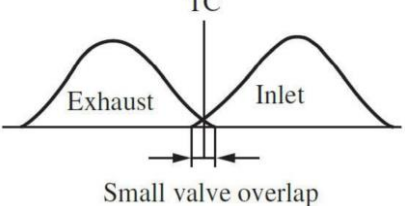


Source: Adapted from (MAHLE 2013)

Currently, the engines have been used valve variable control operation as function of the engine speed and load instead of fixed valve timing operation. The

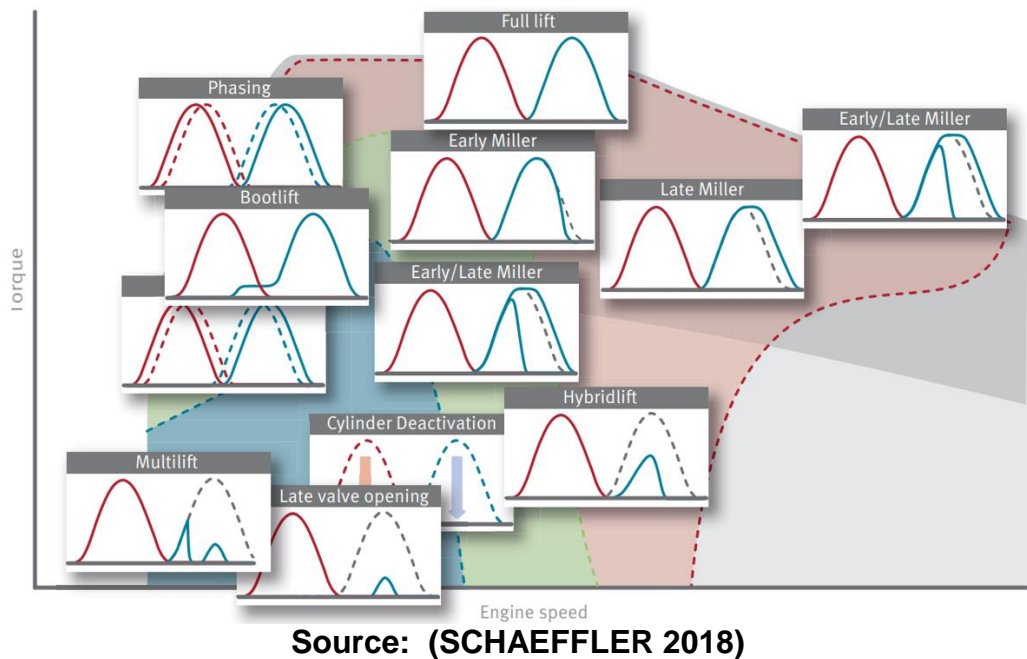
simplest valve variable control mechanism varies the valve phase via a cam phaser aiming to improve the air flow at high engine speeds and increase the engine torque at low engine speed. More sophisticated valve control systems, such as Variable Valve Actuation – VVA, can control the valve lift, duration, and timing. The VVA systems enable the engine to operate in alternative operating cycles such as Miller and Atkinson, control the residual burned gas inside the combustion chamber, decrease the pumping losses, and reduce the engine fuel consumption and emission levels, (HEYWOOD 2018). The Table 21 illustrates three typical valve timing characteristics for the engine performance objectives and Figure 99 illustrates the application of the UniAir VVA system over the engine operation map.

Table 21 – Typical valve timing characteristics for the engine performance objectives

Engine performance objectives	Required valve timing characteristics
Greater maximum power	 <p>Long valve open duration (intake and exhaust)</p>
Greater low-speed torque	 <p>Early IVC</p>
Better idle combustion stability	 <p>Small valve overlap</p>

Source: (HEYWOOD 2018)

Figure 99 – UniAir VVA system applied over the engine operation map

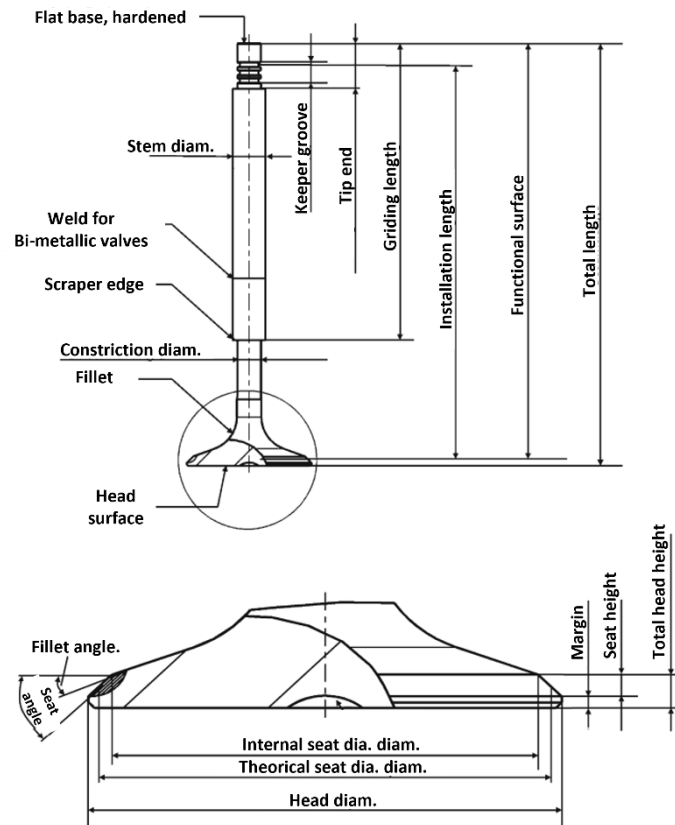


2.3.13.2. Valves

The valves are components highly mechanically and thermally stressed, as well as exposed to corrosive conditions. They are responsible for the engine gas exchange control and the combustion chamber sealing.

Currently, the poppet-valve design is widely used in internal combustion engines. In terms of function and operational safety, the poppet valve has proven to be particularly suitable for internal combustion engines application. However, from the thermodynamic point of view, the poppet valve is not optimal in all respects. The valve stem leading through the gas ducts is an obstacle that reduces the port cross-section, and the stem to head fillet geometry along with the seat may only be a compromise between mechanical or tribological necessity and aerodynamic requirements. Although the poppet-valve has its issues, it has a decisive advantage to seal automatically the combustion chamber under internal pressure, (F. SCHÄFER 2017). Figure 100 presents the poppet valve nomenclature.

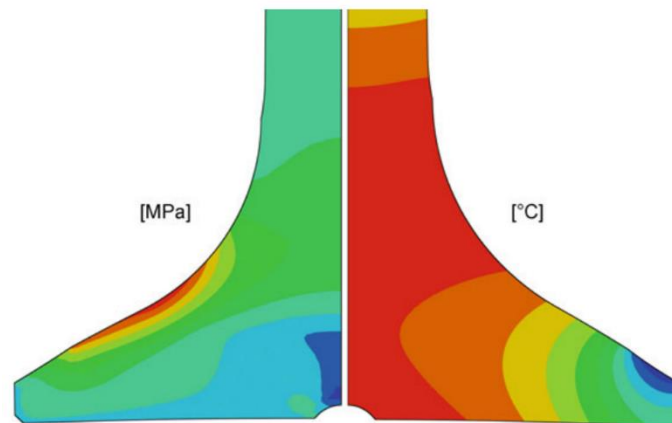
Figure 100 – Poppet-valve nomenclature



Source: (F. SCHÄFER 2017)

The mechanical load in the valve is generated by the valve head bending under ignition pressure and due to hard contact during the valve closing. The mechanical load can be influenced by the valve material strength and valve head design. As the valve head has a significant portion of the combustion chamber area, the valve absorbs heat from the combustion process. In addition, the exhaust valve is further heated on the valve head-back surface due to the hot exhaust gas flow. The heat from the valve is mainly dissipated through the valve seat, however a small percentage of the heat flows through the valve guide. The intake valves can reach temperatures that range from 300 to 500°C and the exhaust valves may reach 600 to 800°C under normal engine operating conditions. The exhaust valves under severe engine operating conditions could achieve temperatures about 1000°C. In case of the valve seat the seal does not work properly, a local overheating and melting can occur leading to a valve failure, (Pischinger 2012). Figure 101 illustrates a typical valve temperature and stress distribution under the engine ignition pressure.

Figure 101 – Temperature and stress distribution in the valve under ignition pressure

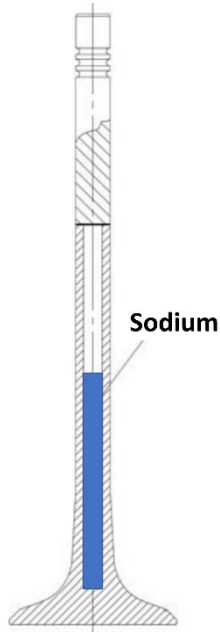


Source: (MAHLE 2013)

The valves used in internal combustion engines are essentially into three main groups: monometallic valves, bimetallic valves, and hollow valves. The monometallic valves, as its own name implies, are made in one piece frequently using X45CrSi93 as material. The bimetallic valves allow a combination of the optimum materials for the valve stem and the valve head. In case of bi-metallic valves, a hot-formed valve head is connected to the valve stem by friction welding. Usually, it is used the X50CrMnNiNb219 and X45CrSi93 materials for the valve head and the valve stem, respectively. The weld seam is positioned in such a way that it is half length deep in the guide when the valve is closed, or about 6 mm above the scraper edge. It should be noted that, for manufacturing reasons, the length of the cylindrical part on the valve head before welding is at least one and a half times the valve stem diameter. In case of the valve head wear resistance is not enough on its own in the bimetallic valves, the seating surface can be reinforced by means a build-up welding or nitriding. The hollow valves are mainly used on the exhaust side and under special circumstances also on the intake side, in order to, primarily, to lower the temperatures in the valve fillet and valve head area, and occasionally to reduce the valve weight. The hollow valves used to lower the valve temperature have the cavity filled with metallic sodium to about 60% of its volume. The sodium is free to move in the cavity of the valve stem. Depending on the engine operating condition, the liquid sodium (melting point 97.5°C) is set in linear motion transporting a significant amount of heat generated at the valve head and the fillet to the valve stem and valve guide to the cooling circuit. The achievable temperature reduction with optimal heat dissipation and the tightest possible running clearances is up to 170°C, (F. SCHÄFER 2017). Figure 102 illustrates a bimetallic

hollow valve filled with sodium and the Table 22 presents several valve material properties and they application field.

Figure 102 – Bimetallic hollow valve filled with sodium



Source: Adapted from (F. SCHÄFER 2017)

Table 22 – Valve material properties and application fields

Short name	X45Cr Si93	X85Cr MoV182	X53CrMn NiN219	X50CrMn NiNbN	X60CrMn MoVNb	NiCr20TiAl
Brief description	Cr Si- Steel	Cromo 193	21-4N	LV 21-43	Resis TEL	Nimonic 80A
Material number	1.4718	1.4748	1.4871	1.4882	1.4785	2.4952
Field application	Intake valve, normal stress bimetal valve head	Intake valve, higher stress, good wear resistance	Intake and exhaust valve, high thermal and corrosion resistance, exhaust valve with stellite reinforcement, for passenger cars	Intake and exhaust valve, high thermal and corrosion resistance, high dynamic strength, exhaust valve without stellite reinforcement, for trucks	Intake and exhaust valve, high thermal and wear resistance, high dynamic strength, exhaust valve without stellite reinforcement, for trucks	Exhaust valve with highest stress level, for racing engines or large engines in heavy-oil operation
Density [g/cm ³]	7.6	7.8	7.8	7.9	7.8	8.17
Thermal cond. [W/cm]	0.210	0.210	0.147	0.147	0.147	0.122
Thermal Expansion coef. [1/K] at 20 - 800°C	13x10 ⁻⁶	12 x10 ⁻⁶	18.5 x10 ⁻⁶	19 x10 ⁻⁶	18 x10 ⁻⁶	15.1 x10 ⁻⁶

Tensile strength [MPa]	1100-1350	1000-1200	≥1000	≥950	≥1000	≥1000
Elongation at rupture	12	8	8	12	8	15
0,2% yield strength [MPa]:						
Cold	750	900	600	580	800	900
at 500°C	400	500	350	340	500	800
600°C	240	280	300	310	450	780
700°C	80	120	250	260	400	750
800°C	-	-	200	220	350	550
900°C	-	-	-	120	-	360
Hardness at the end of the skirt HRC	≥56	≥50	-	-	-	-
at the seat HV 30	≥500	≥480	≥30*	≥30*	≥32*	≥38*
at the groove HV 30	≥550	≥490				

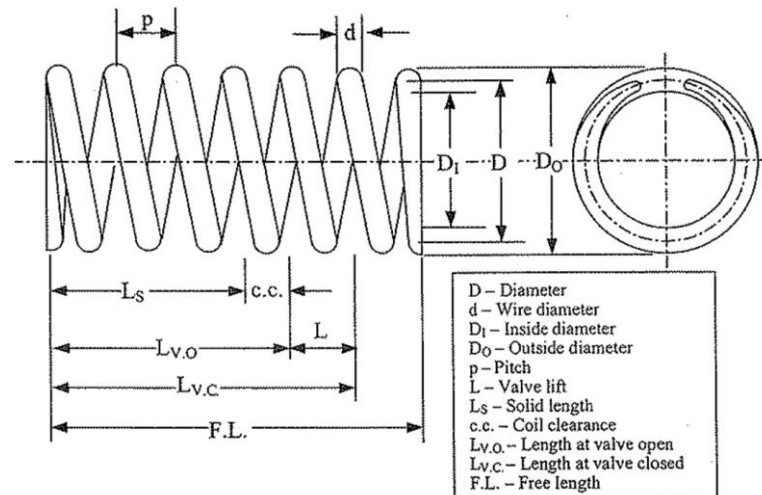
* After precipitation hardening

Source: (Pischinger 2012)

2.3.13.3. Valve spring

The valve springs are helical compression springs which the task is to ensure that the valve closes reliably in all engine operation conditions. Furthermore, it should maintain the frictional connection between the valve actuating camshaft and cam follower, which is very important for reliable engine function, especially at the speed reversal point (valve maximum lift) and after the valve has closed. During the acceleration period, the cam exerts a positive accelerating force on the follower. The force magnitude is equal to the product of the valvetrain mass and its acceleration at an operation speed. The valvetrain acceleration must exceed the limit value over which the valve will fly-off the cam profile or bounce at the closing phase. These situations can increase the valvetrain components wear or damage them, (MAHLE 2013). Figure 103 presents the valve spring nomenclature

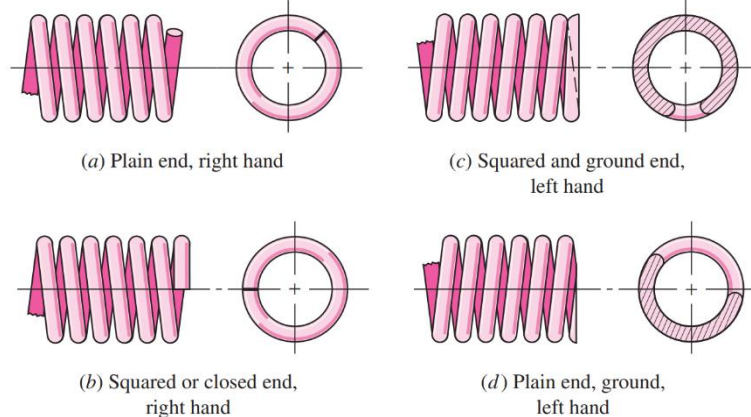
Figure 103 – Valve spring nomenclature



Source: (Y. WANG 2007)

Typically, there are four types of ends used for compression springs as shown in Figure 104. A plain ends spring has a non-interrupted helicoid like a long spring which had been cut into sections. A spring with plain ends that are squared or closed is obtained by deforming the ends to a zero-degree helix angle. For applications which is required a better load transfer such as valvetrain systems, it is advisable to use a both square and ground spring, (MAHLE 2013).

Figure 104 – Typical valve spring end types

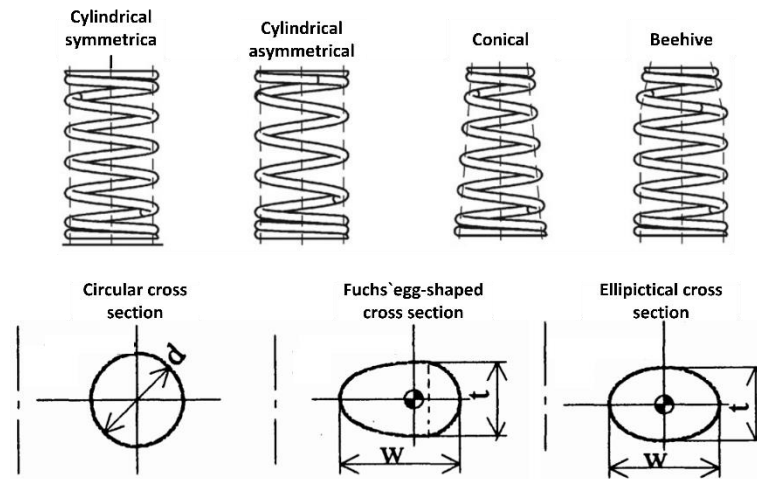


Source: (Budynas and Nisbett 2011)

Along with the valve spring type, the valve spring can be characterized according to its shape and the wire profile. The selection of the spring shape and wire profile is made based on the valve spring application requirements and the cost target. The simplest and cheapest valve spring design is a cylindrical, symmetrical, circular wire valve spring. However, the other designs have an advantage to have a lower moving spring mass. Furthermore, the conical and beehive valve springs designs also

offer a further potential of valvetrain mass reduction by using a smaller upper valve spring plate. In the case of asymmetrical designs, the additional effort involved in aligning the assembly must be considered. From the wire profile point of view, the round wire although is the cheapest and easier to manufacture, it has some drawbacks like higher solid and installed heights, heavier weight, higher shear stresses when compressed and lower natural frequency compared the elliptical and Fuchs' egg-shape, (Y. WANG 2007; Miyamura et al. 1993). Figure 105 illustrates the typical valve spring shapes and wire profiles.

Figure 105 – Typical valve spring shapes and wire profiles



Source: (Miyamura et al. 1993; MAHLE 2013)

The maximum stress in the valve spring is computed by superposition of the direct shear stress and the torsional shear stress on a round valve spring wire. The maximum shear stress, τ_{max} in [MPa], can be calculated using Equation 137, (Budynas and Nisbett 2011).

$$\tau_{max} = K_B \frac{8 \cdot FS_{max} \cdot D}{\pi \cdot d^3} \quad (137)$$

Where the FS_{max} is the maximum force applied on the spring in [N], the D is the spring mean diameter in [mm], d is the spring wire diameter and the K_B is a stress concentration factor calculated according Equation 138.

$$K_B = \frac{4 \cdot C + 2}{4 \cdot C - 3} \quad (138)$$

Where the C is the spring index which is the spring diameter to wire diameter ratio. The preferred value of the spring index ranges from 4 to 12, (Budynas and Nisbett 2011).

For very small deflections the spring force is not reproducible, and near to the closed state, nonlinear behavior begins as the number of active turns diminishes as coils begin to touch. The valve spring should be designed for an operating point of 75 percent of the curve between no load and solid state. Which in turn, the maximum operating force should be limited. The parameter fractional overrun to closure (ξ), is used to take into account to calculate an over force that should be used during a spring design process. It is recommended an $\xi \geq 0.15$, (Budynas and Nisbett 2011). The over force, F_s in [N], can be calculated using Equation 139.

$$F_s = (1 + \xi) \cdot FS_{max} \quad (139)$$

The valve spring rate, k in [N/mm], can be calculated using Equation 140.

$$k = \frac{d^4 \cdot G}{8 \cdot D^3 \cdot N_a} \quad (140)$$

Where the G is the shear modulus in [GPa] and the N_a is the number of active coils. The preferred value of number of active coils ranges from 3 to 15, (Budynas and Nisbett 2011). The spring total number of coils, N_t , can be obtained using Equation 141.

$$N_t = N_a + 2 \cdot N_i \quad (141)$$

Where the N_i is the number of inactive coils.

A spring under its working condition must not be totally compressed. Otherwise, it becomes a solid body. As reference, a spring over-travel of 1.5 to 2.5mm can be considered in order to avoid the spring total compression, (Budynas and Nisbett 2011). The spring solid length, also called solid height, can be calculated using Equation 142.

$$L_s = (N_t - a) \cdot d \quad (142)$$

Where a varies with an average of 0.75.

The valve spring free length, L_f in [mm], is calculated using Equation 143.

$$L_f = p \cdot N_a + 2 \cdot d \quad (143)$$

Where the p is the spring pitch in [mm].

The valve springs can be made of several different materials like plain high-carbon steels, low-alloy chromium-vanadium steels, chromium-silicon steels, stainless steels, and high-temperature alloys. Among these materials, the chromium-vanadium and the chromium-silicon are the more efficient in terms of mass and spring rate, (Y. WANG 2007). The Table 23 presents some spring wires mechanical properties.

Table 23 – Some spring wires mechanical properties

Material (ASTM)	Min. Tensile Strength [MPa]	Elastic Modulus [GPa]	Shear Modulus [GPa]	Hardness [HRc]	Max. Allowable Temperature [°C]
High-Carbon Steel					
A227 Hard Drawn	1010-1950	210	80	31-52	120
A229 Oil Tempered	1140-2020	210	80	42-55	120
A230 Carbon, Valve Spring Quality	1480-1650	210	80	45-49	120
Alloy Steel					
A231, A232 Cr-V	1310-2070	210	80	41-55	220
A401 Cr-Si	1620-2070	210	80	48-55	245
Stainless Steel					
A313 SS302 (18-8)	860-2240	190	69	35-45	290
A313 SS631	1620-2310	200	76	38-57	340
High-Temperature Alloys					

Inconel 718	1450-1720	200	77	45-50	590
A-286	1100-1380	200	72	35-42	510

Source: Adapted from (Y. WANG 2007)

Based on a comparison of the spring materials tensile strength related to its wire size, it was observed that the graph of tensile strength versus wire diameter is almost a straight line for some materials when plotted on log-log scale. Equation 144 represent the line equation from these graphs and parameters A and m are presented in the Table 24 for several spring materials.

$$S_{ut} = \frac{A}{d^m} \quad (144)$$

Where the S_{ut} is the ultimate tensile strength in [MPa]. The wire diameter in Equation 144 must be entered in [mm].

The maximum allowable shear stress, τ_{all} in [MPa], for a compression spring can be calculated using Equation , (Budynas and Nisbett 2011).

$$\tau_{all} = 0,56. S_{ut} \quad (145)$$

The compression springs can buckle when the deflection becomes too large. In order to avoid the spring buckling, it should be design according to the stability criteria. The condition for absolute spring stability related to the spring free length is presented by Equation , (Budynas and Nisbett 2011).

$$L_f < \frac{\pi. D}{\alpha} \left[\frac{2. (E - G)}{2. G + E} \right]^{1/2} \quad (146)$$

Table 24 – Constants A and m for the spring ultimate tensile strength estimative

Material	ASTM No.	Expoent m	A [MPa]	Diameter [mm]
Music wire	A228	0.145	2211	0.10 - 6.5
OQ&T wire	A229	0.187	1855	0.5 - 12.7
Hard-drawn wire	A227	0.190	1783	0.7 - 12.7

Chrome-vanadium wire	A232	0.168	2005	0.8 - 11.1
Chrome-silicon wire	A401	0.108	1974	1.6 - 9.5
302 Stainless wire	A313	0.146	1867	0.3 - 2.5
Phosphor-bronze wire	B159	0.263	2065	2.5 - 5
		0.478	2911	5.0 - 10
		0	1000	0.1 - 0.6
		0.028	913	0.6 - 2.0
		0.064	932	2.0 - 7.5

Source: Adapted from (Budynas and Nisbett 2011)

Where the E is the material Young's module and the α is the End-condition constant which for spring supported between flat parallel surfaces (fixed ends) $\alpha = 0,5$.

For the elliptical or Fuchs' egg-shape spring wires, the stress concentration factor K_B is calculated differently using Equation 147.

$$K_{B_{ell-egg}} = a_0 + \frac{a_1}{C} + \frac{a_2}{C^2} \quad (147)$$

Where $K_{B_{ell-egg}}$ is the stress concentration factor for the elliptical or Fuchs' egg-shape spring wires, C is the spring index defined as the bottom mean coil diameter to round wire equivalent diameter to ovate ratio, and a_0 , a_1 and a_2 are the constants values available in the Table 25 in function of the aspect ratio r_{sp} . The aspect ratio can be calculated using Equation 148, (Miyamura et al. 1993).

$$r_{sp} = \frac{w}{t} \quad (148)$$

Where the w and t are the wire width and thickness, respectively as presented in Figure 105.

Table 25 – Constants values a_0 , a_1 and a_2 for stress concentration factor calculation

Aspect ratio r_{sp}	Elliptical shape			Fuchs' egg-shape		
	a_0	a_1	a_2	a_0	a_1	a_2

1.00	1.01	1.28	1.16	1.01	1.28	1.16
1.02	1.00	1.28	1.18	0.99	1.30	1.19
1.04	0.99	1.27	1.21	0.99	0.96	2.96
1.06	0.98	1.27	1.24	1.02	0.54	4.10
1.08	1.00	0.73	3.65	1.05	0.11	5.15
1.10	1.02	0.46	4.22	1.08	-0.11	5.04
1.12	1.03	0.31	4.23	1.10	-0.13	4.11
1.14	1.05	0.16	4.32	1.12	-0.14	3.56
1.16	1.06	0.13	3.84	1.14	-0.15	3.09
1.18	1.08	-0.03	4.16	1.15	-0.18	3.07
1.20	1.10	-0.04	3.72	1.16	-0.24	3.31
1.22	1.11	-0.04	3.37	1.17	-0.19	3.00
1.24	1.12	-0.05	3.12	1.18	-0.18	2.81
1.26	1.14	-0.11	3.25	1.19	-0.18	2.66
1.28	1.15	-0.17	3.54	1.20	-0.19	2.58
1.30	1.15	-0.14	3.27	1.21	-0.19	2.45
1.32	1.16	-0.12	3.07	1.22	-0.19	2.40
1.34	1.17	-0.10	2.92	1.23	-0.20	2.34
1.36	1.18	-0.09	2.78	1.24	-0.21	2.34
1.38	1.18	-0.09	2.67	1.25	-0.22	2.30
1.40	1.19	-0.09	2.62	1.26	-0.23	2.27
1.42	1.20	-0.14	2.85	1.27	-0.23	2.26

Source: (Miyamura et al. 1993)

At high engine speeds, the spring surge phenomenon may reduce the spring effective force and allow the follower to leave the cam. The spring surge occurs due to a resonance condition between the valve spring natural frequency and the frequency generated by the action of the cam against its follower, (Y. WANG 2007). The valve spring natural frequency, f in [Hz] can be calculated using Equation 149, (Budynas and Nisbett 2011).

$$f = \frac{1}{2} \sqrt{\frac{k \cdot g}{W}} \quad (149)$$

Where the g is the gravity in $[m/s^2]$ and the W is the spring active part weight calculated using Equation 150.

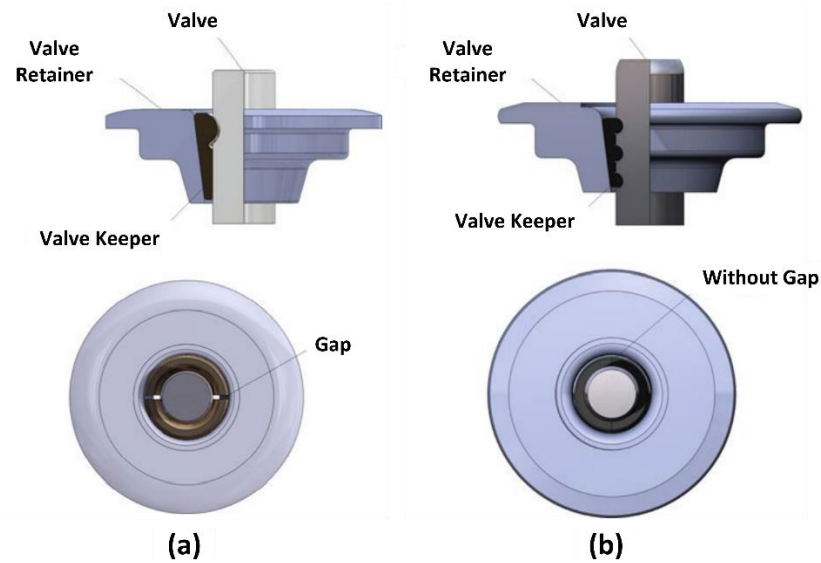
$$W = \frac{\pi^2 \cdot d^2 \cdot D \cdot N_a \cdot \gamma}{4} \quad (150)$$

Where the γ is the specific weight in $[N/m^3]$. The fundamental critical frequency should be greater than 11 times. However, a ratio as low as 9 could be used with follower dynamics and a smooth acceleration curve. (Y. WANG 2007).

2.3.13.4. Valve Keeper

The valve keepers, also known as valve locks, valve keys, or cotters, are fitted on the valve stem grooves. The valve keeper function is to secure the valve stem to the valve spring retainer using the spring load. Currently, the valve key commonly used are the single-bead and the three-bead as shown in Figure 106. The single-bead valve keepers are designed to not butt against each other leaving a small gap between the keepers at both ends, see Figure 106. Thus, it results in a circumferential contact with the valve stem. In general, the single-bead can be used when little or no valve rotation is required. On the other hand, the three-bead valve keepers are designed mainly to improve the valve rotation capabilities compared to the single-bead. A higher valve rotation can improve the valve seat cleaning which in turn contributes to a larger maintenance interval, (Y. WANG 2007).

Figure 106 – Valve keepers single-bead (a) and three-bead (b)



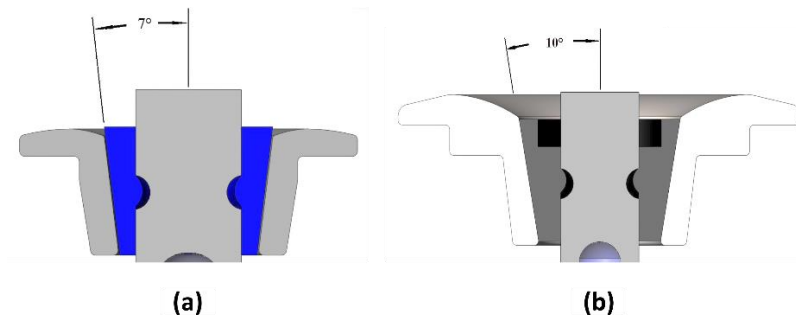
Source: Adapted from (F. SCHÄFER 2017)

Typical materials for the valve keepers are the hardenable steel or low-carbon steel such as SAE 1010. Although these materials can be machined, frequently they are cold formed and then carbonized or carbonitrided with a layer depth of 0.2. The typical surface hardness for the valve keepers is about 58 HRc, (Y. WANG 2007).

2.3.13.5. Valve Retainer

The mate component of the valve keepers is the valve retainers or valve plate. The valve retainer function is to secure the valve stem through the valve keepers. The valve retainer is commonly manufactured with the cone angle of 7 or 10 degrees as shown in Figure 107, however different angles have been applied like 6 and 8 (super 7) degrees. The valve retainer of 7 degrees is normally applied on OEM (Original Equipment Manufacturer) engines in which the spring load is relatively low. On the other hand, the 10 degrees valve retainer is applied in engines with high spring load like motorsport engines. Due to a higher spring load, the valve retainer of 10 degrees is preferably used because it is easier to be removed, (Ferrea 2021).

Figure 107 – Valve retainer 7 degrees (a) and 10 degrees (b)



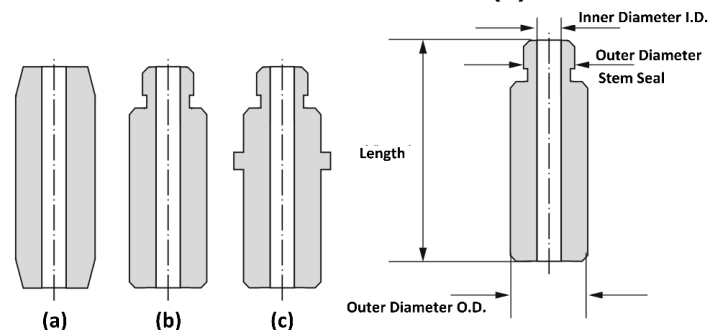
Source: (Ferrea 2021)

For the valve retainer material, typically is used the SAE 1010, 1018, or the 1215. Although the low-carbon steels are usually machined, often it has been cold formed and then carbonized or carbonitrided with a layer of 0.2 thickness. The surface hardness for this application is about 55 HRc, (Y. WANG 2007).

2.3.13.6. Valve Guide

The valve guide, as its name imply, guides the valve coaxially to the valve seat insert and the valve actuation system. Furthermore, it serves as axial bearings for the valve stem and heat sinks to cool the valves. Typically, the valve guides are hollow metallic cylinders, although other materials such as ceramic and ceramic-coated metals have been used on experimental studies, (Y. WANG 2007). Figure 108 presents the common types of the valve guides and the nomenclature used to refer to its dimensions.

Figure 108 – Valve guide smooth bore (a), machined cold end (b) and flanged machined cold end (c)

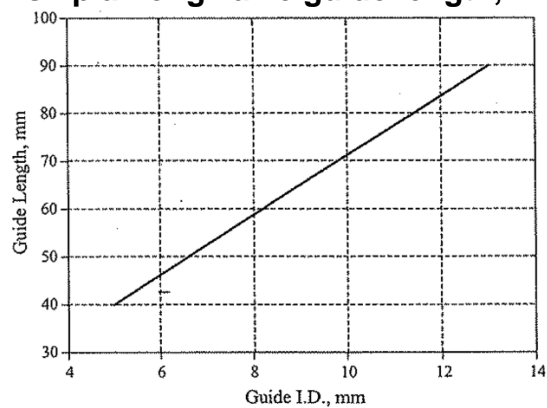


Source: Adapted from (F. SCHÄFER 2017)

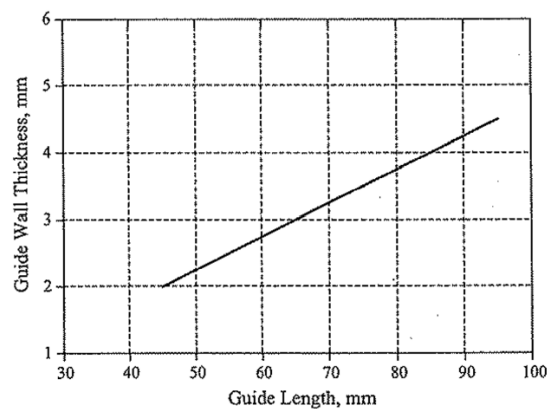
The valve guide length should be long enough to provide adequate support for the valve and to transfer heat away from the valve. For the exhaust valve guides, it is

advisable to avoid its protrusion into the hot exhaust gas stream. The hot exhaust gas stream will reduce the valve guide ability to serve as a heat sink and will increase scuffing tendencies. As an overall reference, the valve guide length should be about seven times the valve stem diameter. Figure 109 presents the typical relationship of the valve guide length, the valve guide I.D. and wall thickness according to the function and tooling limitations, (Y. WANG 2007).

Figure 109 – Relationship among valve guide length, I.D and wall thickness



(a)



(b)

Source: (Y. WANG 2007)

The diametric clearance between the valve stem and the valve guide is typically 0.02 – 0.05 mm for intake valves and 0.04 – 0.07 mm for the exhaust valves. For the valve guide assembly in the cylinder head, it is recommended an interference fit about 0.04 – 0.08 mm for aluminum and 0.02 – 0.08 mm for cast iron cylinder heads, (Y. WANG 2007).

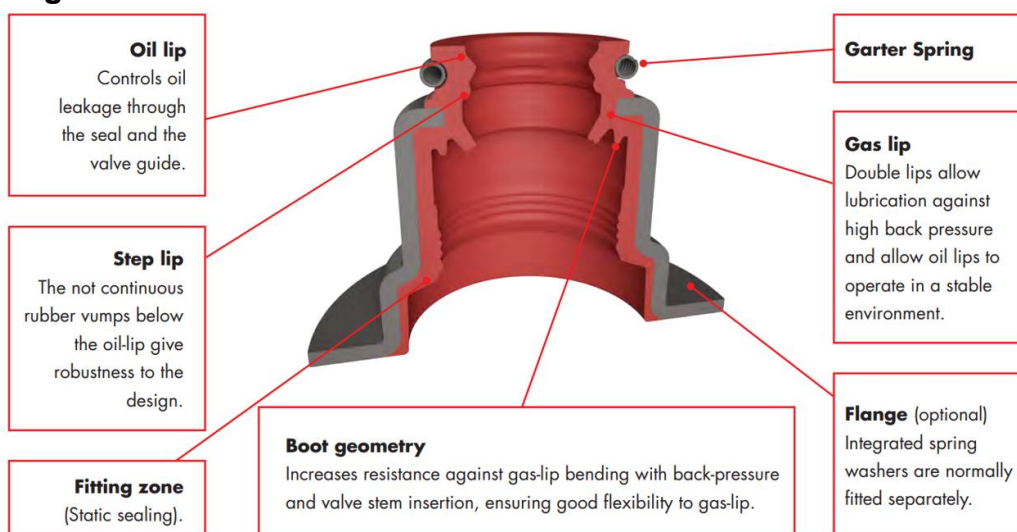
The valve guides are typically made from grey cast iron, brass, and sintered materials. The sliding, thermal, and wear characteristics are optimized by using special alloying components. The valve guide materials available from (Mahle 2015) are:

- **B** – CuZnAl alloy with good wear resistance as well as good fatigue and corrosion resistance. For applications with medium loads;
- **B1** – CuSn alloy with the addition of phosphorus for increased wear resistance. Suitable for applications with high loads;
- **G1** – Grey cast iron alloy with perlitic microstructure and good wear resistance. For applications with normal loads;
- **G2** – Grey cast iron alloy with perlitic microstructure and increased phosphorus content. The reticular distribution in the material structure results in higher wear resistance and improved operation under marginal lubrication. Suitable for applications with high loads;
- **CN** – CuNi alloy with increased hardness and thermal conductivity as well as wear and abrasion resistance. For high strength even in heavy-duty applications;
- **SM** – Sintered metal alloy with high mechanical stability, which is even maintained at extremely high temperatures. Developed for high-performance engines.

2.3.13.7. Valve Stem Seal

The valve stem seal is designed to allow a small amount of oil lubricant to pass through its lips in order to lubricate the valve stem. In a case of an excessive oil passes through the lip of the seal, the engine oil consumption and emissions levels will be worsened, and coke builds up on the valve which could lead to power loss or even engine failure. On the other hand, in case of oil lubricant shortage passing through the valve stem seal lip, the valve will not receive enough lubrication and the valve will scuff which can cause it to seize. Ideally, the oil metering rate should lie between these conditions. A typical oil metering rate down the guide by the stem seal is in range of 0.01 – 0.2 cc/10 hours, (SKF 2020; Y. WANG 2007) Figure 110 presents the technical features and nomenclature of a valve stem seal.

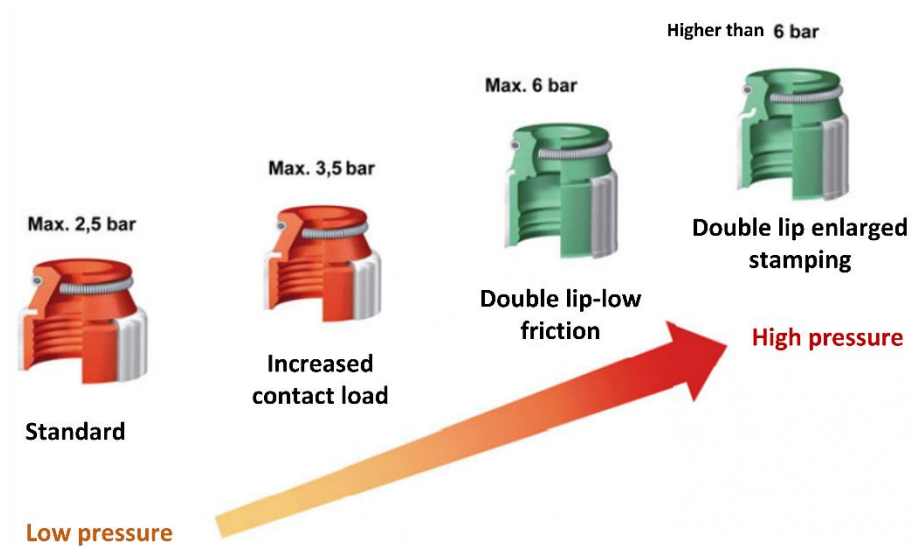
Figure 110 – Valve stem seal technical features and nomenclature



Source: (Corteco 2019)

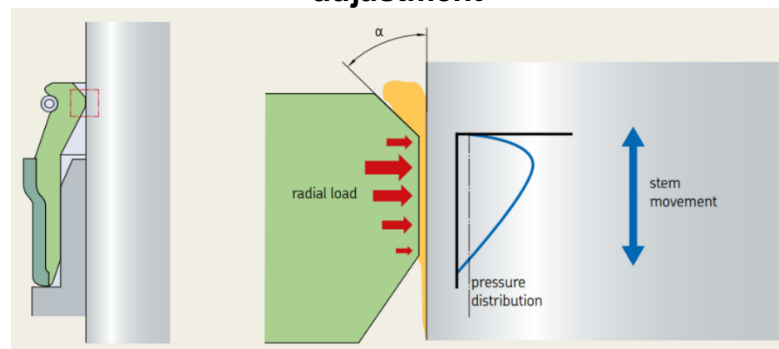
The valve stem seals can be characterized as an incorporated spring seat or as non-incorporated spring seat. On both designs, the sealing material is vulcanized onto a sheet metal carrier. The contact pressure of the sealing lip against the valve stem is set not only by the geometry of the sealing lip but also by a spiral spring arranged on the circumference. In addition to the movement profile and the surface quality of the valve stem, the contact pressure controls the leakage rate and is therefore a key factor influencing wear in this tribological system. Efforts to minimize the overall oil consumption of internal combustion engines have also led to more difficult running conditions. Furthermore, the insufficient lubrication is a direct consequence supercharging with downsizing engines. The pressure drops between the port side and the seal control chamber increases. Hence, most of the oil can be pushed back into the control room and is therefore no longer available in sufficient quantity for valve stem lubrication. The manufacturers of valve stem seals have developed several solutions aiming to solve this problem with different lip pressure, geometry, and number of lips, (SKF 2020; MAHLE 2013). Figure 111 presents the different valve stem seal lip-pressure designs and Figure 112 illustrates the valve stem seal contact pressure profile for the oil metering rate adjustment.

Figure 111 – Lip pressure of different valve steam seal designs



Source: (SKF 2020)

Figure 112 – Valve stem seal contact pressure profile for the oil metering rate adjustment

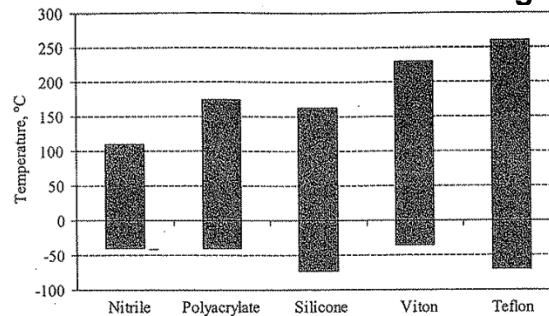


Source: (SKF 2020)

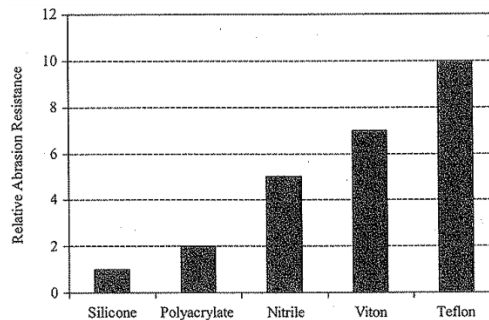
The valve stem seal material is chosen depending on its application. The valve stem seal can be made of nitrile, polyacrylate, Fluoroelastomer (Viton or FKM rubber), silicone, or polytetrafluoroethylene (nylon or Teflon PTFE). The Nitrile is the most commonly sealing material and is one of the least expensive materials used for intake valve seals. A step up from nitrile is polyacrylate which has a working temperature range higher than nitrile and it can withstand extreme pressure lubricants. For a wide working temperature range and low-friction application, the silicone seals are well suited. However, it has poor compatibility with oxidized oils, some extreme pressure additives, and abrasive contaminants. Nylon is a hard material with a wide working temperature range and impervious to oil. On the other hand, it can melt if the engine overheats. The Fluoroelastomer (Viton or FKM rubber) costs roughly ten times the Nitrile seals but it has a wider working temperature range making them some of the best high-temperature seals available. The Teflon is the highest rated positive seal

material. The Teflon has the highest abrasion wear resistance and the lowest friction. However, the Teflon is a hard material and hence, it cannot handle as much run out between the valve stem and the valve guide as much more flexible seal material. Furthermore, the Teflon is the most expensive material, (Y. WANG 2007). Figure 113 presents the applicable temperature ranges and the abrasive wear resistance ranking for several stem seals materials.

Figure 113 – Valve stem seal materials applicable temperature ranges and the abrasive wear resistance ranking



(a)



(b)

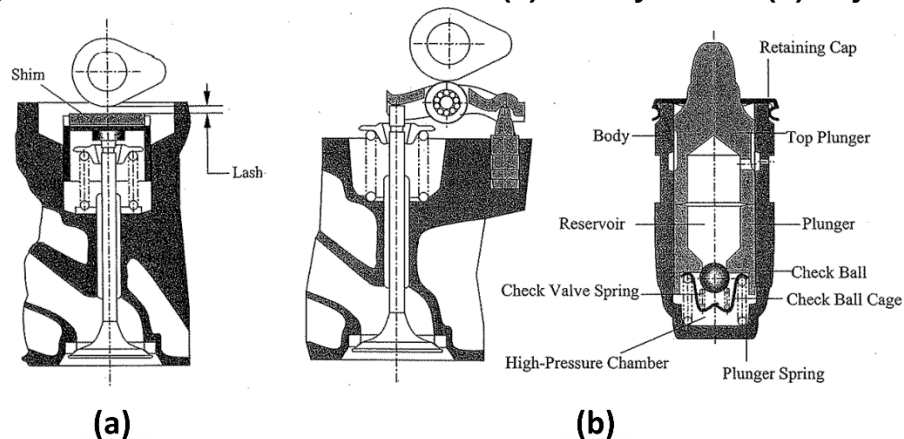
Source: (Y. WANG 2007)

2.3.13.8. Valve Lash Adjuster

The lash is the gap or space in a valvetrain system used to compensate manufacturing variation, assembly, wear, and thermal expansion aiming a proper valve sealing and timing actuation. In case of a valvetrain system without lash or an automatic compensation mechanism, the valve could be held open and lose its sealing function. The valvetrain lash has a direct effect in the engine performance. An insufficient lash will not allow the valve to close, and an excessive lash can lead to higher seating velocities and valve closing noise. There are two types of lash compensation methods, the mechanical or manual and the hydraulic or automatic. For

the mechanical method, a shim usually is used to establish the system lash typically about 0.2 – 0.75mm. The mechanical lash adjustment presents advantages from being lighter and no oil supply is required. On the other hand, it presents disadvantages of individual valve adjustment during an engine manufacturing and maintenance, lash values changed due to different engine running conditions e engine wear. The hydraulic lash adjusters quietly transfer the rotary motion of the cam to the valve while maintaining zero lash. The advantages of the hydraulic lash adjuster over the mechanical are that no assembly lash adjustments are required, no valvetrain noise due to lash and more accurate valve timing. On the other hand, the disadvantages are that an oil supply is required, and the system is heavier, (Y. WANG 2007). Figure 114 illustrates the mechanical (a) and the hydraulic (b) lash adjust mechanism typically used in lately engines.

Figure 114 – Valve lash mechanical (a) and hydraulic (b) adjuster

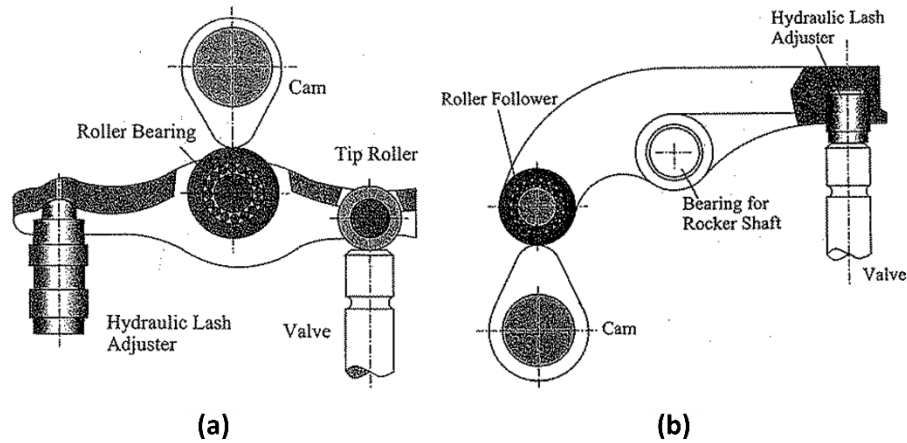


Source: (Y. WANG 2007)

2.3.13.9. Rocker Arm

The rocker arm is a component used to transfer the rotation motion of the camshaft lobe to the reciprocating motion of the valves. The typical rocker arm configurations can be divided into two groups based on the pivot and cam locations as end-pivot with the cam above the rocker arm and center-pivot with the cam below the rocker arm, as shown in Figure 115, (Y. WANG 2007).

Figure 115 – Rocker arm end-pivot (a) and center-pivot (b)



Source: (WANG, 2007)

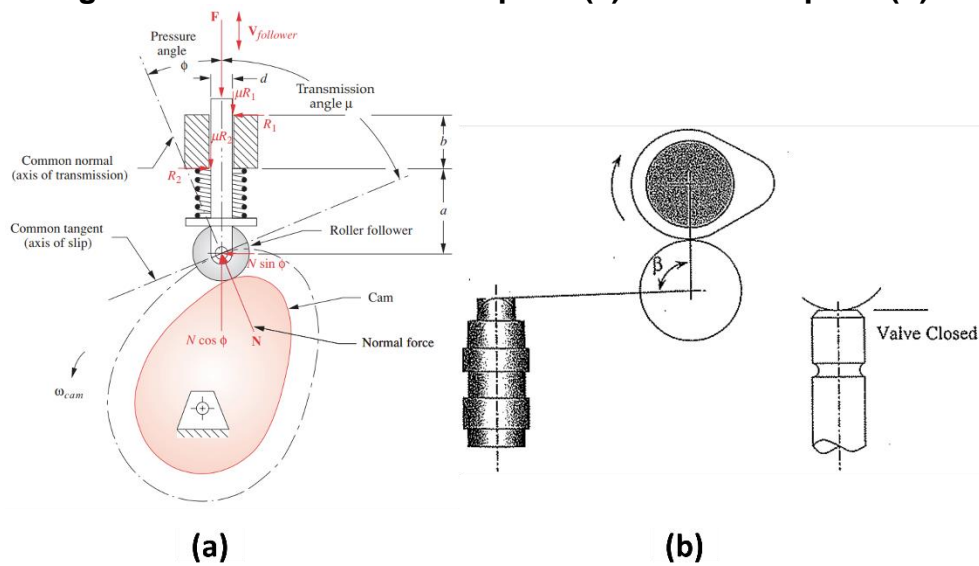
The rocker arm design begins with the valvetrain system geometry and package. The most critical parameters in the rocker arm design are the rocker arm ratio, the camshaft base circle radius, and the roller diameter. The rocker arm ratio is calculated according Equation 151.

$$RR = \frac{R_1}{R_2} \quad (151)$$

Where the R_1 is the distance from the lash adjuster pivot point to the valve tip contact point in [mm], and the R_2 is the distance from the lash adjuster pivot point to the cam-follower contact point in [mm]. It is worth to point out that the rocker ratio is a not constant value due to the valve tip contact location changes. The rocker arm ratios range from 1.2 to 1.9 for center-pivot design and from 1.5 to 2.0 for end-pivot rocker arms. A downside of the rocker arm approach is that any camshaft lobe manufacturing error could be magnified on the valve lift, (WANG, 2007).

The cam base circle radius and roller diameter, as well as the position between them two can affect the pressure angle, ϕ . The pressure angle is the angle, at any point, between the cam lift normal vector and the direction of the follower motion. The pressure angle should be maintained as minimum as possible which the value of 30 degrees is a general arbitrary limit for all followers. Furthermore, the angle of the centerlines of cam/roller and roller/pivot, β , is recommended 90° when the valve is half open or about $95 - 105$ degrees when the valve is at closed position, (Y. WANG 2007; Rothbart 2004). The

Figure 116 – Rocker arm end-pivot (a) and center-pivot (b)



Source: (Norton 2012; Y. WANG 2007)

The typical rocker arm materials are SAE 1008, 1010, 4140 and 8620 or 16MnCr5 and often are carburized or carbonitrided with a 0.375mm layer depth for a surface hardness of 90HR. Other materials such as 15-5 PH stainless steels are also used. Studies using the aluminum alloys have been carried out due to its lightweight characteristic, however due to material strength requirements the aluminum alloy is not a best choice. The roller bearing, including the outer roller, needle, and axle are made of SAE 52100 or equivalent, with surface hardness of 60 HRC, (Y. WANG 2007).

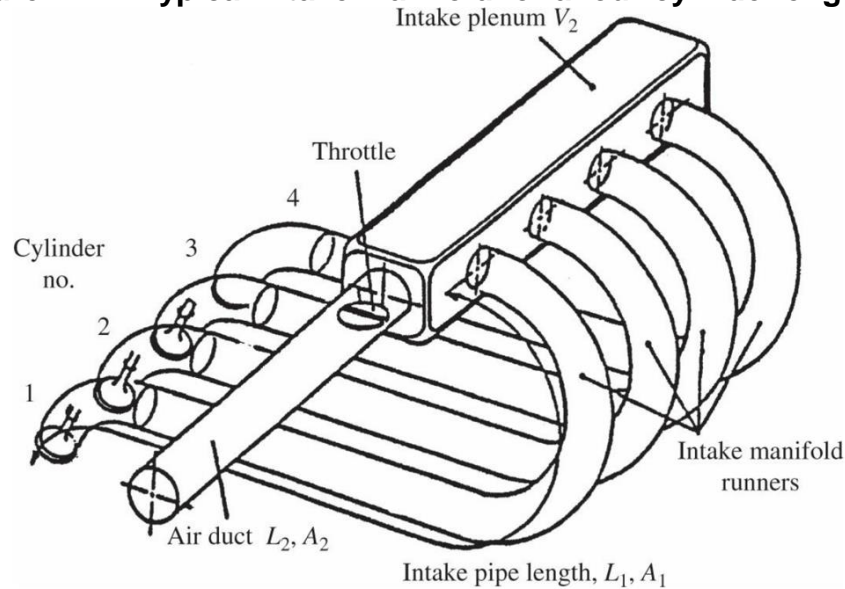
2.3.14. Intake Manifold

The engine intake manifold is responsible for receive the air supplied from inlet air inlet system, storage it and supplied it for each cylinder according to the valve timings. The intake manifold consists of the inlet air duct, the throttle valve, the plenum, and the manifold runners. A well-designed intake manifold should combine the plenum volume, the runners length and cross section area to maximize the air supplied to each cylinder, (Blair 1999).

Figure 117 presents a typical intake manifold for a four-cylinder engine. It shows the inlet air duct leading to larger plenum volume passing through the throttle, which feeds air to cylinders via the runners, ports, and valves. This intake system can be tuned, basically, in two ways: one, based on the length of the flow path from plenum to the intake valve which can provide additional airflow at a required engine speed; and

the other based on the air duct and plenum geometry using it as a Helmholtz resonator in order to enhance airflow at mid-engine-speeds, (HEYWOOD 2018).

Figure 117 – Typical intake manifold for a four-cylinder engine



Source: (HEYWOOD, 2018)

The airflow inside the intake manifold is subject to gas-dynamic effects. When the intake valve opens and the piston starts to move down, the pressure in the intake port falls and a rarefaction wave travels towards the plenum at the speed of sound. As this wave reaches the intake plenum it faces an impedance mismatch and thus, a compression wave, which increases the pressure, moves back toward the valve enabling an additional air to be supplied to the engine. The instantaneous intake port pressure during the early stages of the intake process is governed by the valve flow area and the instantaneous piston speed. Thereafter, the wave resonances action dominates the process. The wave intensity that follows the intake valve opening is defined by the depth of the early depression caused by the piston movement. Thus, a favorable pressure ratio between the intake port and the cylinder can be achieved by the rapid downward piston motion which reduce the in-cylinder pressure and by the wave action that increases the instantaneous pressure in the port. It is worth to point out that the wave action only makes difference if at least, but no more than, one complete oscillation of the pressure at its resonant frequency occur while the intake valve is open. Furthermore, in case of multi-cylinder engines, the dynamic behavior of one runner can affect the others engine runners. Similar phenomenon happens in the exhaust port. However, due to the higher temperature gradient throughout the exhaust

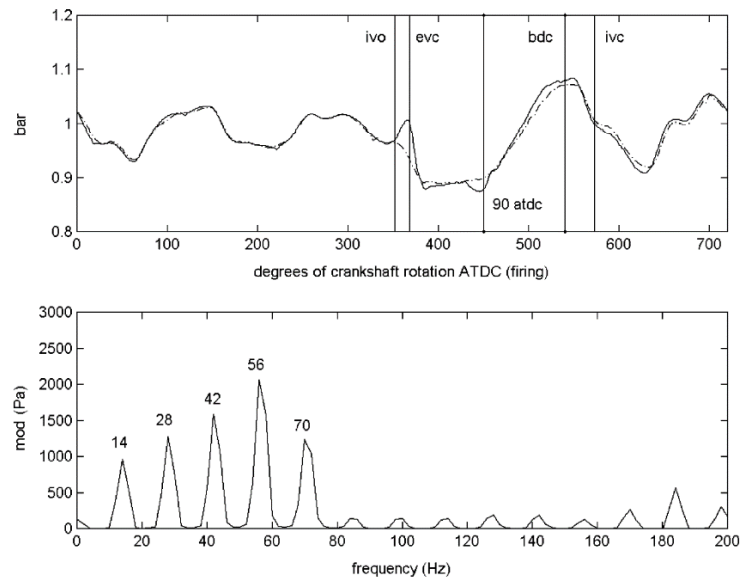
manifold, the speed of sound changes substantially and hence the wave frequency, (Harrison and Stanev 2004; Smith and Morrison 1972). The wave pulsation frequency inside the runners and ports can be evaluated as a standing wave in an open-closed pipe and it can be calculated using Equation 152.

$$f_{run} = \frac{n_{modes} \cdot a}{4 \cdot L_1} \quad (152)$$

Where the f_{run} is the resonant frequency in [Hz], the n_{modes} corresponds to odd numbers of quarter wavelengths, the a is the speed of sound in [m/s] and the L_1 is the runner plus port length in [m], (HARRISON; STANEV, 2004; SMITH; MORRISON, 1972). In order to take advantage from the gas-dynamic effects in the intake pipe, the plenum volume should be about from 1.5 to 3.0 times the engine displacement, (Trzesniowski 2010).

One method utilized to evaluate the dominant frequency of the intake runners and ports is perform a FFT (Fast Fourier Transform) of the intake instantaneous pressure signals. Figure 118 illustrates a frequency spectrum from the intake instantaneous pressure signal in which the dominant frequency on the intake runner was the fourth harmonic. This method can be applied in an engine computational model for several engine speeds in order to predict in which engine running condition the intake pipe would be tuned, (Harrison and Stanev 2004).

Figure 118 – Intake instantaneous pressure signal frequency spectrum (1690 rpm)



Source: (Harrison and Stanev 2004)

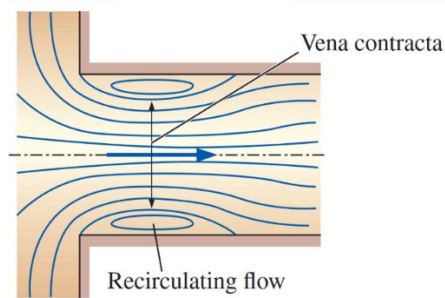
The plenum used as Helmholtz resonator is another way to improve the engine volumetric efficiency and attenuate the intake system noise. The air dynamic behavior inside the intake manifold leads to a pressure oscillation at a frequency calculated by Equation 153. Thus, if the plenum geometry leads to a frequency that match the air pulsating frequency of the runners, a higher plenum pressure can generate an extra air to be pushed into each cylinder throughout the intake stroke, (HEYWOOD 2018).

$$f_{Hel} = \frac{a}{2 \cdot \pi} \sqrt{\frac{A_2}{L_2 \cdot V_2}} \quad (153)$$

Where the f_{Hel} is the Helmholtz frequency in [Hz], the A_2 is the air duct cross sectional area in [m²], the L_2 is the air duct length in [m], and the V_2 is the plenum volume in [m³].

The junction among the runners and the plenum should be designed in such way in order to avoid a sharp-edge at the pipe inlet. A sharp-edge pipe inlet generates a flow contraction at the pipe entrance called Vena contracta which leads to a lower flow coefficient of discharge as shown in Figure 119, (ÇENGEL and Cimbala 2006).

Figure 119 – Flow contraction associated to a sharp-edge pipe inlet

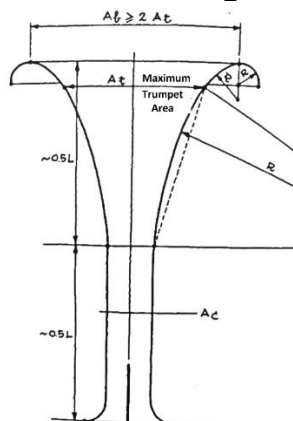


Source: (ÇENGEL and Cimbala 2006)

The round shape of a pipe inlet is usually called bellmouth or trumpet. Several bellmouth designs have been developed and tested aiming the best flow behavior. Figure 120 the final bellmouth design proposed by (di Giacomo A. Pignone 2003). From his work, the minimum enlarged area of the pipe entrance, A_t in [m²], can be calculated using Equation 154 which takes to account the piston mean speed, S_p in [m/s], the piston area, A_p in [m²], a Mach Index IM_t and the speed of sound a in [m/s]. The Mach index value of 0.125 achieved the best flow behavior according to (DI GIACOMO A. PIGNONE, 2003). For a smooth airflow through the bellmouth, the trumpet inlet area, A_b , should be at least twice the minimum inlet area A_t and the transition from the entrance to the pipe diameter should be designed with a larger radius. Equation 154 can be also used to calculate the throttle valve diameter, (DI GIACOMO A. PIGNONE, 2003).

$$A_t = \frac{S_p \cdot A_p}{IM_t \cdot a} \quad (154)$$

Figure 120 – Bellmouth design for a pipe inlet



Source: (DI GIACOMO A. PIGNONE, 2003)

2.3.15. Bolts and Clamping Force

A hypothetical bolted assembly of crankcase, the cylinder head, and the gasket is shown in Figure 121. There are three members in the grip of the bolt, and they act as compression springs in series. The combined stiffness of the joint, k_c in [N/m], is calculated using Equation 155.

$$\frac{1}{k_c} = \frac{1}{k_1} + \frac{1}{k_2} + \frac{1}{k_g} \quad (155)$$

Where the k_1 and the k_2 are the stiffness of the crankcase and the cylinder head in [N/m], respectively, and the k_g is the gasket stiffness in [N/m], (BHANDARI 2010).

As the machine element stiffness, k in [N/mm], is the load required to produce a unit deflection, the bolt stiffness, k_b in [N/mm²], can be calculated according to Equation 156.

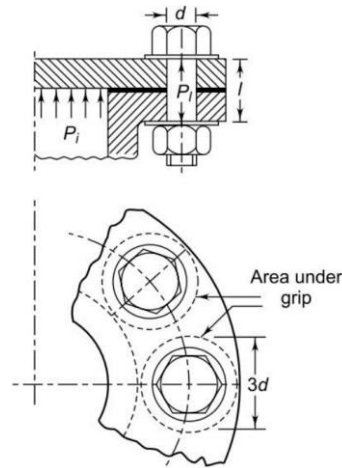
$$k = \frac{A \cdot E}{l} \therefore k_b = \left(\frac{\pi \cdot d_b^2}{4} \right) \frac{E}{l} \quad (156)$$

Where the A is the area in which the load is applied in [mm²], the E is the material Young's module in [N/mm²], the d_b is the bolt diameter in [mm], and the l is the total thickness of the parts to be held together by the bolt, also called effective length, in [mm], (BHANDARI, 2010).

For the k_1 , k_2 and k_g calculation, it is assumed a hollow circular area of $(3 \cdot d_b)$ and (d_b) as the outer and inner diameters respectively under the bolt grip as shown in Figure 121. Thus, the area under the bolt grip, A_{ubg} in [mm²] can be calculated using Equation 157, (BHANDARI, 2010).

$$A_{ubg} = \frac{\pi}{4} \cdot [(3 \cdot d_b)^2 - d_b^2] = 2 \cdot \pi \cdot d_b^2 \quad (157)$$

Figure 121 – Joint bolted assembly



Source: (BHANDARI, 2010)

The k_1 , k_2 and k_g can be calculated Equation 158.

$$k = \frac{2 \cdot \pi \cdot d_b^2 \cdot E}{t} \quad (158)$$

Where t is the member under compression thickness in [mm].

When the preload, P_l in [N], is applied to the joint, the bolt is elongated by an amount δ_b in [mm], and the members of the joint are compressed by an amount δ_c in [mm]. Considering the stresses within the elastic limit, the bolt and the joint deflection are calculated using Equation 159 and Equation 160, respectively.

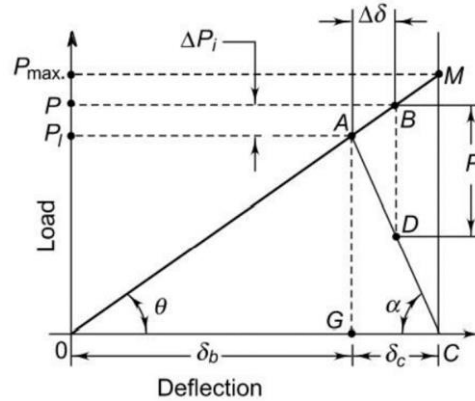
$$\delta_b = \frac{P_l}{k_b} \quad (159)$$

$$\delta_c = \frac{P_l}{k_c} \quad (160)$$

The joint diagram, as shown in Figure 122, is used to evaluate the bolt and the joint members deformation under load. The segments \overline{OA} and \overline{CA} represent the bolt and joint members elongation respectively due the applied preload. The slope of the segment \overline{CA} is negative because it indicates compression. The bolted assembly during service is further subjected to an external load, P_i in [N], due to the internal pressure inside the cylinder. The bolt is further elongated by amount of $(\Delta\delta)$ by the increased (ΔP_i) load further the preload represented by the segment \overline{AB} . On the other hand, the joint members are relieved by amount of $(\Delta\delta)$ corresponding to the load reduction

$(P_i - \Delta P_i)$ which is represented by the segment \overline{AD} . The maximum external load allowable is limited up to the joint members be totally relieved, (Shoberg 2018).

Figure 122 – Joint diagram for bolted assembly



Source: (BHANDARI, 2010).

From the joint diagram Equation 161 and Equation 162 can be obtained.

$$k_b = \frac{\Delta P_i}{\Delta \delta} \quad (161)$$

$$k_c = \frac{(P_i - \Delta P_i)}{\Delta \delta} \quad (162)$$

Dividing Equation 161 to Equation 162, Equation 163 is obtained.

$$\Delta P_i = P_i \cdot \left[\frac{k_b}{k_b + k_c} \right] \quad (163)$$

The resultant load, P in [N], on the bolt is given by Equation 164.

$$P = P_i + \Delta P_i = P_i + P_i \cdot \left[\frac{1}{1 + \left(\frac{k_c}{k_b} \right)} \right] \quad (164)$$

In order to evaluate the bolted joint assembly in terms of stress, the loads applied on the bolted joint are divided by the area in which the load is applied. The maximum and minimum stress are calculated according Equation 165 and Equation 166, respectively, (BHANDARI, 2010).

$$\sigma_{max.} = \frac{P_l}{A} + \frac{\Delta P_i}{A} \quad (165)$$

$$\sigma_{min.} = \frac{P_l}{A} \quad (166)$$

The mean (σ_m) and alternating (σ_a) components of stresses, in [MPa], are given by Equation 167 and Equation 168, respectively.

$$\sigma_m = \frac{P_l}{A} + \frac{\Delta P_i}{2.A} \quad (167)$$

$$\sigma_a = \frac{P_l}{2.A} \quad (168)$$

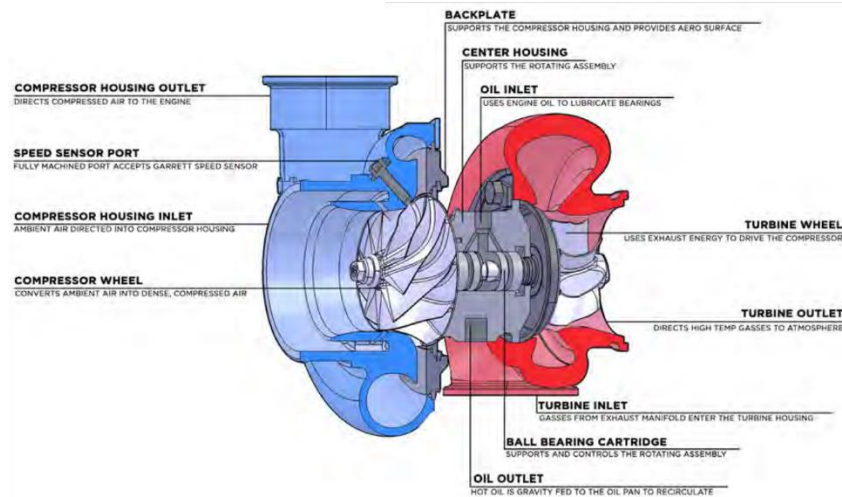
Replacing Equation 168 in Equation 167, Equation 169 is obtained, (BHANDARI, 2010).

$$\sigma_m = \frac{P_l}{A} + \sigma_a \quad (169)$$

2.4. Turbocharger

The turbocharger is responsible to take the thermal energy from the engine exhaust gases and converted into rotational kinetic energy through the turbine, which drive the compressor using a shaft to compress the engine inlet air. The turbocharger consists of a Central Housing and Rotating Assembly (CHRA), a turbine, a compressor, and an actuator to control it. The compressor and the turbine are fitted on the CHRA and connected through a shaft, (SANTOS 2018). Figure 123 illustrates a typical turbocharger assembly.

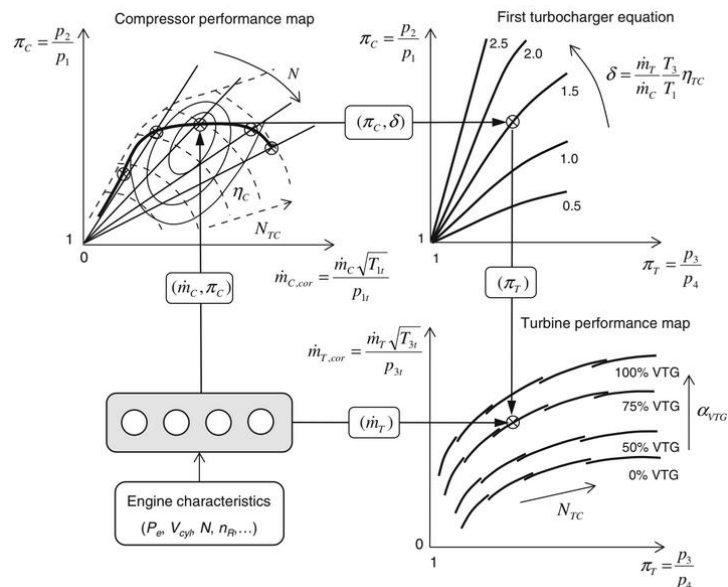
Figure 123 – Turbocharger assembly



Source: Adapted from (SANTOS, 2018)

The turbo-matching is the procedure to size a turbocharger according to its application by means of some engine information and the turbocharger performance maps. Figure 124 presents a turbo-matching methodology developed by (H.N. SCHÄFER 2015). In this methodology, it is possible to use some base engine parameters such as the maximum power required, the engine displacement volume, maximum engine speed among others to perform a turbo-matching.

Figure 124 – Turbo-matching methodology



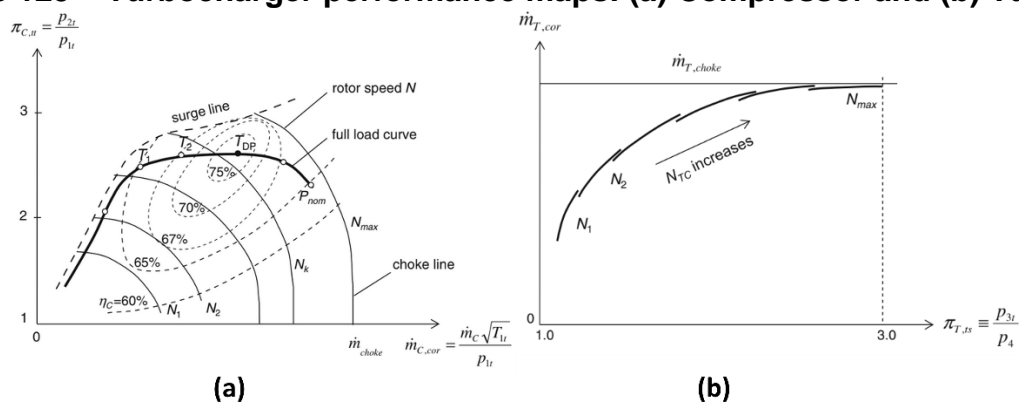
Source: (SCHÄFER, 2015)

The turbocharger performance maps are charts of the compressor and the turbine which describe the main performance characteristics from each one as shown in Figure 125. These performance maps are plotted related to corrected mass flow and

pressure ratio of the fluid passing through the turbocharger, which for the compressor side is a compression ratio and for the turbine is an expansion ratio. The compressor map indicates the compressor surge line, the choke line, the rotor speed limit, and the efficiency islands. On the other hand, the turbine map is simpler than the compressor map which is presented the rotor speed limit as well as the mass flow limit, (SANTOS, 2018).

The surge line is the most left boundary on the compressor map and represents a region of flow instability. This region is characterized by pressure fluctuation, and it must be avoided during the turbocharger operation otherwise a continued operation in this region could lead to the turbocharger failure. On most right side is the choke line boundary. The choke line establishes the maximum mass flow rate capability of the compressor or turbine. The turbo speed is commonly measured in rpm and it is used to monitoring the occurrence of a turbo over-speed condition. The efficiency island are concentric regions that represent the compressor efficiency at any point on the map. The engine operation points on the compressor map are illustrated by solid line called full load curve in Figure 125 (a), (SCHÄFER, 2015).

Figure 125 – Turbocharger performance maps: (a) Compressor and (b) Turbine



Source: (SCHÄFER, 2015)

The turbocharger requires a minimum amount of energy to overcome the system inertia and start to work. The delayed time that the turbocharger requires to achieve 90% of the maximum torque from idle condition is called turbo-lag. The engines fitted with larger turbochargers, mainly sized for high engine speeds, present a higher turbo-lag, which can lead in lower engine torque output at lower engine rpm, (Hiereth and Prenninger 2003).

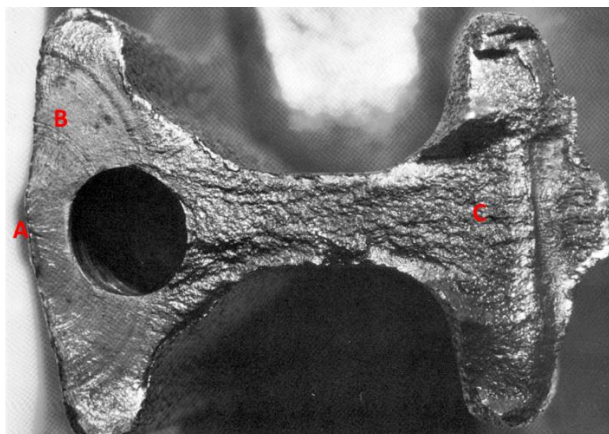
2.5. Fatigue Analysis

A machine part that fails statically usually develop a very larger deflection due to excessive load beyond its yield strength and it is replaced before fracture occurs. Thus, many static failures give a visible warning in advance. However, this warning is not usually given by dynamic fails. Frequently, machine members are found to have failed under action of fluctuating stress even with the maximum stresses below the ultimate tensile stress and the yield stress. The main characteristic of these failures is that the stresses have been repeatedly applied on the component during a very large number of times. Therefore, this type of failure is called fatigue failure, (Budynas and Nisbett 2011; ASM 1996).

The fatigue failure occurs due to a material crack formation and propagation. Typically, the fatigue crack formation initiates at a material discontinuity where the cyclic stress is a maximum. Furthermore, the fatigue crack initiation could be accelerated due to residual stress in the component, elevated component temperature, temperature cycling, a corrosive environment and high-frequency cycling, (Budynas and Nisbett 2011).

Figure 126 illustrates a fatigue fracture of a forged connecting rod. The fatigue crack initiated at the forging flash line, point A. The fatigue crack propagated halfway around the oil hole, as showed by the “beach marks” on the region B and then a final fast fracture occurred on region C, (BUDYNAS; NISBETT, 2011).

Figure 126 – Fatigue fracture surface of a forged connecting rod of AISI 8640 steel



Source: Adapted from (BUDYNAS; NISBETT, 2011)

A new machine part that will be subjected to fluctuating loads must be designed against fatigue failure. The main three fatigue-life methods used to design and analyze a component are the stress-life method, the strain-life method, and the linear-elastic fracture mechanism method. The objective of these methods is to predict the component life in number of cycles, N_c , for a specific level of loading. A component life of $1 \leq N_c \leq 10^3$ is usually classified as low-cycle fatigue whereas beyond that, ($N_c > 10^3$), is considered high-cycle fatigue, (ASM 1996).

The stress-life method requires only the component stresses levels to be performed. Furthermore, it is the most traditional method, it is easiest to implement for a wide range of design applications, there is an ample supporting data, and it represents high-cycle applications adequately. However, the stress-life method is not suitable for low-cycle applications, (BUDYNAS; NISBETT, 2011).

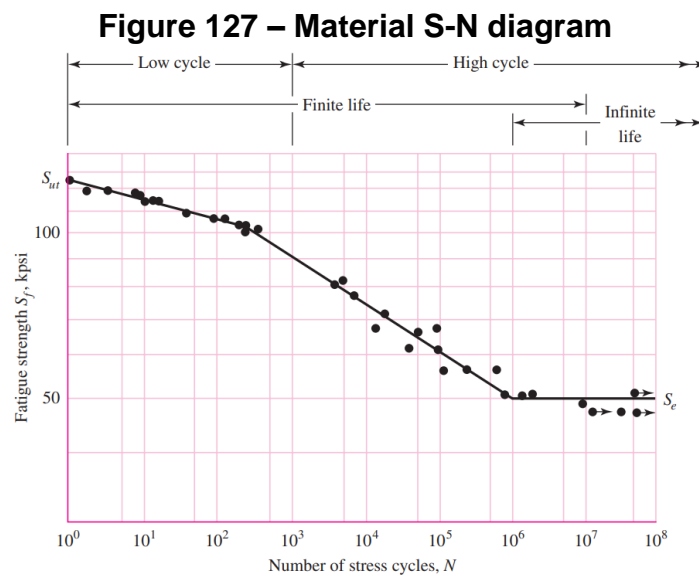
The stress-life method will be used to evaluate the components developed in this work. Therefore, only this method will be exploit in detail the following paragraphs.

2.5.1. S-N Diagrams

In order to determine the material strength under the action of the fatigue loads, specimens are manufactured and subjected to specified magnitude repeated loads while the cycles are counted up to the component destruction. As a result, it is created the strength to cycles diagram also known as S-N diagrams, as shown in Figure 127, (BUDYNAS; NISBETT, 2011).

The steels presented a well-defined knee on the high-cycle region. The strength corresponding to this knee is called endurance limit, S_e , and beyond this knee failure

will not occur regardless the number of cycles. It is worth to point out that nonferrous metals and alloys do not present a well-defined endurance limit and usually the endurance limit is reported at a specific number of cycles. For aluminum usually is considered $N_c = 5 \cdot 10^8$. The distinction between finite and infinite life region is not clear excepted for a specific material, although, it lies somewhere between 10^6 and 10^7 cycles, (Budynas and Nisbett 2011; Juvinall and Marshek). The S-N diagrams could be available in atlas books as made by (Boyer 1983).



Source: (Budynas and Nisbett 2011)

2.5.2. Endurance Limit and Fatigue Strength

The endurance limit tests are performed in material laboratories using fatigue test machines. For steels, based on several S-N diagrams, the uncorrected endurance limit, S'_e in [MPa], can be calculated using Equation 170, (BUDYNAS; NISBETT, 2011).

$$S'_e = 0,5 \cdot S_{ut} \quad (170)$$

As the material is normally submitted to working conditions different of the laboratory environment in which the endurance limit is obtained, it is required to correct the uncorrected endurance limit by several factors. The corrected endurance limit, S_e in [MPa], can be calculated using Equation 171, (BUDYNAS; NISBETT, 2011).

$$S_e = k_{sur} \cdot k_{siz} \cdot k_{load} \cdot k_{temp} \cdot k_{rel} \cdot k_{mis} \cdot S'_e \quad (171)$$

Where the k_{sur} is the surface condition modification factor, the k_{siz} is the size modification factor, the k_{load} is the load modification factor, the k_{temp} is the temperature modification factor, the k_{rel} is the reliability factor, and the k_{mis} is the miscellaneous factor.

The k_{sur} factor depends on the surface finish quality of the component and on the material ultimate strength. The k_{sur} factor can be calculated using Equation 172, (BUDYNAS; NISBETT, 2011).

$$k_{sur} = a \cdot S_{ut}^b \quad (172)$$

Where the constants a and b can be found in the Table 26.

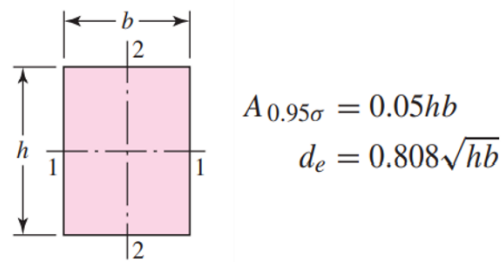
Table 26 – Constants values a and b for surface modification factor

Surface finish	a	b
Ground	1.58	-0.085
Machined or Cold-drawn	4.51	-0.265
Hot-rolled	57.7	-0.718
As forged	272.0	-0.995

Source: (BUDYNAS; NISBETT, 2011).

The k_{siz} factor depends on the component diameter and the kind of load applied to it. For noncircular cross section, it must be used the equivalent diameter estimated in Figure 128. For axial load the $k_{siz} = 1$, whereas for bending and torsion it can be calculated using Equation 173, (BUDYNAS; NISBETT, 2011).

Figure 128 – Equivalent diameter of noncircular cross section for size factor calculation



Source: (BUDYNAS; NISBETT, 2011)

$$k_{siz} = \begin{cases} 1,24 \cdot d^{-0,107}, & 2,79 \leq d \leq 51 \\ 1,51 \cdot d^{-0,157}, & 51 < d \leq 254 \end{cases} \quad (173)$$

The k_{load} factor is related to the endurance limit differing related to the material ultimate strength depending on the type of load applied on it. Equation 174 gives the k_{load} factor in function of the load type.

$$k_{siz} = \begin{cases} 1.00 \text{ bending} \\ 0.85 \text{ axial} \\ 0.59 \text{ torsion} \end{cases} \quad (174)$$

The k_{temp} factor depends on the component temperature under working conditions. The k_{temp} factor can be obtained from the Table 27, (BUDYNAS; NISBETT, 2011).

Table 27 – The temperature modification factor

Temperature [°C]	k_{temp}
20	1.000
50	1.010
100	1.020
150	1.025
200	1.020
250	1.000
300	0.975
350	0.943
400	0.900
450	0.843
500	0.768

550	0.672
600	0.549

Source: (BUDYNAS; NISBETT, 2011)

The k_{rel} factor takes to account for standard deviations of endurance limit measurements once the most of endurance limit values are reported as mean values. The k_{rel} factor can be obtained from the Table 28, (BUDYNAS; NISBETT, 2011).

Table 28 – Reliability factor

Reliability [%]	k_{rel}
50	1.000
90	0.897
95	0.868
99	0.814
99.9	0.753
99.99	0.702
99.999	0.659
99.9999	0.620

Source: (BUDYNAS; NISBETT, 2011)

The k_{mis} factor takes to account for any further effect that could reduce the endurance limit.

The fatigue strength, S_f in [MPa], is only smaller than the ultimate tensile strength and it is considered in the region of the low-cycle fatigue. The fatigue strength can be estimated using Equation 175, (BUDYNAS; NISBETT, 2011).

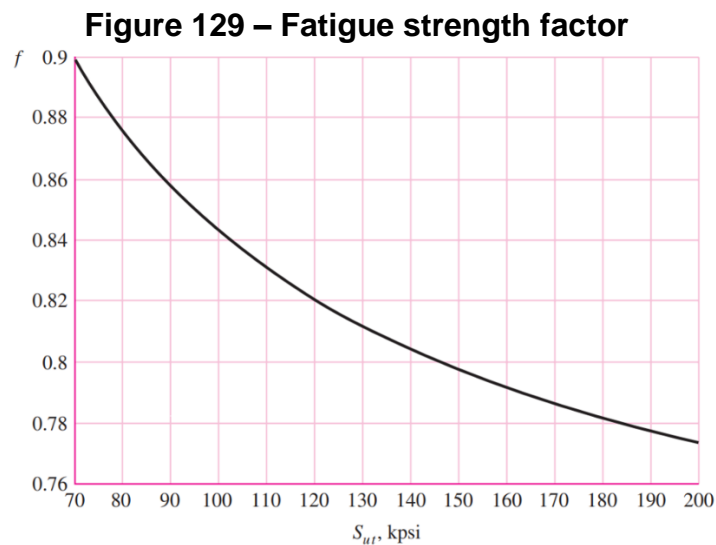
$$S_f = a \cdot N_c^b \quad (175)$$

Where the constants a and b are calculated using Equation 176 and Equation 177, respectively.

$$a = \frac{(f \cdot S_{ut})^2}{S_e} \quad (176)$$

$$b = -\frac{1}{3} \cdot \log\left(\frac{f \cdot S_{ut}}{S_e}\right) \quad (177)$$

Where the f is the fraction of the ultimate strength that could be obtained from Figure 129, (BUDYNAS; NISBETT, 2011).



Source: (BUDYNAS; NISBETT, 2011)

2.5.3. Characterizing Fluctuating Stresses and Failure Criteria

The fluctuating stresses in machinery usually take periodic patterns which exhibit a single maximum, σ_{max} , and a single minimum stress, σ_{min} in [MPa], for a given operation condition. These maximum and minimum stresses are used to characterize the stress pattern. The midrange, σ_m in [MPa], steady component of the stress and the amplitude of the alternating component, σ_a in [MPa], of the stress are calculated by Equation 178 and Equation 179, (Juvinal and Marshek).

$$\sigma_m = \frac{\sigma_{max} + \sigma_{min}}{2} \quad (178)$$

$$\sigma_a = \left| \frac{\sigma_{max} - \sigma_{min}}{2} \right| \quad (179)$$

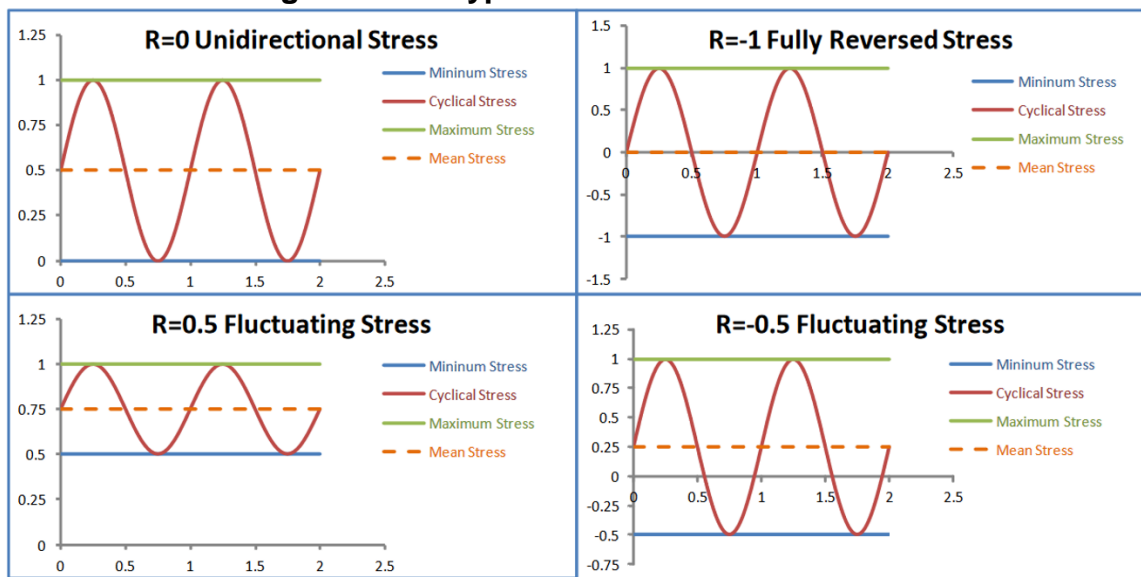
Further characterization of fluctuating stresses can be performed using the stress ratio, R , and the amplitude ratio, A_a , parameters. The stress ratio indicates the amount of minimum stress related to the maximum stress. On the other hand, the amplitude ratio indicates the amount of alternating stress related to the midrange

stress. The stress ratio and the amplitude ratio can be calculated using Equation 180 and Equation 181, respectively, (BUDYNAS; NISBETT, 2011).

$$R = \frac{\sigma_{min}}{\sigma_{max}} \quad (180)$$

$$A_a = \frac{\sigma_a}{\sigma_m} \quad (181)$$

Figure 130 – Types of fluctuation stresses

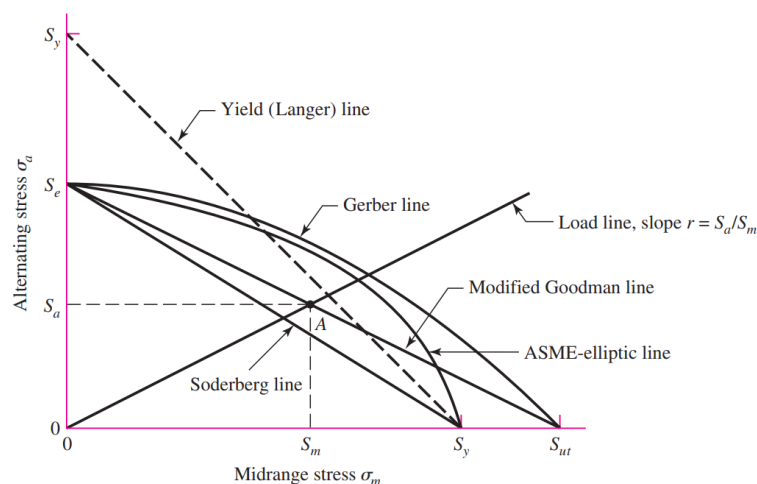


Source: Adapted from (ASM 1996)

Once the fluctuating stress can be characterized by the previous equations, the fatigue failure criteria can be applied. There are several fatigue failure criteria available such as Soderberg, Gerber, Langer, Goodman and ASME-elliptic as shown in Figure 131. In this work will be used the Goodman criteria. It was defined this criterion to be used in this work due to the more conservative aspect of the criteria related to the safety region in which a dynamic component can work.

According to the Goodman criterion, any combination of the midrange and alternating stress that lies below the Goodman line indicate that component will operate safely. The factor of safety established by the Goodman criterion can be calculated using Equation 182, (BUDYNAS; NISBETT, 2011).

Figure 131 – Fatigue Failure criteria



Source: (BUDYNAS; NISBETT, 2011)

$$\frac{\sigma_a}{\sigma_m} + \frac{\sigma_a}{\sigma_m} = \frac{1}{n} \quad (182)$$

2.6. Numerical simulation

The numerical simulation has been largely used to predict the engine structural, thermal, and fluid dynamic performance. Based on an engine CAD model, several interactions among engine systems are performed throughout the engine design process. The main goal by using numerical simulation is to reduce the overall time and cost required to develop or optimize an engine, (F. SCHÄFER 2017).

The main approaches to numerically simulate an engine are the FEM and CFD methods. The FEM is used to investigate the structural component behavior under mechanical and thermal loads. On the other hand, the CFD method is used to study the fluid and the heat flow throughout the engine systems. Furthermore, 1D-Models have been coupled to these approaches in order to simplify the overall numerical simulation process, (H. K. Versteeg 1995).

It is worth to point out that the aim of this chapter is not to present a detailed description of each model but only to highlight the calculation methods and some particularities of the models. For a deeper comprehension of the FEM and CFD models, it is suggested the following literature (H. K. Versteeg 1995; Vasconcelos 2018; VAZ 2018).

2.6.1. Finite Element Method


The Finite Element Method – FEM (or Finite Element Analysis – FEA) has as a base idea to build complex objects with simple blocks or divided a complicated object into smaller and manageable pieces. Mathematically, this is limit concept which a smooth object is represented by a finite number of pieces and increasing the number of such pieces will improve the accuracy of this representation, (Yijun Li and Chen 2015).


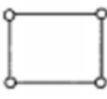

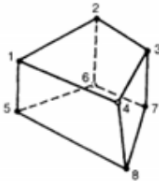
In order to perform a FEM simulation, the following procedure is required in general:

- Create a mesh geometry by dividing the CAD geometry in small elements;
- Apply loads and boundary conditions;
- Solve the system of equations involving unknown quantities at the nodes;
- Calculate the desired quantities (strains and stresses) at elements or nodes, (LI; CHEN, 2015).

The mesh creation is the result of a discretization process in which a continuous part is divided into finite elements. Currently this process is carried out automatically by FEM software. There are several ways to obtain a mesh depending on the discretization parameters. The main parameters that affect a mesh generation are the element size, the element order, and the element type. The element size is usually defined as the smaller circumference that fit inside of the element. Different element sizes can be applied to the mesh in order to better evaluate some particular region behavior under load. The element order is defined by the element shape order, and it describes the displacement field inside the element. Higher element order frequently is used to achieve the same result although using a lower number of elements. There are different types of elements and depending on the CAD geometry a specific element could be better to use. The Table 29 presents the different types of finite elements usually available in modern FEM software, (Vasconcelos 2018).

Table 29 – Types of finite elements

Element	Name
	1D Linear Element

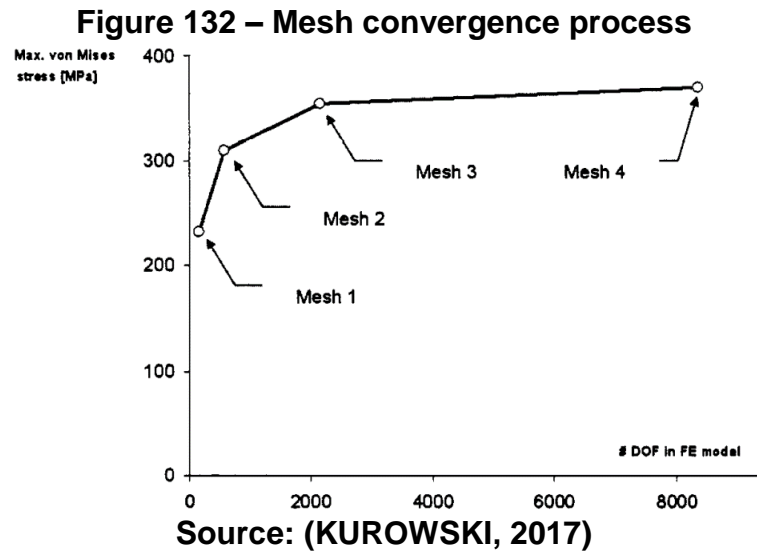
	2D Triangular Element
	2D Rectangular Element
	3D Tetrahedral Element
	3D Hexahedral Element

Source: Adapted from (VASCONCELOS, 2018)

The FEM approach presents some errors inherent to the modeling process that influence the simulation results. The simulation overall error has three main sources: error from model creation, error from the model discretization, and numerical error. The model creation error is associated with the approximations and simplifications made in relation to the real problem. On the other hand, the model discretization error is associated to the type, size and shape of the finite element chosen to represent the mathematical model. The discretization errors can be minimized by refining the mesh and studying its impact on simulation results. This process is called converge process. A refined mesh reduces the discretization error, as shown in Figure 132, however it increases the computational requirements. The convergence error, E_{conv} , can be calculated using Equation 183. Finally, the numerical error depends on the algorithm type used to perform the simulation, (Kurowski 2017).

$$E_{conv} = \left| \frac{ReS_{(w)} - ReS_{(w-1)}}{ReS_{(w)}} \right| \quad (183)$$

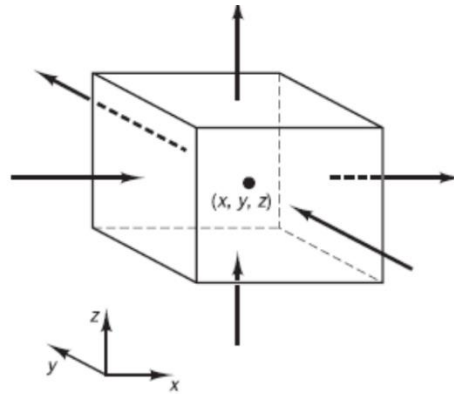
Where the $ReS_{(w)}$ is the simulation result at instant w and the $ReS_{(w-1)}$ is the simulation result at the previous instant ($w - 1$).



2.6.2. CFD Simulation

The Computational Fluid Dynamics (CFD), similarly to the FEM approach, divides a domain in smaller pieces and evaluate the main fluid properties in each piece and the interaction of it with the neighboring pieces. However, instead of use finite elements, the CFD method uses Finite Volume Method (FVM) (Figure 133) for discretization the flow domain. For each finite volume, it is applied Equations of mass conservation, momentum conservation and energy conservation at the center of the volume for the fluid scalar properties calculation such as pressure, temperature, density, internal energy, enthalpy and species concentration. The vectorial properties (mass flow, flow velocity, etc.) are calculated at volume boundary, (H. K. Versteeg 1995; VAZ 2018).

Figure 133 – Finite volume element representation



Source: (KUROWSKI, 2017)

The mass conservation equation also known as continuity equation is write on its compact form according to Equation 184.

$$\frac{\partial \rho}{\partial t} + \frac{\partial(\rho u_i)}{\partial x_i} = S \quad (184)$$

Where the ρ is the fluid density in [kg/m³], the t is time in [s], the x_i is the i direction, the u_i is the velocity in [m/s], and the S is the source term which can correspond to a computational sub-model.

The momentum conservation equation is obtained by the Newton second law which states that the fluid particle momentum rate is equal to the sum of forces acting on the particle. Equation 185 presents the conservation momentum equation.

$$\frac{\partial \rho u_i}{\partial t} + \frac{\partial(\rho u_i u_j)}{\partial x_j} = \frac{\partial P}{\partial x_i} + \frac{\partial \tau_{ij}}{\partial x_j} + S \quad (185)$$

Where P is the pressure in [kPa], u_j is the velocity in [m/s] and τ_{ij} is the viscous stress tensor in [N/m²], S is the source term, which, for Equation 185, can represent gravitational forces or sources of mass. For a Newtonian fluid, the viscous stresses are proportional to the strain rates as shown in Equation 186.

$$\tau_{ij} = \mu \left(\frac{\partial u_i}{\partial x_j} + \frac{\partial u_j}{\partial x_i} - \frac{2}{3} \cdot \delta_{ij} \cdot \frac{\partial u_k}{\partial x_k} \right) \quad (186)$$

Where μ is the dynamic viscosity in [Pa.s], and the δ_{ij} is the Kronecker delta.

The energy conservation equation is presented according to Equation 187.

$$\begin{aligned}
\frac{\partial}{\partial t}(\rho e) + \frac{\partial}{\partial x_j}(\rho e u_j) \\
= -P \frac{\partial u_j}{\partial x_j} + \tau_{ij} \frac{\partial u_i}{\partial x_j} \left(K_t \frac{\partial T}{\partial x_j} \right) + \frac{\partial}{\partial x_j} \left(\rho D \sum h_k \frac{\partial Y_k}{\partial x_j} \right) \\
+ S
\end{aligned} \tag{187}$$

Where the e is the internal energy in [kJ/kg], the K_t is the thermal conductivity in [W/m.K], the D is the mass diffusion coefficient in [m²/s], the h_k is the specific enthalpy of each specie k in [kJ/kg], the T is temperature [K], the Y_k is the mass fraction of the specie k , and the S represents the source of specific energy gain or loss.

2.7. State of art

In this section is made a presentation of the most current works of the scientific community related to SI engine fuel conversion efficiency improvements by means of ethanol used as fuel and the increase in the volumetric compression ratio, use of direct injection, variable valve timing system, water injection and turbocharger.

2.7.1. Ethanol used as fuel

Ahmed et al. (2022) found improved performance and lower pollutant emissions when using a 12% ethanol blend by volume in gasoline compared to the pure fossil fuel. Experimental tests in a single-cylinder engine revealed an average gain of 5.27% in brake torque, up to a 5% increase in thermal efficiency, and average reductions in CO and HC emissions by 22.35% and 32.20%, respectively. In a 1.5 L, 4-cylinder, naturally-aspirated engine operating at 2000 rpm, a 20% blend of ethanol in gasoline led to a 1.09 MPa in-cylinder pressure increase, producing lower combustion noise compared to pure gasoline (Chen et al. 2022). The homogeneous lean combustion of a modern downsized ethanol DI engine was evaluated by Golke et al. (2022). At a fixed engine speed of 1500 rpm, the authors could test the engine under partial loads until the limit of lambda 1.4 with stable combustion, assessed through the COV of IMEP below 3.0%. The Ford Ecoboost 1.0 L engine showed up to 9.2% indicated fuel conversion efficiency gains when altering the lambda factor from 1.0 to 1.4.

2.7.2. Volumetric compression ratio

Zhao et al. (2022) studied the performance of turbocharged gasoline SI engine with cooled EGR and high volumetric compression ratios using a 1D simulation model. It was evaluated the engine performance considering the volumetric compression ratio of 9.7:1, 12.5:1 and 14.0:1, and cooled EGR was used to suppress knock. As the baseline volumetric compression ratio was 12.5:1, the maximum and minimum relative improvement of the fuel economy was 29.4% and 4.5% comparing to 9.7:1 and 14.0:1, respectively. According to the authors, the fuel economy improvement for the EGR engine with high volumetric compression ratio was owing to higher air fuel ratio, lower heat-transfer and exhaust losses.

On Pandey and Kumar (2021) work, it was presented an experimental investigation of the engine performance of a hydrogen port fueled SI engine under wide-open throttle by varying its volumetric compression ratio and equivalence ratio. The volumetric compression ratio was varied from 10.0:1 to 15.0:1 and the equivalence ratio from 0.4 to 1.0. The tests were performed at an engine speed of 1400 and 1800rpm. The ignition timing is maintained constant throughout the engine tests. As a results, the brake thermal efficiency increases by an average of 10% from volumetric compression ratio 10.0:1 to 15.0:1, and it also increased by 13.7% by changing equivalence ratio from 0.4 to 0.9.

Mogi et al. (2022) studied the effect of high compression ratio on improving thermal efficiency and NO_x formation in jet plume controlled direct-injection near-zero emission hydrogen engines. Experiments were conducted using a single-cylinder FD1 running at 1000 rpm. Compression ratios of 12.3:1, 15.0:1, 18.0:1 and 20.0:1 were evaluated during the testes by adjusting the piston cavity depth. As a result, a maximum indicated thermal efficiency of 53.0% was achieved in the high lambda range by raising the compression ratio to 20.0:1.

Sahoo and Srivastava (2021) investigated the effect of compression ratio on a bi-fuel CNG engine. Gasoline and CNG were used as test fuels under MBT ignition timing, stoichiometric air-fuel ratio and different engine speeds at high load operating conditions. The compression ratio was varied from 9.0:1 to 12.0:1 and 9.0:1 to 16.0:1 for gasoline and CNG, respectively. The results showed a specific fuel consumption reduction of 9.34% when the compression ratio increased for CNG fueled engine. In gasoline, it was reduced by 4.8%. According to the authors, the reduction percentage

in specific fuel consumption using CNG was higher than gasoline due to high fuel conversion efficiency and improved combustion at higher compression ratio compared to gasoline.

2.7.3. Direct injection System

Lee et al. (2021) presented a review on spray, combustion, and emission characteristics of recent developed direct-injection spark ignition engine system with multi-hole type injector. Based on the author's research it could be concluded that the advantages of a multi-hole GDI injector include flexibility of plume targeting, precise control of the injection timing and quantity, and relatively higher spray velocity. In addition, the multi-hole injectors and spray-guided engines present better emissions characteristics and higher efficiency compared to swirl injectors and wall-guided engines. Furthermore, NO emissions reduction and higher fuel efficiency can be simultaneously achieved using a stratified combustion strategy.

Oliveira et al. (2022) studied the effects of direct injection and mixture enrichment on the combustion of hydrous ethanol and an ethanol-gasoline blend in an optical engine. The experiments were conducted in an optically accessible spark-ignition engine and the lean combustion effects on engine cycle variability, performance, flame morphology, and exhaust emissions were assessed. This study demonstrated that vaporization is a relevant phenomenon affecting ethanol combustion in a direct injection mode. The cooling effect of fuel vaporization presented itself as a powerful means for the reduction of NO_x and aldehydes, even for lean operation. However, the same cooling effect limited the lean limit for ethanol, as well as induced combustion instabilities owing to the excessively low combustion temperature.

Li et al. (2022) investigated the potential benefits of Ethanol Direct Injection (EDI) timing and pressure on particulate emission characteristics in a Dual-Fuel Spark Ignition (DFSI) engine. In this study, the engine operated at the speed of 2000rpm and load of 2 bar Brake Mean Effective Pressure (BMEP). Furthermore, the engine run at stoichiometric condition and the ignition timing was adjusted to MBT condition for all engine operation conditions. The results by delaying EDI timing from 340 to 300 CA showed a reduction of 54.65% and 89.15% of particulate number and mass concentration, respectively. By increasing EDI pressure from 5.5 MPa to 18 MPa, the

droplet size of ethanol spray can be effectively reduced. Thus, improves the fuel atomization and evaporation, which in turn it results in a faster combustion process.

In Park et al. (2022) work was presented effect of fuel injection timing and injection pressure on performance in a hydrogen direct injection engine. The tests were performed at an engine speed of 1500rpm and wide full throttle, the start of fuel injection timing was varied from 350 CA before top dead center to near of top dead center (TDC) and the fuel supply pressure was increased from 5 MPa to 7 MPa. According to the authors, the increase in ignition timing and excess air ratio due to injection timing changes, resulted in a torque increase and in decrease in NOx emissions. However, the retardation of the fuel injection timing is limited by an increase in the in-cylinder pressure. By increasing the fuel injection pressure, the torque performance can be improved by further retarding the fuel injection timing or increasing the fuel injection period.

2.7.4. Variable valve timing system

Li et al. (2018) studied realization of variable Otto-Atkinson cycle using variable timing hydraulic actuated valve train for performance and efficiency improvements in un-throttled gasoline engines. The study was performed using a computational simulation of a single cylinder engine running on stoichiometric condition from 2000 to 3600rpm and wide open throttle. The results showed that variable Otto-Atkinson approach with optimized parameters lead to a 13.5% average improvement in the engine's output and they also showed that the specific fuel consumption could be lowered by 16.1 g/kWh.

Osorio and Rivera-Alvarez (2018) investigated the efficiency enhancement of spark-ignition engines using a continuous variable valve timing system for load control. For this study an analytical model for ideal processes was initially developed to evaluate the performance of both cycles during part-load operation. Then, irreversibility comprising charging dilution effects and heat losses during compression and expansion strokes were considered to approach a more realistic engine operation. The results presented a fuel economy increment of up to 4.1% is obtained for a continuous variable valve timing engine with respect to a throttled engine at a 20% - 30% load, which is typical of a real vehicle engine operation.

Perceau et al. (2021) developed a zero-dimensional turbulence model of a spark ignition engine in a Miller cycle “De-throttling” approach using a variable valve timing system. The model developed in this work could take into account the strong changes of in-cylinder turbulence generated by the variable valve timing and their effects on the combustion. The engine was simulated at 2000 and 3000rpm in several loads from 2 to 14 bar of IMEP in steps of 2 bar. The results showed that the Miller cycle can lead to indicated efficiencies around 44% and the addition of a variable valve timing system can improve the overall efficiency up to 1% over a wide range of engine loads.

Kim et al. (2021) investigated the effect of boosting on a performance and emissions in a port fuel injection natural gas engine with variable intake and exhaust valve timing. In this study, experiments were conducted under the valve timing variations optimized for each engine speed point of 1000 - 2500 rpm under boosted high load conditions in a natural gas engine. According to the authors, the main conclusions: The intake valve closing timing delayed under low-speed and non-boosted conditions lead to fresh charge flowed back to the intake port at the beginning of the compression stroke; thus, the engine performance worsened. In addition, it was advantageous in terms of engine performance to advance the exhaust valve timing to the maximum at low speed under non-boosted conditions. This is because the exhaust gas flowing back to the cylinder interfered with the flow of fresh charge when the exhaust valve timing was retarded. Furthermore, the exhaust valve timing retarded at low speed under boosted conditions lead to an engine performance improvement due to the increase in the expansion work. However, when the exhaust valve timing was excessively retarded, there was a possibility that the amount of exhaust emissions increase and the engine performance deteriorates.

2.7.5. Water injection

Han and Boehman (2022) studied multiple injection strategies with high water port injection rates for enhancing performance and emissions in a boosted SI engine. For this study was utilized a boosted single-cylinder research engine equipped with a water port injector and a piezoelectric gasoline direct injector over a range of water to fuel mass ratio (up to 1.0) and multiple fuel injection (single vs. triple) conditions. The results showed that the drawbacks of water injection including combustion instability, unburned hydrocarbon, and particulate emissions were significantly improved with

multiple fuel injections, and the relative thermal efficiency improvement and nitrogen oxide emission reduction were maximized up to 3.9% and 52.7%, respectively, with the combined injection strategy.

In Wu et al. (2021) work was presented the effects of direct water injection timings on knock suppression, combustion, and emission performance of high compression ratio hydrogen-enriched natural gas engine. For this study, a 3D numerical model for the high volumetric compression ratio hydrogen-enriched natural gas engine was built and calibrated based on experimental data under working condition of 1000 rpm and 10 bar brake mean effective pressure (BMEP). The results showed that the advanced water injection timing from -30 CAdeg to -150 CAdeg lead to knock decrease from 3.2 MPa to 1.3MPa. Furthermore, the indicated thermal efficiency achieved a peak of 40.9% with an increment of 3% compared to baseline condition (water injection timing at -30 CAdeg). In addition, the NO_x emissions decreases significantly, while HC and CO emissions increased to some extent. Therefore, proper water injection timing can not only effectively reduce knock intensity and NO_x emission, but also improve thermal efficiency.

Wan et al. (2021) presented a review of water injection application on spark-ignition engines. In this review work various methods for the implementation of water injection in SI engines were introduced and compared. Furthermore, methods to maximize the working efficiency of water injection and its detailed physical and chemical effects on combustion and emissions were discussed. According to authors the following conclusions could be made: Water injection can improve the combustion and performance of SI engines. Typically, better combustion phasing and thus higher thermal efficiency can be achieved especially under high load conditions. Additionally, the engine emissions such as nitrogen oxides and soot can be largely suppressed. However, crucial issues such as water supply and wall wetting still restrict wide application of water injection technology.

Cesur (2022) investigated effects of water injection strategies on performance and exhaust emissions in an ethanol fueled gasoline engine. For this study a twin-cylinder, port injected, naturally aspirated, four-stroke engine were used. The experiments were carried out in the fully open throttle position and at engine speeds of 1400, 1800, 2200, 2600, 3000 and 3400 rpm. The experiments were carried out in three stages. In the first stage, standard gasoline fuel experiments, secondly gasoline-ethanol blended fuel experiments, and in the last stage, water injection was done into

the ethanol blended fuel at different rates. The results showed that the bigger improvements in effective power and engine torque were obtained with 20% water injection. The highest rate of effective power increase compared to the standard engine was 2.5% at 3400 rpm. The maximum amount of reduction in HC emissions was obtained in 20% water injection, and the amount of reduction was 15.3% at 2200 rpm. According to the standard engine data, the maximum reduction in NO_x emissions was 28.9% at 3000 rpm.

2.7.6. Turbocharger

Serrano et al. (2021) developed a methodological analysis of variable geometry turbine (VGT) technology impact on the performance of highly downsized spark-ignition engines. According to the authors, in parallel to combustion concepts, a key required trend is downsizing based on high engine boosting. New turbocharger technologies, such as variable geometry turbines, become suitable for its application under the demanding operating conditions of SI engines. Based on experimental and computational results it was found that VGT technology shows less limitations in extreme working conditions, such as low- and high-end torque regions, where the regular non-VGT technology represents a limitation in terms of the maximum power output. Furthermore, full load differences become more evident in altitude working conditions. On the other hand, on partial loads, differences in fuel consumption are minor, but potentially beneficial for VGTs.

Ananthakrishnan et al. (2020) presented a study of the impact of turbocharger efficiency for an engine operating at 50% brake thermal efficiency. This work showed how a well matched, optimized turbocharger can impact the engines Brake Thermal Efficiency (BTE). Furthermore, carefully matching and optimizing the turbocharger enables an increase in both open cycle and closed cycle efficiency which are key factors for engine performance. The results presented that the engine BTE was improved by 0.69% with the addition of the high efficiency turbocharger.

Marelli et al. (2020) performed an experimental investigation on the transient response of an automotive turbocharger coupled to an electrically assisted compressor. This work described the experimental set-up and the measuring equipment adopted to test the e-booster coupled to the main turbocharger. The e-booster system (eSC) was maintained in an upstream configuration and the main

instantaneous parameters (pressure, mass flow rate and turbocharger rotational speed) were measured using high frequency response transducers. This layout allowed to analyze the transient response of the main turbocharger and to highlight the gain in turbo-lag when the eSC was working. The results presented that the turbo-lag decreased on average 3.45 seconds when the sSC compared to conventional turbocharger.

Baines et al. (2020) presented the trends in passenger car powertrains and their impact on turbocharger developments. According to the authors, an increase in hybrid gasoline-electric engines continues to provide market opportunities for turbochargers, but a change in the turbocharger design strategy, emphasizing efficiency over size and operating range, is possible and desirable. Such changes are based on known technology and do not require large-scale changes to the turbocharger configuration. The scope for this depends on the rating of the electric machine and the on-board battery capacity. In the most favorable conditions, it might be as much as 5-7 percentage points for the compressor and turbine.

3. METHODOLOGY

The methodology to be presented in this topic was divided in each engine developing step from the basic engine geometric characteristics definition to its CAD model building.

The engine developed in this work aims to use the Brazilian hydrous ethanol as fuel and take advantage from the fuel properties to run the engine at Indicated Mean Effective Pressure (IMEP > 30 bar). Despite of high mechanical stress which engine components are subjected to due to the high IMEP working condition, an engine running at high load and on stoichiometric condition is able to achieve lower values of

specific fuel consumption. Furthermore, since the Proalcool program in Brazil, the hydrous ethanol has not been used in an engine which was designed to exploit the fuel properties. In Brazil, most of the hydrous ethanol application was in flex-fuel engines which have their maximum allowed IMEP limited by gasoline fuel properties (IMEP ~ 26bar).

As the engine developed in this work aims to use exclusively the Brazilian hydrous ethanol, new engine components such as piston, piston pin, connecting rod, crankshaft and crankcase were designed for this application. A comparison between the design of the new engine components and components commonly used in flex-fuel engines leads to a more robust component able to withstand high mechanical load which it was never done before.

In order to simplify the citation reference of the engine designed in this work, from now on the engine developed in this work will be called HBS22 (Highly Boosted by Silva – 2022).

3.1.Engine Development Plan

In order to manage the engine prototype developing process, it was created an engine development plan. Firstly, the basic geometrical engine parameters such as engine displacement, bore, stroke, stroke to bore ratio, connecting rod ratio, volumetric compression ratio, bore pitch, piston-pin offset and crankshaft offset were defined. Once these basic parameters were defined, the engine components were designed on CAD model aiming to bear predicted mechanical and thermal loads.

For the engine design, it was used different softwares such as Siemens NX, Ansys, GT-Suite and Gates Design IQtm. The Siemens NX was used for the engine CAD modeling. This software was chosen due to its modeling flexibility options and the author previous knowledge of how to use it. The Ansys, and GT-Suite were used for engine simulation. The FEM simulation were carried out in Ansys due to its robust simulating tools and the support from the developer in case of any simulation issue. For the 1D-CFD simulation was used the GT-Suite software. The GT-Suite was chosen based on its robust simulation tools and its user friendly interface. The Gates Design IQtm software was used for the timing and accessory drive belt calculations.

3.2. Engine Specification and Basic Data

The engine hardware modeling was performed based on the engine basic parameters showed in the following sections.

3.2.1. Engine Displacement Limit and Number of Cylinders

During the last few years, most of the engine development has followed the downsizing engine concept; however, recent research pointed to rightsizing as the future tendency. The rightsizing engine concept has an aim to achieve a better balance between engine displacement and its vehicle application. A better compromise between engine performance and its vehicle application could lead to lower fuel consumption, reduced engine production costs, reduced engine mechanical stress and improved durability.

In the Brazilian market, the engine rightsizing concept faces an economic barrier. In order to encourage low-cost vehicle purchases, the Brazilian government established the vehicle manufacturing tax IPI (from Portuguese - *Imposto sobre Produto Industrializado*) according to the engine displacement. As shown in Table 30, a vehicle equipped with a flex-fuel engine of up to 1.0 L displacement pays 3.7% less tax than a vehicle equipped with engine displacement higher than 1.0 L. Thus, in case of a 1.0 liter engine applied to a premium vehicle, such as an SUV (Sport Utility Vehicle), it could lead to a cheaper and more efficient vehicle, compared to a larger displacement, naturally aspirated engine. Based on the economic advantage to use an engine up to 1.0 liter, along with the ethanol fuel properties, which allow the engine to run efficiently at high IMEP ($IMEP > 30\text{bar}$), the displacement of 1.0 L was defined for the engine HBS22. Furthermore, in order to keep the engine as compact as possible, a 3-cylinder layout was defined to be used, despite the vibrational stress of the crankshaft due to its first order moment.

Table 30 – Brazilian vehicle manufacturing tax

OEM Brazilian Vehicles	Tax
Flex-fuel engine with up to 1.0 liter	6.6%
Flex-fuel engine between 1.0 and 2.0 liters	10.3%
Gasoline engine between 1.0 and 2.0 liters	12.2%

Flex-fuel engine higher than 2.0 liters	16.9%
Gasoline engine higher than 2.0 liters	23.5%
Utility vehicles – SUV	3.8 - 7.5%
Electric vehicles	6.6 - 16.9%

Source: Adapted from (Economia 2022)

3.2.2. Volumetric Compression Ratio

The definition of the volumetric compression ratio for the engine developed in this work considered several studies, such as (SILVA et al. 2017a; BAËTA, Pontoppidan, and Silva 2015; BAËTA et al. 2018; Ferreira Gomes 2018), which investigated the use of hydrated ethanol as fuel along with different engine technologies. In conclusion from these works, it was realized that an ethanol-fueled engine is able to run efficiently on high boost pressures and high volumetric compression ratios, due to the fuel heat of vaporization. Furthermore, the results from these investigations showed that the combustion process on the MBT (Maximum Brake Torque) condition has a higher contribution to the engine fuel conversion efficiency than the volumetric compression ratio. Thus, the most suitable volumetric compression ratio would be as high as possible, provided that it ensured a regular combustion process, with an upper limit characterized by the knock occurrence.

Considering the technologies intended to be applied to HBS22, such as fuel direct injection and port water injection, as well as the results from previous studies reported in the literature, a 14:1 volumetric compression ratio was defined.

3.2.3. Cylinder Bore and Bore Pitch

The cylinder bore pitch depends on the arrangement of cylinder head studs, crankcase sleeves upper support dimensions and its cooling gallery design, and sufficient crankshaft fatigue strength. According to (Xi-Hou Fu 1994), the bore pitch, B_{pitch} in mm, can be calculated in function of the cylinder bore using Equation 188, and large values are recommended for engines operating with higher combustion pressure, in order to promote adequate cooling between the engine cylinders. For a 4-valve engine fitted with a single piece cylinder head, a bore pitch factor, bp_f , from 1.21 to 1.25 is recommended (XI-HOU FU, 1994).

$$B_{pitch} = bp_f \times B \quad (188)$$

Considering the scarcity of articles that present the entire engine development and optimization, the works presented in the *Internationales Wiener Motorensymposium* were adopted as references for the engine bore definition. Evaluating the bore size of the engines presented in the symposium throughout the last few years, taking into account only engine displacements up to 1.0 L, it could be concluded that majority of the bore size diameters were between 70 and 74 mm, as shown in Table 31, (DE MARINO et al. 2018; LEE et al. 2015; WEBER et al. 2018; Alt et al. 2014). Aiming to design a combustion chamber as compact as possible and higher stroke to bore ratio for the engine displacement previously defined, it was established 70.5 mm as the bore size for HBS22.

Table 31 – Modern 1.0-liter engines bore size

Engine	Bore diameter [mm]
1.0 L GSE Europe	70.0
1.0 L GTDI Ecoboost	71.9
1.0 L T-GDI Kappa	71.0
1.0 L TDI-GM	74.0

Source: Author

Considering 1.23 as the average of the suggested bore pitch factor and the cylinder bore of 70.5 mm, the bore pitch was calculated according to Equation 189.

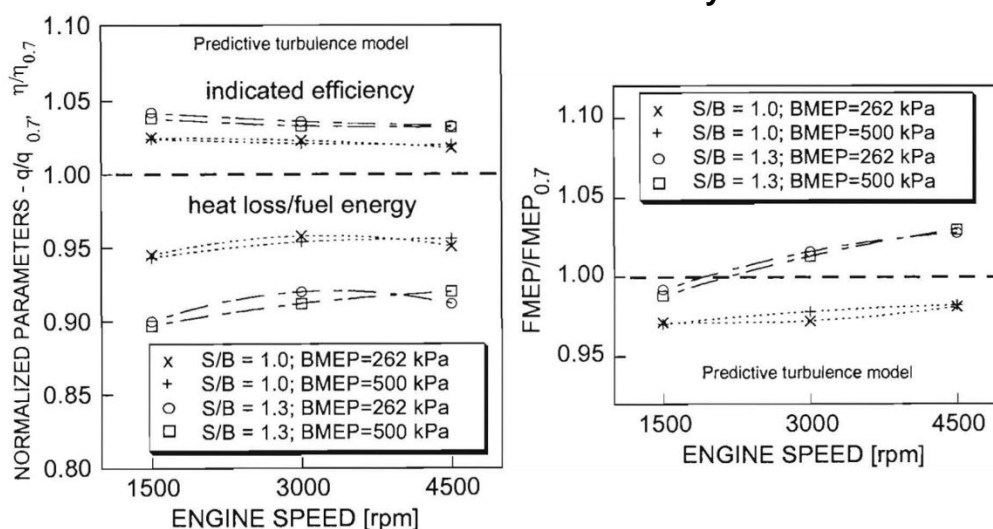
$$B_{pitch} = 1.23 \times 70.5 = 86.7 \text{ mm} \quad (189)$$

3.2.4. Stroke-to-Bore Ratio

The Stroke-to-Bore ratio (S/B) is one of the most important parameters that affects the SI engine fuel conversion efficiency. In general, a higher S/B ratio leads to a higher thermal efficiency through faster combustion process and a lower overall combustion chamber heat loss. However, a higher S/B ratio increases the engine friction losses, mainly at high engine speed, which in turn diminish the thermal efficiency gains, as illustrated in Figure 134. These conclusions are presented in the several studies such as (G.M. Bianchi 1998; Seokwon Cho and Song 2019; Z. S. Filipi 2000; Kevin L. Hoag 2016).

The faster combustion process achieved with higher S/B ratio is related to the turbulence intensity achieved during the intake and compression stroke. A higher turbulence intensity is produced by a higher flow mean velocity, which is a consequence of a higher piston speed and a higher intake flow velocity in the long-stroke engine. The drawbacks of both higher intake flow velocity and higher turbulence intensity on the engine volumetric efficiency can be diminished by means of a turbocharger use. The lower combustion chamber heat loss, as result of the higher S/B ratio, is achieved due to lower combustion chamber surface area to volume ratio. More specifically, the higher S/B ratio leads to a higher combustion flame front area per unit of combustion chamber volume. The increase in the friction losses as the S/B increases has a main source the piston ring pack due to the longer path described by the piston.

Figure 134 – Comparison of the thermal efficiency, the heat and the friction losses of three different S/B ratio normalized by the S/B=0.7 results

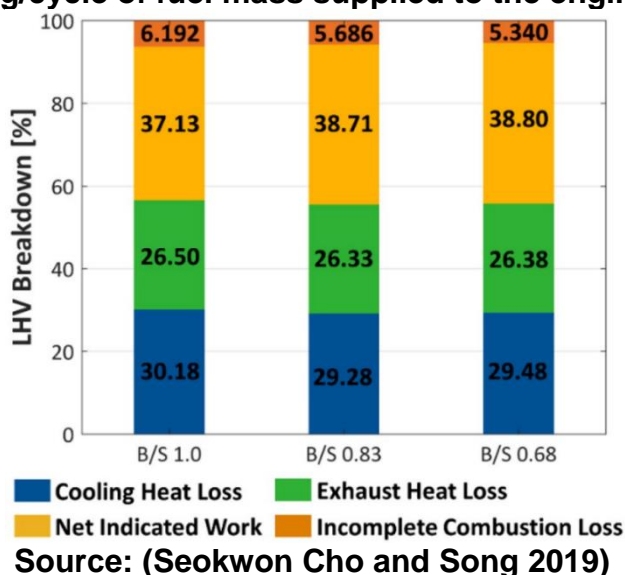


Source: (Z. S. Filipi 2000)

According to the results presented in the studies of (G.M. Bianchi 1998; Seokwon Cho and Song 2019; Z. S. Filipi 2000; Kevin L. Hoag 2016), the engine fuel conversion efficiency improvements showed a non-linear behavior as the S/B ratio increases. Furthermore, the positive fuel conversion efficiency gains are not significant for S/B ratio further than 1.2, as shown in Figure 135.

Based on the results presented by afore mentioned authors related to the S/B ratio study, it was defined the S/B ratio of 1.2 to be applied to HBS22.

Figure 135 – LHV breakdown for different S/B ratio at 2000 rpm, $\lambda=1$ and 26 mg/cycle of fuel mass supplied to the engine



3.2.5. Engine Crank-Stroke and Crank-Radius

The engine crank-stroke is also called engine stroke when the engine has no piston or crankshaft offset. Considering the bore and stroke-bore ratio defined in the

items 3.2.4 and 3.2.5, respectively, the crank-radius was calculated according Equation 190.

$$r = \frac{SB_{ratio} \cdot B}{2} = \frac{1.2 \times 70.5}{2} = 42.3 \text{ mm} \quad (190)$$

In order to maintain the engine calculated values as simple as possible without any significant changes on the engine design, the crank-radius was considered as 42.3 mm for the HBS22.

It is worth to point out that it is intended to applied piston and crankshaft offsets in the cranktrain mechanism of the engine designed in this work which affects the piston stroke. Furthermore, in case of offseted crank-slider mechanism, the connecting rod ratio must be considered for the engine true-stroke calculation.

3.2.6. Connecting Rod Ratio

The connecting rod ratio is a parameter which affect the piston kinetic performance throughout the engine strokes.

It can be noticed that the piston instantaneous position, velocity, and acceleration are directly affect by the connecting rod ratio being its motion behavior defined by the sum of first and second order of the sine and cosine functions. The connecting rod ratio could be considered as a percentage increase of the piston velocity and acceleration over the uniform circular motion of the cranktrain mechanism.

The ideal thermodynamic Otto working cycle has the heat introduced at a constant volume. Thus, an engine which has a lower connecting rod ratio promote a higher piston dwell time at the TDC, which in turn could lead to a combustion process towards to the ideal working cycle condition. However, the engine thermal efficiency is greatly affected by the combustion flame front losing heat to the piston crown surface, (Masatoshi Suzuki 2006). Furthermore, the engine operation with a high degree of constant volume at firing TDC can induced to a high combustion noise, also called the sound of efficiency, due to pressure rise rate, (Gen Shibata 2015; Maurya 2019).

Further than the engine thermal efficiency, the connecting rod ratio affect the engine running smoothness. Considering the engineering range application with the

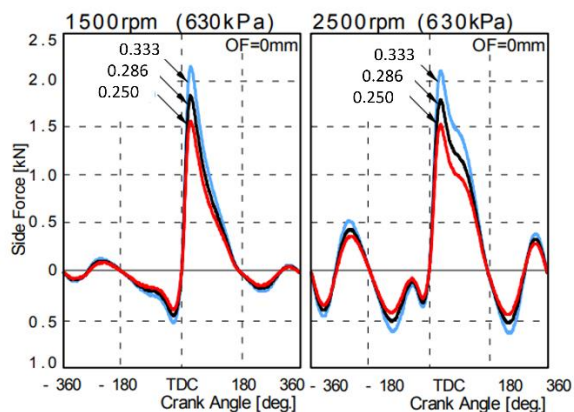
connecting rod ratio up to 1.0, it was presented by the author Kimball (1948) that connecting rod ratios larger than 0.263 starts to promote a dual minimum acceleration behavior and the connecting rod ratio of 0.357 promotes the minimum acceleration on the piston dynamic behavior.

The engine friction loss is another parameter influenced by the connecting rod ratio. Based on Equation 31, it can be concluded that a lower connecting rod ratio leads to a lower connecting rod pivot angle. Which in turn, it reduces the normal (lateral or side) piston force and hence the engine FMEP (Friction Mean Effective Pressure), as shown in Figure 136 (a). However, as shown in Figure 136 (b), the engine FMEP can increase in case of excessive low connecting rod ratio. According to Wakabayashi (2003), the FMEP increase is related to a smaller load bearing area of the piston skirt as a consequence of the lower piston normal force. A proper piston skirt deformation leads to a wider load bearing area and thus it prevents friction from increasing.

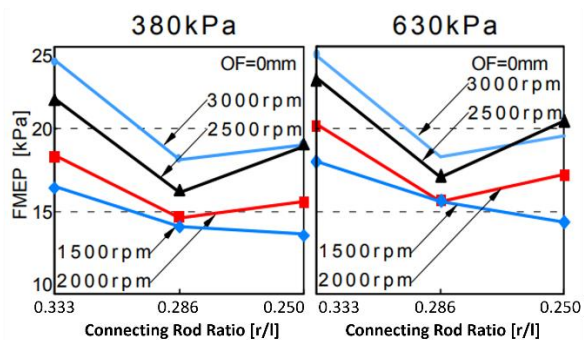
In brief, a proper connecting rod ratio is a balance among its effects on the engine thermal efficiency, the engine running smoothness, and the engine friction. Thus, the connecting rod ratio defined for the HBS22 was 0.295. Figure 137 presents a comparison of the piston acceleration curve related to various a connecting rod ratio for a non-de-axed cranktrain mechanism.

In order to minimize the heat losses from the combustion flame front to the piston crown due to the lower connecting rod ratio, it will be applied a TBC on the piston crown as presented in the topic 3.3.2.

Figure 136 – Effects of the connecting rod ratio on the FMEP related to engine load and speed



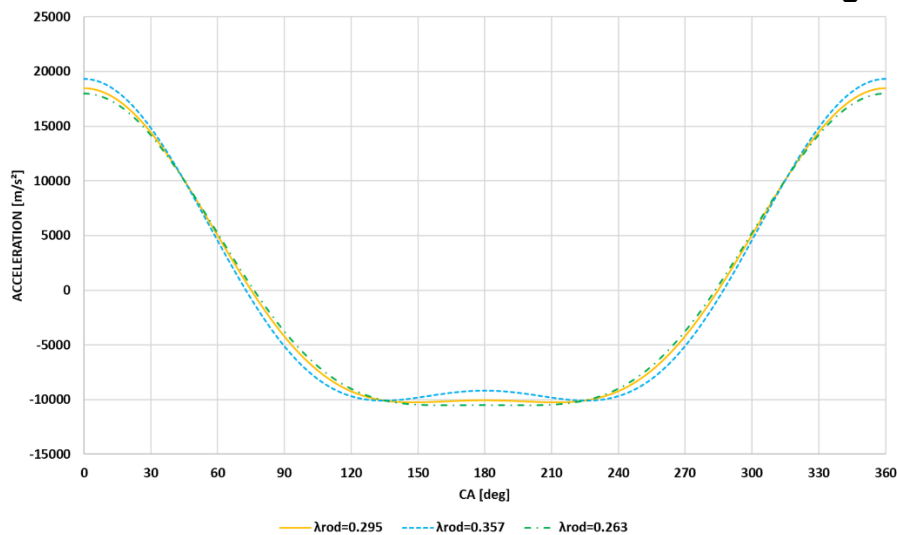
(a)



(b)

Source: (Ryo Wakabayashi 2003)

Figure 137 – Piston acceleration behavior related to connecting rod ratio



Source: Author

Considering afore defined values for crank radius and connecting rod ratio, the connecting rod length was calculated using Equation 191.

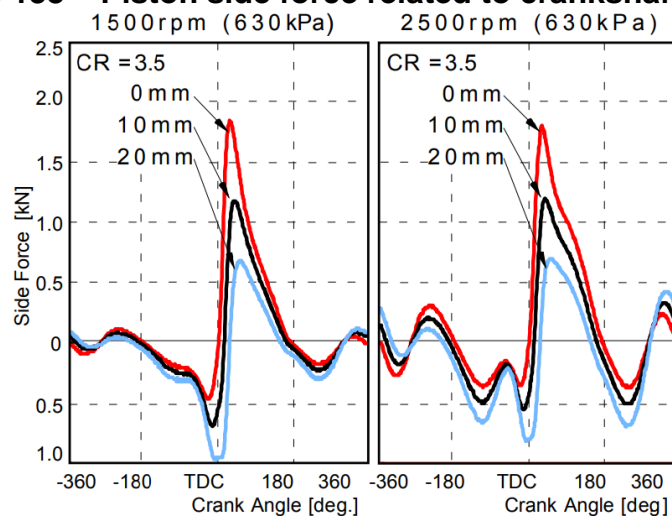
$$l = \frac{r}{\lambda_{rod}} = \frac{42.3}{0.295} = 143.39 \approx 144 \text{ mm} \quad (191)$$

Therefore, the connecting rod length of 144 mm was defined to be applied on HBS22.

3.2.7. Piston Pin and Crankshaft Offset

A further engine friction reduction can be achieved by applying an offset to crankshaft towards the major thrust side. By offsetting the crankshaft center with respect to the cylinder center line, the piston side force distributes appropriately on either thrust or anti-thrust side. Thereby, the piston friction is reduced effectively by offsetting the crankshaft center, as presented in Figure 138.

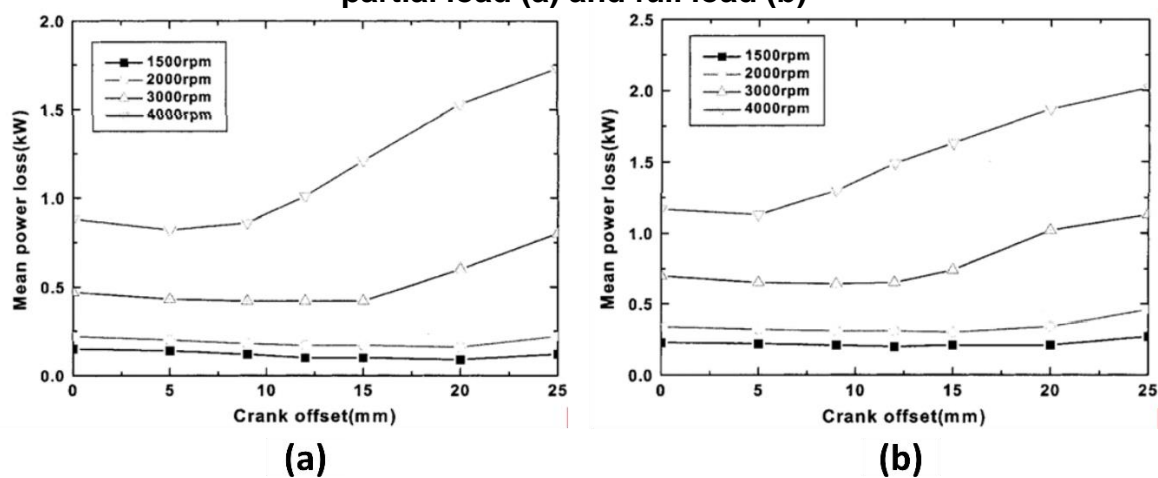
Figure 138 – Piston side force related to crankshaft offset



Source: (Ryo Wakabayashi 2003)

The studies presented by Myung-Rae (2003) and Wakabayashi (2003) concluded that increasing the crankshaft offset leads to the piston friction reduction up to a certain level which the piston normal force is not the major factor on the piston friction. Furthermore, the friction reduction as a result of the crankshaft offset appears greater at low engine speed and low engine load, respectively. Figure 139 presents the crankshaft offset effect on the power loss of the piston skirt at partial load (a) and full load (b). It can be seen that the crankshaft offset for a passenger car engine which has a maximum engine speed about 5500 rpm should be in a range from 5 to 10 mm. A crankshaft offset of 5 mm would minimize the engine power loss at high engine load and speed, whereas a 10 mm of crankshaft offset would improve the engine performance at partial loads and lower engine speeds operation condition.

Figure 139 – Crankshaft offset effect on the power loss of the piston skirt at partial load (a) and full load (b)



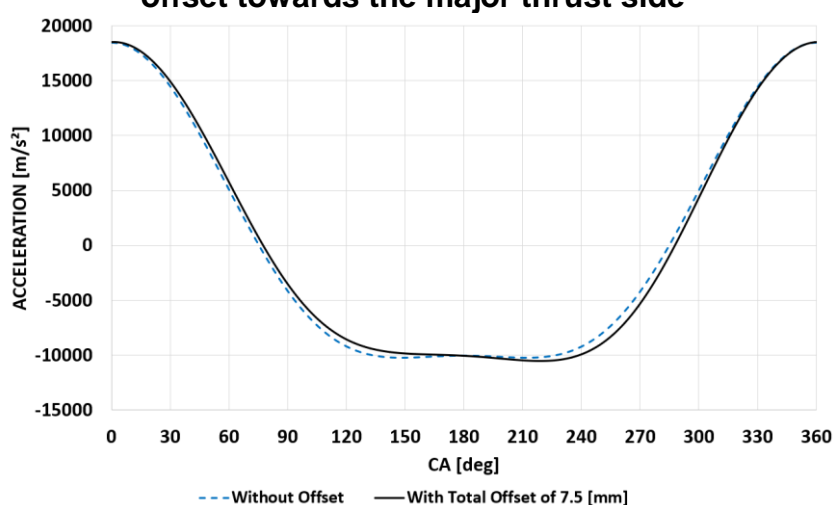
Source: (Myung-Rae Cho 2003)

Further than the piston lateral force, the crankshaft offset also affects the piston instantaneous displacement, velocity, and acceleration throughout the engine strokes.

As shown in Figure 140, a crankshaft offset of 10 mm leads to a higher piston acceleration during piston movement from TDC to BDC and, on the other hand, it leads to a lower piston acceleration during the piston traveling from BDC to TDC. A higher piston acceleration from TDC to BDC can improve the engine thermal efficiency by reducing the amount of heat lost to piston crown. However, the lower piston acceleration from BDC to TDC may affect the flow turbulence dissipation throughout the compression stroke leading to large turbulence eddies at piston TDC. In addition to piston dynamic changes, the crankshaft offset drifts the piston TDC to a delayed position related to the crankshaft angle. Hence, the combustion process is affected due to the in-cylinder instantaneous volume change.

In order to achieve a lower engine noise level, it was applied an offset also to the piston pin. The crankshaft offset along with the piston offset affects the piston friction. The piston pin offset combined with the combustion force determine the moment magnitude of the piston secondary movement. Thus, a greater moment about the pin axis increase the piston tilt, which in turn reduces the oil hydrodynamic film development between piston skirt and cylinder wall increasing friction. The crankshaft offset changes the timing when the piston position moved from the anti-thrust side to the thrust side from near TDC to the middle stroke at which the piston has high speed and the oil film is already formed, (Ryo Wakabayashi 2003; Steve Shin 2004).

Figure 140 – Piston acceleration curve of crankshaft with and without 10 mm offset towards the major thrust side



Source: Author

Considering the effects of the crankshaft offset on the engine performance, the application of the HBS22 in a passenger car, and aiming a smaller piston secondary

movement moment, it was defined a crankshaft offset of 8 mm and a piston pin offset of 0.5 mm towards the major thrust side. By applying the offset to the crankshaft and the piston, the cranktrain presents a total crankshaft offset of 7.5 mm.

3.2.8. Engine Stroke (Piston True Stroke)

The engine stroke of a cranktrain mechanism with the crankshaft and piston offset applied on it is calculated using Equation 192. For this type of cranktrain, the engine stroke is also called piston true stroke.

$$L_{off} = \frac{42.3}{0.295} \times \left(\sqrt{(1 + 0.295)^2 - \left(\frac{7.5}{144}\right)^2} - \sqrt{(1 - 0.295)^2 - \left(\frac{7.5}{144}\right)^2} \right) = 84.7 \text{ mm} \quad (192)$$

3.2.9. Effective Engine Displacement

Considering the engine number of cylinders, bore size and the calculated piston true stroke, the effective engine displacement it is calculated using Equation 193.

$$V_d = 3 \cdot \frac{\pi \cdot B^2}{4} \cdot L_{off} = 3 \times \frac{\pi \times 0.0705^2}{4} \times 0.0847 = 0.992 \times 10^{-3} \text{ m}^3 \approx 0.992 \text{ L} \quad (193)$$

3.2.10. IMEP, Torque and Power Target

The performance targets defined for the engine of this work were established aiming to take advantage of hydrous ethanol properties that allows the engine to run at higher loads (IMEP > 30bar) and use the water injection for further performance improvements. Considering that HBS22 development was a next step of ethanol research on *Centro de tecnologia da Mobilidade (CTM)*, the results achieved by Baêta et al. (2018) were used as reference to defined the target performance parameters in this work. The engine used in Baêta et al. (2018) achieved an IMEP maximum of 33

bar, however there was a margin for further improvements with a new turbocharger. For HBS22, it was defined 35 bar of IMEP as the load target considering its cylinder head port and valve arrangements, combustion chamber geometry and the new turbocharged used on it.

Considering an IMEP of 35 bar and the engine displacement previously defined, the engine indicated torque can be calculated using Equation 194.

$$T_{ind} = \frac{IMEP \cdot V_d}{2 \cdot \pi \cdot n_R} = \frac{3500 \cdot 0,001}{4 \cdot \pi} \approx 279 \text{ N.m} \quad (194)$$

For the engine peak power, it was defined 135 kW at 5500 rpm based on the engine power predicted in Baêta et al. (2018). Furthermore, it was established an additional of 250 rpm after the engine peak power speed as the maximum engine speed. Thus, the maximum engine speed was defined as 5750 rpm.

3.2.11. Engine Specification Summary

After all engine basic data calculation as shown in this topic, the engine specification can be summarized as shown in the Table 32.

Table 32 – Basic engine specification

Engine type	Turbocharged, 3 cylinder in-line
Engine cycle	Four-stroke, spark ignited
Engine displacement	0,992 liter
Engine max. power	135 kW
Engine max. torque	279 N.m
Engine max. speed	5750 rpm
Crank radius	42.3 mm
Bore x Stroke	70.5 x 84.7 mm
Bore pitch	86.7 mm
Volumetric compression ratio	14.0:1
Connecting rod length	144 mm
Stroke to bore ratio	1.2

Connecting rod ratio	0.295
Crankshaft offset (thrust side)	8 mm
Piston offset (thrust side)	0.5 mm

Source: Author

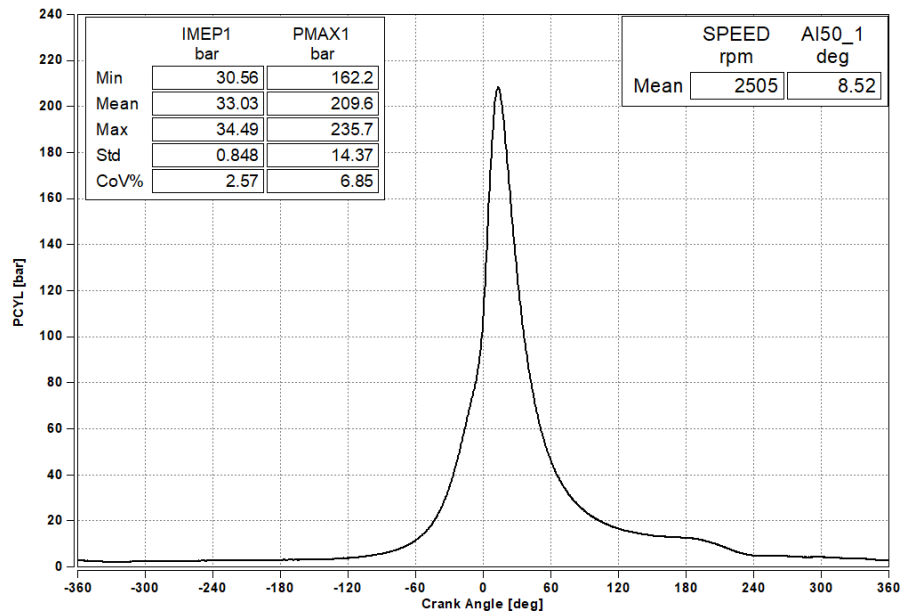
Once the basic engine specifications were defined for the engine developed in this, the engine elements design were made using it as reference.

3.3. Engine Components Design

In this topic it will be presented the engine components design following the data published in Table 32 and the experimental results presented by Baêta et al. (2018). The results presented by Baêta et al. (2018) showed an engine full spark authority under higher loads running on hydrous ethanol and assisted by port water injection. Which means, to operate the engine at IMEP > 30bar, on stoichiometric condition and at MBT (Maximum Brake Torque). However, the prototype engine hardware used for those tests was not suitable to bear such high load level constantly. According to Köhler (2011), the absolute highest in-cylinder pressure (P_{MAX}) value that should be used for an engine components design is the average value of P_{MAX} added by double or triple of P_{MAX} standard deviation. Considering the triple positive standard deviation (+3 σ) design approach means that 99.9997% of the engine cycles are considered as probable engine working condition. Thus, an engine components would be able to withstand a mechanical load higher than average value of P_{MAX}.

For HBS22 components, it was considered from Baêta et al. (2018) study the average maximum pressure and its triple standard deviation as engine running condition reference. Figure 141 shows the in-cylinder pressure trace used as reference for the HBS22 components design. The results presented a mean maximum in-cylinder pressure (P_{MAX_AVG}) of 209.6 bar and an in-cylinder maximum pressure standard deviation (P_{MAX_STD}) of 14.37 bar. Therefore, the maximum in-cylinder pressure that was probable to occur (P_{MAX3SG}) is calculated using Equation 195.

Figure 141 – Reference in-cylinder pressure trace for the engine components design



Source: Adapted from (BAËTA; SILVA; NETTO; MALAQUIAS et al., 2018).

$$P_{MAX3SG} = 209.6 + 3 \times 14.37 = 252.71 \approx 253 \text{ bar} \quad (195)$$

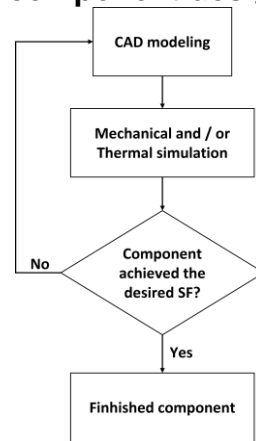
The gas force was calculated considering the in-cylinder peak pressure of 253 bar and the cylinder area using Equation 196.

$$F_{gas} = 25300 \cdot \frac{\pi \cdot 0.0705^2}{4} = 98.76 \text{ kN} \quad (196)$$

The engine components design process followed the steps presented in Figure 142. Firstly, a base component geometry was modeled in CAD considering the engine specification, the references presented in the topic 2.3 of this work, and the components geometries developed by engine manufactures available in the market. Following the base component geometry modeling, it was applied the mechanical and thermal loads on the component in order to evaluate if it was suitable for the engine working conditions. This second step was performed considering the component material properties, the forecasted working boundary conditions, and the component fatigue factor of safety. The fatigue factor of safety was defined individually for each engine component based on its application and manufacturing process. If the simulation results did not achieve the established Safety Factor (SF), the first and second steps were repeated until it's be satisfied. Further than individual component

evaluation, the engine overall assembly was evaluated in relation to the clearances between components and the fastening process.

Figure 142 – Engine component design process flowchart



Source: Author

3.3.1. Engine Skeleton Layout

In order to better manage the engine elements design and the engine components assembly into the CAD software, it was created an Engine Skeleton Layout (ESL) file. The ESL file has the main elements sizes and geometries assembly constrains. Thus, any modification in a specific engine part could be evaluated according to the engine overall layout.

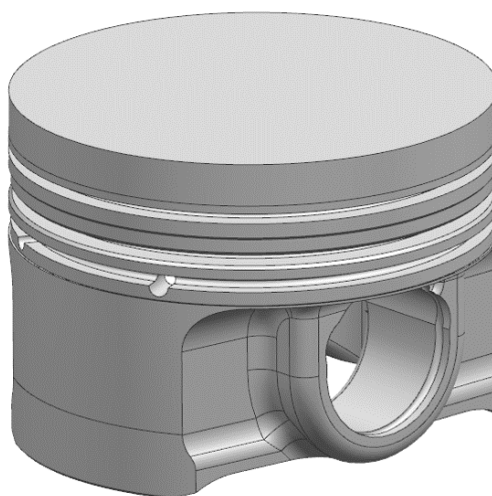
3.3.2. Engine Piston and Piston Rings

As presented in the topic 2.3.4 of this work, the engine piston must bear the heat and pressure from the combustion process. The engine piston for the HBS22 must bear 253 bar of pressure which is similar to diesel engine mechanical load working condition. Therefore, in order to initially model a piston for such high mechanical load, it was used as reference the dimension relation for a diesel piston presented in the Table 6. The Table 33 presents the initial HBS22 piston dimension relation. Aiming to keep the inertial force as lower as possible, the piston skirt was designed as box type. Furthermore, it was designed asymmetrically in order to reduce the piston weight and piston friction loss. Figure 143 illustrates the base engine piston CAD model.

Table 33 – The initial HBS22 piston dimensions relation

Total height GL/D	0.7
Compression height KH/D	0.5
Top land height [mm]	7
1 st ring land height St/D*	0.1
Groove height for 1 st piston ring [mm]	1.5
Skirt length SL/D	0.5
Pin boss spacing NA/D	0.35
Crown thickness s/D	0.07

Source: Author

Figure 143 – Base engine piston CAD model

Source: Author

The piston designed for the HBS22 considered the forging and CNC machining as manufacturing process. The forging manufacturing process improves the piston mechanical strength which is favorable for its high mechanical load application and the CNC machining process promotes a smooth piston surface finish and a close to nominal geometry. (Mahle 2016)

The piston material was chosen from Mahle (2016) materials datasheet. the M-SP25 it was defined as the piston material considering the high mechanical load to applied on it. The M-SP25 is a silicon-free aluminum alloy used exclusively for forged pistons which presents favorable mechanical strengths suitable for severe engine

applications such as racing engines. The Table 34 presents the M-SP25 aluminum alloy mechanical properties.

For the HBS22, it will be use a center injector and spark-plug layout as will be presented in the following topics. Considering this injector and spark-plug layout and the effects of a flat piston surface versus bowl-shaped piston on in-cylinder flow pattern (Figure 144 - (a)) presented by Ikeya et al. (2015), it was designed a bowl-shaped piston crown as a primary piston crown geometry proposal. Figure 144 – (b)) presents the piston CAD model with a bowl-shaped piston crown.

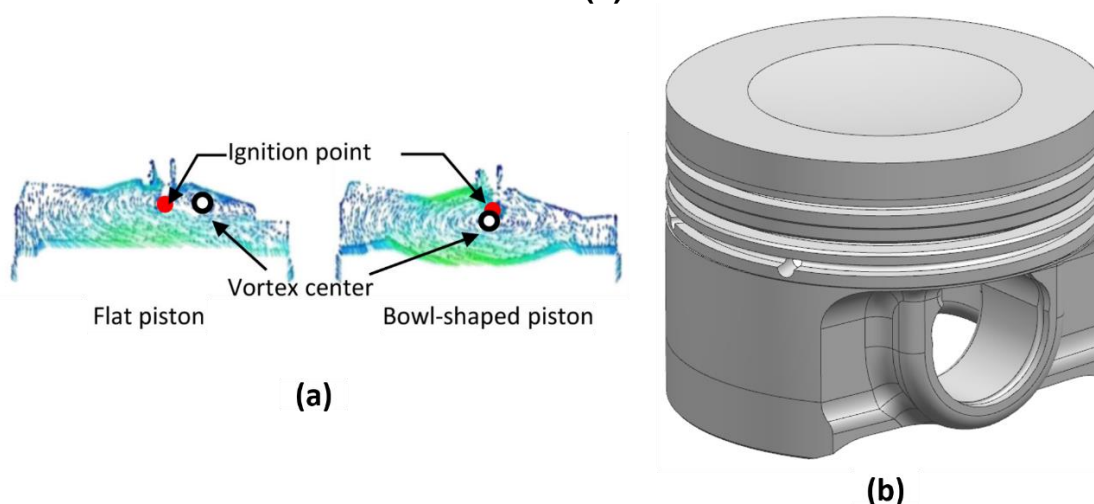
Table 34 – The M-SP25 aluminum alloy mechanical properties

Hardness HB10	20°C	120-150
Tensile strength R_m [MPa]	20°C	350-450
	150°C	350-400
	250°C	130-240
	300°C	75-150
Yield strength $R_{p0,2}$ [MPa]	20°C	320-400
	150°C	280-340
	250°C	90-230
	300°C	50-90
Fatigue strength under reversed bending stress σ_{bw} [MPa]	20°C	120-150
	150°C	110-135
	250°C	55-75
	300°C	40-60
Young's modulus [MPa]	20°C	73500
	150°C	68500
	250°C	64000
	300°C	62000
Thermal conductivity [W/mK]	20°C	140
	150°C	155
	250°C	165

	300°C	170
Thermal expansion [10^{-6} m/mK]	20-100°C	22.4
	20-200°C	24.0
	20-300°C	24.9
Density ρ [g/cm ³]	20°C	2.77

Source: (MAHLE, 2016b)

Figure 144 – In-cylinder flow pattern comparison between flat piston vs. bowl-shaped piston (a), and piston CAD model with a bowl-shaped piston crown (b)



Source: (IKEYA; TAKAZAWA; YAMADA; PARK et al., 2015) and Author

As aforementioned, a lower connecting rod ratio leads to a higher piston dwell time at TDC. Which in turn, it has a positive effect on the engine working cycle which tends to closer to an ideal cycle. On the other hand, it has a negative effect on the engine thermal efficiency due to the combustion flame front heat losses to the combustion chamber walls. In order to minimize the heat losses, it was applied a TBC on the piston crown. It was defined the MgZrO₃ as the coating and NiCrAl as the bond materials, respectively. The MgZrO₃ was selected as coating material due to its lower thermal conductivity and lower thermal expansion compared to other ceramic coatings. Furthermore, its Young's modulus closer to the piston material Young's modulus leads

to a lower stress between the coating layer and the substrate. The NiCrAl provides a strong bond between the coating layer and the substrate mainly under the working temperature limits due to its adhesion strength. Furthermore, the NiCrAl thermal expansion coefficient in between that of the TBC and substrate improves the coating adhesion, as mentioned by Dhomne and Mahalle (2018). The chemical effect of the ethanol as fuel on the TBC was not found available in the literature. Hence, a further investigation is required about it which is out the scope of this work. The Table 35 presents the TBC materials properties used for the piston coating.

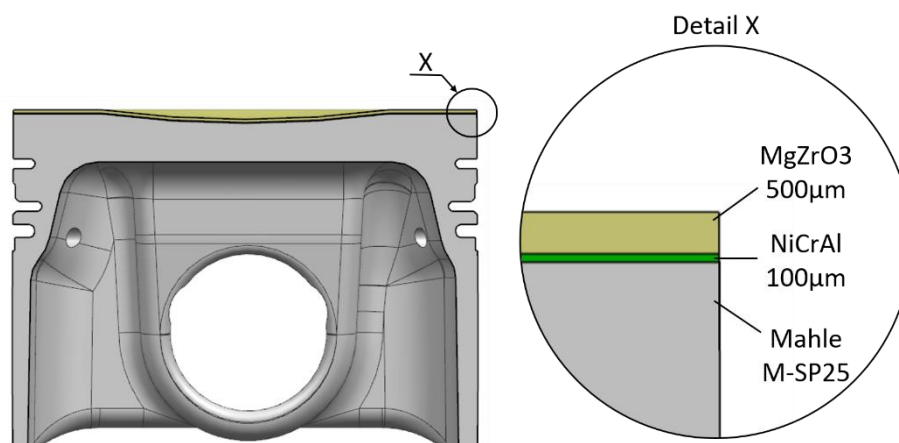
Table 35 – The TBC materials properties

Properties	MgZrO ₃	NiCrAl
Young's modulus [MPa]	46	90
Poisson`s ratio	0.2	0.27
Thermal conductivity [W/mK]	0.8	16.1
Thermal expansion [10^{-6} m/mK]	8	12
Density ρ [g/cm ³]	5600	7870
Specific heat [J/kg. °C]	650	764

Source: (Dhomne and Mahalle 2018)

In addition to the TBC material, the coating thickness is another important parameter to be defined. Considering that the aim of this work is not to evaluate the piston temperature variation in function of the coating thickness, along with the statement that the piston temperature in function of the coating thickness presented a non-linear relationship, it was defined the TBC thickness as the average thickness of the studies presented in the topic 2.5.4.2. Thus, the MgZrO₃ coating and NiCrAl bond layers were modeled being 500 μ m and 100 μ m thick, respectively.

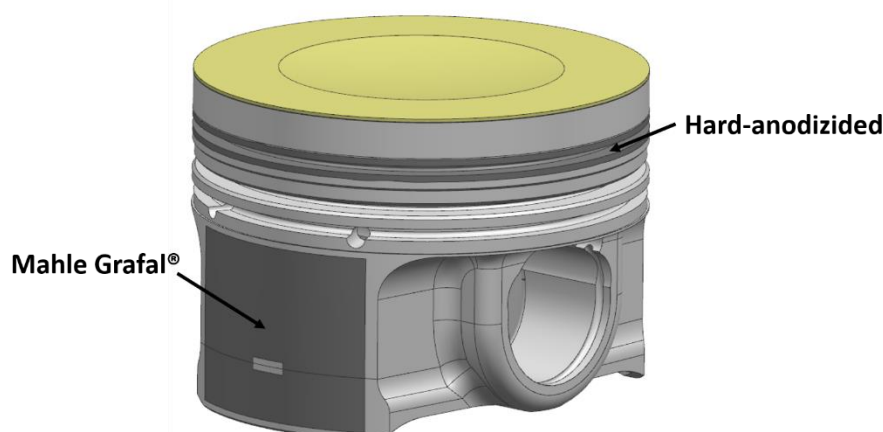
Figure 145 – Piston Ceramic Thermal Coating Barrier



Source: Author

Further than piston crown, the piston first groove and the piston skirt were also coated, as shown in Figure 146. The piston first groove was locally hard-anodized with a coating thickness of 15µm, in order to eliminate the contact between the piston ring groove and the piston ring preventing micro-welding to occur. The piston skirt was coated with a 20 µm thickness of fine graphite particles embedded in a polymer matrix. This provides great seizure resistance for very low clearances and a lack of oil. The company Mahle calls this skirt coating product of Grafal®. The piston pin boss is another region that is usually coated. However, it was not coated in the HBS22 piston considering that the piston pin is intended to be coated.

Figure 146 – Piston ring and piston skirt coatings



Source: Author

The piston ring belt was defined to use the standard three rings layout. Evaluating the engine manufactures pistons available for this work development and the piston rings heights for diesel engines in Kolbenschmidt (2019) catalog, it can be seen that high load engines requires thicker piston rings. Thus, it was defined 1.5, 1.5

and 2 mm as the piston rings heights for the first and second rings, and the oil control ring, respectively. In order to minimize the engine components validation process, it was determined to use the piston rings already available in the market. It is worth to point out that a further piston ring improvement would be to use a rectangular barrel section for the first piston ring and a taper faced napier section for the second ring. These piston ring sections have been used in modern engines in order to better seal the combustion chamber and control the oil scraping process. As the Kolbenschmidt (2019) catalog has not these type of piston ring for dimensions close to use in the HBS22, it would be required to manufacture a specific ring packs for HBS22 application. The piston rings height clearance was defined as 0.05 mm according suggested by Kolbenschmidt (2019). The piston ring gap for the first and second rings was calculated based on the Table 7 and Equation 59. Considering the turbocharger application on the Table 7, it was defined a ring gap factor of 0.0060", 0.0063" and 0.015" for the first, second and oil ring, respectively. It was established a larger gap factor for the second in order to promote a higher stability of the top ring preventing an inter-ring pressure building up and lifting it off the piston groove flank. The rings gap related to the engine bore were calculated using Equation 197, Equation 198 and Equation 199, respectively. It is worth to point out that, these piston rings gap can be adjusted aiming to minimize the blow-by during future experimental tests. The Table 36 presents the characteristics of piston rings used in the HBS22.

$$Gap_{FirstRing} = 0.0060 \times \left(\frac{71.5}{25.4}\right) = 0.01689" \approx 0.43 \text{ mm} \quad (197)$$

$$Gap_{SecondRing} = 0.0063 \times \left(\frac{71.5}{25.4}\right) = 0.01773" \approx 0.45 \text{ mm} \quad (198)$$

$$Gap_{OilRing} = 0.015 \times \left(\frac{71.5}{25.4}\right) = 0.04222" \approx 1.07 \text{ mm} \quad (199)$$

Table 36 – The HBS22 engine piston rings

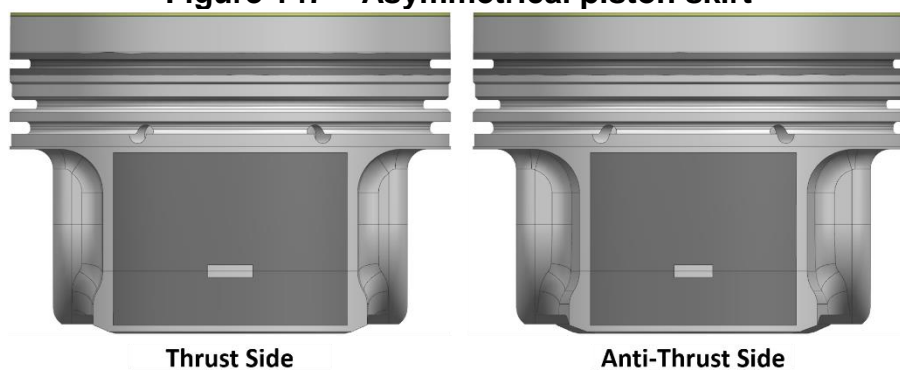
Application	First Ring	Second Ring	Third Ring
Ring Type	Rectangular	Taper faced	Steel rail spring washer
Material	Steel		
Surface Coating	Nitrided	-	Nitrided

Ring height [mm]	1.5	1.5	2.0
Max. Radial Thickness [mm]	2.35	2.6	2.3
Cylinder nominal diameter [mm]	73.0	73.0	73.4
Ring gap	0.43	0.45	1.07
Type of charging	Supercharged with charge air cooling		
Kolbenschmidt Part Number (PN)	80.00580.1.0.000	80.00580.1.0.050	80.00710.1.0.050

Source: Author

In order to design a lightweight piston and minimize the contact path between piston and cylinder liner, the HBS22 piston was designed with an asymmetrical piston skirt, as shown in Figure 147. The piston skirt on the anti-thrust side is smaller than the piston skirt on the thrust side. The piston skirt on the thrust side of an asymmetrical piston is designed with optimum load bearing and friction characteristics. On the other hand, the piston skirt on the anti-thrust side can be smaller considering that it bears a lower thrust load and its main function is to promote a piston stability throughout the engine strokes.

Figure 147 – Asymmetrical piston skirt



Source: Author

The piston geometry is going to be trimmed in order to consider the piston to valve clearances, piston pin lubrication and mechanical stress reduction due to piston pin deformation.

The piston strength was evaluated considering the combined effect of the thermal and mechanical load on it. The thermal and load conditions were evaluated considering the worst conditions between engine maximum torque and maximum

power. The mechanical load on the piston was considered as the gas and inertial force acting on it. It will be calculated later in this work after the piston pin and connecting rod geometry modeling. The thermal load was calculated based on the experimental condition presented in Figure 141 following the methodology presented by Sroka (2012), Esfahanian et al. (2006), Li (1982), Abbas et al. (2004) and Yaohui Lu et al. (2017).

For the thermal load calculation, it is necessary to calculate the piston thermal boundary conditions. The piston thermal boundary conditions consist of:

- The ring land and skirt thermal boundary condition;
- Piston underside thermal boundary condition;
- Piston pin thermal boundary condition;
- Combustion side thermal boundary condition.

The ring land and skirt thermal boundary condition were calculated using the thermal circuit resistances method to model the heat transfer in these regions, as illustrated in the . However, the following assumptions were made:

- The effect of the piston motion on the heat transfer is neglected;
- The rings and skirt are fully engulfed in oil and there are no cavitation;
- The rings do not twist;
- The only heat transfer mode in the oil film is assumed to be conduction.

Figure 148 – Thermal circuit resistances model



Source: Author

The resistances R1, R2, R3 and R4, in [$m^2.K/W$], are the ring resistance, the oil film resistance, the liner resistance and the water-jacket resistance, respectively. The ring resistance, the oil film resistance, the block resistance and the water-jacket resistance are calculated using Equation 200, Equation 201, Equation 202, Equation 203, respectively.

$$R_1 = \frac{\ln(r_2/r_1)}{2 \cdot \pi \cdot H_1 \cdot k_{ring}} \quad (200)$$

$$R_2 = \frac{\ln(r_3/r_2)}{2 \cdot \pi \cdot H_2 \cdot k_{oil}} \quad (201)$$

$$R_3 = \frac{\ln(r_4/r_3)}{2 \cdot \pi \cdot H_3 \cdot k_{liner}} \quad (202)$$

$$R_4 = \frac{1}{h_{water} \cdot A_{eff_coolant}} \quad (203)$$

Where r_1, \dots, r_4 are inner radius of the ring in [m], outer radius of the ring in [m], bore radius in [m] and inner radius of the water-jacket in [m], respectively. The H_1, H_2 and H_3 are the widths of the heat transfer paths in [m]. k_{ring}, k_{oil} and k_{liner} are ring, oil and liner thermal conductivity in [W/m.K]. $A_{eff_coolant}$ is the effective area in contact with the coolant in [m²]. h_{water} is the convective heat transfer coefficient in the water-jacket in [W/m².K].

The effective heat transfer coefficient, h_{eff} in [W/m².K], is obtained using Equation 204.

$$h_{eff} = \frac{1}{R_{tot} \cdot A_{eff_coolant}} \quad (204)$$

Where R_{tot} is the sum of the thermal circuit resistances model in [m².K /W]

The h_{water} is estimated based on the engine water-core CFD simulation. However, it will be used the value of 1500 W/m².K as suggested by Esfahanian et al. (2006) for a first thermal load calculation. Due to the lack of specific ring material properties, the k_{ring} was considered 44.5 W/m.K which is a typical thermal conductivity of a 4340 steel commonly used to manufacture piston rings. Due to the lack of oil thermal properties from oil lubricant manufactures datasheet, The k_{oil} was considered 0.136 W/m.K according to the table A.5 available in Incropera et al. (2011) for an oil temperature of 383 K. Based on the cylinder liner material, ASTM A536-84, the k_{liner} value was defined as 32 W/m.K.

In some part of the engine cycle the ring pack is in contact with the upper surface of the ring groove and during the remaining cycle duration, it is in contact with the lower surface of the ring groove. According to Li (1982), the heat transfer path is from the upper surface for 32% of the engine cycle and 68% of the engine cycle, it is from lower

surface of the ring groove. Thus, the rings effective heat transfer coefficient were calculated according to this upper and lower heat transfer path relation. Furthermore, the inner face of the ring groove was assumed to be adiabatic.

Since there is a small gap between piston and the liner at the piston top land, the captured gas temperature was considered as the mean temperature of the crevice surfaces. Therefore, the heat is conducted through the gas with the heat transfer coefficient, k_{gas} in [W/m.K]. The heat transfer is modeled with a convective heat transfer to the cylinder wall, h_{top_land} in [W/m².K], according to Equation 205.

$$k_{gas} \cdot \frac{T_{piston} - T_{liner}}{\delta} = h_{top_land} \cdot (T_{piston} - T_{liner}) \therefore h_{top_land} = \frac{k_{gas}}{\delta} \quad (205)$$

Where T_{piston} is the piston crown temperature in [K], T_{liner} is the liner temperature in [K] and δ is the crevice clearance in [m].

The crevice clearance was considered as 3.5×10^{-4} m as an initial value based on some pistons available in the market used as benchmarking. The k_{gas} was considered to be 0.0602 W/m.K as an extrapolation of the CO₂ gas thermal conductivity, from the table A.4 available in Incropera et al. (2011) , at 875 K. The temperature considered to established in order to calculate the k_{gas} was considered the mean in-cylinder gas temperature as it will presented later in this work.

The convective heat transfer coefficient for the region between the rings was considered 115 W/m.K for an oil temperature of 383 K, as suggested by Li (1982). .

The piston underside heat transfer boundary condition was calculated based on the effects of oil splash cooling system. As it will be presented later in this work, it is intended to use jet oil mechanism for piston cooling. For the piston underside heat transfer boundary calculation, the piston underside was divided into the crown underside and the skirt underside regions. According to Esfahanian et al. (2006), the convective heat transfer coefficient of the crown underside, h_{und_crown} in [W/m².K], and the skirt underside, h_{und_skirt} in [W/m².K], are calculated using Equation 206 and Equation 207, respectively.

$$h_{und_crown} = 900 \cdot \left(\frac{N_{rpm}}{4600} \right)^{0.35} \quad (206)$$

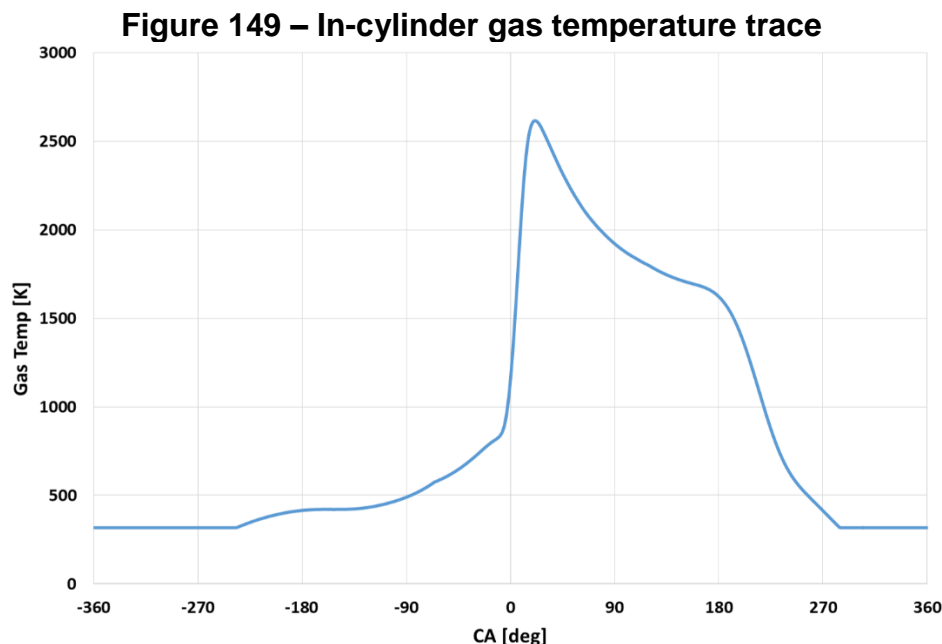
$$h_{und_skirt} = 240 \cdot \left(\frac{N_{rpm}}{4600} \right)^{0.35} \quad (207)$$

Where N_{rpm} is the engine operating frequency in [rpm].

Considering the maximum engine speed presented on Table 32, the h_{und_crown} and the h_{und_skirt} are 973 and 259 W/m².K, respectively.

For the piston pin thermal boundary condition, it was established a heat transfer coefficient of 75 W/m².K for a for an oil temperature of 383 K, as suggested by Li (1982).

The in-cylinder gas temperature was considered as the mean gas temperature throughout the engine cycle. The in-cylinder gas temperature trace, shown in Figure 149, was obtained from the experimental results of Figure 141. The temperature calculation in function of the crankshaft angle explanation can be found in AVL (2012). As this explanation is out of this work context, it was submitted. The average in-cylinder gas temperature was 856 K.



Source: Author

The combustion side convective transfer coefficient, \bar{h}_c in [W/m².K], was calculated as the average of the instantaneous convective transfer coefficient, h_c in [W/m².K], calculated using the Woschini-Classic model presented in Gamma-Technologies (2020). Equation 208 illustrates the Woschini-Classic model.

$$h_c = \frac{K_1 \cdot p^{0.8} \cdot w^{0.8}}{B^{0.2} \cdot T^{K_2}} \quad (208)$$

Where K_1 and K_2 are constants, p is the in-cylinder pressure in [kPa], T is the in-cylinder temperature in [K], B is the cylinder bore in [m] and w is the in-cylinder gas velocity, in [m/s], calculated using Equation 209.

$$w = C_1 \cdot S_p + C_2 \cdot \frac{V_d \cdot T_r}{p_r \cdot V_r} \cdot (p - p_m) \quad (209)$$

Where C_1 and C_2 are constants, S_p is the mean piston speed in [m/s], V_d is the engine displacement volume in [m³], T_r is the fluid temperature prior combustion in [K], p_r is the fluid pressure prior combustion in [kPa], V_r is the fluid volume in [m³] and p_m is the motoring fluid pressure at same angle as p in [kPa]. Table 37 presents the constants values used in the Woschini-Classic model. The calculated combustion side convective transfer coefficient was 1853 W/m².K.

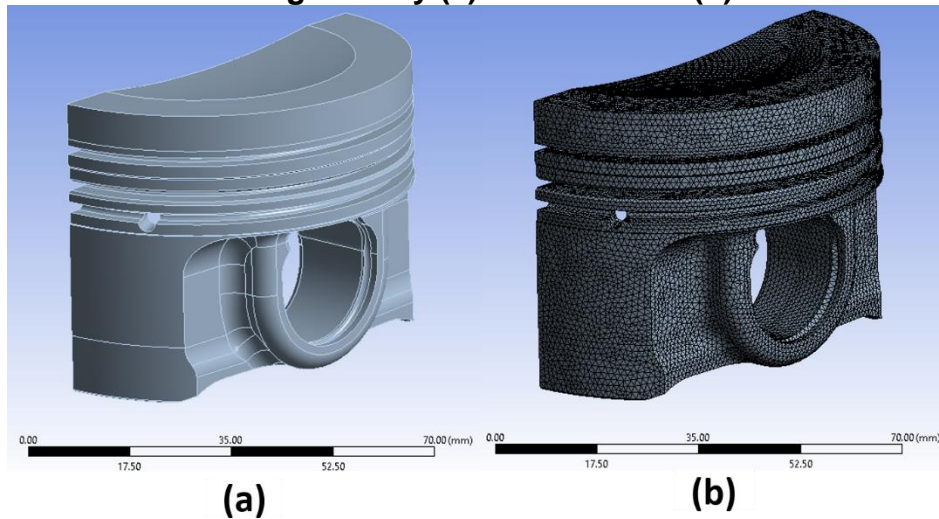
K_1	3.26	
K_2	0.53	
During cylinder gas exchange	C_1	6.18
	C_2	0
During compression	C_1	2.28
	C_2	0
During combustion and expansion	C_1	2.28
	C_2	3.24×10^{-3}

Source: (TECHNOLOGIES, 2020)

Once the thermal boundaries were calculated, the piston CAD geometry was imported into the Ansys software in order to perform the thermal simulation using the FEM method. The piston mesh was made using tetrahedron elements due to the piston geometry complexity and the limited computational power available to perform the simulation. The parameter Mesh Metric Element Quality from Ansys software higher

than 0.60 was used as reference to evaluate the mesh quality as suggested by Nakasone et al. (2006).

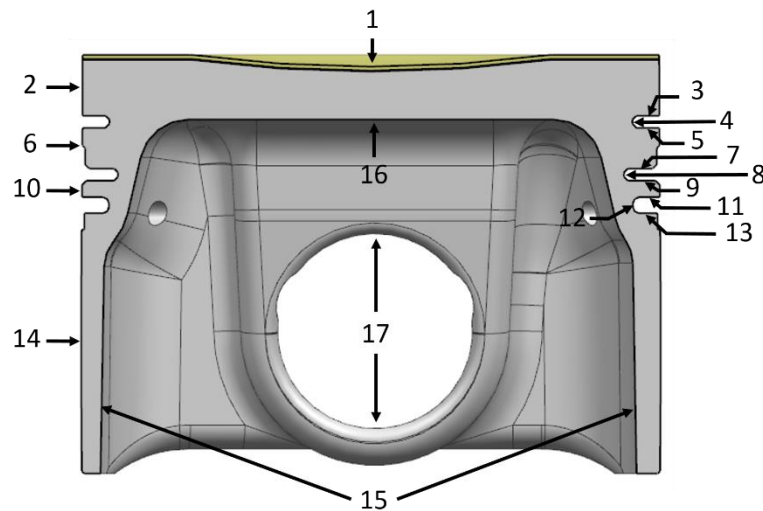
Figure 150 – Piston CAD geometry (a) and its mesh (b) used for simulation



Source: Author

In order to perform the thermal simulation in Ansys, it is required to fill in the software with the convective transfer coefficient and surrounding temperature for characteristic surfaces of the piston. Figure 151 presents the piston characteristic surfaces used for the thermal simulation and Table 38 shows the boundary condition values for each piston characteristic surfaces used for the thermal load simulation.

Figure 151 – Piston characteristic surfaces used for thermal simulation



Source: Author

Table 38 – Piston thermal boundary conditions for thermal simulation

Index	h [W/m ² .K]	T [K]	Description
1	1853	583	Piston crown
2	172	90	Top Land
3	993	90	First ring up
4	-	-	First ring back
5	2111	90	First ring down
6	115	90	Second land
7	775	90	Second ring up
8	-	-	Second ring back
9	166	90	Second ring down
10	115	90	Third land
11	1037	90	Third ring up
12	-	-	Third ring back
13	2204	90	Third ring down
14	1582	90	Skirt outside
15	259	110	Skirt inside
16	973	110	Piston crown underside
17	75	110	Pin boss

Source: Author

In order to compensate the piston thermal and mechanical load deformation, the piston was designed considering a barrel and ovality shape values presented in Table 39. The reference measure planes presented in Table 39 are illustrated in Figure 152. The plane DN was considered as the reference plane for clearance values between piston and liner. The TA and PA dimensions in Figure 152 indicate Thrust Axis and Pin Axis, respectively.

The Figure 153 illustrates a piston geometry comparison between a piston applied to a regular flex-fuel engine and the piston designed for HBS22. The piston applied to a flex-fuel engine has a similar bore size as the piston designed for HBS22. On same scale, it can be realized that the piston designed for HBS22 has higher piston

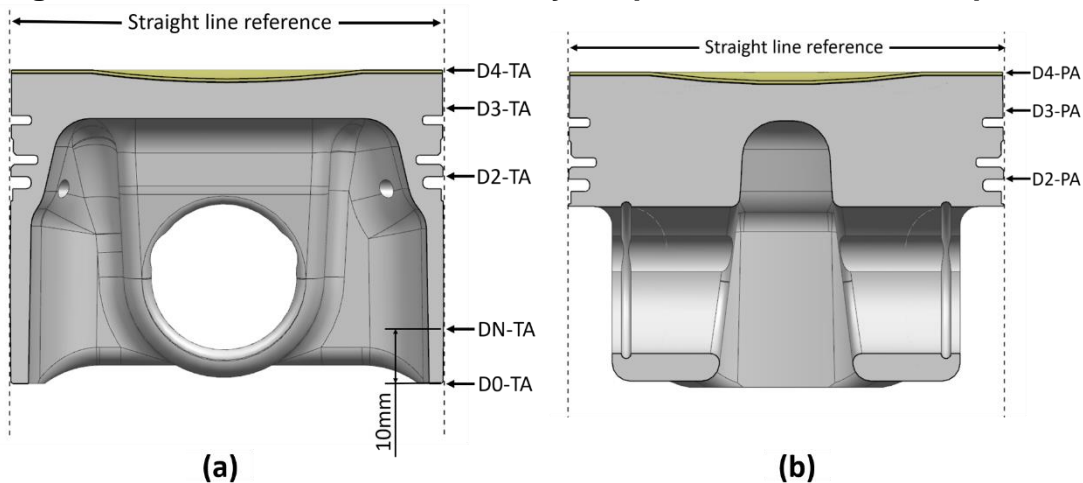
lands and compression height, thicker rings grooves and larger piston pin boss than the piston applied to a flex-fuel engine. These characteristics enables HBS22 to operate at higher loads (IMEP > 30bar) and exploit the ethanol fuel potential which it was not possible considering the normal design concepts applied to piston development.

Table 39 – Piston barrel and ovality shape values

Reference Measure	Value
D0-TA	0.13
DN-TA	0.07
D2-TA	0.16
D3-TA	0.22
D4-TA	0.23
D2-PA	0.13
D3-PA	0.23
D4-PA	0.28

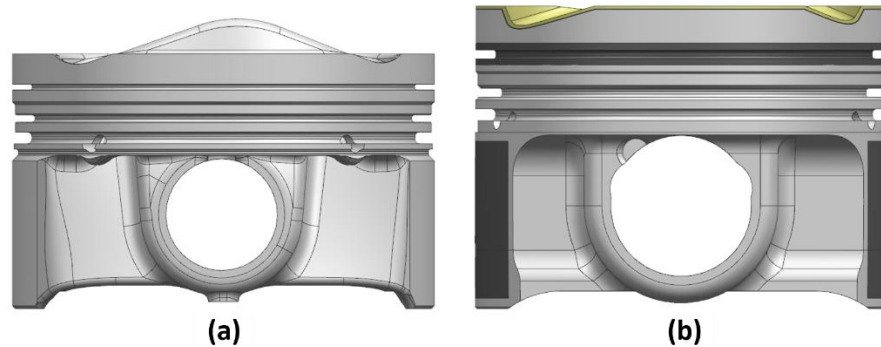
Source: Author

Figure 152 – Piston barrel and ovality shape reference measure planes



Source: Author

Figure 153 – Piston geometry comparison between a piston applied to a flex-fuel engine (a) and the piston designed for HBS22 (b)



Source: Author

3.3.3. Piston Pin

The piston pin is the mechanical connection between the piston and the connecting rod. Which in turn, it must to bear the gas and the inertia forces. The piston pin boss diameter, d_1 , of 24 mm was defined according to piston pins designed by engine manufactures for a similar engine working condition. The piston pin boss diameter to bore ratio calculated by Equation 210 presented a result that fitted the Diesel engine applied to a passenger car in the Table 33 albeit the engine designed in this work is not a diesel engine.

$$\frac{d_1}{B} = \frac{24}{71.5} = 0.336 \quad (210)$$

Where B is the cylinder bore in [mm].

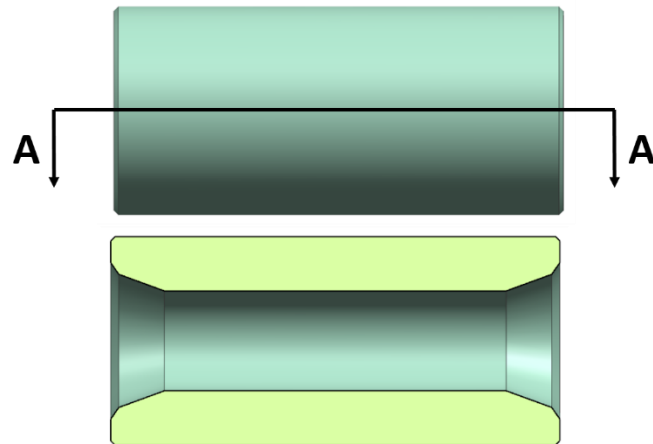
The piston pin inner diameter, d_2 in [mm], and length, l_1 in [mm] for the first proposed geometry were calculated using Equation 211 and Equation 212, respectively, based on the average ratios presented in the Table 33 for a diesel engine applied to a passenger car.

$$d_2 = d_1 \times 0.480 = 11.52 \approx 11.5 \text{ [mm]} \quad (211)$$

$$l_1 = B \times 0.725 = 51.83 \approx 51.8 \text{ [mm]} \quad (212)$$

Figure 154 illustrates the piston pin preliminary geometry.

Figure 154 – Piston pin geometry

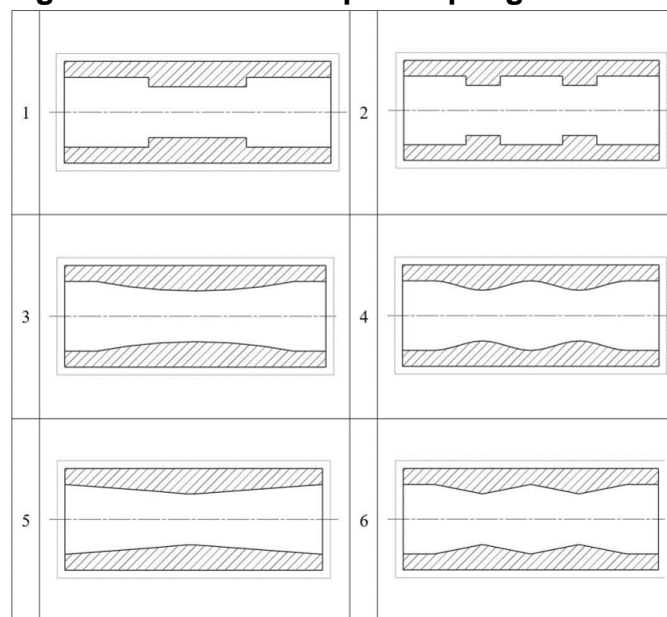


Section A-A

Source: Author

Different internal piston pin geometries have been studied as presented in Figure 155 aiming to optimize its weight regarding the loads required to withstand. However, the high complexity internal geometry leads to an expensive and time consuming manufacturing process. Therefore, the piston pin designed for HBS22 was based on the hollow cylinder geometry with conical ends.

Figure 155 – Different piston pin geometries



Source: (Bohn 2016)

It was defined the nitride steel as the piston pin material due its better volume stability compared to case-hardened steel. Furthermore, it was considered a DLC

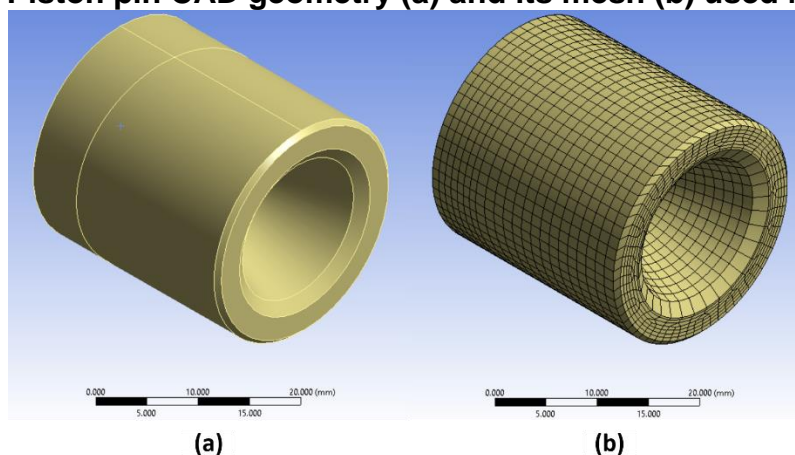
coating thickness of 3 μm aiming to decrease the piston pin friction. The Table 9 presents the piston pin material properties.

The initial clearance, C in [μm], among piston, piston pin and connecting small end bore of 0.0019 times the piston pin diameter as an average of the range suggested by Strozzi et al. (2018) presented in topic 2.5.5 of this work. Equation 213 presents the calculated initial clearance among piston, piston pin and connecting small end bore.

$$C = 0.0019 \times d_1 = 0.0019 \times 24 = 45.6 \mu\text{m} \quad (213)$$

The piston pin was imported into Ansys for mechanical stresses simulation. It was considered 110°C as the piston pin working temperature during the mechanical loads simulation. Due to the piston pin symmetry, the simulation was performed using half of piston pin. The simpler piston pin geometry allows to use hexahedral finite element. The parameter Mesh Metric Element Quality from Ansys software higher than 0.60 was used as reference to evaluate the mesh quality as suggested by Nakasone et al. (2006). Figure 156 illustrates the piston pin CAD geometry and piston pin mesh used for simulation.

Figure 156 – Piston pin CAD geometry (a) and its mesh (b) used for simulation



Source: Author

3.3.4. Piston Circlip

The fully floating pin approach was defined for piston, connecting rod and piston pin assembly due to the high load engine working load. Thus, a piston circlip was

required to hold the piston pin in place. Based on the common circlip geometry applied to engines for a similar engine application, it was defined a round spring wire of 1.6 mm diameter manufactured using DIN EN 10270-1 material. Furthermore, as the piston pin outer diameter of 24 mm, the circlip diameter in the clamped state was also 24 mm.

For the engine designed in this work, it was considered a circlip without hooks in order to have the manufacturing process as simple as possible and keep a lower circlip mass. The lower circlip mass allows the engine to achieve higher speeds. Considering the aforementioned circlip characteristics, the maximum allowed engine speed became a parameter that can be calculated in function of the circlip diameter in the unclamped state. This unclamped circlip diameter established the circlip radial tension in the clamped state. The DIN permissible tolerances for the wire diameter, the diameter of the unclamped ring and the groove base diameter include an uncertainty of 2,000 rpm and more, according to Kohler (2011). Thus, it was defined 3500 rpm over the engine maximum speed as the allowable engine speed for the circlip design. The maximum engine speed allowable for a round circlip without hooks, $\omega_{\max_circlip}$ in rad/s, was calculated using Equation 60. As the circlip is made of steel, the term $\sqrt{E/\rho}$ was considered as 5.17×10^3 m/s. Considering a circlip diameter of 26.1 mm in the unclamped state, the defined maximum allowable engine speed was achieved as calculated by Equation 214.

$$\frac{0.3162 \times 0.0016 \times 5.17 \times 10^3}{0.024 - 0.0016} \cdot \left(\frac{\frac{1}{(0.024 - 0.0016)} - \frac{1}{(0.0262 - 0.0016)}}{0.043 \cdot (1 + 0.295)} \right)^{\frac{1}{2}} \quad (214)$$

$$= 970 \text{ rad/s} \approx 9265 \text{ rpm}$$

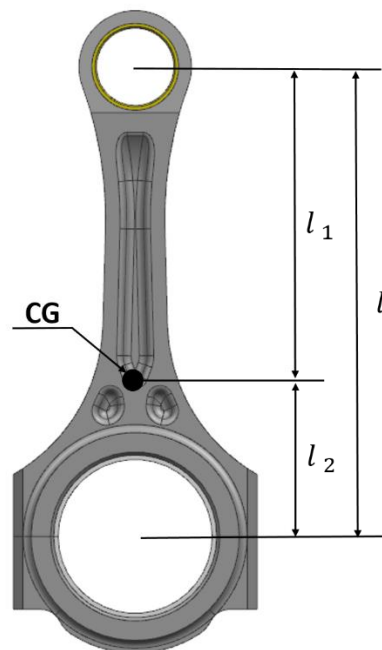
3.3.5. Connecting rod

The connecting rod is a complex engine component which has to withstand compressing, tension and bending loads. As presented in the topic 2.3.7, there are several connecting rod shank profiles that are suitable for different engine application. For HBS22, it was defined an I-section shank profile due to its easier manufacturing

process, lower out-of-plane buckling tendency at high loads and lower contact stresses at the connecting rod pin-eye ends. The connecting rod small end bore was designed considering a press fitted bushing bearing of 1.5 mm thickness with an inner diameter of 24.0 mm. Furthermore, it was considered an The connecting rod big end bore diameter of 50.612 mm was defined based on the crank pin and bearings diameter as presented further in this work. Figure 157 illustrates the connecting rod geometry designed for HBS22.

The total connecting rod length l of 144 mm was calculated in the topic 3.2.6 of this work. Considering the connecting rod geometry designed and its material, the connecting rod center of gravity (CG) resulted in a distance l_1 of 104.57 mm. Consequently, a distance l_2 of 38.43 mm was obtained. These dimensions will be used for connecting rod alternate and rotational mass calculation later in this work.

Figure 157 – Connecting rod geometry



Source: Author

As considered for the piston manufacturing, the forging and CNC machining was defined as manufacturing process for the connecting rod. However, it was defined that the connecting rod big bore will be divided via cracking process. Due to the engine high load working condition predicted, it was defined the 36MnVS4 as material for the connecting rod. Furthermore, it was defined the KS S705 as bushing material for the connecting rod small end bore. The material properties of 36MnVS4 and the KS S705 are presented in the Table 10 and Table 40, respectively.

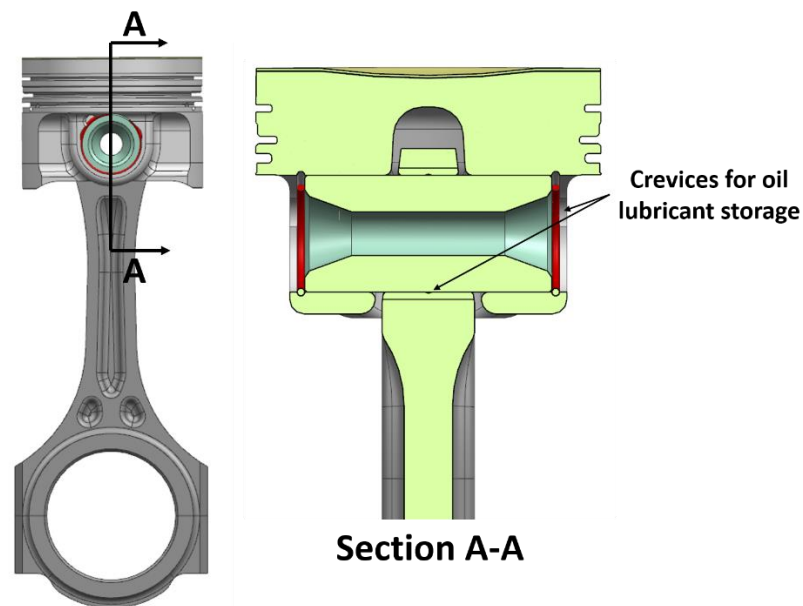
The connecting rod small bore was designed with a tapered profile in order to reduce the connecting rod alternate mass and minimize the contact pressure between piston, piston pin and connecting rod. The connecting rod small end bore lubrication is intended to be made by engine oil lubricant which enter in the clearance between piston pin and piston pin bosses. Furthermore, crevices were designed in the connecting rod small bore bushing and in the piston boss in order to storage oil lubricant. Figure 158 illustrates the tapered connecting rod small end bore and the crevices designed for oil lubricant storage.

Table 40 – Connecting rod bushing material properties (KS S705)

Properties	Value
Young Modulus [GPa]	110
Yield strength [MPa]	>380
Thermal expansion coefficient [K^{-1}]	450 - 600
Thermal conductivity [$W.(m.K)^{-1}$]	80

Source: (Kolbenschmidt 2019)

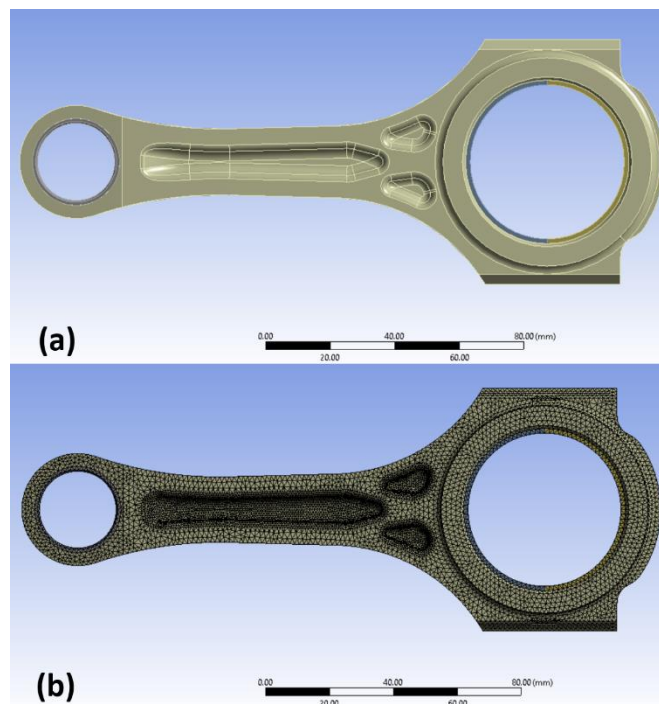
Figure 158 – Connecting rod tapered small end bore design



Source: Author

The connecting rod was imported into Ansys for mechanical stresses simulation. It was considered 110°C as the component working temperature during the mechanical loads simulation. Due to the connecting rod symmetry, the simulation was performed using half of it. The connecting rod mesh was made using tetrahedron elements due to its geometry complexity and the limited computational power available to perform the simulation. The parameter Mesh Metric Element Quality from Ansys software higher than 0.60 was used as reference to evaluate the mesh quality as suggested by Nakasone et al. (2006). Figure 159 illustrates the connecting rod CAD geometry and the connecting rod mesh used for simulation.

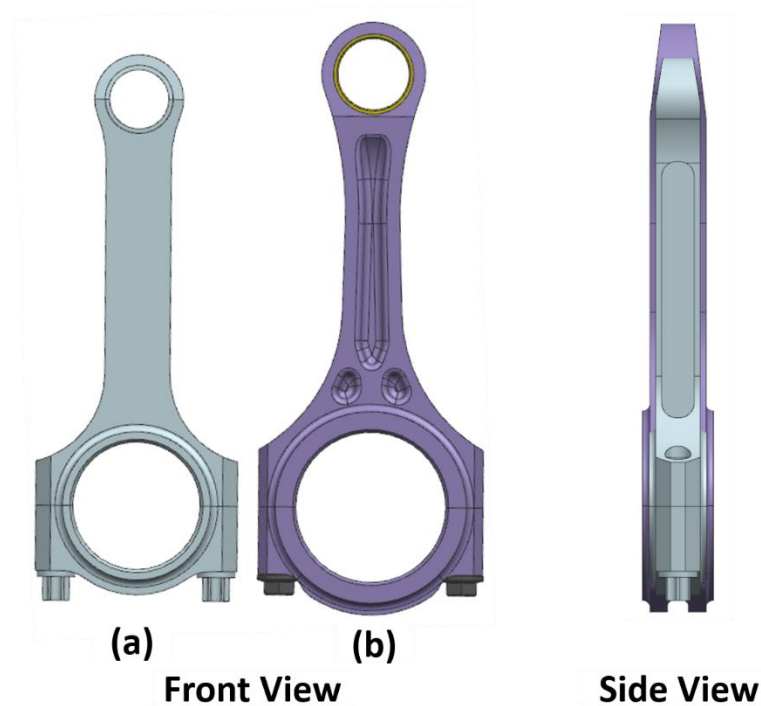
Figure 159 – Connecting rod CAD geometry (a) and its mesh (b) used for simulation



Source: Author

The Figure 160 illustrates a connecting rod geometry comparison between a piston applied to a regular flex-fuel engine and the connecting rod designed for HBS22. On same scale, it can be realized that the connecting rod designed for HBS22 has a thicker shoulder, larger shank profile, smoother transition among shank and small and big bores, and thicker groove in forward face than the piston applied to a flex-fuel engine. Furthermore, the longer connecting rod designed for HBS22 compared to the regular connecting rod presented in Figure 160 tends to reduce the engine friction. Therefore, similarly to the piston, the connecting rod design characteristics enables HBS22 to operate at higher loads (IMEP > 30bar) and exploit the ethanol fuel potential which it was not possible considering the normal design concepts applied to connecting rod development.

Figure 160 – Connecting rod geometry comparison between a piston applied to a flex-fuel engine (a) and the piston designed for HBS22 (b)



Source: Author

Once the connecting rod geometry was defined, it was possible along with the piston and piston pin components to calculate the oscillating inertial force. For the oscillating mass was considered the sum of piston, piston pin and connecting rod oscillating mass. Furthermore, it was considered the maximum piston acceleration at 5500 rpm presented in Figure 137. The maximum oscillating inertial force was calculated using Equation 215.

$$F_{Mass\ Osc.\ Off} = -\left(0.403 + 0.799 \times \frac{38.43}{144}\right) \times 18486 = 11391 \quad (215)$$

$$\approx 11500\ N$$

3.3.6. Crankshaft and Bearings

The crankshaft and the flywheel designed for the HBS22 used as reference the in-cylinder pressure results obtained experimentally from Silva (2017) and Baêta et al. (2018). The crankshaft main dimensions were calculated in this topic and evaluated throughout the FEM simulation process. As some main crankshaft dimensions, such as bore pitch and crank radius, were defined earlier in this work. The crankshaft crank pin diameter was the first parameter to be calculated. The steel 42CrMo4 was defined

as the crankshaft material due to its high strength. Furthermore, it was considered the crankshaft to be forged, machined and hardened the crank pins and journals. A SF of 2 was considered for the initial calculations as suggested by crankshaft design guide lines from engine manufactures. Based on the bending moment at maximum in-cylinder pressure that the crankshaft must bear, the crank pin diameter was calculated using Equation 216.

$$d_c = \sqrt[3]{\frac{32 \cdot F_{gas} \cdot b_1}{\frac{S_y}{SF} \cdot \pi \cdot 2}} = \sqrt[3]{\frac{32 \times 98760 \times 43.35}{209 \times \pi \times 2}} = 47.075 \text{ mm} \quad (216)$$

Considering an average notch radius of 1.42 mm, the diameter discontinuity between the journal and the counterweight bridge of 1.24 and the notch radius to journal diameter ratio of 0.03 from crankshafts available in the market for high loads applications, it was established K_t and K_{ts} as 1.156 and 1.130 from using the tables A-15 available in Budynas (2011). Furthermore, considering the average notch radius of 1.42 mm along with Figure 55, it was established the notch sensitivity for bending and torsion loads q and q_{shear} as 0.78 and 0.8, respectively. Thus, the fatigue stress-concentration factors for bending and torsion, K_f and K_{fs} , were calculated using Equation 217 and Equation 218, respectively.

$$K_f = 1 + 0.78 \times (1.156 - 1) = 1.122 \quad (217)$$

$$K_{fs} = 1 + 0.80 \times (1.13 - 1) = 1.104 \quad (218)$$

The alternating and midrange bending moments, M_a and M_m , along with the alternating and midrange torsion torques, T_a and T_m were calculated based on the gas and tangential forces acting on the crankshaft under the in-cylinder pressure presented on Figure 141 and the crank radius. Table 41 presents the alternating and midrange bending and torsion moments

Table 41 – The alternating and midrange bending and torsion moments

Parameter	Value
M_a [N.mm]	1093348

M_m [N.mm]	847965
T_a [N.mm]	445874
T_m [N.mm]	312663

Source: Author

The steel 42CrMo4 endurance limit was calculated following the procedure described in the topic 2.5.2 in this work. Which in turn, it resulted in an endurance limit of 177 MPa. Finally, the input values were replaced in Equation 219 and the crankshaft journal diameter was obtained.

$$\begin{aligned}
 d_{cJ} = & \left\{ \frac{16 \times 2}{\pi} \cdot \left[4 \cdot \left(\frac{1.122 \times 1093348}{177} \right)^2 + 3 \cdot \left(\frac{1.104 \times 445874}{177} \right)^2 \right. \right. \\
 & + 4 \cdot \left(\frac{1.122 \times 847965}{415} \right)^2 \\
 & \left. \left. + 3 \cdot \left(\frac{1.104 \times 312663}{415} \right)^2 \right]^{1/2} \right\}^{1/3} = 53.961 \\
 & \approx 53.960 \text{ mm}
 \end{aligned} \tag{219}$$

The length of the crank pin and crank journal were calculated based on the allowable pressure on the bearings. It was defined to use the bearings from Kolbenschmidt Company on this work due to its large bearings availability for high load engine operation condition. Kolbenschmidt suggest that should be use the bearings KSX20R or KSX20T. These bearings are plain bearing composed of a steel back, a cast on brass layer and an aluminum-in-copper running surface (sputter coat deposited by the PVD method). The KSX20R was chosen to be used on this project. The bearing KSX20R has a load carrying capacity of 110 MPa that was used for the crank pin and crank journal minimum length calculation according Equation 220 and Equation 221, respectively.

$$L_{b-c} = \frac{F_{Gas}}{p_b \cdot D_c} = \frac{98760}{110 \times 47.075} = 19.07 \approx 19.10 \text{ mm} \tag{220}$$

$$L_{b-cj} = \frac{F_{Gas}}{p_b \cdot D_c} = \frac{198760}{110 \times 53.960} = 16.64 \approx 16.65 \text{ mm} \tag{221}$$

As suggested by Kopeliovich (2019) and Clevite (2005) the bearing minimum and maximum clearance, C_{min} and C_{max} in mm, was calculated using Equation 222 and Equation 223, respectively.

$$C_{min} = 0.00075 \times d_{shaft} \quad (222)$$

$$C_{max} = 0.00150 \times d_{shaft} \quad (223)$$

Where d_{shaft} is the crank pin or journal diameter in inches.

Table 42 presents crank pin and journal diameters, the respectively minimum and maximum clearance for them and minimum and maximum bearing internal diameters converted to millimeters.

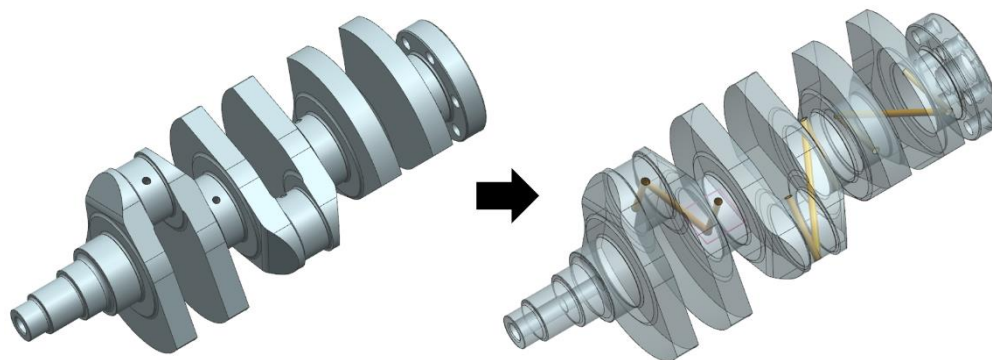
Table 42 – Crankshaft to bearings diameters comparison

Crank pin	C_{min}	C_{max}	Bearing Min. Dia.	Bearing Max. Dia.
47.075	0.035	0.071	47.145	47.217
Crank journal	C_{min}	C_{max}	Bearing Min. Dia.	Bearing Max. Dia.
53.960	0.041	0.081	54.042	54.122

Source: Author

Once the crankshaft main dimensions were calculated, its CAD geometry was created as illustrated in Figure 161. The counterweight thickness and outer diameter were designed to balance the rotational inertia force and minimize the first and second moment order as illustrated in Figure 60. The bearing lubrication were design considering that each crank pin will get oil for its respective crank journal. Furthermore, as suggested by Mavrigian (2013), it was established an axial acceptable clearance between 0.10 to 0.25 mm. The thrust bearing KS79515600 manufactured by Kolbenschmidt were placed in the third crankshaft journal where lower crankshaft distortions tend to occur.

Figure 161 – Crankshaft



Source: Author

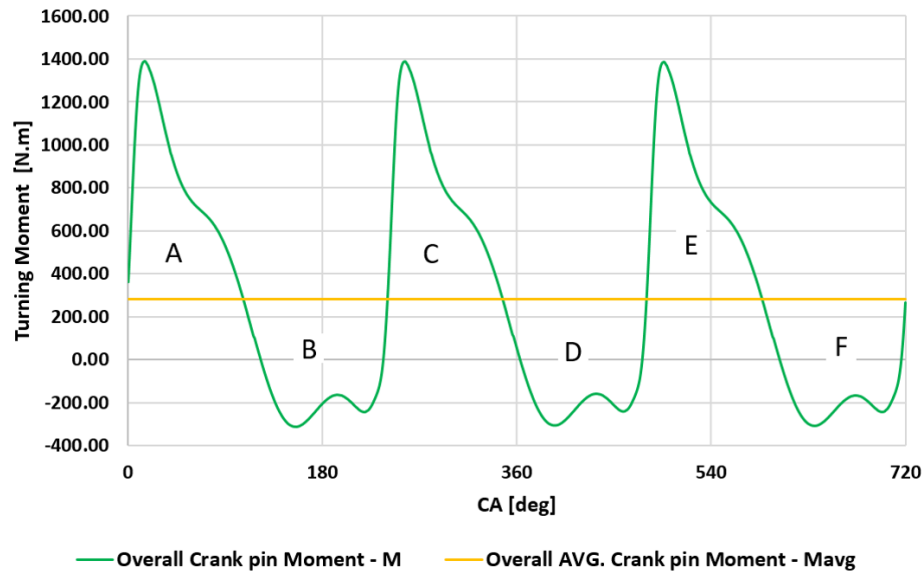
As previously mentioned, the crankshaft torsional balance is achieved by means of a dumper use. Due to a lack of software license it was not possible to calculate a suitable dumper for this project. Therefore, the dumper definition was considered as suggestion for future research. However, a dumper from a similar 3 cylinder engine was fitted to the engine for packaging evaluation and accessory belt layout design.

3.3.7. Flywheel

The flywheel defined to be used on the HBS22 was designed considering the methodology procedure described on topic 2.3.3.1 and an in-cylinder pressure trace experimentally obtained from Silva (2017) engine at idle condition. It was considered the engine idle condition for the flywheel calculation due to lower ignition event frequency.

The rotational kinetic energy was calculated based on areas from torque diagram presented in Figure 162. The areas under the torque diagram curve were calculated using integration Simpson's Rule. Table 43 presents the areas under the torque diagram and the sum of them.

Figure 162 – Torque diagram at engine idle condition



Source: Author

Table 43 – Areas under the torque diagram and the sum of them

Label	Areas	Areas Sum
A	47214	47214
B	-47262	-48
C	47356	47308
D	-47197	111
E	47211	47322
F	-47322	0

Source: Author

Based on values presented in Table 43, the rotational kinetic energy was calculated according Equation 224.

$$W_s = W_{max} - W_{min} = 47322 - (-48) = 47370 \text{ [J]} \quad (224)$$

Considering a degree of irregularity of 0.03 as suggested in Table 4, the flywheel moment of inertia was calculated using Equation 225.

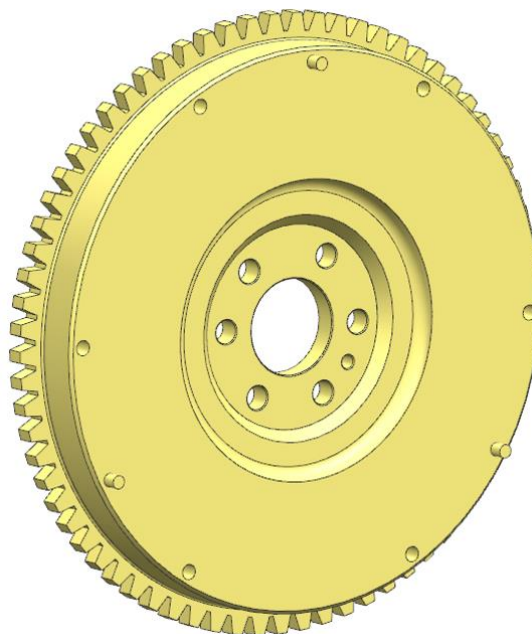
$$I \cong \frac{473700}{0.03 \times (2 \times \pi \times 2000)^2} \cong 9.9 \times 10^{-2} \approx 0.1 \text{ [kg.m}^2\text{]} \quad (225)$$

The outer diameter of the flywheel was limited to 125 mm Due to packaging reasons. Furthermore, it was defined the steel 4340 as flywheel material. The flywheel mass was calculated using Equation 226.

$$m = \frac{I}{R_{gyr}^2} = \frac{0.1}{0.125^2} = 6.4 [kg] \quad (226)$$

Figure 163 illustrates the flywheel designed for the HBS22.

Figure 163 – Engine flywheel

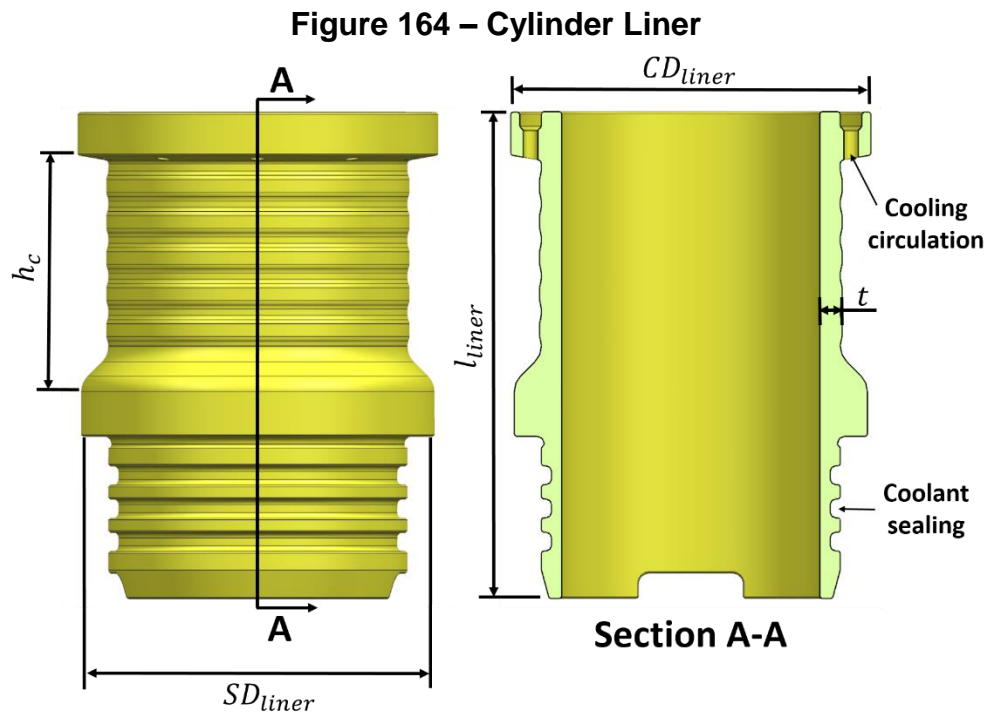


Source: Author

3.3.8. Cylinder liner (sleeve)

A wet cylinder mid-stop liner was designed to be fitted in the engine crankcase and accommodate the piston as presented in Figure 164. The mid-stop design was defined due its more efficient cooling performance and lower stresses at firing deck region compared to the hanging liner design. The cylinder liner was designed as a pressure vessel with a thin wall thickness which the hoop stress was considered as the criterion for determining the cylinder liner thickness. The cast iron DIN 1693 GGG70 was defined as the cylinder liner material due to its high strength, hardness and thermal conductivity. The cylinder liner material properties are presented in Table 44. Furthermore, a Nikasil coating of 0.05 mm thick was applied to the cylinder liner to

achieve a good sealing of the piston rings, low friction power loss, blow-by quantity, and lower oil consumption and the cylinder wear.



Source: Author

Table 44 – Cylinder liner DIN 1693 GGG70 material properties

Properties	Value
Density [g/cm ³]	7.15
Young Modulus [GPa]	170
Yield strength [MPa]	440
Thermal expansion coefficient [K ⁻¹]	1.24x10 ⁻⁵
Thermal conductivity [W.(m.K) ⁻¹]	32

Source: (Matmatch 2019)

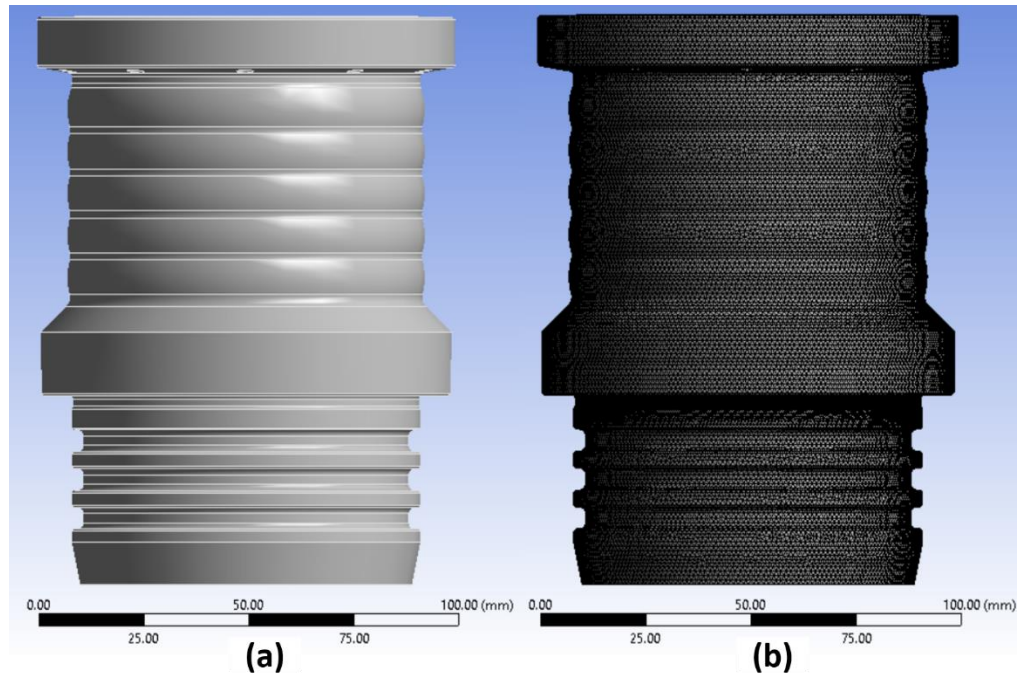
The cylinder liner wall thickness was calculated using Equation 227 considering a safety factor of 2.5. Furthermore, a re-boring allowance R_{all} of 1 mm was added for any re-boring process throughout the engine lifetime.

$$t = \frac{P_{max} \cdot B}{2 \cdot \sigma_{all}} + R_{all} = \frac{25 \times 70.5}{2 \times \left(\frac{440}{2.5}\right)} + 1 = 6.00 \text{ mm} \quad (227)$$

A cylinder liner length, l_{liner} , of 135 mm was defined allowing a piston protrusion of 2.5 mm at BDC. The cylinder liner upper part near of the crankcase fire deck is one of the most critical regarding thermal load. In order to minimize the thermal load in this region several holes of 4 mm of diameter were designed connecting the main water jacket with the upper part of the cylinder liner. Due to water channel designed on upper part the cylinder liner collar diameter, CD_{liner} , was defined as 99.8 mm. As the cylinder liner was fitted in the crankcase from the upper side, it was defined a support diameter, SD_{liner} , of 97.8 mm. According to Figure 76, the water core height, h_c , should be between 33 and 66% of the cylinder liner length. Therefore, it was defined a water core diameter height of 65.5 mm which is 48.5% of the cylinder liner length. Furthermore, several ribs were designed in the in the liner water core region aiming to improve its strength and the heat transfer. The water core sealing was designed at liner bottom part. According to Schäfer (2017), it is suggested to apply a liner protrusion of 0.05 mm for crankcase and liner made in Aluminum and from 0.05 to 0.1 mm for crankcase made in aluminum and liner made of cast iron in order to compensate longitudinal liner deformation due to clamping force. Thus, a 0.1 mm of liner protrusion was applied to the cylinder liner.

The cylinder liner was imported into Ansys for mechanical and thermal load simulation. The cylinder liner mesh was made using tetrahedron elements due to its geometry complexity and the limited computational power available to perform the simulation. The parameter Mesh Metric Element Quality from Ansys software higher than 0.60 was used as reference to evaluated the mesh quality as suggested by Nakasone et al. (2006). Figure 165 illustrates the connecting rod CAD geometry and the connecting rod mesh used for simulation.

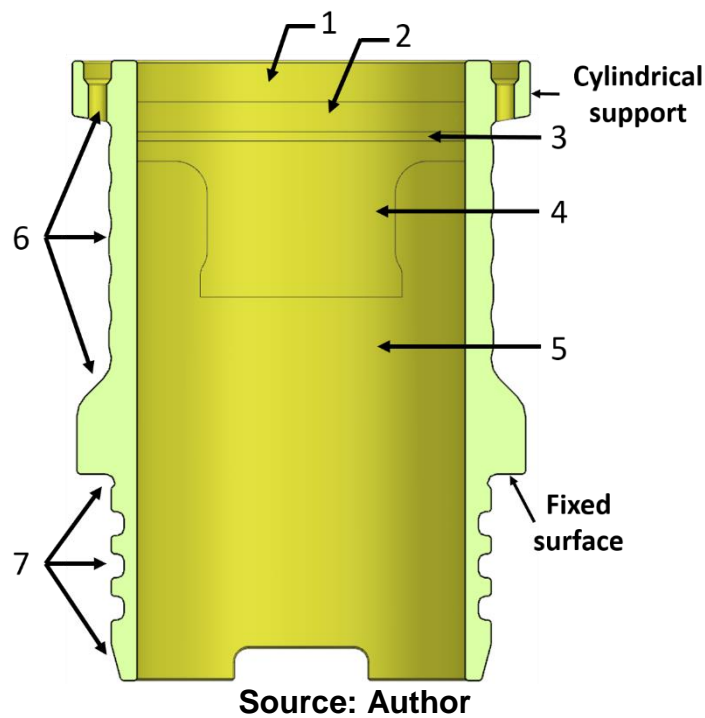
Figure 165 – Cylinder liner CAD geometry (a) and its mesh (b) used for simulation



Source: Author

The piston heat transfer results were used as input for the cylinder liner thermal load simulation. For the water-jacket convective heat transfer coefficient, h_{water} , was used the value of 1500 W/m².K as suggested by Esfahanian (2006). As illustrated in Figure 166, piston surfaces were projected on the cylinder liner in order to establish the thermal boundaries between piston and cylinder liner. Furthermore, it was considered the lower surface of the mid-stop flange and the lateral upper cylinder liner surface as a fixed boundary condition.

Figure 166 – Cylinder liner thermal boundary conditions

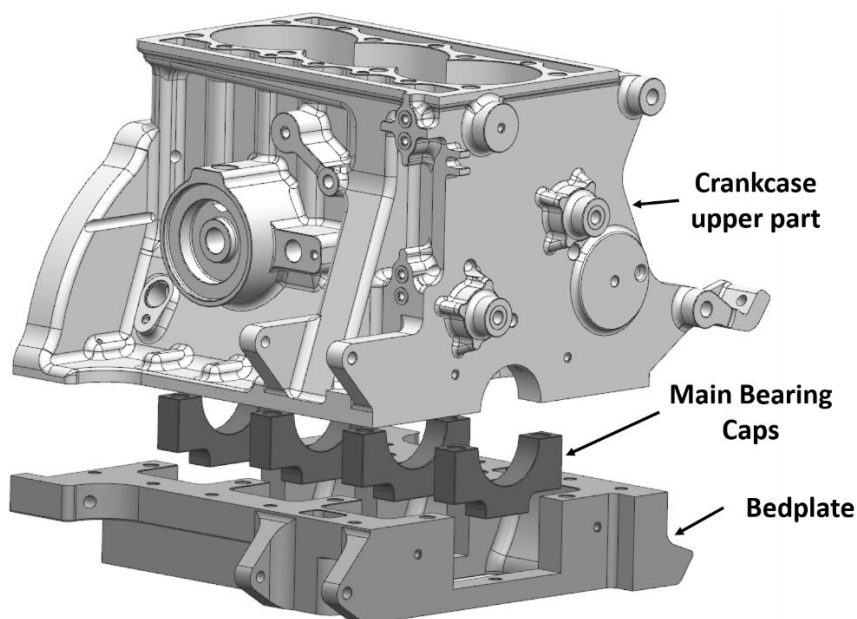


The sleeve o-ring grooves and the o-ring design were performed according Parker (2019) specifications.

3.3.9. Crankcase

The crankcase designed for the HBS22 aimed to achieve a compromise among lower weight, high strength and easy manufacturability. The bedplate design concept was defined to develop the crankcase due its high strength capability. However, in order to minimize the crankcase distortion on the bearing bore region, individual main bearing caps made of AISI 1020 carbon steel were applied on it. On the other hand, aiming to save weight, the crankcase upper part and the bedplate were made of aluminum 6061-T6. The AISI 1020 and 6061-T6 materials properties are presented in Table 45 and Table 15, respectively.

Figure 167 – Crankcase bedplate design concept



Source: Author

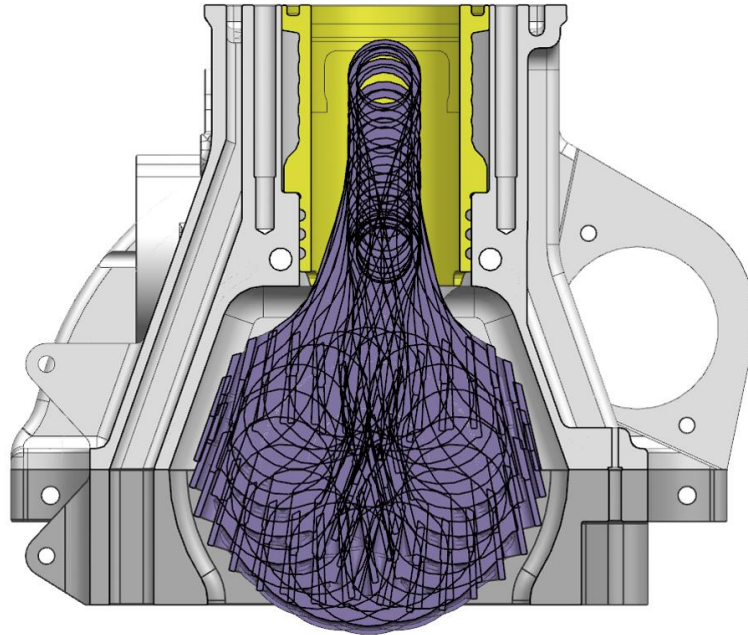
Table 45 – Main bearing caps AISI 1020 carbon steel material properties

Properties	Value
Density [g/cm ³]	7.87
Young Modulus [GPa]	205
Yield strength [MPa]	350
Tensile strength [MPa]	420
Thermal expansion coefficient [C ⁻¹]	11.7x10 ⁻⁶
Thermal conductivity [W.(m.K) ⁻¹]	51.9

Source: (Materials 2013)

In order to evaluate any potential collision between connecting rod and crankcase as well as establish the crankcase internal envelope a connecting rod sweep was performed. Figure 168 illustrates the connecting rod sweep made for the HBS22. Based on the average clearance values suggested by engine design guidelines, it was defined a clearance of 5 mm among connecting rod and near components. It is worth to point out that the crankshaft offset results in a higher connecting rod angle during piston motion from BDC to TDC, which in turn leads to tightest point between connecting rod and crankcase.

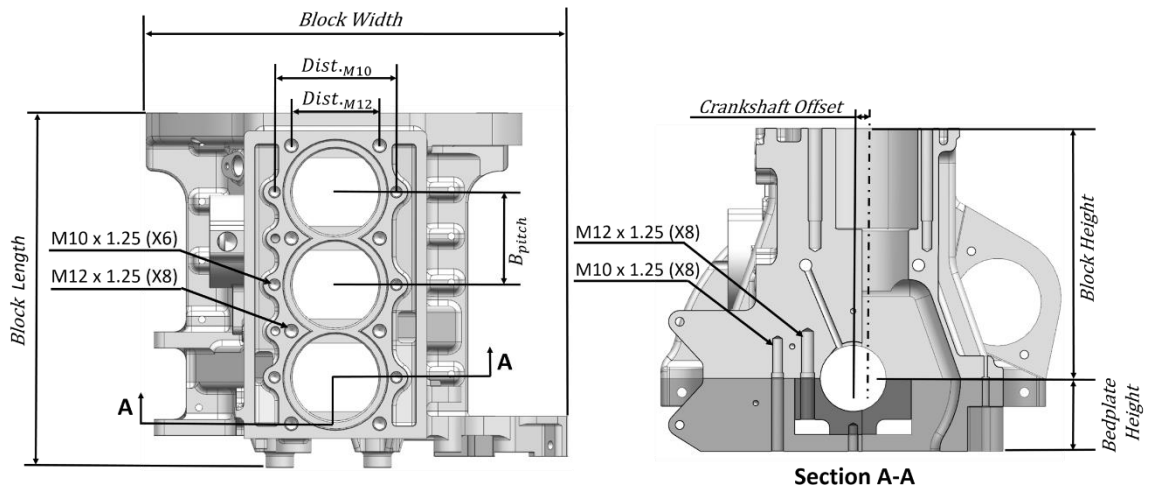
Figure 168 – Connecting rod sweep



Source: Author

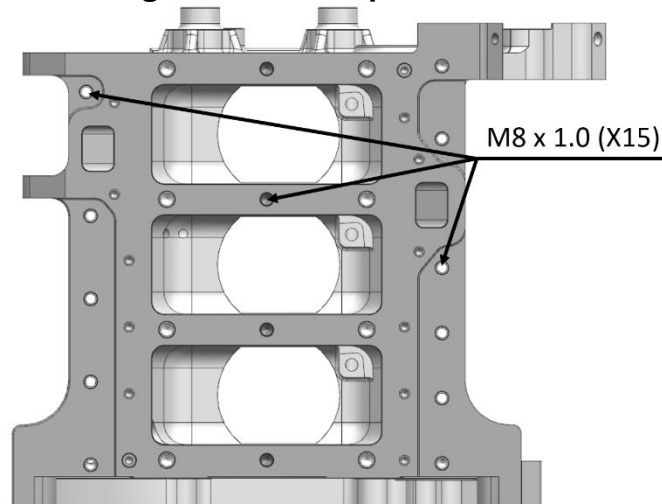
Due to the higher combustion pressure intended to be achieved during engine operation the crankcase mounting fasteners were designed aiming to increase the engine stiffness and strength. As presented in Figure 169, it was defined eight studs M12x1.25 and six studs M10x1.25 to clamp the cylinder head on the crankcase. In order to align as much as possible the mechanical load flow through the crankcase the main bearing caps were fixed by eight studs M12x1.25 along with eight studs M10x1.25 which are the main bedplate fixation as illustrated in Figure 169. Additionally, as shown in Figure 170, fifteen bolts M8x1.00 were applied to bedplate fixation aiming to further improve the crankcase stiffness and strength. The Table 46 summarizes the crankcase main characteristics. The block height was defined aiming to get 0.80 mm of squish height considering a fire-desk gasket thickness of 0.7 mm. The distance among the cylinder head studs were defined in order to minimize the crankcase distortion during engine operation.

Figure 169 – Crankcase main characteristics



Source: Author

Figure 170 – Bedplate fixation



Source: Author

Table 46 – Crankcase main characteristics

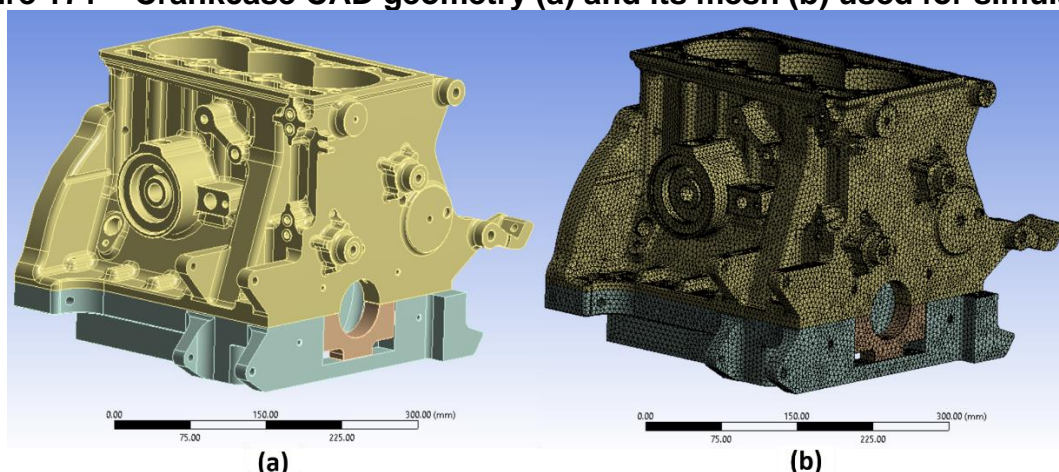
Properties	Value
Bore pitch [mm]	86.7
Crankshaft offset [mm]	8.00
Block height [mm]	220.35
Block length [mm]	336.73
Block width [mm]	400.15
Bedplate height [mm]	65.00
Distance between M12 studs [mm]	84.00
Distance between M10 studs [mm]	116.00

Source: Author

Figure 171 illustrates the crankcase CAD geometry and its mesh used for simulation. The crankcase mesh was made using tetrahedron elements due to the

piston geometry complexity and the limited computational power available to perform the simulation. The parameter Mesh Metric Element Quality from Ansys software higher than 0.60 was used as reference to evaluate the mesh quality as suggested by Nakasone et al. (2006). The crankcase mesh was used in conjunction to cylinder head mesh in order to evaluate the stresses and strain on them due to studs pre-load and engine running forces.

Figure 171 – Crankcase CAD geometry (a) and its mesh (b) used for simulation



Source: Author

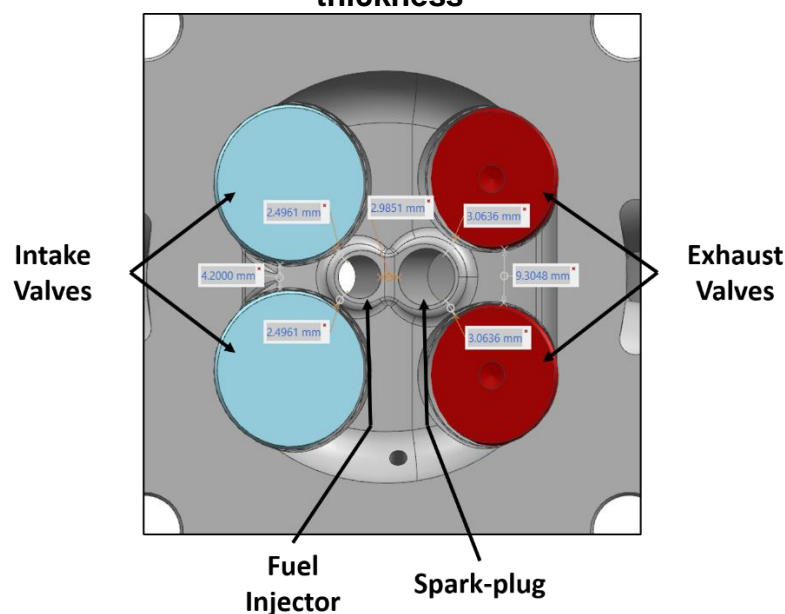
3.3.10. Cylinder Head, Valvetrain System and Fuel injection System

The cylinder head designed for the HBS22 along with its valvetrain system aimed to maximize the engine performance by achieving a balance among cylinder air filling, turbulence intensity, mixture preparation, and component cooling and strength. The cylinder air filling along with the turbulence intensity and mixture preparation are affected mainly by the number and size of the valves, the ports and combustion chamber design, and fuel injector position. As the engine bore diameter and the bore pitch were defined previously, the first step of cylinder head design for HBS22 was to define the size and arrangement of the valvetrain components.

The valvetrain system defined for HBS22 was designed to be as compact as possible. As presented in Figure 80, an arrangement of four-valves with small angle between them promote a higher flow area. Therefore, the four-valve arrangement (2 intake and 2 exhaust valves) was defined to be used in the engine designed in this work. Once the number of valves was defined, the next step was establish the valves size. The largest possible valve diameter was limited by the cylinder bore and the

minimum cylinder head web thickness allowable presented in Figure 81 and Table 19. Thus, it was defined 27.5 and 24.5 mm as the intake and exhaust valves head diameter, respectively. Figure 172 illustrates the overall combustion chamber layout and its minimum web thickness.

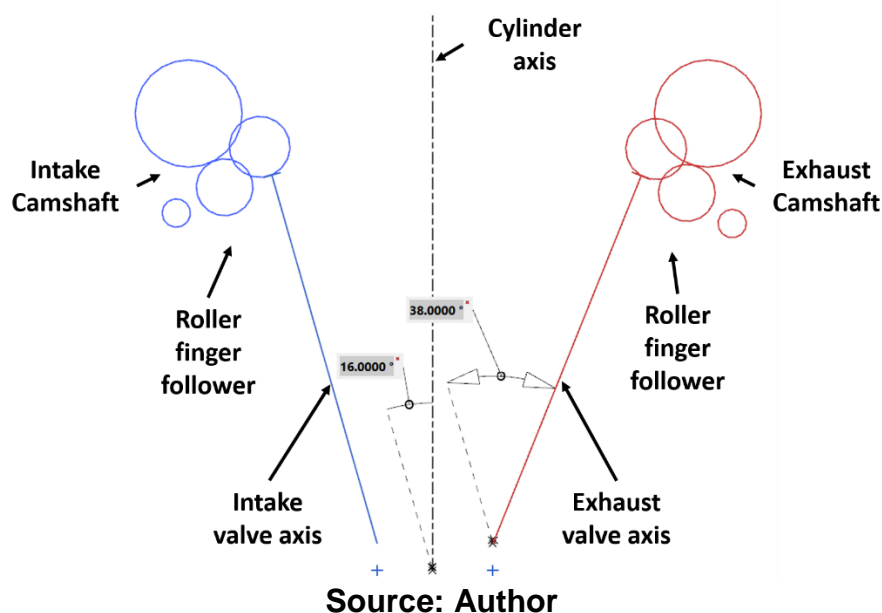
Figure 172 – Overall combustion chamber layout and its minimum web thickness



Source: Author

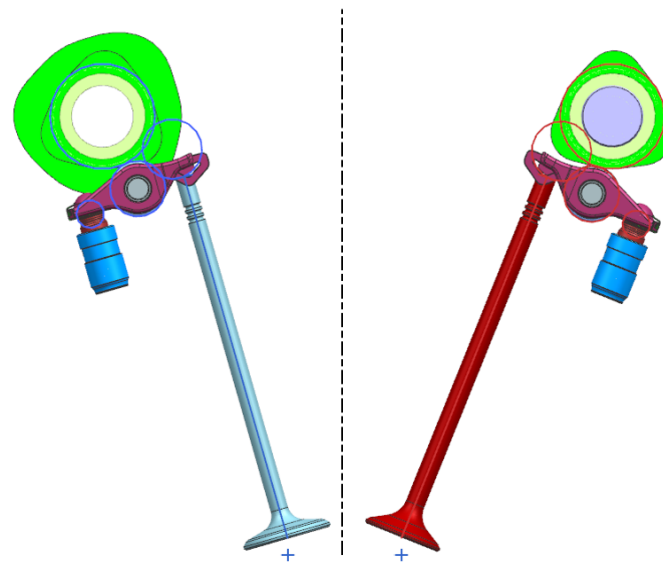
Once the valves diameter were established, the next step was to define the valve position in relation to the cylinder axis. For that, it was included in the engine skeleton file a fully editable valvetrain draft file in order to assist both cylinder head and valvetrain system development. The valvetrain draft file presented in Figure 173 was defined following engine design guidelines from engine manufactures which its details were not allowed to be shared in this work. In the valvetrain skeleton the valves, roller finger followers and the camshafts position were defined. Based on Figure 82, an intake valve angle of 16 degrees was defined aiming to achieve a good compromise between engine torque and power output as suggested by Trzeesniowski (2010). Furthermore, an angle of 38 degrees between the intake and exhaust valves was defined in order to maximize the valves flow area.

Figure 173 – Valvetrain skeleton



Using the valvetrain skeleton as positioning reference, the intake and exhaust valves, roller finger followers, hydraulic lash adjusters, and the intake and exhaust camshafts were assembled on the engine. Figure 174 illustrates the valvetrain basic features assembled. In order to obtain the minimum cylinder head material thickness of 4 mm on regions out of combustion chamber, it was required to use longer intake and exhaust valves. The intake valve is a Mahle 640 VE 31284 00 variation with an extra length of 18.4 mm in order to fit in this project. The intake valve is made of austenitic CrMnNi steel with nitrified surface, also known as 21-4N material, which are to withstand higher mechanical and thermal stresses. For the exhaust valves, it was defined a customized valve made of Inconel-751 and filled with sodium manufactured by Supertech company using the valve FEVI-2401F-HS as a reference. The Inconel-751 material have an ability to function under very high temperatures, severe mechanical stress, and also high surface stability. Furthermore, they have good creep and oxidation resistance. The hollow valves on the one hand serve to reduce weight, and on the other hand to reduce the temperature. Filled with sodium (melting point 97.5°C), the shaker effect of the liquid sodium means that heat can travel from the valve head to the valve stem, and a temperature reduction of between 80°C and 150°C can be achieved.

Figure 174 – Valvetrain basic features positioned

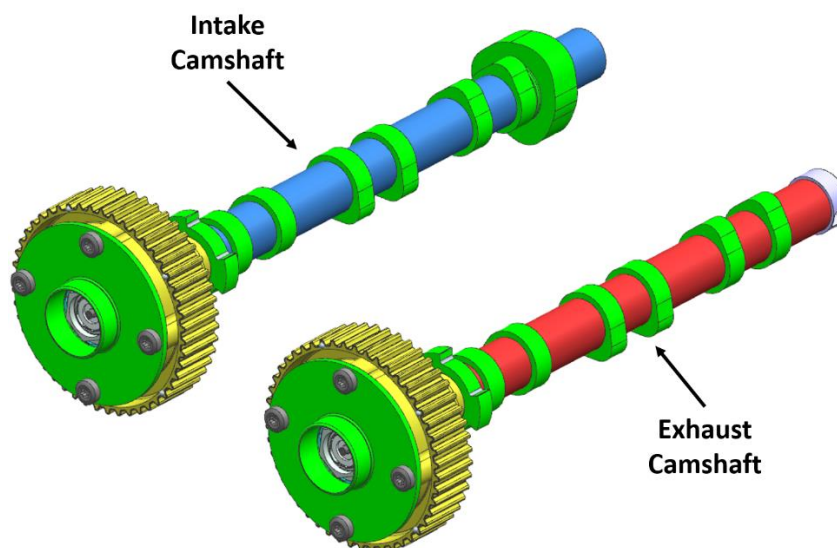


Source: Author

The roller finger follower used on the engine is manufactured by Schaeffler – INA Company with part number F-446067-6. This roller finger follower was chosen for being the smallest one available in the catalog shared with the author. Therefore, a compact valvetrain system could be designed. Furthermore, this roller finger follower has a ratio of 1.83 which was used for the cam lift design. The Hydraulic Lash Adjuster (HLA) used on HBS22 is manufactured by Schaeffler – INA with part number 420.0226.10.

For the intake and exhaust camshafts it was defined to use assembled camshafts. The camshaft core and the camshaft lobes are made of steel E355/1.0580 and steel 100Cr6/1.3505, respectively. The intake camshaft was responsible to actuate the intake valves and drive the High Pressure Fuel Pump – HPFP. On the other hand, the exhaust camshaft was designed to actuate on exhaust valves and drive a vacuum pump Pierburg A598/ 55269802 installed on the cylinder head back-end for vehicle use. Furthermore, it was installed on each camshaft a trigger wheel for engine ECU electronic synchronization. In order to maximize the engine breathing capacity throughout its working speeds and allow to run the engine on the Atkinson and Miller thermodynamic cycles, a Variable Valve Timing (VVT) system was fitted on the engine. The VVT phaser used in this work was provided by Hilite and has a continuous moving range of 40° CA. For the camshaft phaser operation, the engine oil is supplied to the VVT phasers via camshaft core and a cam phaser valve actuated via a solenoid valve is used. Figure 175 illustrates the intake and exhaust camshafts used on this project.

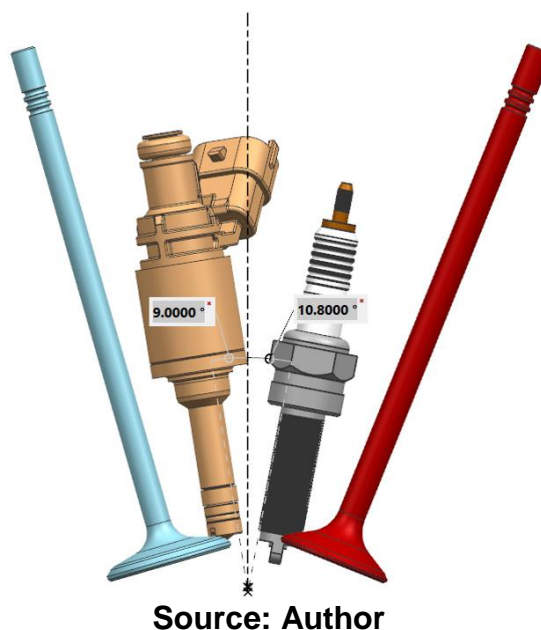
Figure 175 – Intake and exhaust camshafts



Source: Author

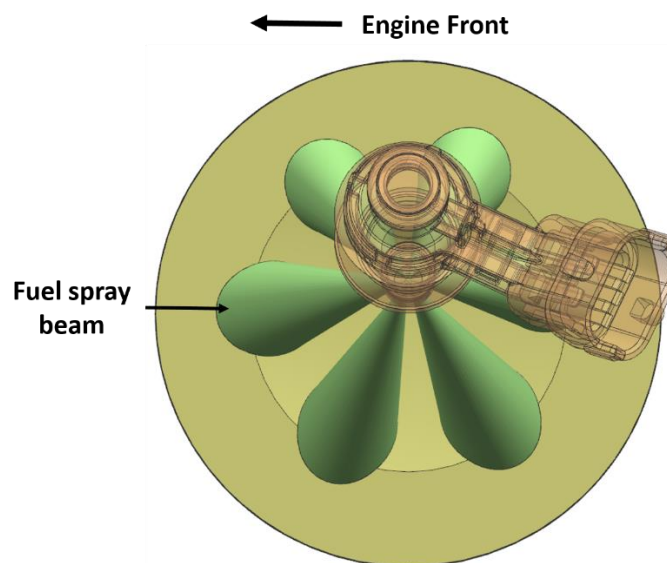
Once the valves positions were defined, the next step was defined the spark-plug and fuel direct injector position. Figure 176 illustrates the spark-plug and fuel direct injector positioned on the engine. The spark-plug was positioned as center as possible of cylinder center axis and later its protrusion was managed to be as close as possible of the combustion chamber center of gravity. Furthermore, the spark-plug was tilted 10.8 degrees towards exhaust valves in order to assist them by exchanging heat. It was defined cooler spark-plug aiming to avoid a hot spot creation which decrease the fuel pre-ignition tendency. The spark-plug installation packaging was also evaluated in order to design an engine as compact as possible. Therefore, an M10 thread along with a higher thread length were defined as basic spark-plug requirements. The spark-plug NGKLMAR9E-J manufactured by NGK Company fitted the engine design requirements and it was chose to be used on the engine. The ignition coil Bosch C90i-Pro Evo was chosen to be used in this project. This coil, designed for direct cylinder head mounting, was developed for engines that need a stable spark because of their higher turbulences at the air fuel mixture inside the cylinder. The main benefits of this high performance coil are its high energy capability and a very good provided high voltage, according to the manufacture.

Figure 176 – Spark-plug and direct fuel injector position



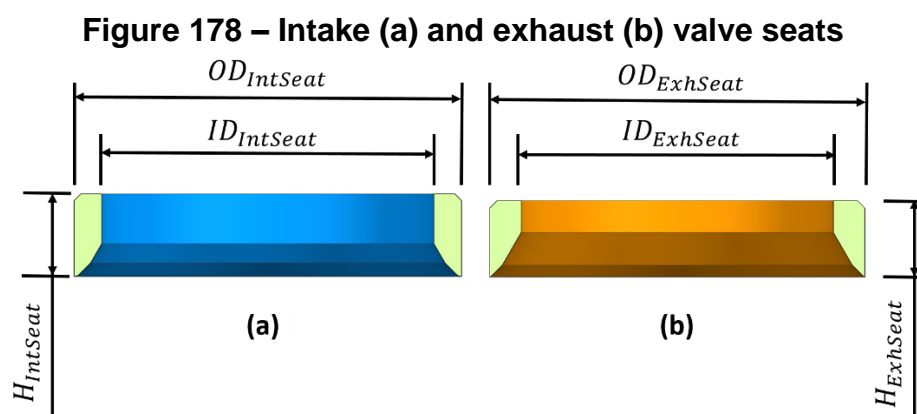
The fuel direct injector position followed a spray guided concept being center mounted on the combustion chamber as close as possible to the spark-plug aiming to promote a better air-fuel mixture preparation and allow the engine to run on stratified lean mode. However, the fuel direct injector was tilted 9.0 degrees towards the intake valves due to packaging reasons. The distance between fuel direct injector and the spark-plug was limited by the minimum cylinder head web thickness required. It was defined Bosch HDEV 5.2 and Bosch HDP 5-LW, both adapted for ethanol use, as the fuel injector and HPFP used in the engine designed in this work. The Bosch HDEV 5.2 is a multi-hole fuel injection (six holes) able to achieve an operating pressure up to 500 bar. The pressure sensor Bosch PSS-600/0261B2378906 was chosen to measure the rail fuel pressure. The fuel injection spray beams were evenly spaced among them targeting the center of piston bowl geometry in order to interact with the in-cylinder charge motion and achieve a better air-fuel mixture preparation. Figure 177 illustrates the fuel injection spray target.

Figure 177 – Fuel injection spray target



Source: Author

In order to further design the cylinder head it was required to design the valve seats, and the valves timings and lift. The valve intake and exhaust seats were designed according to engine design guidelines from engine manufactures based on the intake and exhaust valves head diameter. It was defined to use the standard valve seats with three angles 30, 45 and 70 degrees, and being 45 degrees the valve seating angle. Figure 178 illustrates the intake and exhaust valve seats. The intake and exhaust valve seats main dimensions are summarized in Table 47.



Source: Author

Table 47 – The intake and exhaust valve seats main dimensions
Intake valve seat

Outer diameter [mm]	28.0
Inner diameter [mm]	24.0
Height [mm]	6.0
Seat angle [deg]	45
Exhaust valve seat	
Outer diameter [mm]	25.0
Inner diameter [mm]	20.8
Height [mm]	5.2
Seat angle [deg]	45

Source: Author

The Mahle SM1 material was chosen to manufacture both intake and exhaust valve seats. The Mahle SM1, according to the manufacture, is an extremely high-quality and high-performance sintered material suitable intake and exhaust valve seat inserts with outstanding resistance to wear. Developed for high-performance naturally aspirated and turbocharged engines using petrol, diesel, and gas.

The intake and exhaust cam lobe profiles were designed following the methodology presented by Blair (1999). The cam lobe profile was divided into rump up, main lift up, dwell, main lift down and rump down as illustrated by Figure 179 (a). As presented in Figure 179, it was used specific polynomial to define the displacement or lift curve of the rumps and main lifts phases. During the dwell phase, the lift curve remains constant at its maximum throughout a short period of time. Equation 228 and Equation 229 were the polynomial used for rumps and main lifts phase calculation, respectively.

$$L_{S(rump)} = k_{r0} + k_{r1} \times \theta_s + k_{r2} \times \theta_s^2 + k_{r3} \times \theta_s^3 \quad (228)$$

$$L_{S(main\ lift)} = k_{m0} + k_{m1} \times \theta_s + k_{m2} \times \theta_s^2 + k_{m3} \times \theta_s^3 \quad (229)$$

Where k_{r0} , k_{r1} , k_{r2} , k_{r3} , and k_{m0} , k_{m1} , k_{m2} , k_{m3} are polynomial coefficients for SI engines and their values are presented in Table 48. The L_S and θ_s are specific lift and angle calculated using Equation 230 and Equation 231, respectively.

$$L_s = \frac{L_\theta}{L_v} \quad (230)$$

$$\theta_s = \frac{\theta}{\theta_v} \quad (231)$$

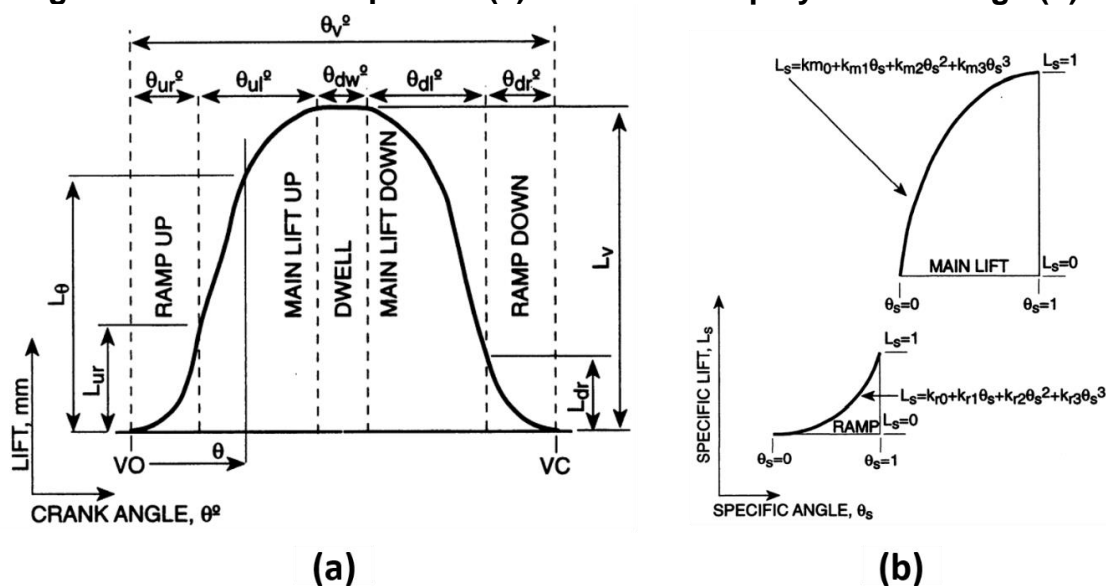
Where L_θ is the instantaneous lift [mm], L_v is the maximum lift for an specific lift curve phase [mm], θ is the instantaneous angle [deg] and θ_v is the lift curve phase angular duration [deg].

Table 48 – Cam lift curve polynomial coefficients

k_{r0}	0.011172
k_{r1}	-0.08034
k_{r2}	0.4686
k_{r3}	0.6119
k_{m0}	-0.00786
k_{m1}	1.7673
k_{m2}	-0.45161
k_{m3}	-0.31158

Source: (Blair 1999)

Figure 179 – Cam lobe phases (a) and cam lobe polynomial design (b)



Source: Adapted from (BLAIR, 1999)

The intake and exhaust valve lift duration were defined aiming to maximize the engine volumetric efficiency as well as enable the engine to operate on alternative thermodynamic cycles. It was defined an intake valve lift duration of 220 CAdeg at 0.2 mm of valve lash and an exhaust valve lift duration of 230 CAdeg at 0.3 mm of valve lash. Furthermore, aiming to keep the engine design as simple as possible it was considered a symmetrical valve lift curves for both intake and exhaust valves. As suggested by Blair (1999), it was considered the valve lift rumps duration of 40 CAdeg and a dwell angle of 3 CAdeg for both intake and exhaust valve lifts. The remaining durations were considered as main lift phase.

Once the intake and exhaust valve lifts were defined, the next step was the intake and exhaust maximum valve lifts. The valve maximum lift L_{max} , in [mm], was calculated using Equation 232 from Blair (1999).

$$L_{max} = \sqrt{\left(\frac{A_t}{\pi \left(\frac{d_{os} + d_{is}}{2}\right)}\right)^2 + \left(\frac{d_{os} - d_{is}}{2}\right)^2} + \frac{d_{os} - d_{is}}{2} \times \tan \phi \quad (232)$$

Where d_{os} is the seat ring external diameter in [mm], d_{is} is the seat ring internal diameter in [mm], ϕ is the angle valve seat angle and A_t is the valve curtain area, in [mm²] at maximum lift calculated using Equation 233.

$$A_t = C_d \times n_v \times \frac{\pi}{4} \times (d_{is}^2 - d_{st}^2) \quad (233)$$

Where d_{st} is the valve stem diameter [mm], n_v is the number of valves per cylinder and C_d is the discharge coefficient.

For the intake and exhaust discharge coefficients calculation were used the empirical Equation 234 and Equation 235, respectively. These empirical equation are available in Blair (1999) work.

$$C_{dint} = 0.86871 - 0.0012452 \times BMEP_N \quad (234)$$

$$C_{dext} = 0.88401 - 0.0021435 \times BMEP_N \quad (235)$$

It was considered the BMEP at engine maximum power of 29 bar for the discharge coefficients calculation. Table 49 summarize the intake and exhaust valve lift calculation input and output. The maximum valve intake and exhaust valve lift was 10.5 and 8.8 mm, respectively. Considering the roller finger follower ratio of 1.83 as aforementioned, the cam lobe profile lift for intake and exhaust valves was calculated as 5.74 and 4.81 mm, respectively.

Table 49 – The intake and exhaust valve lift calculation input and output

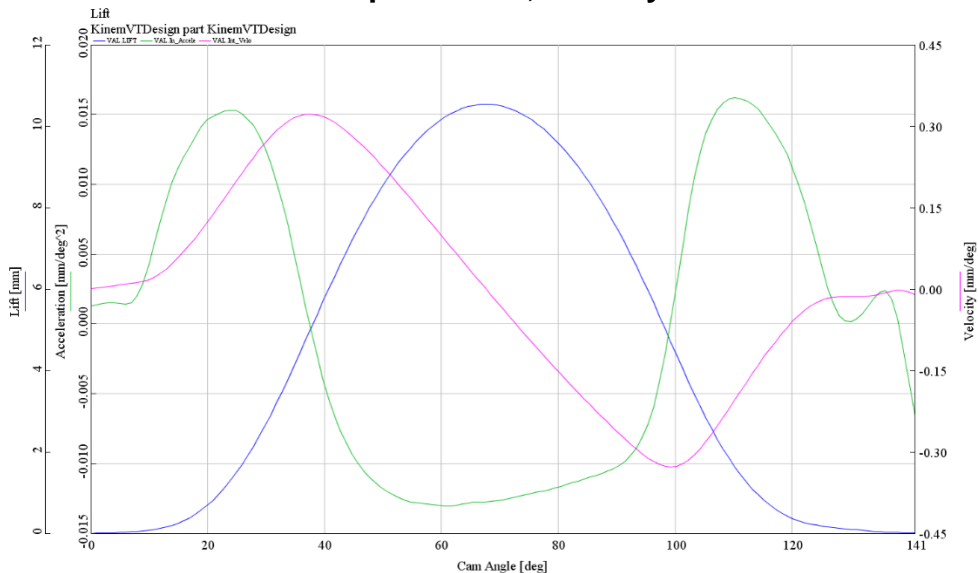
Intake valve	
C_d [-]	0.83
A_t [mm ²]	714
L_{max} [mm]	10.5
Roller finger follower ratio [-]	1.83
Cam lobe lift, L_{cam} [mm]	5.74
Exhaust valve	
C_d [-]	0.82
A_t [mm ²]	512
L_{max} [mm]	8.8
Roller finger follower ratio [-]	1.83
Cam lobe lift, L_{cam} [mm]	4.81

Source: Author

The base calculated valve lift curves required a further interpolation and smoothing process in order to the valvetrain operate as smooth as possible. The interpolation process was performed due to the base lift curve being defined based on a 3rd order polynomial. Which in turn, it leads in to a 1st order acceleration curve. According to Norton (2012), the acceleration valve curve should has minimum 3rd polynomial order. The software VT-Design developed by Gamma Technologies was used for the intake and exhaust lift curves interpolation and smoothing process. The intake and exhaust lift curves were interpolated for a 6th order polynomial. Figure 180 and Figure 181 illustrate, respectively, the intake and exhaust valve displacement, velocity and acceleration curves. The main valvetrain working values limits suggested by Wang (2007) for a roller finger follower valve actuation system were used to validate

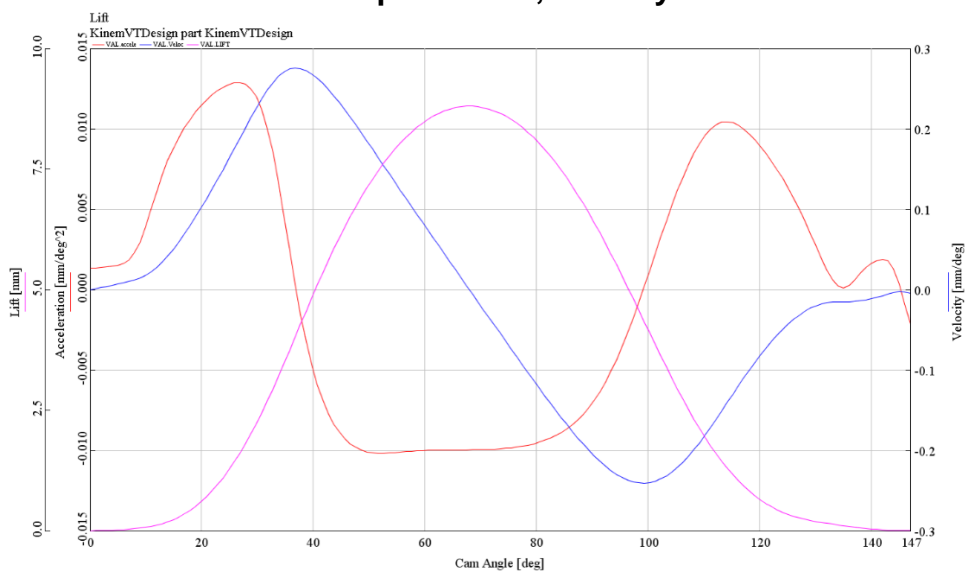
the intake and exhaust camshaft actuation designed for the HBS22. Table 50 presents the comparison values among the intake, exhaust and the reference.

Figure 180 – Intake valve displacement, velocity and acceleration curves



Source: Author

Figure 181 – Exhaust valve displacement, velocity and acceleration curves



Source: Author

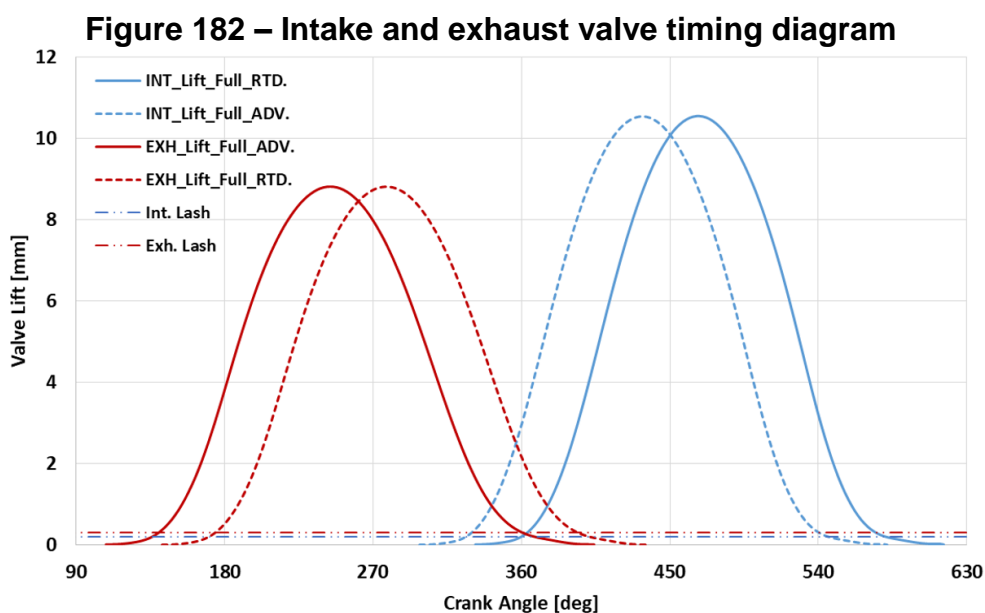
Table 50 – The intake and exhaust valvetrain main working values limits

Parameter	Reference	Intake	Exhaust
-----------	-----------	--------	---------

Max. cam velocity [mm/deg]	0.3200	0.3220	0.2759
Open ramp velocity [mm/deg]	0.0180	0.0169	0.0145
Close ramp velocity [mm/deg]	0.0145	0.0139	0.0140
Max. acceleration open side [mm/deg ²]	0.0190	0.0153	0.0129
Max. acceleration close side [mm/deg ²]	0.0180	0.0162	0.0105
Min. acceleration [mm/deg ²]	0.0076	0.0131	0.0102

Source: Author

Once the intake and exhaust valve lift curves were defined, the next step was to establish the intake and valve timings. The intake and exhaust valve timings were defined aiming to maximize the engine breathy capacity as well as enable the engine to operate on alternative thermodynamic cycles taking into account the 40 [CAdeg] timing variation allowed by the cam phasers. Figure 182 illustrates the Intake and exhaust valve timing diagram and Table 51 presents them valve actuation summary.



Source: Author

Table 51 – Intake and exhaust valve actuation summary

Intake valves

Duration [CAdeg] at 0.2 mm	220
Full Retarded - IVO [°BTDC]	0
Full Retarded - IVC [°ABDC]	40
Advancing Timing Range [CAdeg]	40
Maximum lift [mm]	10.5
Exhaust valves	
Duration [CAdeg] at 0.3 mm	230
Full Advanced - EVO [°BBDC]	6
Full Advanced - EVC [°ATDC]	34
Retarding Timing Range [CAdeg]	40
Maximum lift [mm]	8.8

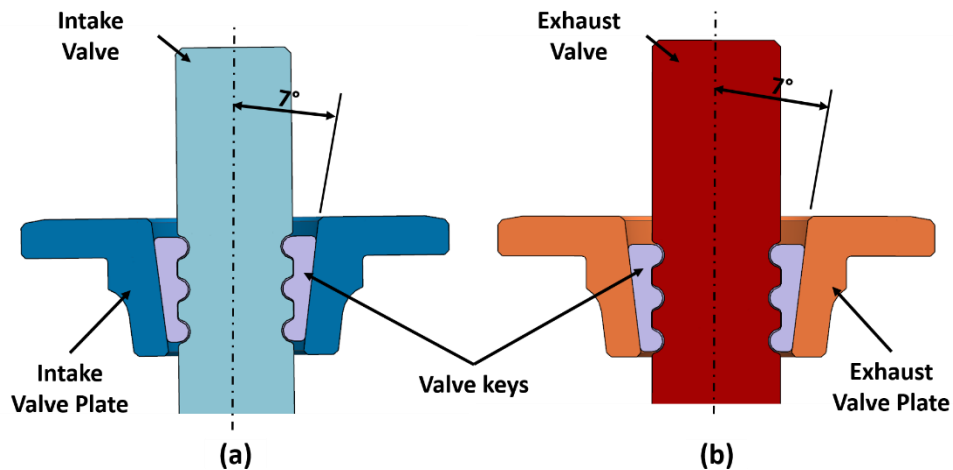
Source: Author

Considering this valvetrain design context, the valve spring and valve guide design as well as the valves plates, keys and retainers are explained at this time.

It was defined valve keys with three-bead in order to promote valve rotation capability improving the valve seat cleaning. The valve plates were different between intake and exhaust valves due to different valve stem diameter between them. However, the valve plates for both intake and exhaust valves have a cone angle of 7 deg. Due to valve spring Beehive concept used in this work, as will be present later, the valves plates have a lower mass which in turn contributes to a lower inertia forces acting on the valvetrain system. Figure 183 illustrates the Intake and exhaust valve keys and plates assembly.

The valve spring for both intake and exhaust valves was designed as Beehive springs with elliptical wire cross section in order to minimize the moving valve spring mass and stresses. It was used the same valve spring for the intake and exhaust valves, however the different spring pre-loads between them were achieved by designing different planes in the cylinder head.

Figure 183 – Intake (a) and exhaust (b) valve keys and plates assembly



Source: Author

The spring rate was the first valve spring parameter to be calculated. The spring rate was calculated using the force acting on the spring and the valve lift. The force acting on the spring was considered as difference between the valve assembly inertial force and the spring pre-load. The inertial force was calculated multiplying the total valve assembly mass by the maximum valve acceleration presented in Table 50. The spring pre-load was calculated considering a pressure of 4 bar acting in the valve back surface which tries to open it when the valve is not being actuated. The intake and exhaust spring rate values were calculated by Equation 236 and Equation 237, respectively.

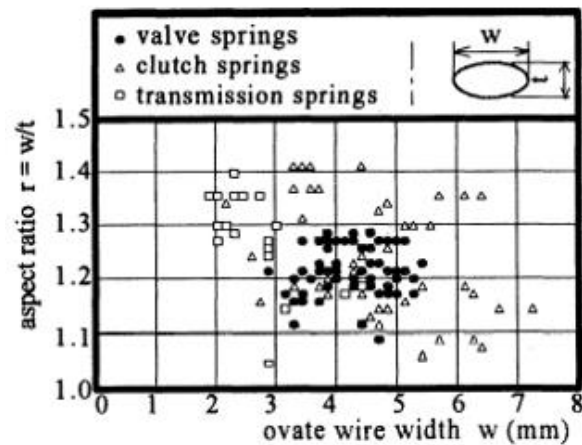
$$K_{int} = \frac{FS_{max} - F_{pre-load}}{lift} = \frac{551 - 304}{10.5} = 23.5 \text{ N/mm} \quad (236)$$

$$K_{exh} = \frac{FS_{max} - F_{pre-load}}{lift} = \frac{440 - 215}{8.8} = 25.5 \text{ N/mm} \quad (237)$$

As it will be used the same for intake and exhaust valves, it was considered the spring rate, K_{spring} , average of 24.5 N/mm from the calculated springs rate.

According to Miyamura et al. (1993) along with Figure 184, the automotive valve springs has on average an aspect ratio of 1.24.

Figure 184 – Spring aspect ratio related to ovate wire width



Source: Author

The elliptical wire section parameters were the next to be calculated. The spring elliptical wire section was calculated using the maximum shear stress according to Equation 238.

$$\tau_{\max} = K_B \frac{8 \cdot FS_{\max} \cdot D}{\pi \cdot de^3} \quad (238)$$

However, the maximum shear stress in Equation 260 it was replaced by the maximum allowable stress calculated using Equation 239.

$$\tau_{all} = 0,56 \cdot S_{ut} \quad (239)$$

The ultimate tensile strength was calculated using Equation 240.

$$S_{ut} = \frac{A}{de^m} \quad (240)$$

Furthermore, a safety factor of 1.2 was considered for the spring design as suggested by Budynas and Nisbett (2011). Therefore, the maximum allowable stress calculated by Equation 241.

$$\tau_{\max} = \frac{0,56 \cdot \frac{A}{de^m}}{1.2} \quad (241)$$

The A401 Cr-Si was defined as the spring wire material due to its higher efficient in terms of mass and spring rate compared to others spring materials as presented by

Wang (2007). Considering A401 Cr-Si material, the constant A and the exponent m in Equation 263 are 1974 and 0.108, respectively, from Table 24.

The spring stress concentration factor was calculated using Equation 242.

$$K_B = a_0 + \frac{a_1}{C} + \frac{a_2}{C^2} \quad (242)$$

The spring index was calculated using Equation 243.

$$C = \frac{D_g}{de} \quad (243)$$

Where D_g is the bottom mean coil diameter in [mm] and de is the round wire diameter equivalent to ovate in [mm]. Due to packaging reasons in the cylinder head, it was considered 20.9 mm as the bottom mean coil diameter.

The valve springs aspect ratio of 1.24 it was used as reference to determine the constants values $a_0 = 1.12$, $a_1 = -0.05$ and $a_2 = 3.12$ from Table 25 .

By replacing the related equations, Equation 244 was obtained.

$$\frac{0,56 \cdot \frac{A}{de^m}}{1.2} = \left(a_0 + \frac{a_1}{\frac{D_g}{de}} + \frac{a_2}{\left(\frac{D_g}{de}\right)^2} \right) \frac{8 \cdot FS_{max} \cdot D_g}{\pi \cdot de^3} \quad (244)$$

Substituting the appropriate values in Equation 245 the round wire diameter equivalent to ovate, de in [mm], was obtained.

$$\frac{0.56 \times \frac{1974}{de^{0.108}}}{1.2} = \left(1.12 - \frac{0.05}{\frac{20.9}{de}} + \frac{3.12}{\left(\frac{20.9}{de}\right)^2} \right) \frac{551 \times 8 \times 20.9}{\pi \times de^3} \therefore de \approx 3.52 \text{ mm} \quad (245)$$

Considering the result from Equation 267, it was defined 3.5 mm as the round wire diameter equivalent to ovate.

The round wire diameter equivalent to ovate can be calculated using Equation 246.

$$de = \sqrt{w \cdot t} \quad (246)$$

Where w and t are the wire width and thickness in [mm], respectively.

The was spring wire thickness calculation was performed using Equation 247.

$$t = \frac{de}{\sqrt{r_{sp}}} = \frac{3.5}{\sqrt{1.24}} \approx 3.1 \text{ mm} \quad (247)$$

The spring wire width was calculated by rearranging Equation 248.

$$w = t \cdot r_{sp} = 3.1 * 1.24 \approx 3.8 \text{ mm} \quad (248)$$

As the bottom mean coil diameter was considered as 20.9 mm and the spring wire width was 3.8 mm, the spring bottom outer and inner diameter was 24.7 and 17.1 mm, respectively. The spring top inner diameter was defined as 12.7 mm in order to properly accommodate the valve plate. Hence, the spring top outer diameter became 20.3 mm.

The number of active coils of the spring was calculated using Equation 249.

$$N_a = \frac{de^4 \cdot G}{8 \cdot Dg^3 \cdot K_{spring}} = \frac{3.5^4 \times 77200}{8 \times 20.9^3 \times 24.5} = 6.47 \quad (249)$$

In order to keep the engine design as simple as possible, it was considered 6.5 as the number of active coils. It was defined the squared and ground type of the spring ends aiming a better load transfer. Thus, according to Budynas and Nisbett (2011), the spring total number of coils was calculated using Equation 250.

$$N_t = N_a + 2 = 6.5 + 2 = 8.5 \quad (250)$$

The spring solid length, also called solid height, can be calculated using Equation 251.

$$L_s = (N_t - 0.75) \cdot de = (9.5 - 0.75) \times 3.5 = 30.6 \text{ mm} \quad (251)$$

The over force on spring, was calculated using Equation 252.

$$F_s = (1 + 0.15). FS_{max} = 1.15 \times 551 = 633.65 \text{ N} \quad (252)$$

The valve spring free length was calculated using Equation 253.

$$L_f = \frac{F_s}{K_{spring}} + L_s = \frac{633.65}{24.5} + 30.6 = 56.46 \text{ mm} \quad (253)$$

In order to keep the engine design as simple as possible, it was considered 56.5 mm as the valve spring free length.

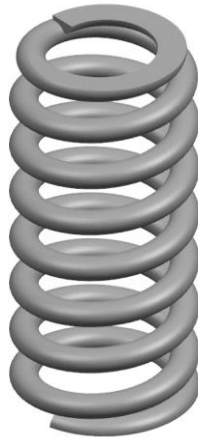
The spring active part weight and the valve spring natural frequency were calculated using Equation 254 and Equation 255, respectively for the spring surge evaluation.

$$W = \frac{\pi^2 \cdot de^2 \cdot Dg \cdot N_a \cdot \gamma}{4} = \frac{\pi^2 \times 0.0035^2 \times 0.0209 \times 6.5 \times 76500}{4} = 0.31 \text{ N} \quad (254)$$

$$f = \frac{1}{2} \sqrt{\frac{K_{spring} \cdot g}{W}} = \frac{1}{2} \sqrt{\frac{24500 \times 9.81}{0.31}} = 440 \text{ Hz} \quad (255)$$

The maximum camshaft frequency at the highest engine speed is 47.9 Hz. Therefore, the spring natural frequency to the maximum camshaft frequency ratio is 9.18 Hz which is compatible to the advisable ratio for a better dynamics behavior.

Figure 185 – Designed spring for the HBS22



Source: Author

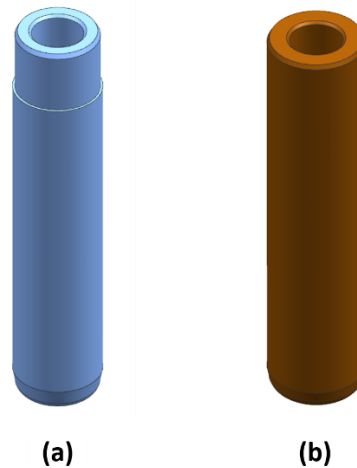
The valve guided was designed according to Figure 109. For the valve guide internal diameter it was considered the intake and exhaust valve stem diameter added, respectively 0.03 and 0.04 mm as diametric clearance. It was defined B1 (CuSn alloy) with the addition of phosphorus for its suitable high engine load applications.

Table 52 – Intake and exhaust valve guide

Parameter	Intake	Exhaust
Valve stem diameter [mm]	5.5	6.0
Diametric clearance [mm]	0.03	0.04
Guide internal diameter [mm]	5.53	6.04
Guide length [mm]	43.3	46.4
Guide wall thickness [mm]	1.91	2.07
Guide external diameter [mm]	9.4	10.2

Source: Author

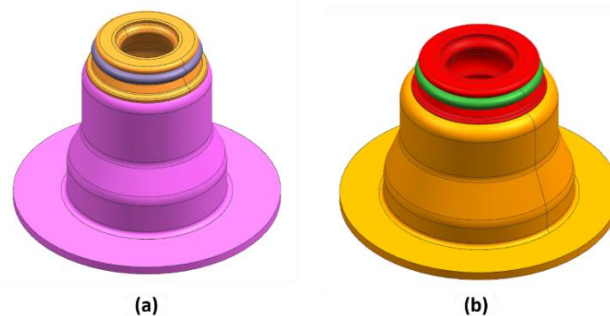
Figure 186 – Intake (a) and exhaust (b) valve guide



Source: Author

The integrated spring seat double lip low friction valve stem seals used for the HBS22. It was defined these valve stem seals due to their capability to bear manifold pressures up to 6 bar and being manufactured using FKM rubber which can withstand a higher temperature range and promote lower friction losses. The intake and exhaust valve stem seals are identified by the PN 19036644 and 19036522, respectively, on the manufacture Corteco catalog. Figure 187 illustrates the intake and exhaust valve stem seal.

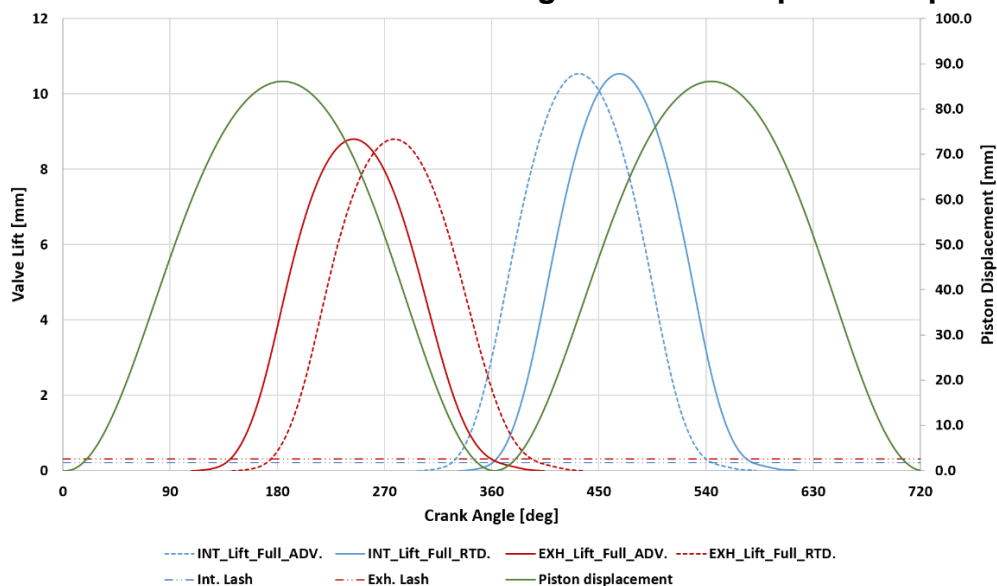
Figure 187 – Intake (a) and exhaust (b) valve stem seal



Source: Author

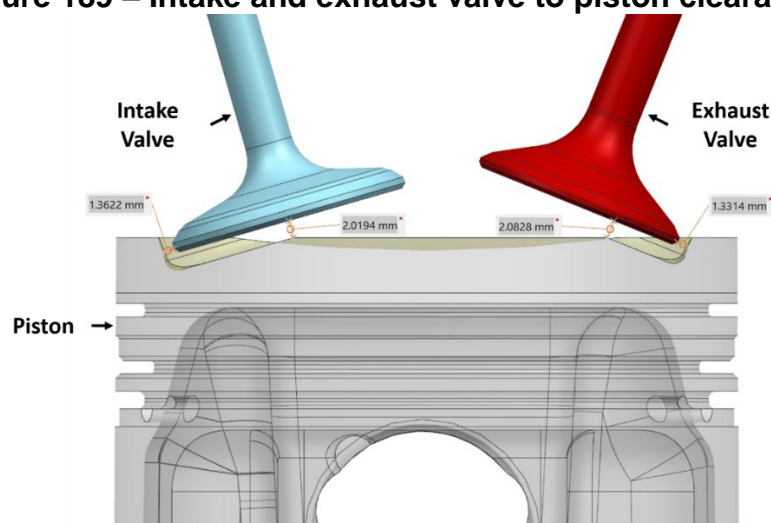
Once all the valvetrain components were designed or defined the next development step was the valve to piston clearance definition and piston trim. The intake and exhaust valve diagram was compared to the piston displacement in order to establish the worst scenario for valve and piston interference as illustrated in Figure 188. As suggested by Motorsport (2020) and Mavrigian (2013), it was defined an axial and a radial valve to piston clearance of 2.0 and 1.3 mm, respectively. Figure 189 illustrates the intake and exhaust valve to piston clearance.

Figure 188 – Intake and exhaust valve diagram related to piston displacement



Source: Author

Figure 189 – Intake and exhaust valve to piston clearance

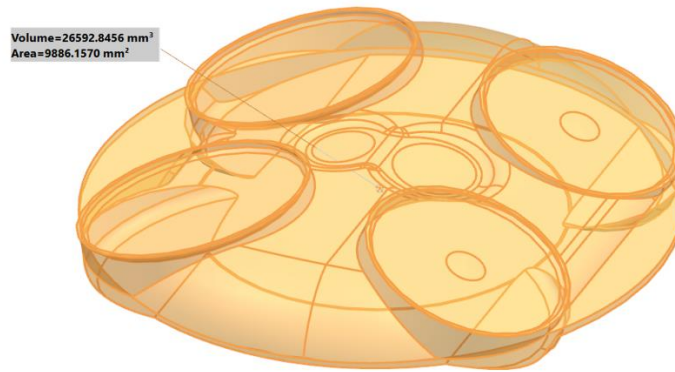


Source: Author

As the valvetrain system was designed and the piston was trimmed, the combustion chamber was the next cylinder head feature designed. The combustion chamber shape was determined by the arrangement of the valves and the position of the spark plugs. Its design was developed aiming to obtain as compact as possible combustion chamber which reduces combustion path. Furthermore, it was established 0.8 mm as the minimum height on the combustion chamber squish area and the final combustion chamber volume was defined aiming to achieve the volumetric compression ratio of 14.0:1. It is worth to point out that it was designed a valve masking

between the intake valves in order to minimize the cylinder filling losses due to flow interaction in this region. Figure 190 illustrates the designed combustion chamber, and its volume and area.

Figure 190 – Combustion chamber main volume and area



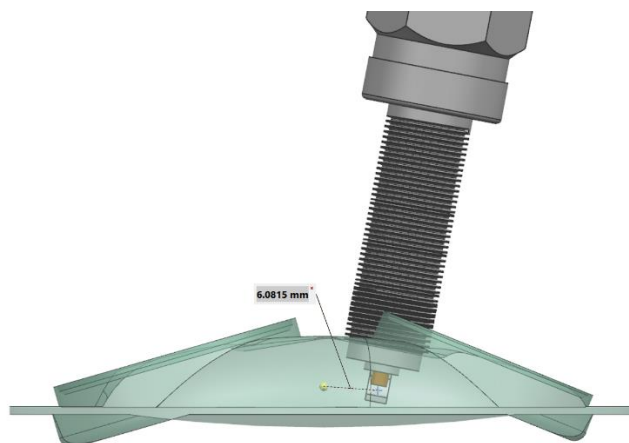
Source: Author

Considering the combustion chamber volume presented in Figure 190, the achieved volumetric compression ratio was calculated using Equation 256.

$$r_{c_{off}} = 1 + \frac{\pi \cdot B^2 \cdot L_{off}}{4 \cdot V_c} = 1 + \frac{\pi \times 71.5^2 \times 86.13}{4 \times 26592} = 14.004 \quad (256)$$

Once the combustion chamber shape was defined, its central of gravity was used as reference to define the spark-plug protrusion. As presented on Figure 191, the lowest distance between the spark-plug kernel formation center and the combustion chamber central of gravity was approximately 6.08 mm.

Figure 191 – Spark-plug to combustion chamber center of gravity position

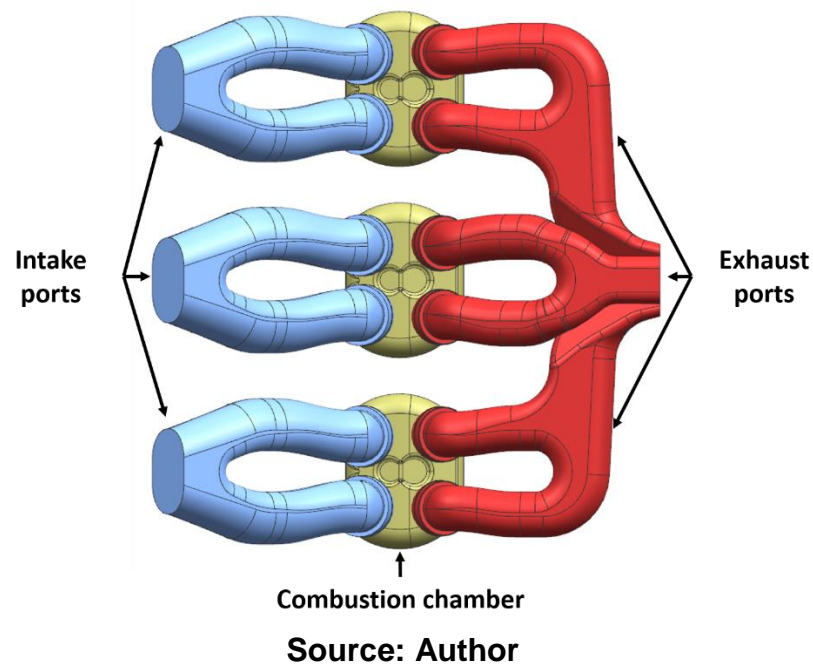


Source: Author

Following the cylinder head design process, the intake and the exhaust ports were designed. Considering the port to cylinder axis angle effect on the engine torque and power along with the aiming to reach an IMEP of 35 bar, the intake ports were designed to have as close as possible port to cylinder axis angle of 50 deg. Due to valvetrain system and intake manifold assembly constrains, the port to cylinder axis angle was defined as 58 deg. In order to minimize the exhaust gases pulsation behavior from a cylinder to another, it was designed individual exhaust ports. Although, the middle cylinder has an exhaust port length different from the others cylinders, its effect on the amount of residual gases trapped in the combustion chamber can be tolerated. This statement was based in engine test bench results from a 3-cylinder engine with similar exhaust port arrange. However, these results were not allowed to be shared in this work. Figure 192 illustrates the intake and exhaust ports.

An important characteristic on intake port design that was considered was the manifold-port area ratio. It was considered the range between from 0.9 to 1.0 in order to keep the flow velocity through the valves lower enough to not overcome $MI = 0.5$. The final intake port geometry presented a manifold-port ratio of 0.908, which is within the suggested range. The first intake and exhaust ports CFD simulations were presented in Ramos (2020). Improvements from those simulation were performed however it was not possible to re-simulate the updated geometry due to computational power availability at the university.

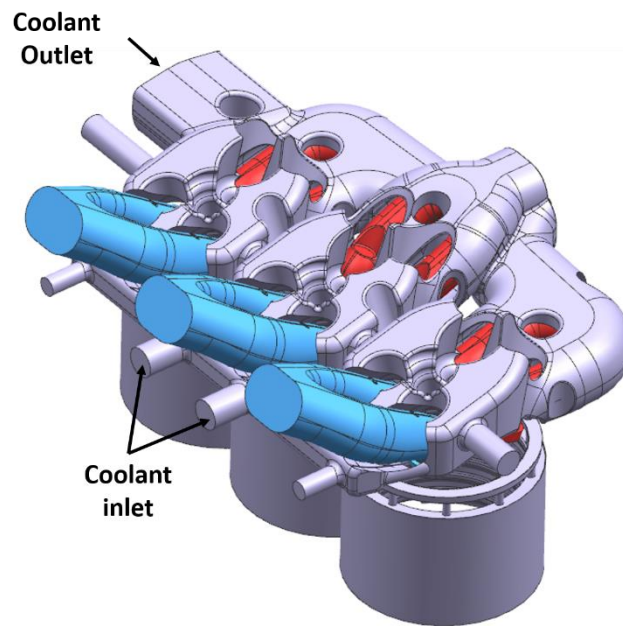
Figure 192 – Intake and exhaust ports



An integrated exhaust manifold was designed to the HBS22 aiming to obtain the advantages from the technology such as weight reduction, lower manufacture cost, fuel consumption reduction, lower temperatures of the exhaust gases and inner walls and faster engine warm-up. Therefore, although there is an advisable range for exhaust manifold-port ratio, the advisable ratio was not reached once the exhaust port outlet areas were limited by the turbine housing inlet diameter.

The integrated exhaust manifold approach required a cooled exhaust manifold. The exhaust cooling geometry was incorporated into the cylinder head water-jacket geometry. As illustrated by Figure 193 cross-flow water-jacket was designed for the HBS22 following design guide lines from engine manufactures which were not allowed to be shared in this work. The direct fuel injector and the spark-plugs were surrounded by the water-jacket in order to improve a heat exchange in the region which in turn avoid a component damage.

Figure 193 – Engine water-jacket



Source: Author

The coolant fluid defined to be used in the engine is a mixture of anti-freeze and water manufactured by Wolf Company called Longlife G13. The coolant fluid has density, $\rho_{coolant}$, and heat capacity, $C_{p_{coolant}}$, at 20°C of 1080 kg/m³ and 3.6 kJ/kg.K respectively, which are required to calculate the required coolant flow for a given delta temperature. For this project, it was considered an increase temperature of 10 K between coolant outlet, $T_{coolout}$, and inlet T_{coolin} . According to Küntscher and Hoffmann (2015), the heat rejection per engine power is about 0.55, which for the HBS22 maximum output indicated power of 135 kW results in a heat rejection to cooling system, $\dot{Q}_{coolant}$, of 74.25 kW. The required coolant flow was calculated using Equation 257.

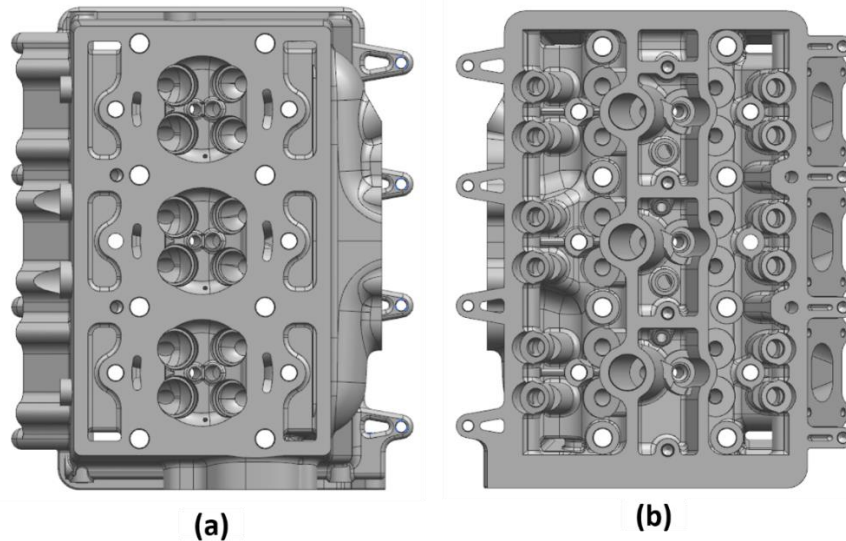
$$\begin{aligned} \dot{V}_{coolant} &= \frac{\dot{Q}_{coolant}}{\rho_{coolant} \cdot C_{p_{coolant}} \cdot (T_{coolout} - T_{coolin})} \\ &= \frac{74.25}{1080 \times 3.6 \times 10} = 1.91 \times 10^{-3} \text{ m}^3/\text{s} \\ &\approx 114.58 \text{ l/min} \end{aligned} \quad (257)$$

Based on the calculated required coolant flow and aiming to provide coolant to the engine according to its operation condition, it was defined to be used an electrical fuel coolant pump. The Pierburg CWA200 was the electrical coolant pump chosen to fit on the engine. This pump has a flow rate of 116 l/min at a differential pressure of 0.45 bar and it works based on a 12V PWM signal. As an electrical coolant pump was fitted to the engine, it was not required to use a thermostatic valve. According to

Küntscher and Hoffmann (2015), and Robinson et al. (2003), the coolant velocity should stay within the range of from 1.0 to 5.0 m/s, thus the water-jacket inlet were designed to have 402 mm² resulting in a coolant velocity of 4.75 m/s.

Once all the main features which constitute the cylinder head interior were designed, the cylinder head geometry was developed. The AlSi7Mg0.6 alloy was the material chosen to manufacture the cylinder head due its high ductility which prevent thermal fatigue cracks to occur. Furthermore, it was considered the cylinder head to be casted as manufacturing process. Figure 194 illustrates the cylinder head top and bottom views.

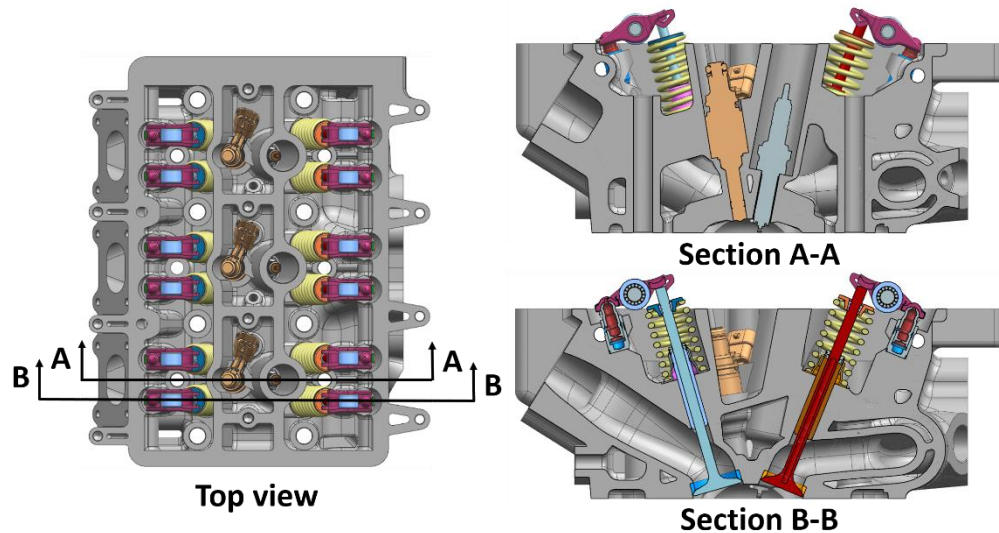
Figure 194 – Cylinder head Top view (a) and Bottom view (b)



Source: Author

As presented in Figure 195, the direct fuel injector and the spark-plug were isolated from lubricant oil at the middle of the cylinder from where the valvetrain system was assembled. It is worth to point out that it was designed a small coolant channel between the direct fuel injector and the spark-plug aiming to avoid a hot spot creation between them, as presented in Figure 195 Section A-A. Figure 195 Section B-B illustrates the designed arrangement of intake and exhaust ports, valvetrain system and the water-jacket.

Figure 195 – Cylinder head and its sub-components assembled

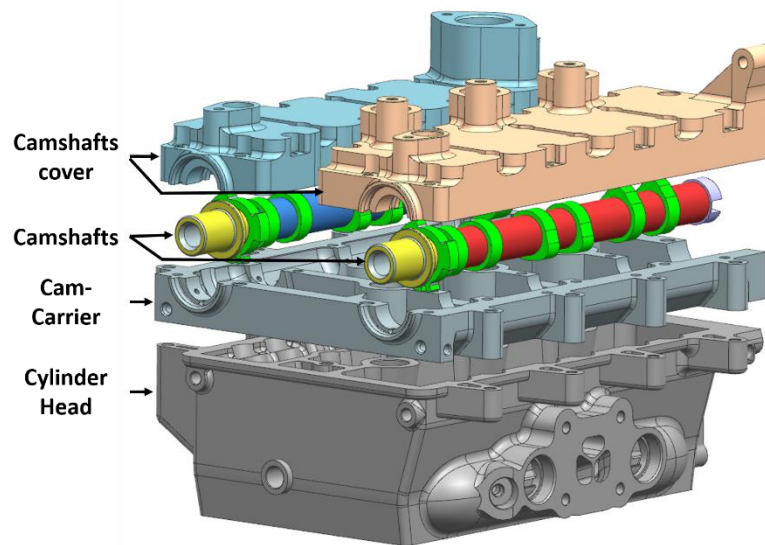


Source: Author

In order to simplify the engine prototyping process the cylinder head was the only casted component and for all the others engine main components it was defined milling as the manufacture process. Aiming a further simplification, it was designed a cam-carrier component to lay the camshafts on it. The cam-carrier and the camshaft covers were bolted in the cylinder head. Figure 196 illustrates the Cylinder head, cam-carrier and cam-covers assembly arrangement. It is worth to point out that after the engine experimental tests and cylinder head optimization it is possible to integrate the cam-carrier into cylinder head. The aluminum 6061-T6 was defined as the cam-carrier and cam-covers material due to its mechanical properties suitable for highly loaded structural applications. Aiming to minimize the engine components, the cam-covers were designed considering the assembly of the HPFP, the vacuum pump, the fuel rail and the sensors for camshaft position (Bosch 0232103037). Furthermore, the cam-covers have the role to also establish the camshaft axial clearance.

For the sealing among components were used o-rings designed according to Parker (2009) specifications.

Figure 196 – Cylinder head, cam-carrier and cam-covers assembly arrangement



Source: Author

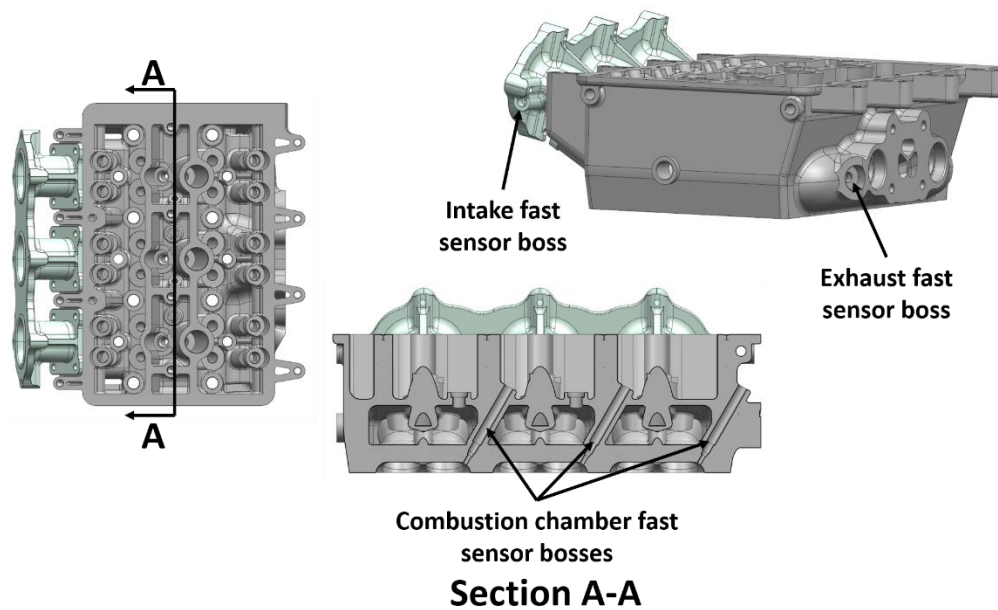
The fuel rail was designed considering to be made by aluminum 6061-T6 and milling manufactured. The fuel rail thickness, t_{fuel_rail} in [mm], was calculated considering the maximum allowable hoop stress, σ_{all} in [MPa] for the maximum pressure, a factor safety of 2.5 and a fuel rail inner diameter, d_{inner} in [mm], of 12.5, according to Equation 258.

$$t_{fuel_rail} = \frac{P_{Fuel_max} \cdot d_{inner}}{2 \cdot \sigma_{all}} = \frac{50 \times 12.5}{2 \times \left(\frac{310}{2.5}\right)} = 2.5 \text{ mm} \quad (258)$$

The injector bosses were designed according to the injector manufacturer specification.

In order to evaluate the indicated engine performance during future experimental measurements, it was considered the use of fast pressure sensors in the combustion chamber of all cylinders. Furthermore, in order to perform a TPA analysis, it was considered to be installed fast pressure sensors on the intake runner and exhaust port of the first cylinder. Figure 197 illustrates the Fast sensors bosses for indicated measurements. The sensors LP12DA, GH14DK and LP22DA with gasket SG45 were the sensors considered to be used in the engine for intake, combustion chamber and exhaust pressure measurements respectively.

Figure 197 – Fast sensors bosses for indicated measurements



Source: Author

3.3.11. Clamping forces

In this section will be presented the clamping force for the cylinder head on crankcase and the connecting rod on crankshaft assembly.

3.3.11.1. Cylinder head on crankcase clamping force

A cylinder head designed with the usual arrangement of 4 bolts per cylinder requires a higher load from the bolts to maintain the cylinder head fitted to the crankcase once one cylinder shares the bolt pre-load with the cylinder on the side. In summary, this design end up by being bolts per cylinder. In order to achieved a better bolt load distribution and maintain the cylinder head attached to crankcase at high engine load operation condition, it was defined to use four bolts per cylinder as presented in Figure 169. According to Kohler (2011), the bolts clamping force or pre-load should be 2.5 times the maximum F_{gas} in order to avoid any cylinder head lift during engine operation. Thus, the required clamping force for the HBS22 was obtained using Equation 259.

$$P_l = 2.5 \times F_{gas} = 2.5 \times 98,76 = 247 \text{ [kN]} \quad (259)$$

According to Shoperg (2018), the M12x1.25 and M10x1.25 bolts class 12.9 are able to bear 80.4kN and 52.9kN, respectively, being the bolt friction losses already considered. As illustrated in Figure 169, it was defined to use the M12x1.25 bolts closer to the cylinder and the M10x1.25 bolts slightly far from it. Therefore, it was considered 2 bolts M12x1.25 + 2 bolts M10x1.25 per cylinder. The preload coverage ratio, P_{LCR} , which determines how much of the required bolt preload was achieved considering an defined arrange of bolts was calculated using Equation 260.

$$\begin{aligned}
 P_{LCR} &= \frac{n_{bolts_M12} \cdot F_{Bolt_M12} + n_{bolts_M10} \cdot F_{Bolt_M10}}{P_l} \\
 &= \frac{2 \times 80.4 + 2 \times 52.9}{247} = 1.08
 \end{aligned}
 \tag{260}$$

After the bolts definition, it was calculated the load factor based on the joint combined stiffness and the bolt stiffness. The cylinder head, k_{CH_10} , crankcase, k_{CK_10} , and gasket stiffness, k_{GT_10} , were calculated using Equation 261, Equation 262 and Equation 263, respectively for the M10 bolts. As well as, the cylinder head, k_{CH_12} , crankcase, k_{CK_12} , and gasket stiffness, k_{GT_12} , were calculated using Equation 264, Equation 265 and Equation 266, respectively for the M12 bolts. It was considered the steel SUS301L as gasket material.

$$k_{CH_10} = \frac{2 \cdot \pi \cdot d_b^2 \cdot E}{t} = \frac{2 \times \pi \times 10^2 \times 73000}{65} = 705650 \text{ [N/mm]}
 \tag{261}$$

$$k_{CK_10} = \frac{2 \cdot \pi \cdot d_b^2 \cdot E}{t} = \frac{2 \times \pi \times 10^2 \times 68900}{82.5} = 524741 \text{ [N/mm]}
 \tag{262}$$

$$\begin{aligned}
 k_{GT_10} &= \frac{2 \cdot \pi \cdot d_b^2 \cdot E}{t} = \frac{2 \times \pi \times 10^2 \times 193000}{0.8} \\
 &= 151581846 \text{ [N/mm]}
 \end{aligned}
 \tag{263}$$

$$k_{CH_12} = \frac{2 \cdot \pi \cdot d_b^2 \cdot E}{t} = \frac{2 \times \pi \times 12^2 \times 73000}{65} = 1016136 \text{ [N/mm]}
 \tag{264}$$

$$k_{CK_12} = \frac{2 \cdot \pi \cdot d_b^2 \cdot E}{t} = \frac{2 \times \pi \times 12^2 \times 68900}{82.5} = 755627 \text{ [N/mm]}
 \tag{265}$$

$$k_{GT_{12}} = \frac{2 \cdot \pi \cdot d_b^2 \cdot E}{t} = \frac{2 \times \pi \times 12^2 \times 193000}{0.8} = 218277857 \text{ [N/mm]} \quad (266)$$

The joint combined stiffness for M10, k_{c10} , and M12, k_{c12} , were calculated using Equation 267 and Equation 268, respectively.

$$\begin{aligned} \frac{1}{k_{c10}} &= \frac{1}{k_{CH_{10}}} + \frac{1}{k_{CK_{10}}} + \frac{1}{k_{GT_{10}}} \\ &= \frac{1}{705650} + \frac{1}{524741} + \frac{1}{151581846} \therefore k_{c10} \\ &= 300352 \text{ [N/mm]} \end{aligned} \quad (267)$$

$$\begin{aligned} \frac{1}{k_{c12}} &= \frac{1}{k_{CH_{12}}} + \frac{1}{k_{CK_{12}}} + \frac{1}{k_{GT_{12}}} \\ &= \frac{1}{1016136} + \frac{1}{755627} + \frac{1}{218277857} \therefore k_{c12} \\ &= 432506 \text{ [N/mm]} \end{aligned} \quad (268)$$

The bolts stiffness for M10, k_{b10} , and M12, k_{b12} , were calculated using Equation 269 and Equation 270, respectively.

$$k_{b10} = \left(\frac{\pi \cdot d_b^2}{4} \right) \frac{E}{l} = \left(\frac{\pi \times 10^2}{4} \right) \times \frac{210000}{148.3} = 111216 \text{ [N/mm]} \quad (269)$$

$$k_{b12} = \left(\frac{\pi \cdot d_b^2}{4} \right) \frac{E}{l} = \left(\frac{\pi \times 12^2}{4} \right) \times \frac{210000}{148.3} = 160151 \text{ [N/mm]} \quad (270)$$

The load factor for M10, δ_{b10} , and M12, δ_{b12} , were calculated using Equation 271 and Equation 272, respectively.

$$\delta_{b10} = \frac{k_{b10}}{k_{b10} + k_{c10}} = \frac{111216}{111216 + 300352} = 0.27 \quad (271)$$

$$\delta_{b12} = \frac{k_{b12}}{k_{b12} + k_{c12}} = \frac{160151}{160151 + 432506} = 0.27 \quad (272)$$

The calculated load factor of 0.27 leads to a fluctuating force of 27.4kN for each bolt, which in turn results in 10.8% of fluctuation to pre-load ratio. According to Shoberg (2018) and Budydas and Nisbett (2011), it is advisable to design an joint with a fluctuation to pre-load ratio from 10 to 15% maximum.

3.3.11.2. Connecting rod clamping force

The connecting rod clamping force was determined using also joint stiffness evaluation. However, the bolt pre-load should be defined as a balance between avoid the connecting rod bearing deformation and maintain the connecting rod tight under the maximum inertial force actuation. It was defined a bolt M8x1.00 class 12.9 with 45mm length as the bolt chosen to be used in this engine.

The connecting rod joint stiffness, k_{rod} [N/mm] and the connecting rod bolt stiffness, $k_{b_{rod}}$ in [N/mm], were calculated using Equation 273 and Equation 274 respectively.

$$k_{rod} = \frac{2 \cdot \pi \cdot d_b^2 \cdot E}{t} = \frac{2 \times \pi \times 8^2 \times 208000}{50} = 1672835 \text{ [N/mm]} \quad (273)$$

$$k_{b_{rod}} = \left(\frac{\pi \cdot d_b^2}{4} \right) \frac{E}{l} = \left(\frac{\pi \times 8^2}{4} \right) \times \frac{200000}{43} = 233792 \text{ [N/mm]} \quad (274)$$

The load factor for the connecting rod joint was calculated using Equation 275.

$$\delta_{rod} = \frac{k_{b_{rod}}}{k_{b_{rod}} + k_{rod}} = \frac{233792}{233792 + 1672835} = 0.12 \quad (275)$$

The calculated load factor of 0.12 leads to a fluctuating force of 1.38kN for each bolt, which in turn results in 12% of fluctuation to pre-load ratio.

According to Shoberg (2018), a bolt M8x1.00 class 12.9 can bear 33.9kN before yielding and being the bolt friction losses already considered. As suggested by and Budydas and Nisbett (2011), the pre-load for longer life joint application can be

considered as 0.9 of the force or stress before the component yield. Thus, the connecting rod pre-load, $P_{L_{rod}}$ in [N] was calculated using Equation 276.

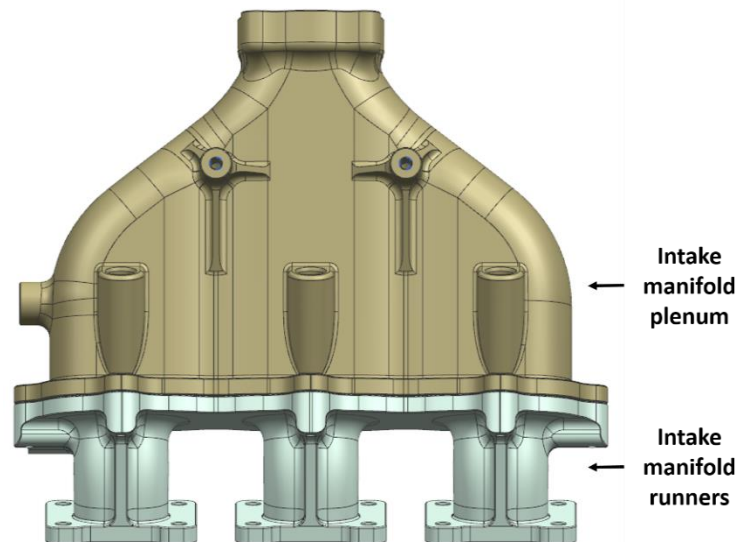
$$P_{L_{rod}} = 33.9 \times 0.9 = 30.51 \text{ [kN]} \quad (276)$$

The calculated load factor of 0.12 leads to a fluctuating force of 1.38kN, which in turn results in 4.5% of fluctuation to pre-load ratio.

3.3.12. Intake manifold and Water injection System

The intake manifold designed for the engine was divided into intake runners and the plenum aiming to use the milling as manufacture process. As also used for the cam-carrier and cam-covers, the aluminum 6061-T6 was defined as the intake manifold material due to its mechanical properties suitable for highly loaded structural applications. Figure 198 illustrates the designed intake manifold.

Figure 198 – Intake manifold



Source: Author

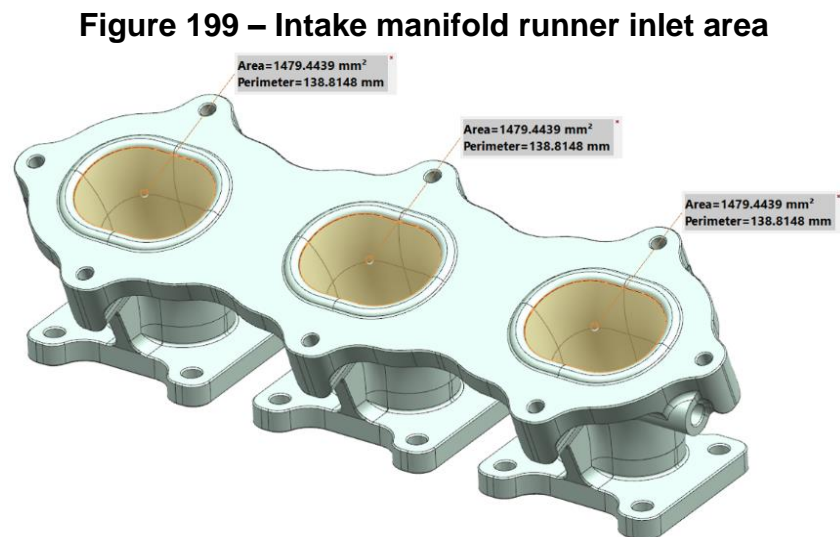
The intake manifold runners were design as a single piece to be fitted in the cylinder head. The runner outlet geometry was designed being 1 mm smaller in its perimeter in order to avoid any fluid disturb from geometry mismatch assembly between intake manifold and cylinder head. Furthermore, the runner inlet was designed as a bellmouth shape aiming to minimize the Vena contracta effect. The runner inlet area, A_t in m^2 , was calculated using Equation 277 considering the engine

speed at peak power as reference condition. The piston mean speed calculated for this condition and the piston area resulted in 15.8 m/s and 0.004015 m². It was considered the speed of sound of 343 m/s at 20°C and a Mach Index of 0.125 as suggested by Pignone (2003).

$$A_t = 2 \cdot \frac{S_p \cdot A_p}{IM_t \cdot a} = \frac{15.8 \times 0.004015}{0.125 \times 343} = 1.479 \times 10^{-3} \text{ m}^2 \quad (277)$$

$$\approx 1479 \text{ mm}^2$$

It is worth is to point out that the suggested area over bellmouth radius was not achieved due to package reasons. Figure 199 illustrates the designed intake manifold runner inlet area. The intake runner length was defined as 60 mm in order to improve the engine volumetric efficiency at higher engine speeds.



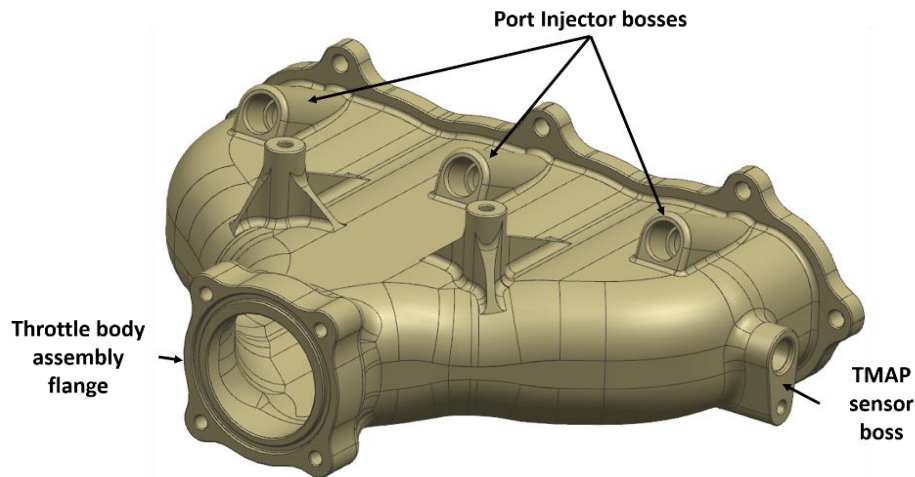
Source: Author

The intake manifold plenum was designed as a central air entrance concept. The initial intake manifold geometries were evaluated by Ramos (2020) and the better results regarding air metering among cylinders was achieved by the central air entrance concept.

The intake manifold plenum volume was defined as 1.5 l following a design guide line from engine manufacture which suggest that the intake manifold plenum volume should be 1.5 times the engine displacement for turbocharger engine application. Figure 200 illustrates the designed intake manifold plenum highlighting the

port injector bosses, the TMAP sensor boss. The TMAP sensor Bosch 0261230423 was chosen to be used in the intake manifold.

Figure 200 – Intake manifold plenum



Source: Author

The runner inlet area afore calculated was used as reference to establish the throttle body diameter, D_{th} in [mm]. The throttle body diameter was calculated using Equation 278.

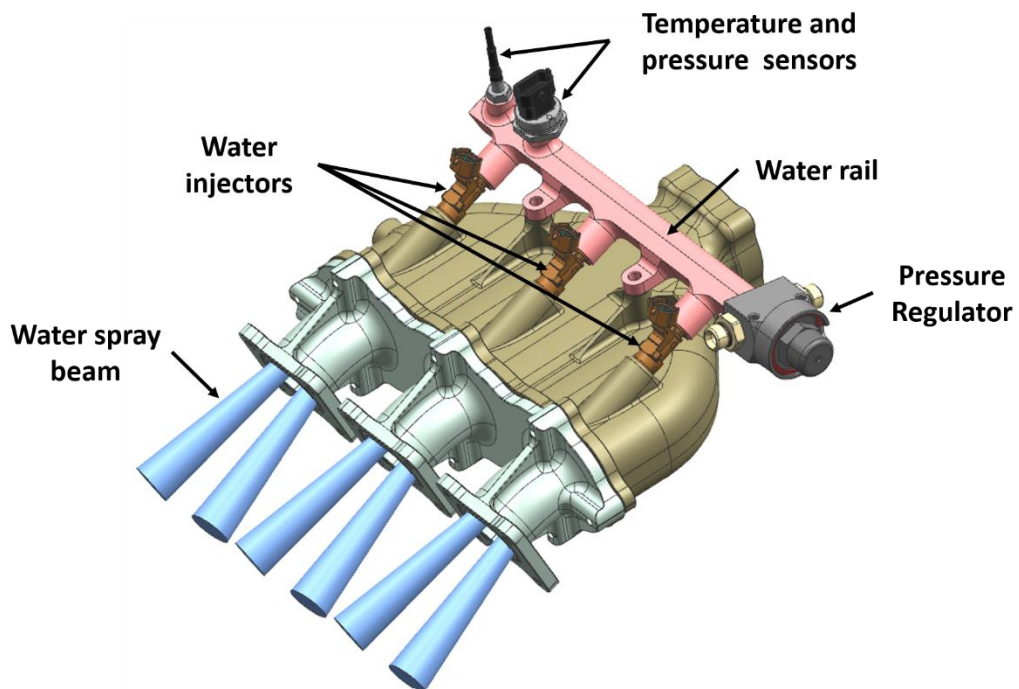
$$D_{th} = \sqrt{\frac{4 \cdot A_t}{\pi}} = \sqrt{\frac{4 \times 1479}{\pi}} = 43.39 \text{ mm} \quad (278)$$

The throttle body Bosch 0280.750.137 which has 44 mm of diameter was chosen to be used in this project.

For the sealing among the throttle body, plenum, runners and cylinder head were used o-rings designed according Parker (2019) specifications.

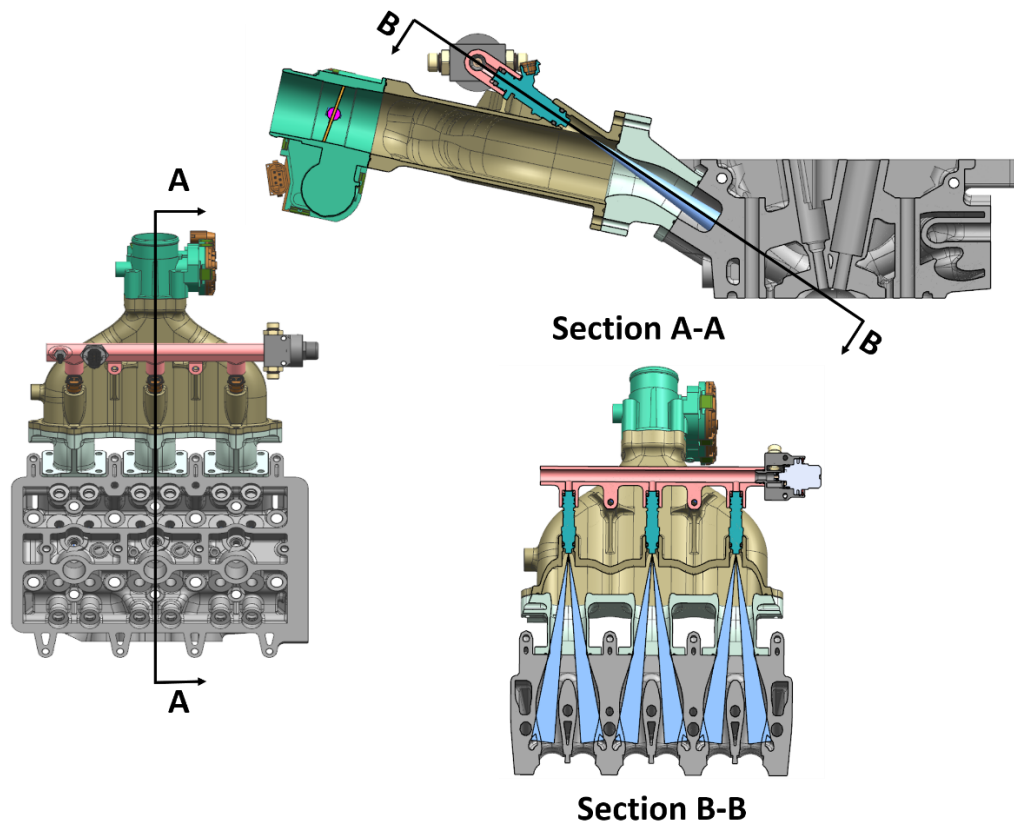
As presented in Figure 201 the water injection system fitted on the intake manifold plenum is constituted by the water injectors Bosch EV14S/0280158200, the pressure regulator and its adapter Bosch F02U.V02.172-01 and Bosch F02U.V02.248-01, respectively, the water rail and the temperature and pressure sensors Bosch F 02U V00 509-01 and Bosch F 02U V01 268-01, respectively.

Figure 201 – Water injection system



The water rail was designed considered to be made by aluminum 6061-T6 and manufactured via milling process. The injector bosses were designed according to the injector manufacturer specification. The water injector was chosen aiming to be able to supply at least 25% of the highest fuel injection flow and not operate in the injector ballistic region for small water injection amount. Furthermore, dual spray beam injectors were chosen in order to inject water into each intake port as close as possible of intake valves, as illustrated in Figure 202. The pressure regulator is able to work with pressure up to 10 bar.

Figure 202 – Water injector spray target

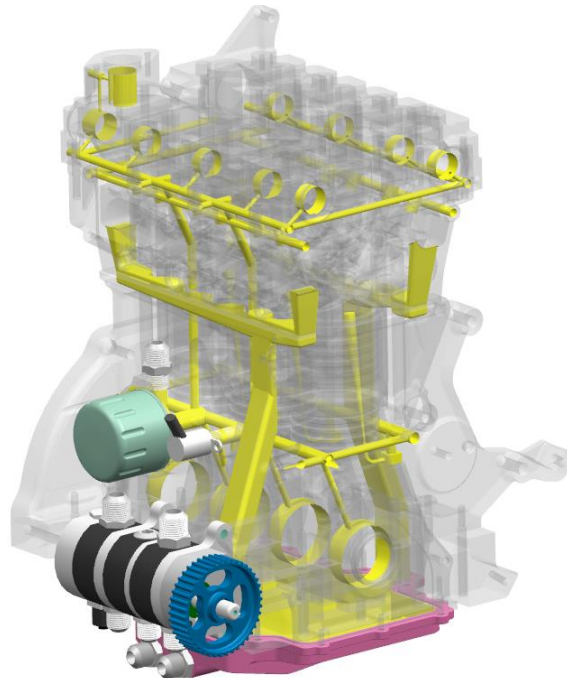


Source: Author

3.3.13. Lubricant oil circuit

In order to supply lubricant oil for each component which requires, it was designed the engine oil circuit. A dry sump concept system was chosen to be applied to the engine aiming a better piston rings stability and lower piston movement resistance. The blow-by gases sucked by the oil scavenging pump was designed to return to the engine at turbocharger inlet. The oil pump PN07843 has two scavenging stages and one of oil supply to the engine. It is manufacture by the Aviaid Company. The oil pump is driven by the engine crankshaft using a belt and it was defined a ratio 1.75 times the crankshaft speed for the oil pump working condition. It is worth to point out that the oil pump drive belt was installed behind the engine dumper in order minimize the belt height displacement from the crankshaft nose non-rotational movement. Figure 203 illustrates the engine oil lubricant system.

Figure 203 – Engine oil lubricant system



Source: Author

The oil pressure was controlled via a two-stage solenoid valve installed on the engine block connecting the oil high pressure line to the oil sump. The two-stage solenoid valve limits the oil pressure at 4.2 bar and 1.35 bar, thus depending on the engine running condition it could be chosen between high pressure and low pressure oil supply in order to minimize the engine passive losses. The two-stage solenoid valve is manufactured by Ford Company and it has the PN CM5G6C880DA/ 1882102.

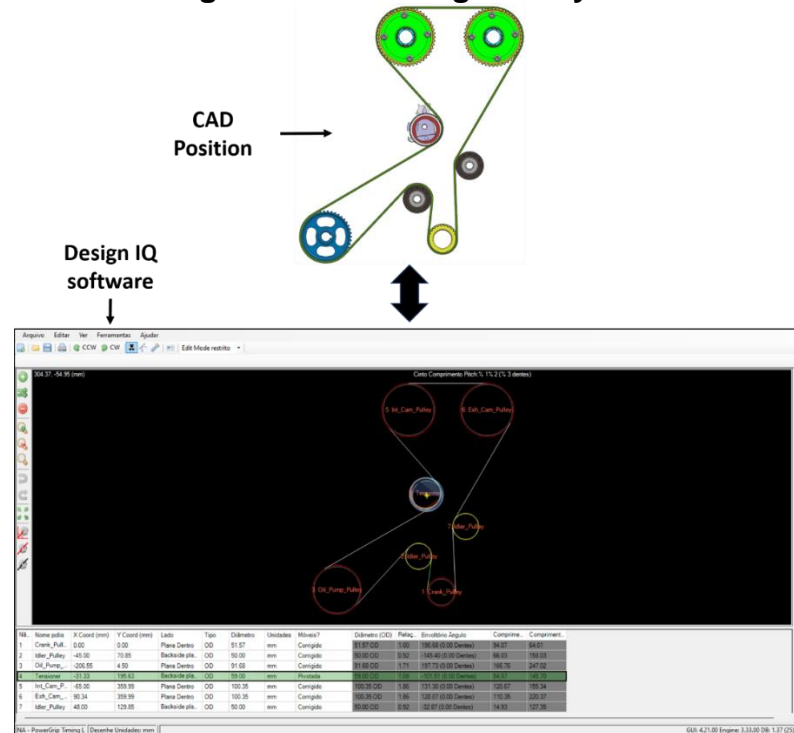
The oil lubricant MaxPro Synthetic 0W-30 manufactured by Mopar and identified by the number K68444159LA was defined to be used in the engine. This oil was chosen considering that it has been used in turbocharged flex-fuel engines in Brazil, which in turn it has the chemical compatibility with Brazilian ethanol and suitable properties for engine high load application. The lubricant oil working temperature it was defined to be on average 110°C and limited to 125 °C.

3.3.14. Engine timing belt

The engine synchronization was designed to be made by a dry timing belt. The synchronization by belt was defined considered to be easier to any mechanical intervention and the camshaft phasers require the use of a belt. The timing belt layout was defined using the software Gates Design IQ. As presented in Figure 204, the

camshafts phasers, oil pump pulley, idlers and the tensioner were positioned in the Desing IQ according to the engine geometry CAD for the timing belt calculation.

Figure 204 – Timing belt layout



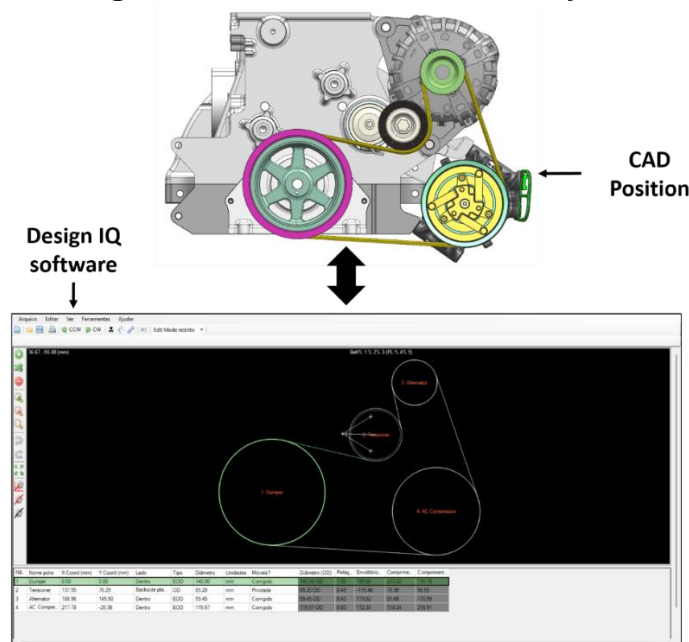
Source: Author

The software belt design result output suggested some pulleys repositioned for an improved torque transmission, however the crank and camshaft pulleys position were not modified. Furthermore, the software result output established that is required a belt length of 1729 mm for the engine timing synchronization. As the camshaft phasers require a belt with 7 mm of belt pitch, the belt must have 247 teeth. Additionally, the camshaft phasers also require to be used a belt with top width of 24 mm. A belt of this length was not available in the Gates catalog, however the company has an option for special belts development. The timing belt is intended to be manufactured according the Gates RPM® Timing Belts series. This belts series are constructed of HNBR elastomeric composites with the belt tooth jacket reinforced with high-performance nylon material aiming to minimize wear. It was used a Roltens RT6009 as a belt tensioner and flanged idler pulleys FYTPBSN50-25 manufactured by Dongguan Forrun Hardware Company.

3.3.15. Engine Accessories and Starter

The engine was fitted with the alternator Denso 52067420 and an air conditioned compressor Mahle ACP-221/ 52094150. A similar approach used for the timing belt definition was used for the accessory drive belt as illustrated in Figure 205. As a result from Gates Design IQ software, the accessory belt K050415RPM / 855295415 was defined to be used in this project. The accessory belt is a micro-v type belt with 5 ribs, it has 1054 mm of effective length and 17 mm width. In order to maintain the suitable belt tension during engine operation, the belt tensioner Rolteks RT6770.

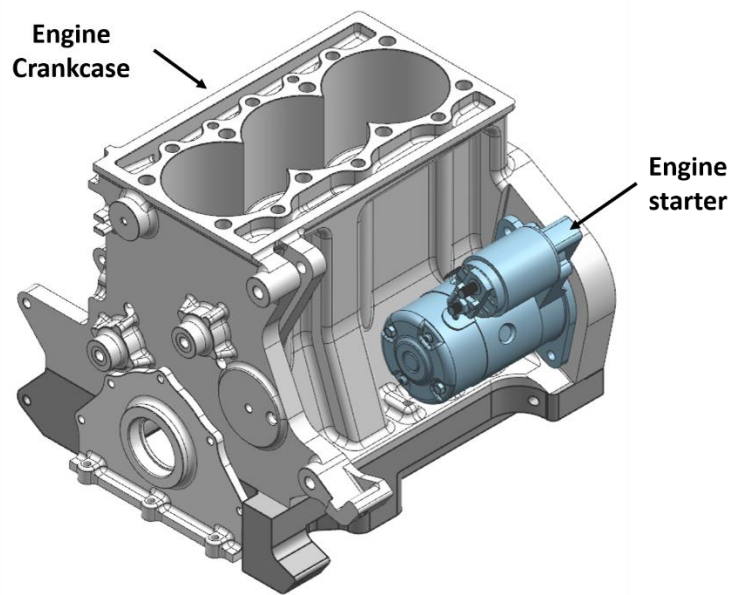
Figure 205 – Accessories belt layout



Source: Author

For the engine start process, it was chosen the starter Denso BC4380002590 due to its small size and clockwise rotation suitable for this project. Furthermore, this engine starter is available in the market on engines which have slightly lower volumetric compression ratio than used on the HBS22, which in turn tends to not present lack of power to start the engine developed in this work. Figure 206 illustrates the chosen engine starter fitted on the engine crankcase.

Figure 206 – Engine starter



Source: Author

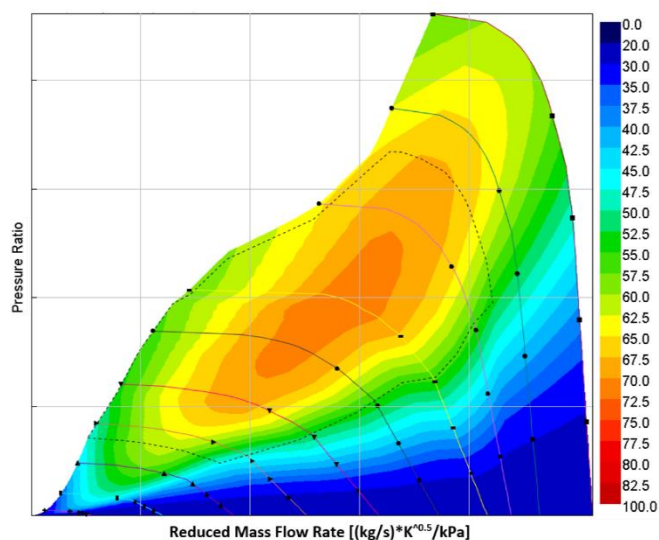
3.3.16. Turbocharger

Several turbocharger maps, provided by BorgWarner, were used throughout the turbo-matching procedure.

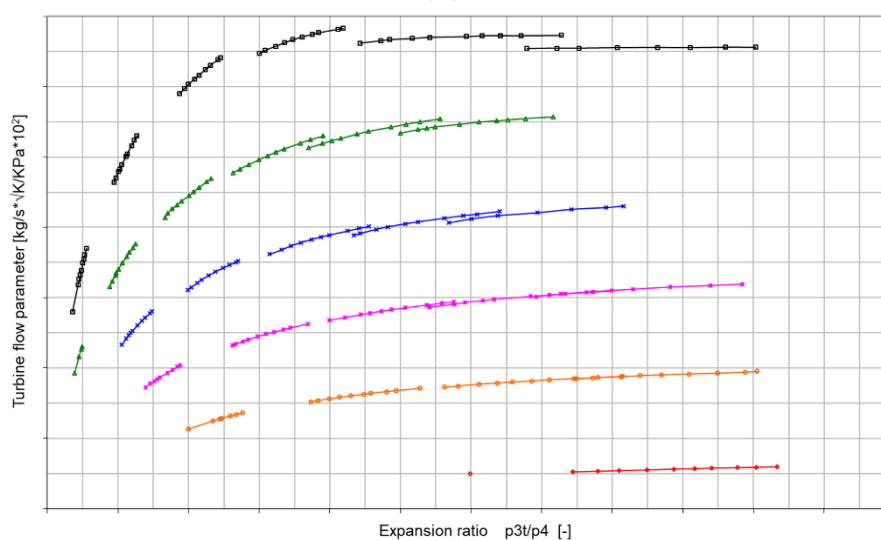
The turbo-matching procedure applied to compressor evaluation was performed considering the predicted corrected air mass flow and the intake manifold to ambient pressure ratio required to achieve the established performance. For turbine evaluation, it was considered the total mass flow predicted to pass through turbine corrected by exhaust predicted temperature and pressure. The exhaust predicted temperature and pressure were performed based on previous simulation and experimental results.

Due to engine requirements to achieve high torque values at a low engine speed and high power output, a VTG (variable turbine geometry) was chosen to be used in the engine. Some advantages arising from the use of a VTG were presented by Kluin (2017) and Schäfer (2017). Figure 207 illustrates the compressor and turbine map.

Figure 207 – (a) Compressor map and (b) turbine map



(a)



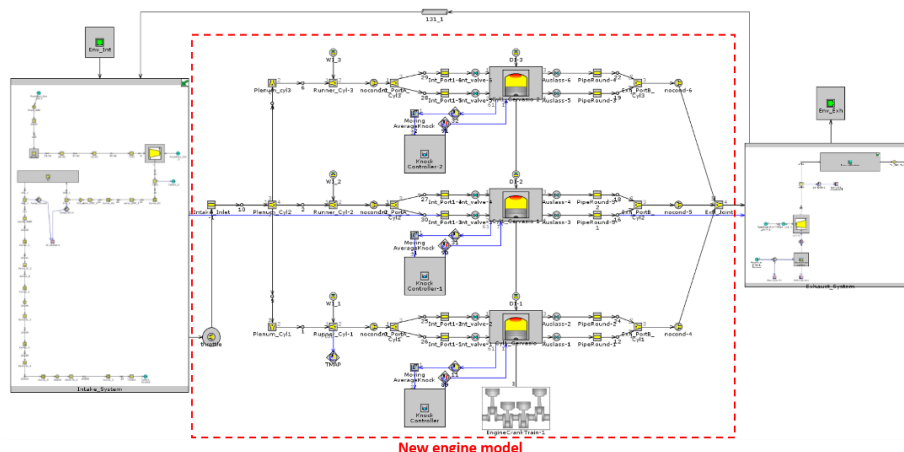
(b)

Source: Author

3.4. 1D Numerical Simulation Model

For the 1D numerical simulation, the GT-Suite software was used, whose choice is justified by its robust simulation tools and its user-friendly interface. The 1D model built in this work was based on the engine 3D geometry, which physically defines the system's load losses, employing the vehicle intake and exhaust systems used in the engine model presented by Baêta et al. (2018). Thus, the main engine model was constructed from the throttle body inlet to the exhaust ports outlet, as shown in Figure 208.

Figure 208 – Engine numerical simulation model



Source: Author

The main numerical model inputs used were as follows: engine friction, engine coolant, lubricant oil and intake air temperatures, fuel properties, the exhaust backpressure as the first reference value and the intake manifold pressure, intake and exhaust valve timing and the water mass injected to assist the combustion process.

The predicted engine friction input was taken from Baêta et al. (2018). However, as it was intended to fit the engine with modern accessory drive, the engine friction input was only used to make the simulation run. For the engine coolant and lubricant oil temperature, the values were 90 °C and 110 °C, respectively. The intake air temperature boundary condition was defined as 50 °C, considering the modern water cooler air charge (WCAC) system fitted in the vehicle, which was able to maintain the temperature required throughout the entire engine running conditions. As previously mentioned, the engine developed in this work runs exclusively on Brazilian ethanol (E100) by means of a DI system. Thus, the Brazilian ethanol properties presented in Table 53 were configured into the model. Furthermore, all the engine simulation was conducted for a stoichiometric air-fuel mixture

The exhaust backpressure values on the first simulation loop were predicted based on experimental results from a similar 3-cylinder engine, which is fitted with a similar cylinder head designed with integrated exhaust manifold technology. However, the exhaust backpressure values were extrapolated for the higher mass flow rate achieved by HBS22.

Table 53 – Main fuel properties the Brazilian ethanol used in the model

Parameter	Value
-----------	-------

Density [kg/m ³]	805.2
MON [-]	91.8
RON [-]	>100
Heat Value [MJ/kg]	24.76
Stoichiometric AF ratio	8.36:1

Source: Author

To determine the intake and exhaust valve timings, an optimization tool available in the GT-Power software was used, which was configured to maximize the engine volumetric efficiency by varying the intake and exhaust valve timings within the VVA phaser limits used for this project. During the valve timing optimization procedure, the engine was considered to be running in a motoring condition and the inlet and outlet air state as a simple boundary condition.

The water was injected into the engine intake runners and its injected mass was defined as a ratio between the water and the fuel mass supplied to the engine. The parameter water-to-fuel ratio (WFR) was defined to illustrate this relation. The water temperature was defined as 25°C and a differential pressure of 5 bar related to the intake manifold pressure was defined for water injection pressure. The water injection aim is to assist the combustion process and promote a full spark authority. Therefore, the amount of water injected was established in order to place the MFB50% (mass fraction burned) at 8.0° CA. The first WFR values configured in the model were calculated based on the linear response of water consumption associated with the load increase presented by Baêta et al. (2018).

For the combustion process, the combustion model presented by Gervásio (2017) was used. However, the model was adapted to the engine developed in this work. Furthermore, it was included in the model a knock controller in order to manage the knock onset during the engine simulation. The knock controller is based on the model developed by Douaud and Eyzat (1978), and its output value was used in a PID (Proportional Integral Derivative) controller to change the spark timing input of the engine model. The knock model was validated considering the experimental data obtained by Baêta et al. (2018). Table 54 presents a comparison from Baêta et al. (2018) and the predicted performance for the engine developed in this work at 2500 rpm and 33 bar of IMEP.

Table 54 – Combustion and knock model validation

Parameter	Results from Baêta et al. (2018)	This work
Engine Speed (rpm)	2500	2500
IMEP (bar)	33.1	33.3
MFB50% (° CA)	8.6	8.7
MFB10–90% (° CA)	18.1	16.8
Indicated Power (kW)	66.7	69.3
Indicated Torque (N.m)	260.8	264.9
WFR (%)	10.7	10.7
Lambda (-)	1.00	1.00

Source: Author

The VGT turbocharger maps presented in 3.314 were entered in the model. The VGT position related to each engine operation condition was established using the optimization tool available in GT-Power. The optimization was configured to target the required air mass flow for the engine performance, minimizing the exhaust backpressure. During the VGT position optimization process, the intake air was modeled as a simple boundary condition and the complete exhaust system was used. Once the VGT positions were established, the compressor feature along with the entire intake system were included in the model and several compressor maps were evaluated to avoid a compressor surge and choke condition throughout the engine simulation. Furthermore, it was intended that one would place the higher compressor polytropic efficiencies in a range of the most common speeds predicted for this engine application.

4. RESULTS

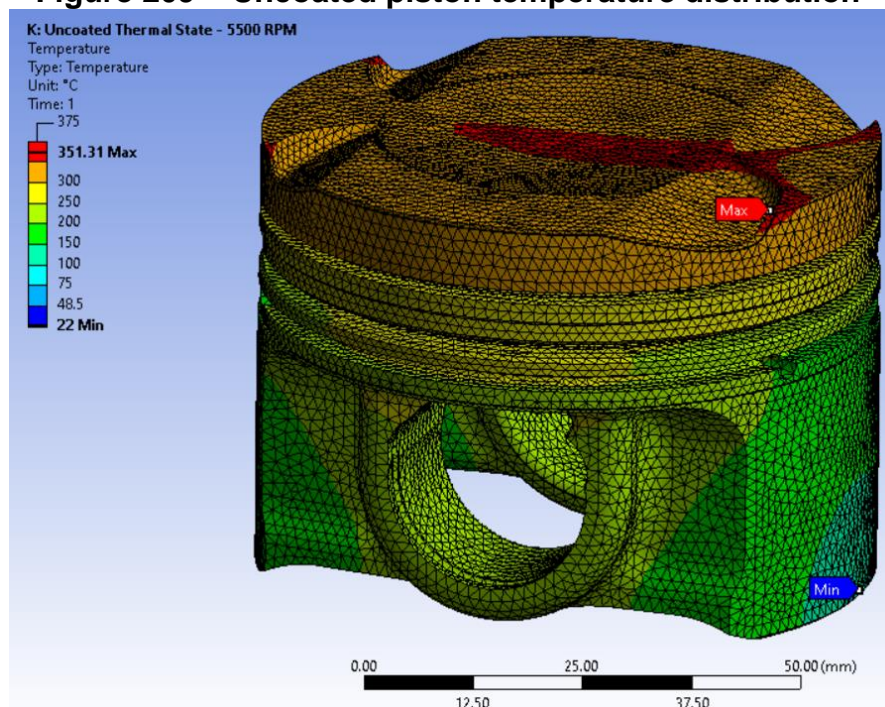
This chapter presents the results obtained according to the methods explained in the previous chapter. The results were divided in FEM numerical simulation and 1D numerical simulation.

4.1. FEM numerical simulation

4.1.1. Piston

The piston thermal load results were the first to be evaluated. An uncoated piston simulation was performed in order to validate the thermal inputs considered in the simulation. The uncoated piston temperature distribution is shown in Figure 209. Based on the achieved results, it could be concluded that the piston temperature distribution presented a good match with the values predicted by Mahle (2016) available in Table 5.

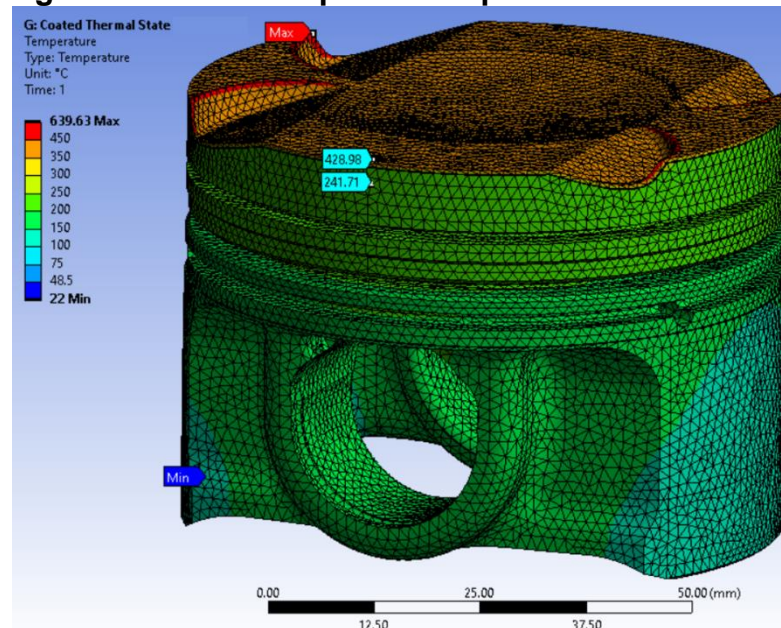
Figure 209 – Uncoated piston temperature distribution



Source: Author

As illustrated in Figure 210, the coated piston temperature distribution presented a high heat concentration on the piston crown which lead to a temperature reduction of about 188°C between piston crown and top land. This results showed similar temperature drop behavior as presented by Reghu et al. (2020) in his work where about 100 and 125µm of TBC thickness could lead to a piston temperature drop of 40 to 48C°and adding more 25µm it could drop the piston temperature further 40%.

Figure 210 – Coated piston temperature distribution

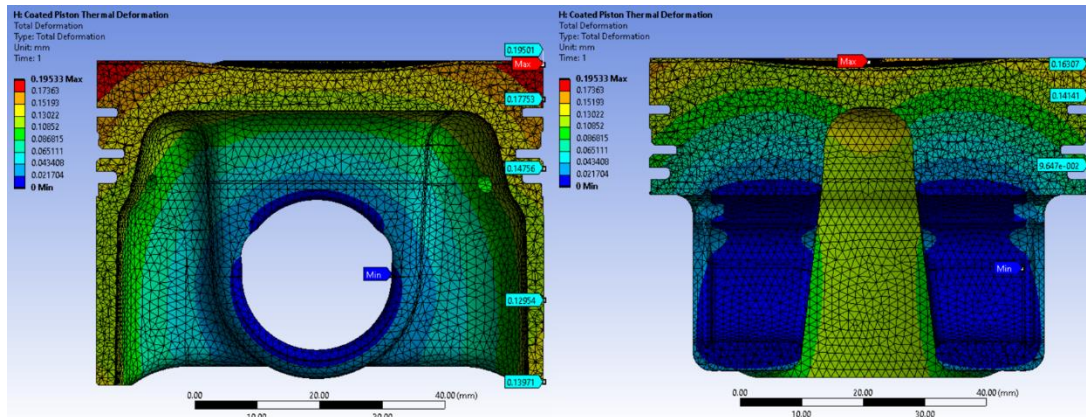


Source: Author

It is worth to point out that the higher heat trapped in the combustion chamber could lead to a higher knock tendency. For the engine designed in this work the higher knock on set will be addressed by changing the amount of water injected in order to keep the combustion phase at its optimum timing. The amount of heat trapped in the combustion chamber compared to the amount of that the air-fuel-water mixture absorb will be performed in futures steps of this work, in order to evaluate the amount of apparent heat available to produce work.

Figure 211 shows the piston profile deformation due to thermal load. Comparing the resulted deformation with the designed clearance from Table 39 it can be concluded that the piston will be not get stuck in the cylinder liner. However at plane DN-TA it was indicated an oversize of 0.06mm. It is worth to point out that piston to wall clearance is also affected by the cylinder liner. The final piston to wall clearance will be evaluated after cylinder liner thermal deformation simulation. However, depending on the allowable piston skirt pressure on lubricant oil film this skirt support could lead to a more stable piston secondary movement as suggested by Yanjun Lu et al. (2018).

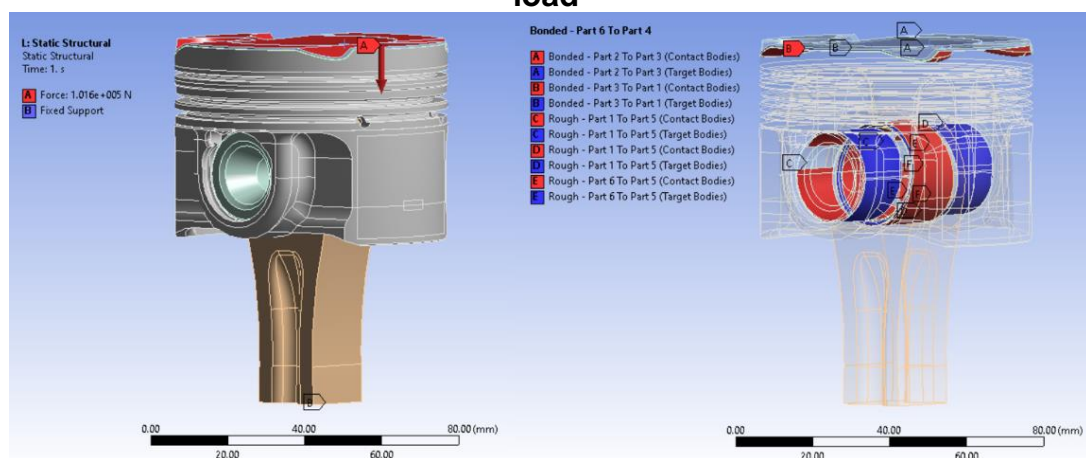
Figure 211 – Piston profile thermal deformation



Source: Author

After the thermal load being applied to the piston, the results from mechanical load were obtained. In order to not impose a higher stiffness than the geometries have, it was used the assembly piston, piston pin and connecting rod trimmed by a plane 60 mm far from the piston pin for the mechanical load simulation.

Figure 212 – Piston, piston pin and connecting rod contacts and mechanical load



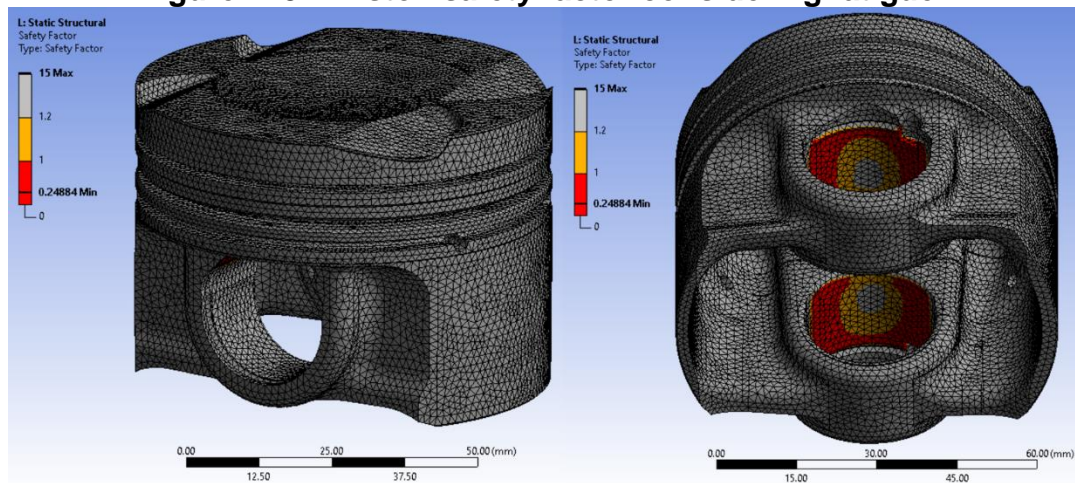
Source: Author

The piston performance under the mechanical load application was evaluated from the component fatigue point of view according to the Goodman criteria and 5.10^8 load cycles as the piston is made of aluminum. The gas and inertia forces application on the components were modeled as a mechanical load ratio of -0.11 which corresponds to the inertia to gas forces ratio. As suggested by the piston manufactures guide-lines, it was considered 1.2 as factor of safety for the piston evaluation.

As presented in Figure 213, the piston safety factor achieved values over 1.2 almost on its entire geometry. However, on the upper part of the piston pin bore there

were critical areas which the safety factor is lower than 1.2. Similar critical area was identified by Silva (2006) and it was suggested to address it by hard anodizing the piston pin bore. On the other hand, Kolbenschmidt (2018) suggest that the piston pin boss should be bushed for high load applications. For the engine developed in this work, it is intended to first evaluate the piston behavior with the hard anodizing and after, if it is necessary, bush the piston pin boss.

Figure 213 – Piston safety factor considering fatigue

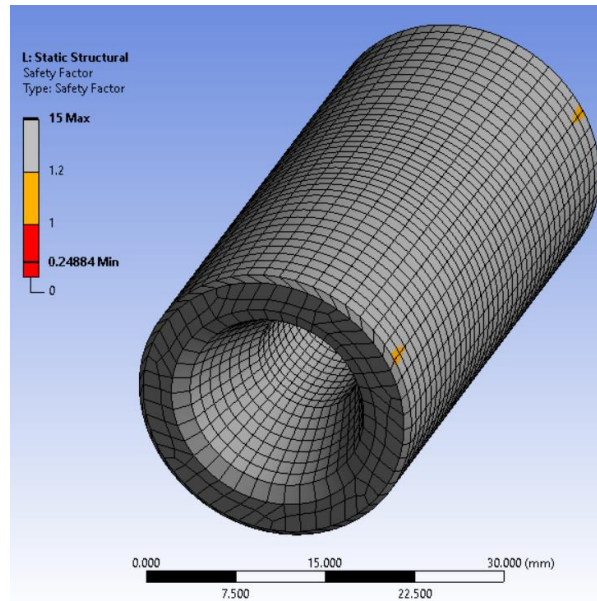


Source: Author

4.1.2. Piston Pin

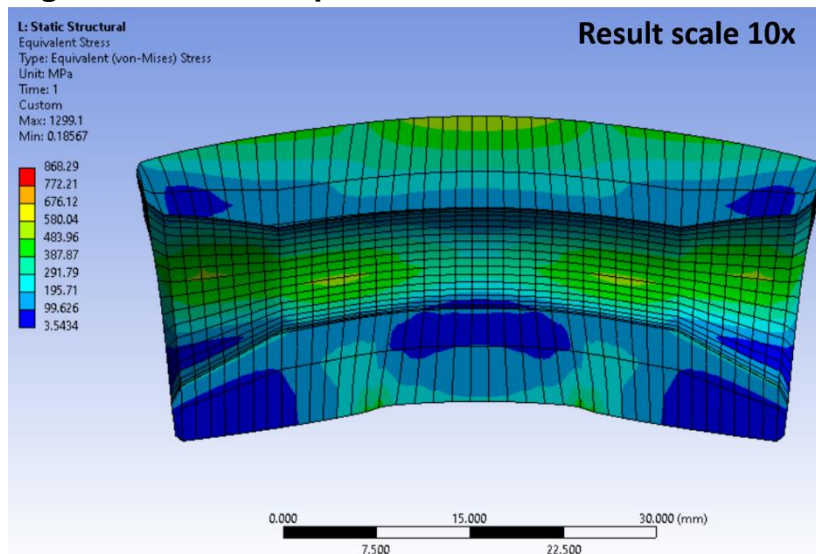
As illustrated in Figure 212 the piston pin mechanical load simulation was carried out along with the piston simulation. Likewise the piston, it was considered 1.2 as factor of safety for the piston pin evaluation. The results from the mechanical load application on the piston pin are presented in Figure 214. According to the simulation results, the proposed piston pin geometry was able to bear the mechanical load applied on it. Furthermore, the simulation results of Von Misses stress distribution presented a similar trend as presented by Bohn (2016).

Figure 214 – Piston pin safety factor considering fatigue



Source: Author

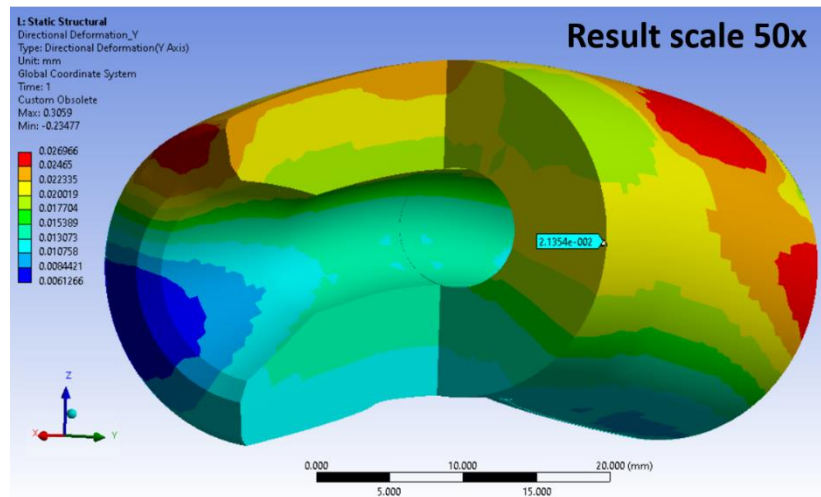
Figure 215 – Piston pin Von Mises stress distribution



Source: Author

The piston pin ovality is one of the main parameters that affects the piston pin performance and life usage. As presented in topic 2.5.5.1, it is suggested to not have an ovalization higher than $25\mu\text{m}$. The results from the piston pin simulation presented an ovalization of $21.3\mu\text{m}$ as presented in Figure 216.

Figure 216 – Piston pin ovalization

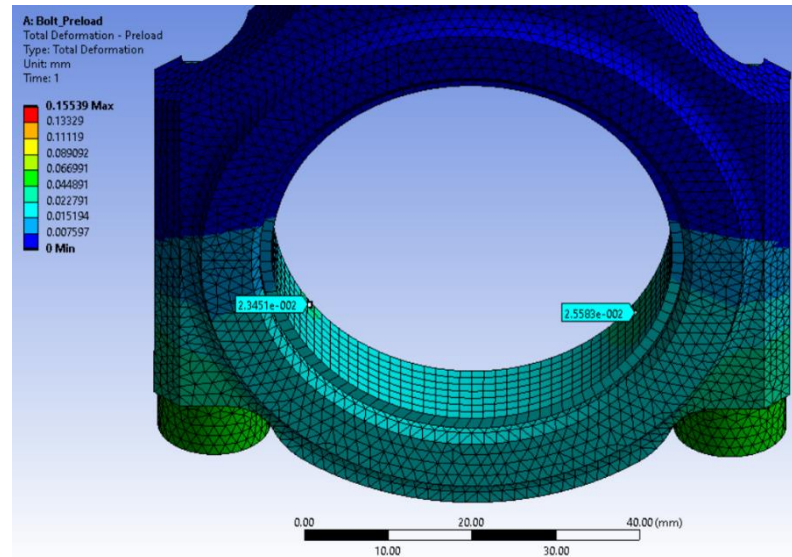


Source: Author

4.1.3. Connecting rod

The connecting rod was evaluated according to the mechanical load applied on it, firstly due to preload applied on the connecting rod bolts and after the gas and inertia forces. As defined in the topic 3.3.11.2, the preload applied to the bolts were 30.51kN and it is expected from it to achieve a compromise between connecting rod bearing deformation and maintain the connecting rod tight under inertia forces actuation. Figure 217 shows the overall connecting rod deformation on the big bore region due to the bolts preload. It was noticed that a connecting rod bearing deformation of 25.8 μ m was punctually presented. According to Kopeliovich (2019), the maximum ovality suggested to be achieved in a bearing is 25.0 μ m. Therefore, considering to be a small region where the high deformation appeared on the bearing along with the maximum deformation is similar to maximum deformation advisable to limit, the connecting rod clamping force was validated from the bearing deformation point of view.

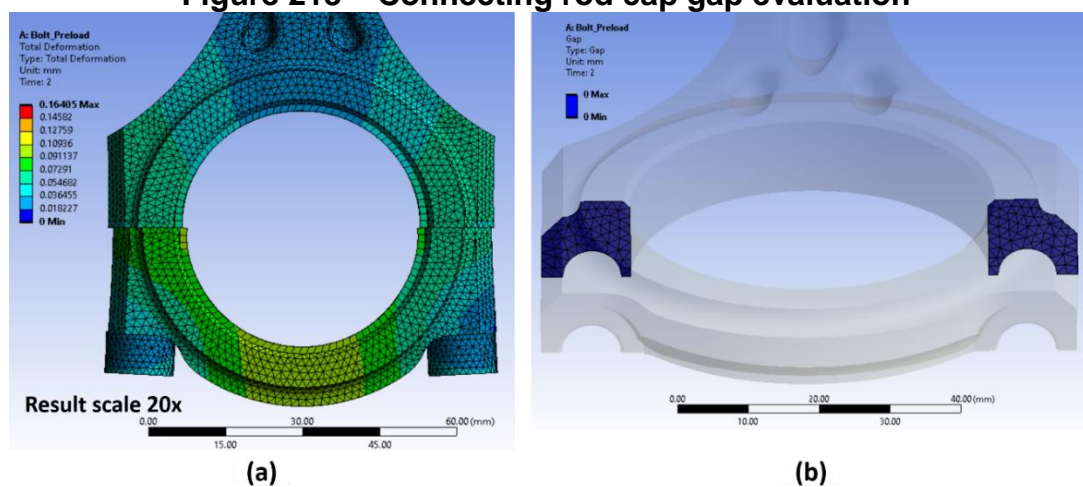
Figure 217 – Connecting rod bearing deformation due to bolts preload



Source: Author

Once the preload was applied on the connecting rod bolts, the inertia force was applied on the lower bearing in order to evaluate the tightness between connecting rod and connecting rod cap, as presented in Figure 218a. The contact type between connecting rod and connecting rod cap were defined as frictionless and thus it was allowed motion between them. The gap tool feature available in the software was used to evaluate the tightness between connecting rod and connecting rod cap. As presented in Figure 218b the surfaces remained attached on to another, in other words the gap was zero, and after the inertia force being cyclic applied on it. Which in turn, validate the preload defined for the connecting rod bolts.

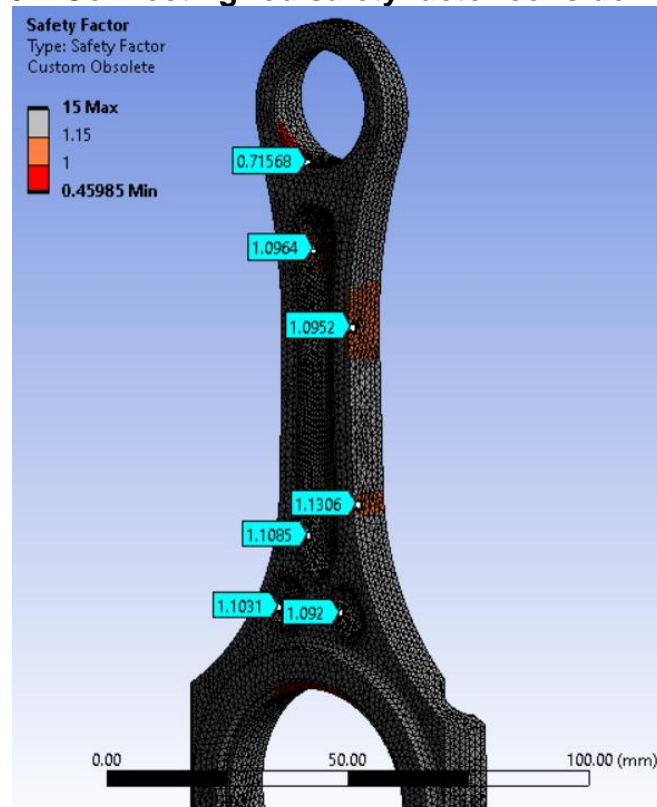
Figure 218 – Connecting rod cap gap evaluation



Source: Author

The connecting rod performance under the mechanical load application was evaluated from the component fatigue point of view according to the Goodman criteria. The gas and inertia forces application on the components were modeled as a mechanical load ratio of -0.11 which corresponds to the inertia to gas forces ratio. As suggested by the piston manufactures guide-lines, it was considered 1.15 as factor of safety for the piston evaluation. As presented in Figure 219, the connecting rod safety factor achieved values higher than 1.15. However, some locally connecting rod regions achieved between 1.00 and 1.15. As these regions did not achieved values than 1.00, the connecting rod proposed was considered suitable for the application and if any optimization be required it would be addressed during the prototyping phase. The indicated safety factor lower than 1.00 in Figure 219 could be evaluated as eddies effect on the estimated stress, and this connecting rod will be evaluated during prototyping phase.

Figure 219 – Connecting rod safety factor considering fatigue

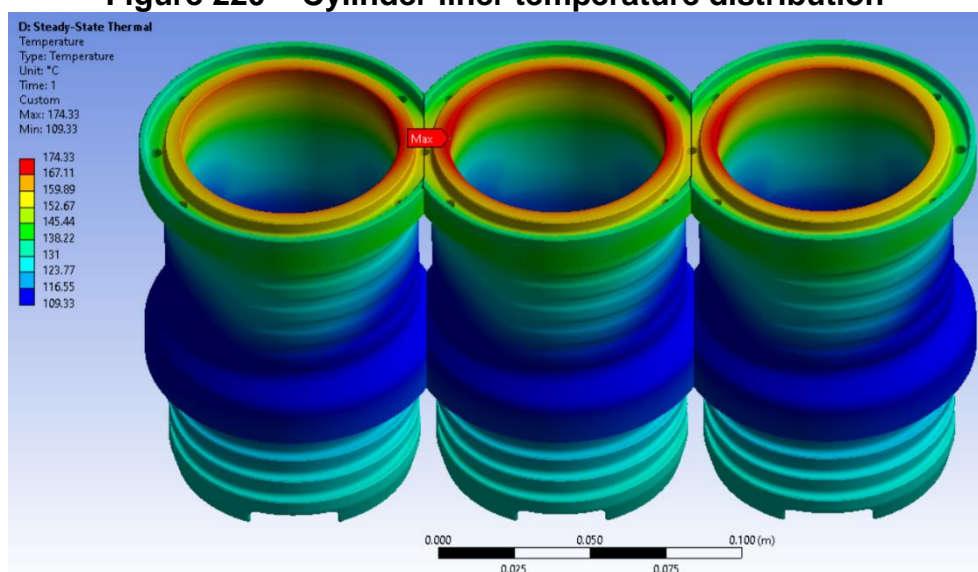


Source: Author

4.1.4. Liner

Figure 220 presents the cylinder liner temperature distribution. The higher temperatures were achieved among cylinders which the maximum temperature reached was 174°C. This value temperature distribution presented a similar behavior as presented by Ning (2010) although with lower temperatures. The lower temperatures could be justified by the coolant channel designed in the liners near of the fire deck. According to Gamma Technologies (2020), the cylinder liners temperature the fire deck region stays in a range between from 170 to 210°C.

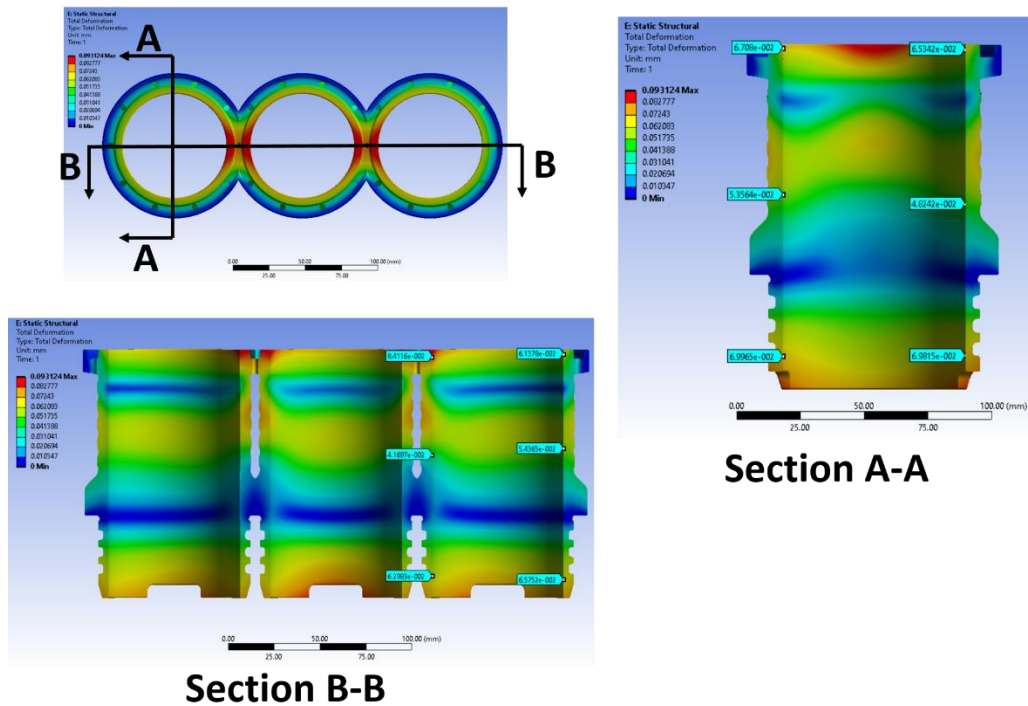
Figure 220 – Cylinder liner temperature distribution



Source: Author

Ideally the cylinder liners simulation regarding the mechanical load applied on them should be performed along with the crankcase. However, due to a lack of computational power the simulation considering the cylinder liner with the crankcase and cylinder head assembled together was not possible. The cylinder liner contact interfaces with crankcase were considered as fixed boundaries. The cylinder liners distortion due to the thermal load is presented in Figure 221. The results indicated that the cylinder liner did not presented significant distortions when compared measurements from three different points, measured on the thrust and anti-thrust axis. However, due to the temperature and support difference and between cylinders and liner, a slightly 2nd order distortion was presented. The final liner distortion evaluation should be performed taking in to account the cylinder head assembly bolt pre-load. This evaluation will be performed in a next step using a higher computational power availability.

Figure 221 – Cylinder liner distortion due to thermal load

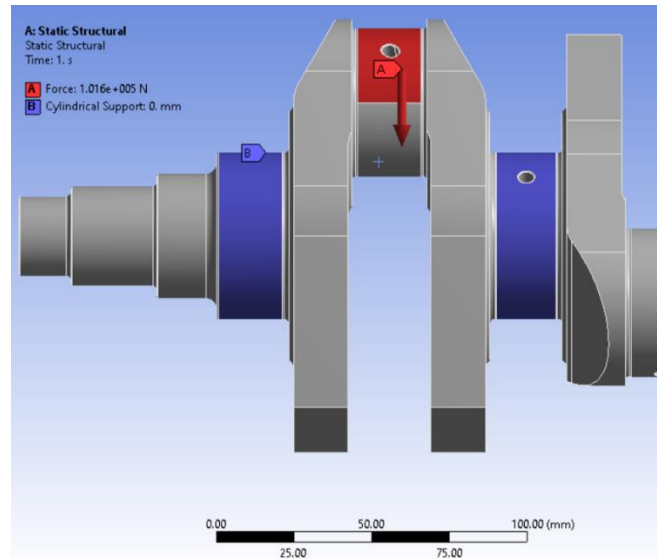


Source: Author

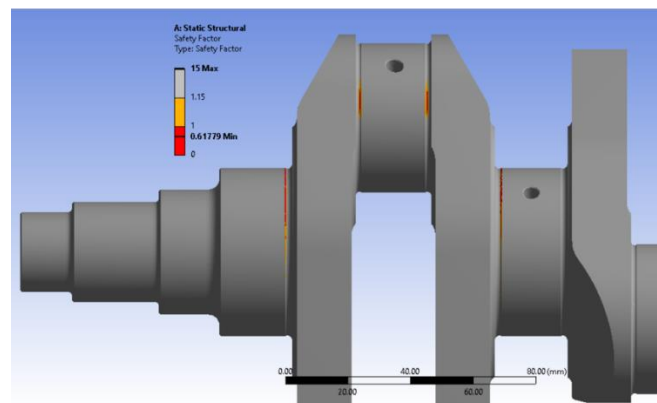
4.1.5. Crankshaft

The crankshaft performance under the mechanical load application was evaluated from the component fatigue point of view according to the Goodman criteria. The gas and inertia forces application on the components were modeled as a mechanical load ratio of -0.11 which corresponds to the inertia to gas forces ratio. As suggested by the piston manufactures guide-lines, it was considered 1.15 as factor of safety for the crankshaft evaluation. The mechanical load applied on crankshaft as normal force is illustrated in Figure 222.

Figure 222 – Normal force applied on the crankshaft



(a)



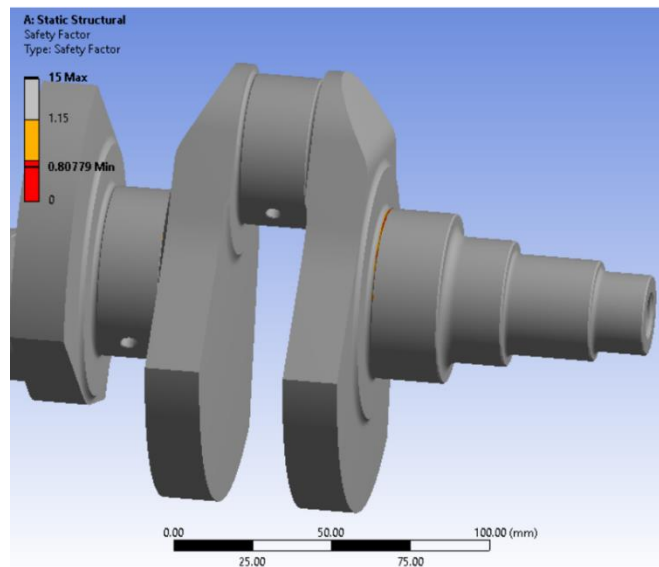
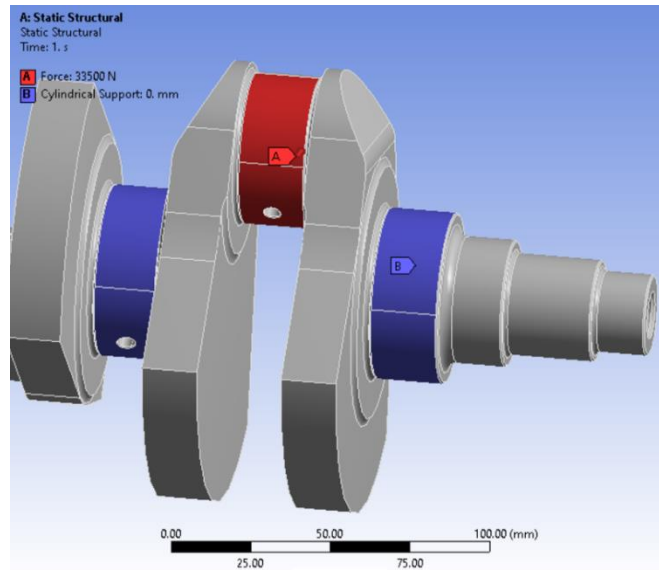
(B)

Source: Author

As an overall the crankshaft was able to bear the cyclic force applied on it achieving a safety factor higher than 1.15. However, some tiny regions stayed with a safety factor lower than 1. In order to reinforce the region, the crankshaft will be nitride and prototyping tests performed.

The mechanical load applied on crankshaft as tangential force is illustrated in Figure 223. Similarly to the results from normal force application, the results from tangential force application indicated that the crankshaft as an overall was able to bear the cyclic load applied on it. However, some tiny regions stayed with a safety factor lower than 1. In order to reinforce the region, the crankshaft will be nitride and prototyping tests performed.

Figure 223 – Tangential force applied on the crankshaft



Source: Author

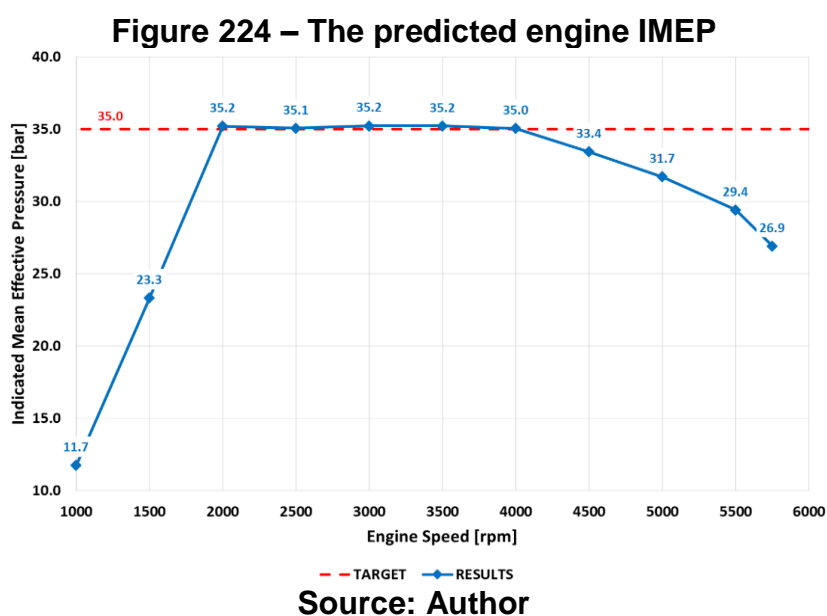
4.1.6. Crankcase

As this project were developed using a regular computer, it was not possible to perform the simulation of the crankcase fitted with liner, cylinder head, bedplate and main bearing caps. Therefore, this simulation will be performed in a next step using a higher computational power availability.

4.2. 1D Numerical Simulation

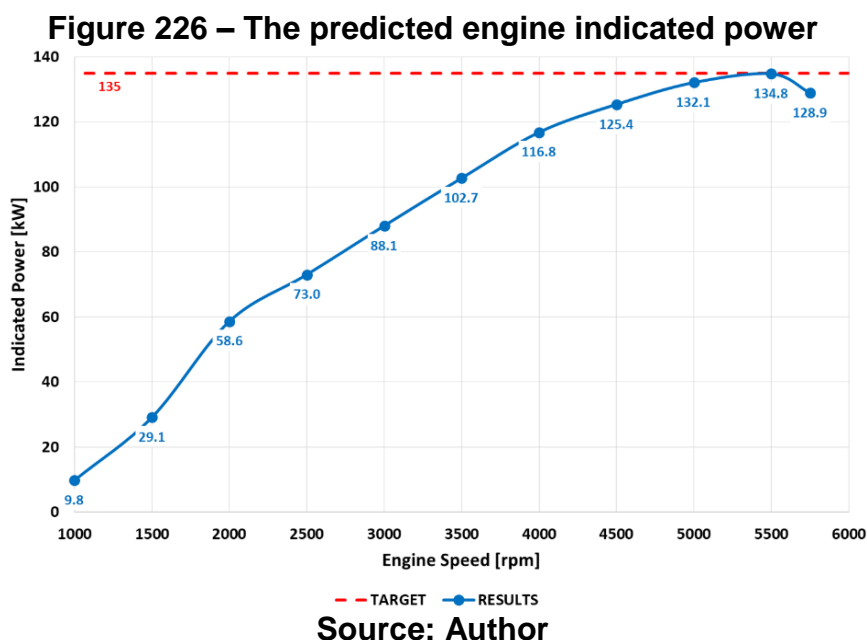
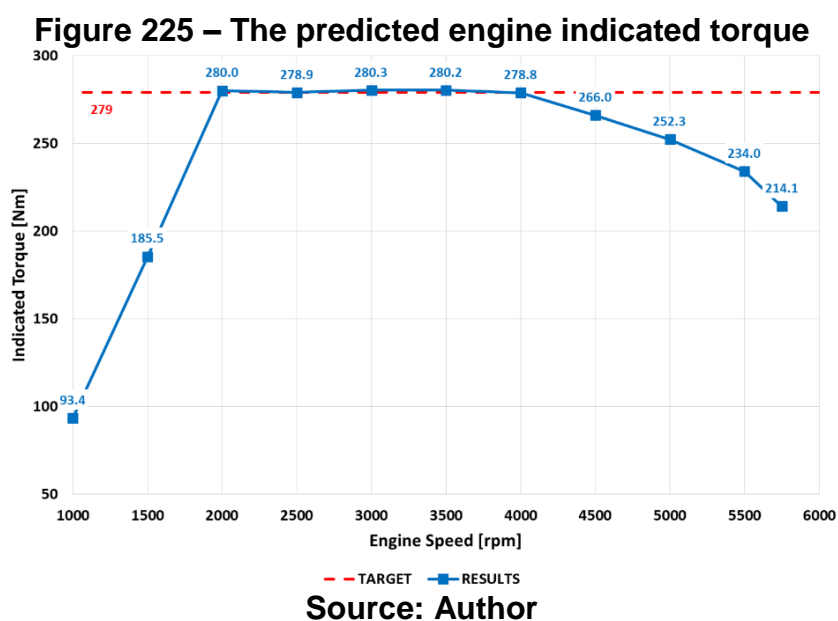
In this section, the simulation results of the engine overall predicted performance, the required amount of water injected and the engine turbo-matching are carefully discussed. As presented in Table 4, the engine developed in this work aims to achieve an indicated power of 135 kW at 5500 rpm and 279 Nm of maximum indicated torque. To reach the desired torque output, it was required to run the engine at 35 bar of IMEP, considering the engine displacement volume. Those engine performance parameters were established based on the results presented by Baêta et al. (2018) . The engine simulations were conducted based on the IMEP required to achieve the established engine overall performance. Considering a new accessory drive package to fit the engine developed in this work, the results were evaluated related to the indicated parameters.

The downsized engine should reach the maximum indicated torque at the lowest possible engine speeds to promote satisfactory vehicle drivability. Based on the downsized engines available on the market, 2000 rpm was determined as the lowest speed for the engine to achieve the maximum indicated torque, which must be maintained for additional 2000 rpm. These requirements imposed a challenge on the engine turbo-matching procedure. Figure 224 shows the predicted IMEP according to the engine speed.



As the cylinder head used on the engine developed in this work was designed with integrated exhaust manifold technology, the maximum indicated torque ending at 4000 rpm was defined, taking into consideration the compromise between achieving

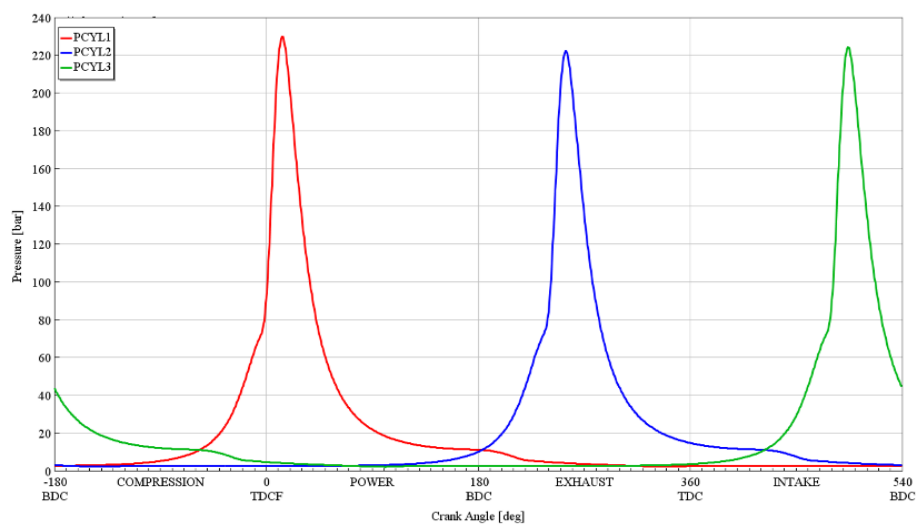
the required engine performance and keeping the exhaust temperature and backpressure as low as possible. Additionally, the engine IMEP levels from 4000 to 5500 rpm were determined to promote a smooth engine running transition from maximum torque to maximum power. In this regard, Figure 225 and Figure 226 present the predicted engine indicated torque and power curves, respectively.



The in-cylinder peak pressure and its standard deviation are important parameters used to design engine components. Frequently, the in-cylinder pressure plus three times its standard deviation is considered as a reference for the limit operation condition. The experimental result obtained by Baêta et al. (2018) at the

highest load had an in-cylinder peak pressure of 220 bar and a standard deviation of 14.37 bar. Comparatively, the simulation results from the model of this work presented an in-cylinder peak pressure average of 225.3 bar, as exhibited in Figure 227. Throughout the engine speed values, the average of the in-cylinder peak pressure slightly overcomes 220 bar, as presented in Figure 228. Therefore, the in-cylinder peak pressure value of 220 bar and its three times standard deviation values choice as a reference for the engine components design is considered a reasonable approach.

Figure 227 – In-cylinder pressure trace simulation result at 2500 rpm



Source: Author

Figure 228 – In-cylinder pressure trace simulation result related to engine speed

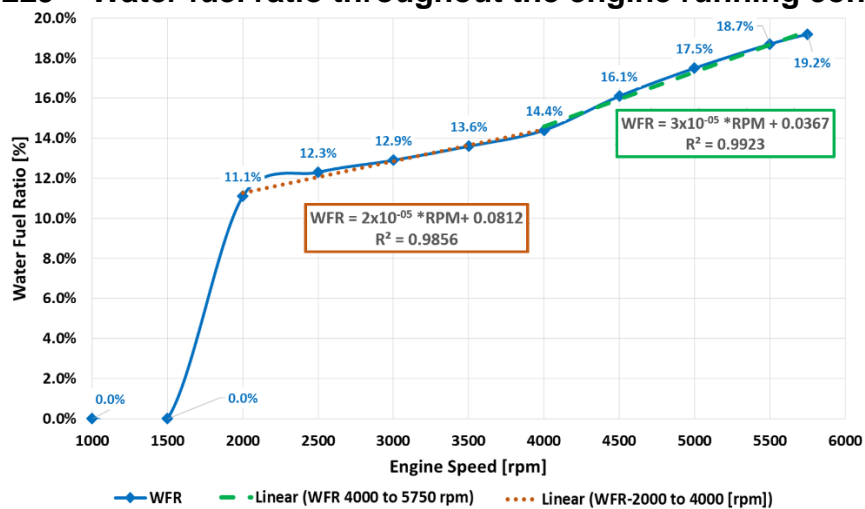


The water injection was used to assist the combustion process and promote a full spark authority to the engine, regardless of the operation condition. The full spark authority is characterized by MFB50% around 8.0° CA. The amount of water mass injected was correlated to the amount of fuel mass injected by cycle using the parameter WFR. As shown in Figure 229, the water consumption presented two linear responses throughout the engine operating conditions. The first linear sector occurred between 2000 and 4000 rpm and the second linear sector took place between 4000 and 5750 rpm. The inflection behavior between the linear sectors occurred at 4000 rpm. This inflection effect could be justified based on the exhaust backpressure increase from 4000 rpm onwards, which can be observed in Figure 230(a). In the case of a higher exhaust backpressure running condition, a higher amount of residual gas remains trapped in the combustion chamber, which in turn enhances the knock occurrence tendency. In order to mitigate the knock onset, a larger amount of water is required. However, by injecting more water, the total mass flow through the engine increases, also raising the backpressure. The compromise between the amount of water injected and exhaust backpressure is critical for the engine performance.

The water consumed by the engine to assist the combustion process decreases the exhaust temperature. As shown in Figure 230(b), besides the abrupt exhaust temperature increase onwards 4000 rpm, the water injection was able to maintain the exhaust temperature under the safety limit of 950 °C for the exhaust valves. The highest amount of water injected was 19.2% of WFR. At peak power, the WFR reached

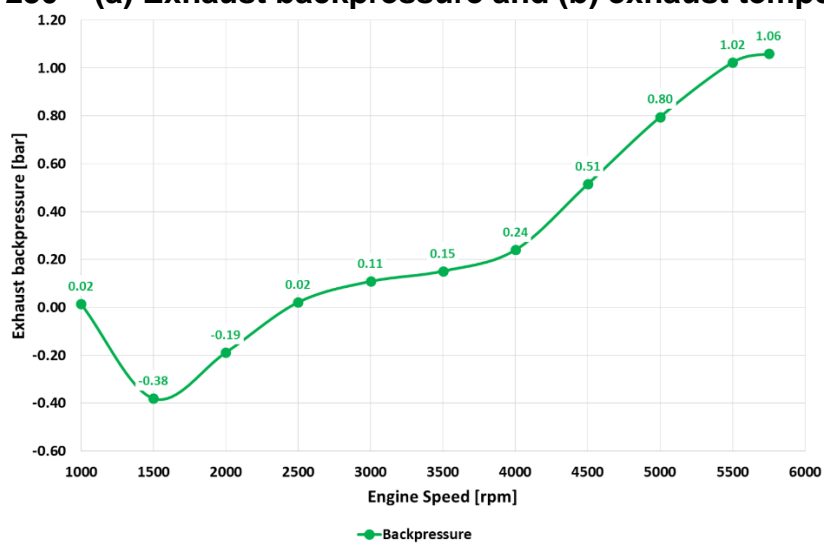
18.7%. It was 3.5% higher than that estimated by Baêta et al. (2018) for the same indicated power output. The higher amount of water injected could also be justified due to the higher exhaust backpressure of the novel engine portrayed in this work.

Figure 229 – Water fuel ratio throughout the engine running conditions

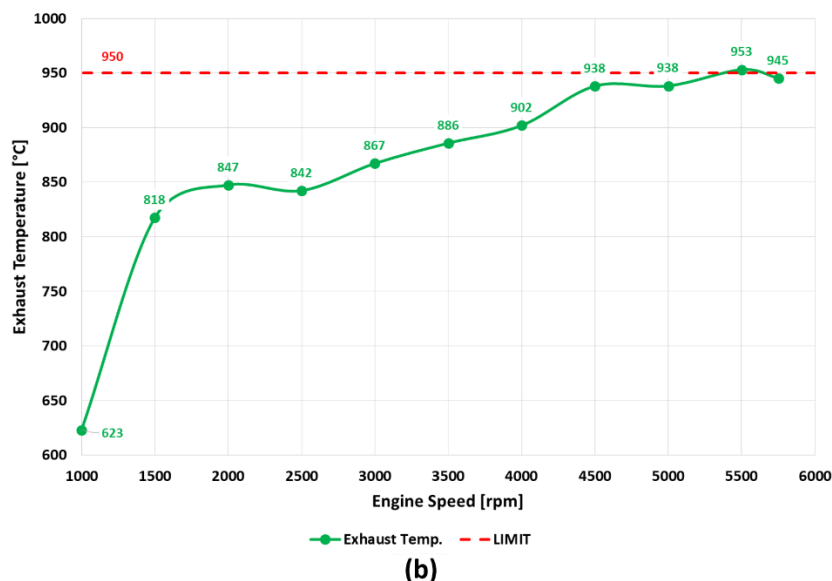


Source: Author

Figure 230 – (a) Exhaust backpressure and (b) exhaust temperature



(a)

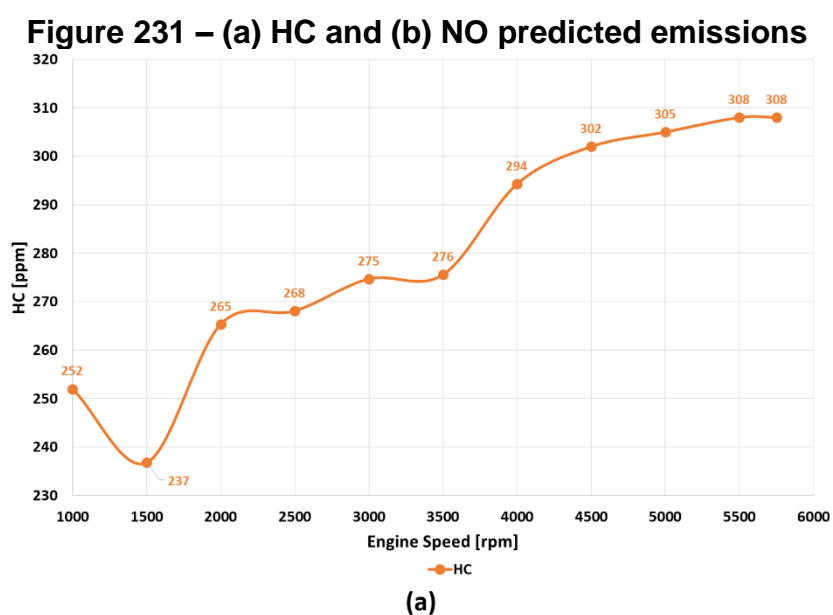


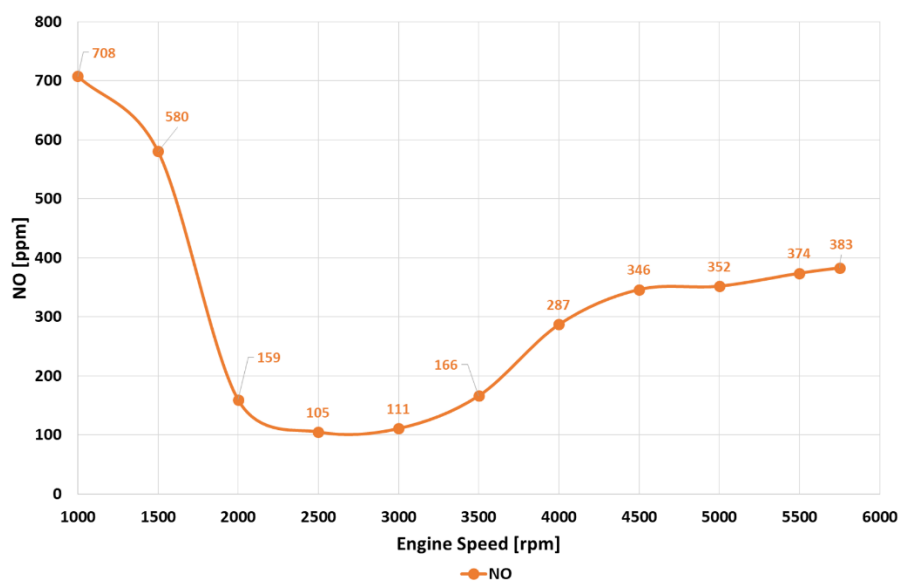
Source: Author

The WI approach was focused on promoting a combustion phasing at the MBT condition, rather than managing the engine emissions. The water acts as a charge dilution agent, which may lead to an incomplete combustion process. In addition, the water could end up being trapped in the piston crevice, resulting in inefficient combustion in this region. These adverse effects could lead to an increase in CO and HC emissions. Figure 231(a) presents the engine HC predicted emissions primarily determined by the exhaust gas equivalence ratio. Therefore, as the engine was simulated running in the stoichiometric condition, the HC emissions increase was related to the amount of water injected. A similar behavior is expected for CO, as it is also affected by the charge dilution levels and incomplete combustion process. It is worth pointing out that the high latent heat of vaporization of ethanol requires a smaller amount of water to be injected to achieve a combustion phasing at MBT compared to gasoline Durst et al. (2017), Harrington (1982), Nicholls (1969), Rohit et al. (2017) and Jeremy et al. (2017). Furthermore, Brazilian ethanol contains 6% of water, which contributes to lower water consumption.

The higher heat of vaporization achieved by combining ethanol and water injection leads to lower in-cylinder charge temperature, which in turn results in lower NO emissions. However, as the combustion phasing was adjusted to MBT condition, the in-cylinder charge temperature tends to increase, diminishing the NO emissions' reduction potential. Figure 231(b) illustrates the NO emissions throughout the engine full load condition. It was noticed that the lowest NO emissions values were achieved

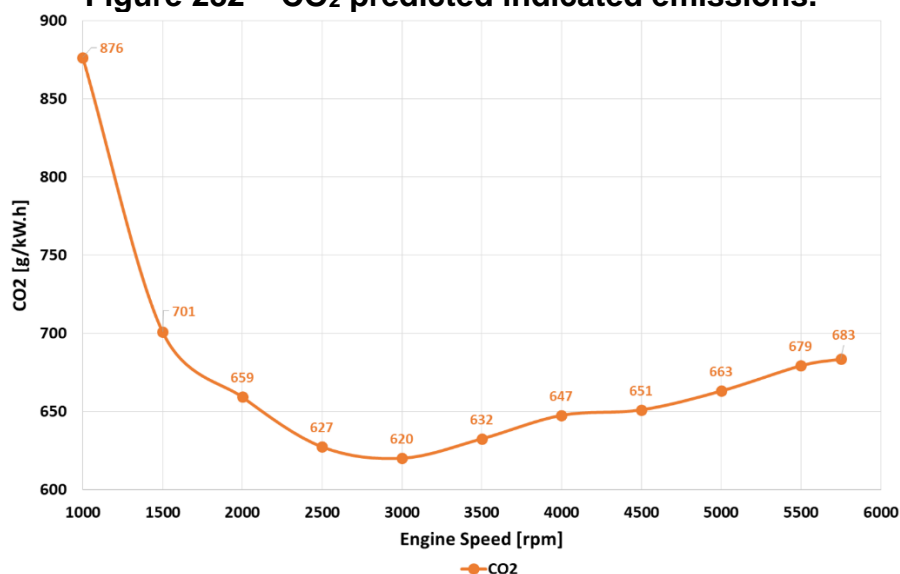
between 2000 and 3500, and they started to increase at higher engine speeds. As the exhaust backpressure also increased at higher engine speeds, the amount of water injected was only enough to mitigate the knock onset, while a higher amount of water would be required to minimize the NO emissions. Figure 232 illustrates the CO₂ emissions values predicted for the engine, which presented a well-correlated tendency according to the engine indicated fuel conversion efficiency, as the CO₂ formation is closely related to the engine fuel consumption pattern. The lowest CO₂ emission value was 620 g/kW·h at 3000 rpm. Despite the WI effectiveness to promote a full spark authority to the engine, the WI approach requires attention to its possible adverse effects. Some of them are the engine lubricant oil dilution, the chemical incompatibility of the engine components materials and the water, and the development of control strategies to protect the engine by downgrading its performance in case of lack of water.





(b)

Source: Author

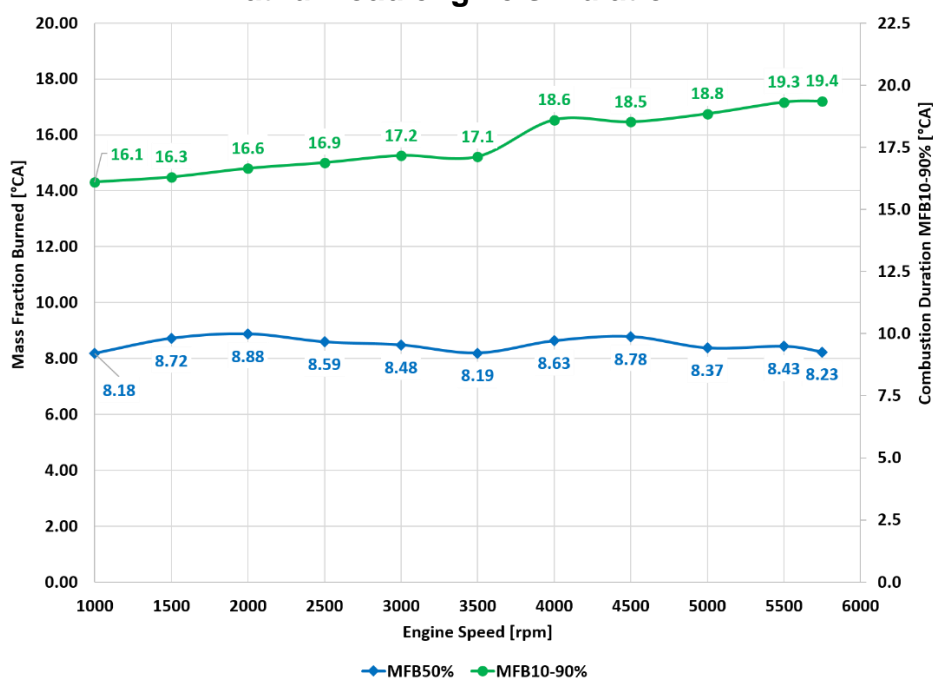
Figure 232 – CO₂ predicted indicated emissions.

Source: Author

The water injection assists the combustion process by mitigating knock occurrence, and thus enabling the engine to run at the MBT condition (MFB50% - 8.0° CA). Furthermore, the water injection affects the combustion duration by delaying it. However, for the small percentages of injected water used in this work, the slower rate of combustion was compensated by the advanced spark ignition. Similar combustion rate behavior was presented by Baêta et al. (2018), Boretti (2013) and Bozza et al. (2016). Figure 233 presents the MFB50% and the combustion duration (MFB10–90%) results for the full load engine simulation. The purpose of combining a high volumetric

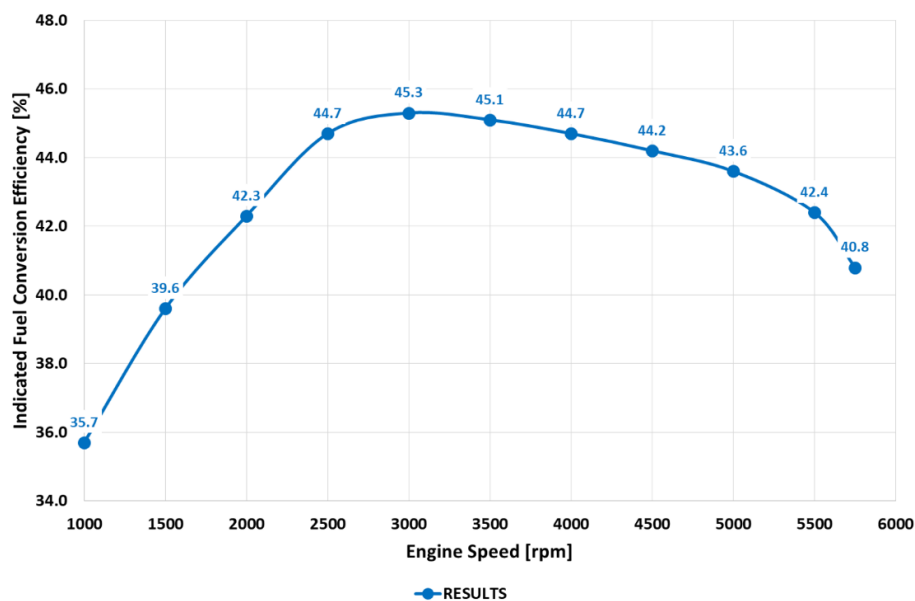
compression ratio, high boost levels, a biofuel whose properties can reach such high loads, running on a stoichiometric mixture and using the water injection to assist the combustion process is to achieve the highest possible indicated fuel conversion efficiency. Figure 234 presents the engine indicated fuel conversion efficiency simulation results, and the highest value achieved was 45.3% at 3000 rpm, which reinforces the great potential arising from the proposed methodology of combining the WI system, ethanol as fuel and highly boosted engine design. Additionally, the technologies used in the engine developed in this work achieved over 40% indicated fuel conversion efficiency during almost its entire full load condition.

Figure 233 – The MFB50% and the combustion duration MFB10-90% achieved at full load engine simulation.



Source: Author

Figure 234 – The engine indicated fuel conversion efficiency.

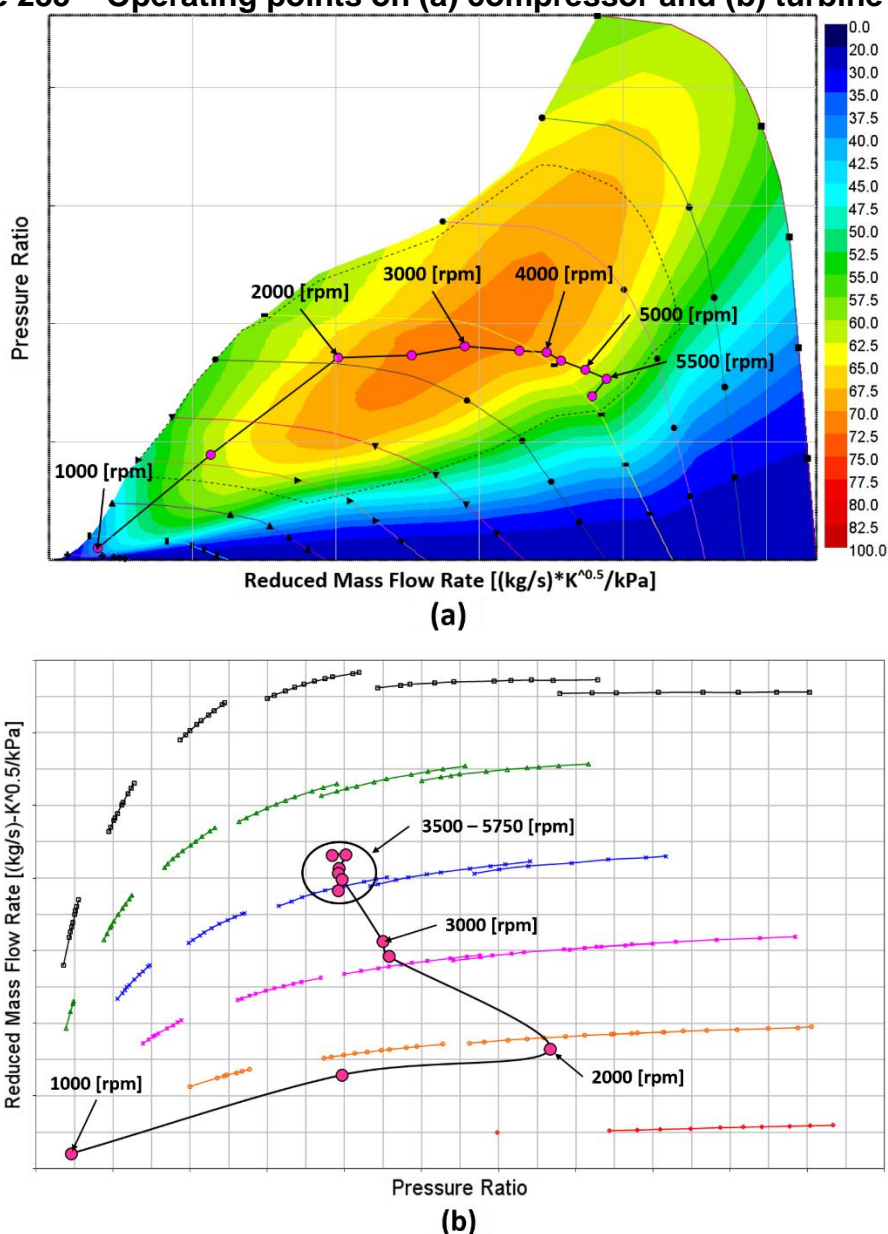


Source: Author

The turbocharger used in this work was instrumental in enabling the engine to achieve the aforementioned performance and overall efficiency. It was defined through a turbo-matching procedure. To do so, several compressor and turbine maps supplied by BorgWarner were evaluated. In order to reach the desirable engine performance at low-end torque and maximum power, a VGT was used in this application. The compressor and turbine fitted on the engine are modern and highly efficient components, designed to withstand the higher working temperatures compared to diesel engines. The operating points of the compressor and turbine maps are presented in Figure 235.

Figure 235(a) shows that the compressor turbo-matching resulted in the highest compressor efficiency coincident, with relevant engine speeds for driving cycles of vehicles equipped with the engine developed in this work, ranging from 2500 to 3500 rpm. Furthermore, a reasonable safety margin from the compressor surge curve at the engine low-end torque could be established. Additionally, the engine was able to reach the required peak power without achieving a compressor choke condition. Similarly, as illustrated in Figure 235(b), the turbine was able to work at the highest total mass flow, far from turbine choke condition. This fact indicates that the use of smaller, and consequently lighter, turbine wheels could be considered to improve the turbo lag response. Furthermore, it could be concluded that the exhaust ports' design had a major contribution to the exhaust backpressure increase.

Figure 235 – Operating points on (a) compressor and (b) turbine maps



Source: Author

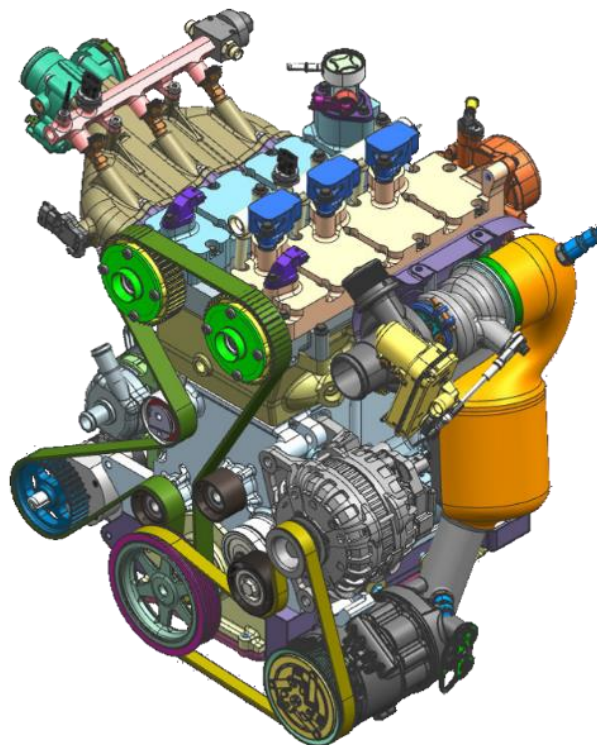
Regarding the turbocharger working reliability and protection, the turbine working condition should be in accordance with the manufacturer's specification. The engine exhaust temperature and the turbocharger wheel speed are the two most important parameters to be managed. The turbocharger manufacturer specified the values of 970 °C and 240,000 rpm as the limit for the exhaust temperature and turbocharger wheel speed, respectively. As presented in Figure 230(b), the highest exhaust temperature achieved by the engine was 17 °C lower than the upper limit specified by the turbocharger manufacturer. In the same way, the maximum turbocharger wheel speed achieved was approximately 9000 rpm lower than the

specified limit. As the engine simulation was carried out considering the ambient conditions at sea level, the safety turbocharger margin related to the surge, choke and over-speed conditions allow the engine to maintain its performance in higher altitude regions.

4.3. Highly boosted prototype engine

A new highly boosted prototype engine running on ethanol and assisted by water injection was the final result obtained from this work as presented in Figure 236. This novel internal combustion engine was designed according to modern design concepts, it was equipped with state-of-the-art technologies and conceived to operate with the exclusive use of ethanol as a fuel. Thus, it is understood as an innovative and promising pathway for Brazilian future mobility, from both technological and sustainability perspectives.

Figure 236 – Designed highly boosted prototype engine



Source: Author

5. CONCLUSION

The conclusions of this work refer to the methodology proposed, and the results obtained from the development procedure of a highly boosted prototype engine running on ethanol and assisted by water injection according to the proposed specific objectives.

The engine development procedure was established based on an extensive and detailed literature research for each engine system or component regarding modern technologies and required design characteristics. Furthermore, the engine design guide lines created by engine manufactures were followed throughout the development process which contributed to the project robustness.

The prototype engine development started with the engine main geometric dimensions calculation aiming to maximize the engine fuel conversion efficiency running exclusively on Brazilian ethanol. Brazilian ethanol was selected as the fuel option, since its physicochemical properties allow the engine to achieve higher loads, but also due to its important role as a renewable energy source that is largely available in the national energy matrix, being considered one of the most promising biofuels in the world. Furthermore, a port-water injection system was fitted to the engine in order to assist the combustion process by mitigating the knock tendency.

Based on the calculated engine main dimensions, the engine components were design using CAD method. Each engine component was designed or defined considering the international modern technologies trends applied on internal combustion engines. Additionally, the engine components performance were evaluated regarding thermal and mechanical loads from the fatigue point view by means of FEM method. Experimental data from a similar engine were used as input for the development of the new prototype engine. Considering the factor of safety suggested by the literatures and guide lines, the designed engines components were considered suitable for the proposed application.

In order to predict the overall engine performance, a 1D-CFD model was built based on the engine 3D geometry. Considering the results achieved by Baêta et al. (2018), it was defined 35 bar was defined as the highest IMEP to be reached, which corresponds to 279 Nm of the maximum indicated torque and 135 kW of maximum indicated power. The results demonstrated that the engine was able to achieve the required maximum indicated torque from 2000 to 4000 rpm and the maximum indicated power at 5500 rpm. A VGT turbine was used to enable the engine to achieve the highest torque at the engine low-end speed and also allowed a higher mass flow for

the maximum engine power. The water injection promoted a full spark authority condition for the entire engine maximum load performance. Therefore, the engine was capable to run with MFB50% at about 8.0° CA. The water consumption presented a linear behavior in two separate regions of the full load performance. The water consumption at higher engine speeds was greater than the trend presented at lower engine speeds, due to the exhaust backpressure. The results presented a WFR maximum of 19.2%, which makes the WI approach along with the use of ethanol fuel an attractive solution. The WI detrimental effect on the fuel burning rate due to the flame temperature reduction was counterbalanced by the spark timing adjustment to maintain a fast combustion process. As a result of each parameter specifically designed and tuned for the engine designed in this work, a maximum indicated fuel conversion efficiency of 45.3% was achieved. Moreover, the engine was capable of achieving over 40% of the indicated fuel conversion efficiency during almost its entire full load curve.

Finally, the topics raised in the conclusion section demonstrate the success of this approach, from both environmental and technological points of view, by combining modern design concepts with state-of-the-art engine technologies and the use of biofuels. Which in turn, it point out a possible pathway for the sustainable future of both the Brazilian and the global automotive fleet.

5.1. Suggestions for Future Research

Considering the achieved results afore evaluated and aiming the continuity of this work, the following activities are suggested:

- In-cylinder charge motion 3D-CFD simulation and evaluation regarding the turbulent kinetic energy achieved values;
- 3D-CFD simulation of the fuel and water injection spray interaction with in-cylinder charge motion in order to evaluate the air-fuel-water mixture preparation;
- Study of air metering among engine cylinders for different engine operation conditions taking into account the predicted exhaust backpressure;
- Engine water-jacked 3D-CFD simulation of current CAD model for the heat exchange performance optimization;

- Development of the engine thermal map for different engine operation conditions and its effects on engine structure;
- Study of the suitable torsional vibration dumper to be fitted in to the engine considering different engine operating conditions;
- Investigation of the crankcase under pressure condition on engine performance and emissions.

REFERENCE

A. M. DOUAUD, P. E. "Four-Octane-Number Method for Predicting the Anti-Knock Behavior of Fuels and Engines," SAE Technical Paper 780080. SAE 1978.

ABBES, M. T.; MASPEYROT, P.; BOUIF, A.; FRENE, J. A thermomechanical model of a direct injection diesel engine piston. **Proceedings of the Institution of Mechanical Engineers, Part D: Journal of Automobile Engineering**, 218, n. 4, p. 395-409, 2004/04/01 2004.

AGARWAL, A. K.; VARGHESE, M. B. Numerical investigations of piston cooling using oil jet in heavy duty diesel engines. *IMechE*: 12 p. 2006.

AHMED, W.; USMAN, M.; HARIS SHAH, M.; ABBAS, M. M. *et al.* A Comparison of Performance, Emissions, and Lube Oil Deterioration for Gasoline–Ethanol Fuel. *Processes*, 10, n. 5, 2022.

ALT, M.; SUTTER, T.; JOHNNEN, T.; FULTON, K., DAILY, R., COCOCETTA, R. *et al.* Powerful, efficient and smooth: The new Small Gasoline Engine family from General Motors. Wien, Austria: Internationales Wiener Motorensymposium 2014.

ANANTHAKRISHNAN, P.; EGAN, S.; ARCHER, J.; SHIPP, T. Maximum turbocharger efficiency for an engine operating at 50% brake thermal efficiency. *In*, 2020. p. 191-203.

ANDERSSON, L.; EK, K.; KASTENSSON, Å.; WÅRELL, L. Transition towards sustainable transportation – What determines fuel choice? *Transport Policy*, 90, p. 31-38, 2020/05/01/ 2020.

ANP. **Glossário**. 2016. Disponível em: <http://www.anp.gov.br/wwwanp/glossario>. Acesso em: 27/03/17.

ANP, A. N. D. P. Resolução ANP Nº 19. ANP, A. N. D. P.-. 11 p. 2015.

ANP, A. N. D. P. Produção de Etanol e GNV. São Paulo: 2 p. 2018.

ASHBY, M. F.; JONES, D. R. H. *Engineering Materials - An Introduction to their Properties and Applications*. Butterworth-Heinemann: 322 p. 2005.

ASM. *Fatigue and Fracture*. ASM International Handbook Committee: 2592 p. 1996.

AUDI. **Rightsizing**. 2018. Disponível em: https://www.audi-technology-portal.de/en/mobility-for-the-future/audi-future-lab-mobility_en/audi-future-engines_en/rightsizing_en.

AVL. *AVL IndiCom User's Guide*. Graz, Austria: AVL: 882 p. 2012.

BAINES, N. C.; KRIVITZKY, E.; BAI, J.; ZHANG, X. Trends in passenger car powertrains and their impact on turbocharger developments. *In*, 2020. p. 341-359.

BARAGETTI, S. Design Criteria for High Power Engines Crankshafts. *The Open Mechanical Engineering Journal*, 9, p. 271-281, 04/23 2015.

BAÊTA, J. G. C. **METODOLOGIA EXPERIMENTAL PARA A MAXIMIZAÇÃO DO DESEMPENHO DE UM MOTOR MULTICOMBUSTÍVEL TURBOALIMENTADO SEM PREJUÍZO À EFICIÊNCIA ENERGÉTICA GLOBAL**. 2006. 257 f. (Doutorado) - Departamento de Engenharia Mecânica, Universidade Federal de Minas Gerais, Belo Horizonte.

BAËTA, J. G. C.; PONTOPPIDAN, M.; SILVA, T. R. V. Exploring the limits of a down-sized ethanol direct injection spark ignited engine in different configurations in order to replace high-displacement gasoline engines. **Energy Conversion and Management**, 105, p. 858-871, 11/15/ 2015.

BAËTA, J. G. C.; SILVA, T. R. V.; NETTO, N. A. D.; MALAQUIAS, A. C. T. *et al.* Full spark authority in a highly boosted ethanol DISI prototype engine. **Applied Thermal Engineering**, 139, p. 35-46, 7/5/ 2018.

BERTOCCHI, L.; GIACOPINI, M.; DINI, D. **Analysis of the Lubrication Regimes at the Small End and Big End of a Connecting Rod of a High Performance Motorbike Engine**. 2012.

BHANDARI, V. B. Design of Machine Elements. Tata McGraw-Hill: 959 p. 2010.

BIZJAN, F. Position of the Spark Plug in a Symetrical Combustion Chamber. Journal of Mechanical Engineering 45(1999)11,403-411: 9 p. 1999.

BLAIR, G. P. Design and Simulation of Four-Stroke Engines. SAE International: 847 p. 1999.

BLAIR, G. P. The Right Lift. SPECIAL INVESTIGATION: 9 p. 2003.

BOCANEGRA-BERNAL, M. H.; MATOVIC, B. Mechanical properties of silicon nitride-based ceramics and its use in structural applications at high temperatures. **Materials Science and Engineering: A**, 527, n. 6, p. 1314-1338, 2010/03/15/ 2010.

BOHN, J. Piston Pin Testing. Norwegian University of Science and Technology: 88 p. 2016.

BONNEAU, D.; FATU, A.; SOUCHET, D. Internal Combustion Engine Bearings Lubrication in Hydrodynamic Bearing. ISTE Ltd: 229 p. 2014.

BORETTI, A. Water injection in directly injected turbocharged spark ignition engines. **Applied Thermal Engineering**, 52, n. 1, p. 62-68, 2013/04/05/ 2013.

BOYER, H. E. Atlas of Fatigue Curves. ASM International: 534 p. 1983.

BOZZA, F.; DE BELLIS, V.; TEODOSIO, L. Potentials of cooled EGR and water injection for knock resistance and fuel consumption improvements of gasoline engines. **Applied Energy**, 169, p. 112-125, 2016/05/01/ 2016.

BP. BP Statistical Review of World Energy. BP: 54 p. 2018.

BRAZILGOVNEWS. **Brazil launches Route 2030 to boost sustainable car development**. 2018. Disponível em: <http://www.brazil.gov.br/about-brazil/news/2018/07/brazil-launches-route-2030-to-boost-sustainable-car-development>.

BUDYNAS, R. G.; NISBETT, J. K. SHIGLEY'S MECHANICAL ENGINEERING DESIGN. McGraw-Hill Companies. NINTH EDITION: 1109 p. 2011.

BUYUKKAYA, E.; CERIT, M. Thermal analysis of a ceramic coating diesel engine piston using 3-D finite element method. **Surface and Coatings Technology**, 202, n. 2, p. 398-402, 2007/11/25/ 2007.

CALICO. HPT Ceramic Coating. Calico 2021.

CARLEY, L. Valve Stem Seals Materials and Designs. Engine Builder: 8 p. 2008.

CASTINGS, M. Die Casting vs. CNC Machining (Video). MRT Castings 2019.

CESUR, I. Effects of water injection strategies on performance and exhaust emissions in an ethanol fueled gasoline engine. **Thermal Science and Engineering Progress**, 34, p. 101397, 2022/09/01/ 2022.

CHAN, S. H.; KHOR, K. A. The effect of thermal barrier coated piston crown on engine characteristics. **Journal of Materials Engineering and Performance**, 9, n. 1, p. 103-109, 2000/02/01 2000.

CHEN, Z.; DENG, J.; ZHEN, H.; WANG, C. *et al.* Experimental Investigation of Hydrous Ethanol Gasoline on Engine Noise, Cyclic Variations and Combustion Characteristics. **Energies**, 15, n. 5, 2022.

CLARK, K.; ANTONEVICH, J.; KEMPPAINEN, D.; BARNA, G. Piston Pin Dynamics and Temperature in a C.I. Engine. **SAE International Journal of Engines**, 2, n. 1, p. 91-105, 2009.

CLEVITE. How much clearance do your bearings need? Ann Arbor, MI: Clevite Engine Parts 2005.

CLEVITE, M. Bearings Guide. Mahle Motorsport: 184 p. 2016.

CORTECO, F. Corteco Valve Stem Seals. Freudenberg: 35 p. 2019.

DE MARINO, D. I. C.; MAIORANA, D. I. G.; PALLOTTI, D. I. P.; QUINTO, D. I. S. *et al.* The Global Small Engine 3 and 4 Cylinder Turbo: The New FCA's Family of Small High-Tech Gasoline Engines. *In: Internationales Wiener Motorensymposium*, 2018, Viena, Austria. p. 38.

DHOMNE, S.; MAHALLE, A. Thermal barrier coating materials for SI engine. **Journal of Materials Research and Technology**, 8, 09/01 2018.

DI GIACOMO A. PIGNONE, U. R. V. Motori ad alta potenza specifica. *Illustrata*. Vol.2: 560 p. 2003.

DURST, D.-I. B.; LANDERL, D. T. C.; POGGEL, D.-I. J.; SCHWARZ, P. D.-I. C. *et al.* BMW Water Injection: Initial Experience and Future Potentials. *In: Internationales Wiener Motorensymposium*, 2017, Viena, Austria. p. 17.

ECONOMIA, M. D. IPI - Imposto sobre produtos industrializados. Receita Federal 2022.

EDUARD KÖHLER, R. F. Verbrennungsmotoren Motormechanik, Berechnung und Auslegung des Hubkolbenmotors. Springer Fachmedien Wiesbaden GmbH: 570 p. 2011.

EMBRAPA. BRS 508: o sorgo sacarino com alto teor de açúcar no caldo. Embrapa Milho e Sorgo, 2012. (CNPMS), E. M. E. S. Sete Lagoas 2012.

ESFAHANIAN, V.; JAVAHERI, A.; GHAFFARPOUR, M. Thermal analysis of an SI engine piston using different combustion boundary condition treatments. **Applied Thermal Engineering**, 26, n. 2, p. 277-287, 2006/02/01/ 2006.

FERREA, R. High Power Valvetrain Components. Ferrea Racing Components: 140 p. 2021.

FERREIRA GOMES, P., LOPES, G., BRUNOCILLA, M., MENDES, C. High efficiency flex-fuel engines, a sustainable alternative for mobility. SAE Technical Paper 2018-36-0037, 2018. SAE 2018.

G.M. BIANCHI, G. C., E. MATTARELLI, G. GUERRINI, F. PAPETTI. The Influence of Stroke-to-Bore Ratio and Combustion Chamber Design on Formula One Engines Performance, SAE Technical Paper 980126. SAE 1998.

GEN SHIBATA, K. I., HIROOKI USHIJIMA, YUSHI SHIBAIKE, HIDEYUKI OGAWA, DAVID E. FOSTER. Optimization of Heat Release Shape and the Connecting Rod Crank Radius Ratio for Low Engine Noise and High Thermal Efficiency of Premixed Diesel Engine Combustion," SAE Technical Paper 2015-01-0825. SAE 2015.

GERVÁSIO, D. T. METODOLOGIA DE CORRELAÇÃO E ANÁLISE DE MODELOS FLUIDODINÂMICOS 1D PARA MOTORES DE COMBUSTÃO INTERNA. Pernambuco, Recife: UNIVERSIDADE FEDERAL DE PERNAMBUCO: 126 p. 2017.

GOLKE, D.; PRANTE, G. A. F.; GARLET, R. A.; ROHRIG, M. *et al.* Exploring the part load lean limit of a direct injection spark ignition engine fueled with ethanol. **International Journal of Engine Research**, p. 14680874221092729, 2022.

GONÇALVES, F. D. O.; LOPES, E. S.; SAVIOLI LOPES, M.; MACIEL FILHO, R. Thorough evaluation of the available light-duty engine technologies to reduce greenhouse gases emissions in Brazil. **Journal of Cleaner Production**, 358, p. 132051, 2022/07/15/ 2022.

GOTOU, T.; YANAGISAWA, N. Development of Reciprocating Parts and Crankshaft in Honda's Third Formula One Era. Honda R&D: 376 p. 2009.

H. K. VERSTEEG, W. M. An introduction to computational fluid dynamics - The finite volume method. Longman Scientific & Technical: 267 p. 1995.

HAN, T.; BOEHMAN, A. L. Multiple injection strategies with high water port injection rates for enhancing performance and emissions in a boosted SI engine. **Fuel**, 326, p. 124982, 2022/10/15/ 2022.

HARRINGTON, J. Water Addition to Gasoline-Effect on Combustion, Emissions, Performance, and Knock. **SAE Technical Paper**, p. 28, DOI: <https://doi.org/10.4271/820314>.

HARRISON, M. F.; STANEV, P. T. A linear acoustic model for intake wave dynamics in IC engines. **Journal of Sound and Vibration**, 269, n. 1, p. 361-387, 2004/01/06/ 2004.

HEYWOOD, J. B. Combustion Engine Fundamentals. Mc Graw Hill: 1213 p. 2018.

HIERETH, H.; PRENNINGER, P. Charging the Internal Combustion Engine. SpringerWienNewYork: 283 p. 2003.

IEA. Global Energy Review 2021, IEA, Paris. 2021.

IKEYA, K.; TAKAZAWA, M.; YAMADA, T.; PARK, S. *et al.* Thermal Efficiency Enhancement of a Gasoline Engine. SAE International; Honda R&D Co Ltd: 8 p. 2015.

IMAI, N.; NISHIDA, H. Development of Laser Clad Welded Valve Seat. Honda R&D 2009.

INCROPERA, F. P.; BERGMAN, T. L.; LAVINE, A. S.; DEWITT, D. P. Fundamentals of Heat and Mass Transfer. JOHN WILEY & SONS: 1076 p. 2011.

JEREMY, W.; JEFFREY, N.; JOEL, D.; SAM, B. *et al.* Water Injection as an Enabler for Increased Efficiency at High-Load in a Direct Injected, Boosted, SI Engine. **SAE Int. J. Engines**, p. 951-958, DOI: <https://doi.org/10.4271/2017-01-0663>.

JUVINALL, R. C.; MARSHEK, K. M. FUNDAMENTALS OF MACHINE COMPONENT DESIGN. Wiley: 912 p.

K., R.; SRI, L. J.; V., M.; BHUPAL, R. D. B. R. Optimization of Petrol Engine Flywheel for Variable Speeds. IOSR Journal of Mechanical and Civil Engineering: 15 p. 2015.

KAWASAKI, M.; TAKASE, K.; KATO, S.; NAKAGAWA, M. *et al.* Development of Engine Valve Seats Directly Deposited onto Aluminum Cylinder Head by Laser Cladding Process. SAE International 1992.

KEVIN L. HOAG, B. M., TERRENCE ALGER, ZAINAL ABIDIN, CHRISTOPHER WRAY, MARK WALLS, CHRISTOPHER CHADWELL. "A Study Isolating the Effect of Bore-to-Stroke Ratio on Gasoline Engine Combustion Chamber Development," **SAE Int. J. Engines** 9(4):2022-2029. SAE 2016.

KIM, J.; RYU, I.; KIM, J.; HAN, D. *et al.* Hyundai-Kia's SmartStream 1.6L DI-Turbo Motor. Internationales Wiener Motorensymposium: 24 p. 2018.

KIM, S.; PARK, C.; JANG, H.; KIM, C. *et al.* Effect of boosting on a performance and emissions in a port fuel injection natural gas engine with variable intake and exhaust valve timing. **Energy Reports**, 7, p. 4941-4950, 2021/11/01/ 2021.

KIMBALL, W. S. OPTIMUM RATIO BETWEEN CRANK ARM AND CONNECTING ROD FOR SMOOTH OPERATION OF RECIPROCATING ENGINES. JOURNAL FRANKLIN INSTITUTE, Vol. 242 1948.

KOLBENSCHMIDT. KS Aluminum Pistons. Kolbenschmidt Pierburg Group: 8 p. 2018.

KOLBENSCHMIDT. Piston Ring Sets. Kolbenschmidt: 927 p. 2019.

KOPELIOVICH, D. Geometry and dimensional tolerances of engine bearings. King Engine Bearing Specialist: 8 p. 2019.

KUROWSKI, P. M. Finite Element Analysis for Design Engineers. SAE: 284 p. 2017.

KÖNIGSTEDT, J.; BONN, G.; BRINKMANN, C.; FRÖHLICH, G. The new 3.0l V6 TFSI engine from Audi. Internationales Wiener Motorensymposium: 25 p. 2016.

KÜNTSCHER, V.; HOFFMANN, W. Kraftfahrzeugmotoren - Auslegung und Konstruktion. Vogel Buchverlag: 1784 p. 2015.

LAWTON, B.; CRUTCHER, D. E. G. Paper 7: Mechanical Stresses in Pistons, Gudgeon Pins, and Connecting Rods. **Proceedings of the Institution of Mechanical Engineers, Conference Proceedings**, 181, n. 8, p. 20-30, 1966/06/01 1966.

LEE, H. M. S.; M.SC., J. K.; M.SC., K. H.; Y. KIM B.SC. *et al.* Hyundai-Kia's New 3-Cylinder 1.0L Turbo GDI Engine. *In*: Internationales Wiener Motorensymposium, 2015, Viena, Austria. p. 19.

LEE, M. K.; LEE, H.; LEE, T. S.; JANG, H. Buckling sensitivity of a connecting rod to the shank sectional area reduction. **Materials & Design**, 31, n. 6, p. 2796-2803, 2010/06/01/ 2010.

LEE, Z.; KIM, T.; PARK, S.; PARK, S. Review on spray, combustion, and emission characteristics of recent developed direct-injection spark ignition (DISI) engine system with multi-hole type injector. **Fuel**, 259, p. 116209, 2020/01/01/ 2020.

LI, C.-H. Piston Thermal Deformation and Friction Considerations. SAE International: 18 p. 1982.

LI, X.; LI, D.; LIU, J.; AJMAL, T. *et al.* Exploring the potential benefits of Ethanol Direct Injection (EDI) timing and pressure on particulate emission characteristics in a Dual-Fuel Spark Ignition (DFSI) engine. **Journal of Cleaner Production**, 357, p. 131938, 2022/07/10/ 2022.

LI, X.; WANG, W.; ZOU, X.; ZHANG, Z. *et al.* Simulation and Test Research for Integrated Exhaust Manifold and Hot End Durability. SAE International: 8 p. 2017.

LI, Y.; CHEN, X. Finite Element Modeling and Simulation with ANSYS Workbench. CRC Press: 408 p. 2015.

LI, Y.; KHAJEPOUR, A.; DEVAUD, C. Realization of variable Otto-Atkinson cycle using variable timing hydraulic actuated valve train for performance and efficiency improvements in unthrottled gasoline engines. **Applied Energy**, 222, p. 199-215, 2018/07/15/ 2018.

LU, Y.; LI, S.; WANG, P.; LIU, C. *et al.* The Analysis of Secondary Motion and Lubrication Performance of Piston considering the Piston Skirt Profile. **Shock and Vibration**, 2018, p. 3240469, 2018/03/27 2018.

LU, Y.; ZHANG, X.; XIANG, P.; DONG, D. Analysis of thermal temperature fields and thermal stress under steady temperature field of diesel engine piston. **Applied Thermal Engineering**, 113, p. 796-812, 2017/02/25/ 2017.

M53. Calculations for I.C. Engine Crankshafts. IACS: 69 p. 2017.

MAHLE. Ventiltrieb - Systeme und Komponenten. Springer Fachmedien Wiesbaden: 321 p. 2013.

MAHLE. Piston Ring Guide. Mahle Original: 96 p. 2014.

MAHLE. Technical information: Valves, Valve guides and Valve seat inserts. Mahle Original: 5 p. 2015.

MAHLE. Cylinder components - Properties, applications, materials. Springer Fachmedien Wiesbaden: 143 p. 2016a.

MAHLE. Pistons and engine testing. Springer Vieweg 2016b.

MALAQUIAS, A.; NETTO, N.; COSTA, R.; TEIXEIRA, A. *et al.* An evaluation of combustion aspects with different compression ratios, fuel types and injection systems in a single-cylinder research engine. **Journal of the Brazilian Society of Mechanical Sciences and Engineering**, 42, p. 497, 09/01 2020.

MALAQUIAS, A. C. T.; NETTO, N. A. D.; FILHO, F. A. R.; DA COSTA, R. B. R. *et al.* The misleading total replacement of internal combustion engines by electric motors and a study of the Brazilian ethanol importance for the sustainable future of mobility: a review. **Journal of the Brazilian Society of Mechanical Sciences and Engineering**, 41, n. 12, p. 567, 2019/11/18 2019.

MALHEIRO DE OLIVEIRA, E. R.; HENRIQUE RUFINO, C.; TEIXEIRA LACAVA, P. Effects of direct injection and mixture enleament on the combustion of hydrous ethanol and an ethanol-gasoline blend in an optical engine. **Fuel**, 327, p. 125137, 2022/11/01/ 2022.

MARELLI, S.; USAI, V.; CAPOBIANCO, M. Experimental investigation on the transient response of an automotive turbocharger coupled to an electrically assisted compressor. *In*, 2020. p. 219-229.

MASATOSHI SUZUKI, S. I., HAYATO MAEHARA, YASUO MORIYOSHI. "Effect of the Ratio Between Connecting-rod Length and Crank Radius on Thermal Efficiency," SAE Technical Paper 2006-32-0098. SAE 2006.

MATERIALS, A. AISI 1020 Carbon Steel. 7 p. 2013.

MATMATCH. DIN 1693-1 Grade GGG-70 cast condition. 6 p. 2019.

MATTHIAS KLUIN, C. G., INGO HERMANN, ACHIM KOENIGSTEIN. Variable Turbine Geometry – Evaluation of a Charging Concept for Future High-Efficiency Gasoline Engines. Wien, Austria: Internationales Wiener Motorensymposium: 20 p. 2017.

MAURYA, R. K. Reciprocating Engine Combustion Diagnostics: In-Cylinder Pressure Measurement and Analysis. Minneapolis, MN, USA: Springer: 625 p. 2019.

MAVRIGIAN, M. Modern Engine Blueprint Techniques. CarTech: 194 p. 2013.

MAXWORX. Billet Blocks. Mazworx Racing Engines 2020.

MAY, U.; STROMBERGER, F.; KOHL, J.; SCHUBERT, J. *et al.* Technology Potential of Ceramic Piston Pins. MTZ: 6 p. 2008.

MELO, T. C. C. **ANÁLISE EXPERIMENTAL E SIMULAÇÃO COMPUTACIONAL DE UM MOTOR FLEX OPERANDO COM DIFERENTES MISTURAS DE ETANOL HIDRATADO NA GASOLINA.** Orientador: CARLOS RODRIGUES PEREIRA BELCHIOR, M. J. C. 2012. 223 f. (Doutorado) - Departamento de Engenharia Mecânica, UFRJ, Rio de Janeiro, Brasil.

METALS, A. A. S. Aluminum 6061-T6 Data-sheet. ASM Material Data Sheet: 2 p. 2018.

MINGRUI, W.; THANH SA, N.; TURKSON, R. F.; JINPING, L. *et al.* Water injection for higher engine performance and lower emissions. **Journal of the Energy Institute**, 90, n. 2, p. 285-299, 2017/04/01/ 2017.

MIYAMURA, N.; KUNOU, T.; SAITOH, K.; MATSUMOTO, Y. *et al.* Design and Testing of Ovate Wire Helical Springs. SAE International: 14 p. 1993.

MOGI, Y.; OIKAWA, M.; KICHIMA, T.; HORIGUCHI, M. *et al.* Effect of high compression ratio on improving thermal efficiency and NO_x formation in jet plume controlled direct-injection near-zero emission hydrogen engines. **International Journal of Hydrogen Energy**, 47, n. 73, p. 31459-31467, 2022/08/26/ 2022.

MOLLENHAUER, K.; TSCHOEKE, H. Handbook of Diesel Engines. Springer-Verlag: 631 p. 2010.

MORGENSTERN, R.; KIEßLING, W.; REICHSTEIN, S. **Reduced Friction Losses and Wear by DLC Coating of Piston Pins.** 2008.

MOTORSPORT, M. Piston Coatings. Mahle 2018.

MOTORSPORT, M. Application Guide - Racing Components. Mahle Motorsport: 44 p. 2020.

MYUNG-RAE CHO, D.-Y. O., TAE-SEON MOON, DONG-CHUL HAN. Proc. Instn Mech. Engrs Vol. 217 Part D: J. Automobile Engineering: IMechE 2003.

NAKASONE, Y.; YOSHIMOTO, S.; STOLARSKI, T. A. Engineering Analysis with ANSYS Software. Elsevier Butterworth-Heinemann 2006.

NESHAN, A. Integration of exhaust manifold with engine cylinder head towards size and weight reduction. 30, p. 55-65, 04/01 2013.

NESHAN, A.; KESHAVERZ, A.; JAZAYERI, S.; GHASEMIAN, A. **Thermo-Fluid Analysis of the Exhaust Manifold Integrated With Cylinder Head.** 2012.

NICHOLLS, I. A. E.-M., H. K. NEWHALI. Inlet Manifold Water Injection for Control of Nitrogen Oxides — Theory and Experiment. **SAE 1969 Transactions-V78-A**, p. 10, DOI: <https://doi.org/10.4271/690018>.

NORTON, R. L. Design of Machinery - An Introduction to the Synthesis and Analysis of Mechanisms and Machines. McGraw-Hill: 897 p. 2012.

NOVAK, J. M.; BLUMBERG, P. N. Parametric Simulation of Significant Design and Operating Alternatives Affecting the Fuel Economy and Emissions of Spark-Ignited Engines. SAE Technical Paper: 17 p. 1978.

OSORIO, J. D.; RIVERA-ALVAREZ, A. Efficiency enhancement of spark-ignition engines using a Continuous Variable Valve Timing system for load control. **Energy**, 161, p. 649-662, 2018/10/15/ 2018.

PANDEY, J. K.; KUMAR, G. N. Effect of variable compression ratio and equivalence ratio on performance, combustion and emission of hydrogen port injection SI engine. **Energy**, 239, p. 122468, 2022/01/15/ 2022.

PARK, C.; KIM, Y.; OH, S.; OH, J. *et al.* Effect of fuel injection timing and injection pressure on performance in a hydrogen direct injection engine. **International Journal of Hydrogen Energy**, 47, n. 50, p. 21552-21564, 2022/06/12/ 2022.

PARKER. O-Ring Handbook. Parker Pradifa: 164 p. 2019.

PATEL, D. J. Optimization of flywheel design for internal combustion engines. University of Missouri at Rolla: 56 p. 1965.

PERCEAU, M.; GUIBERT, P.; GUILAIN, S. Zero-dimensional turbulence modeling of a spark ignition engine in a Miller cycle «Dethrottling» approach using a variable valve timing system. **Applied Thermal Engineering**, 199, p. 117535, 2021/11/25/ 2021.

PERRY, R. H.; GREEN, D. W. **Perry's Chemical Engineers' Handbook**. 8th Edition ed. Kansas, USA: McGraw-Hill, Inc, 2008. 2735 p.

PISCHINGER, S. *Internal Combustion Engines*. Aachen: Rheinisch-Westfälische Technische Hochschule Aachen. Vol.1: 407 p. 2012.

POULOS, S. G.; HEYWOOD, J. B. The Effect of Chamber Geometry on Spark-Ignition Engine Combustion. SAE Technical Paper: 27 p. 1983.

PULKRABEK, W. W. **Engineering Fundamentals of the Internal Combustion Engine**. First Edition ed. New Jersey, USA: Prentice Hall, 1997. 411 p.

RAMOS, C. L. **Modelagem e simulação computacional de coletores de admissão para motor de combustão interna de três cilindros**. Universidade Federal de Minas Gerais: 55 p. 2020.

REGHU, V. R.; MATHEW, N.; TILLETI, P.; SHANKAR, V. *et al.* Thermal Barrier Coating Development on Automobile Piston Material (Al-Si alloy), Numerical Analysis and Validation. **Materials Today: Proceedings**, 22, p. 1274-1284, 2020/01/01/ 2020.

ROBINSON, K.; HAWLEY, J. G.; HAMMOND, G. P.; OWEN, N. J. Convective coolant heat transfer in internal combustion engines. **Proceedings of the Institution of Mechanical Engineers, Part D: Journal of Automobile Engineering**, 217, n. 2, p. 133-146, 2003/02/01 2003.

ROCHA, D. D.; RADICCHI, F.; LOPES, G.; BRUNOCILLA, M. *et al.* Study of the water injection control parameters on combustion performance of a spark-ignition engine. **Energy**, 217, p. 119346, 02/01 2021.

ROHIT, A.; SATPATHY, S.; CHOI, J.; HOARD, J. *et al.* Literature Survey of Water Injection Benefits on Boosted Spark Ignited Engines, 2017, SAE International, DOI: 10.4271/2017-01-0658. Disponível em: <https://doi.org/10.4271/2017-01-0658>.

ROTHBART, H. A. **CAM DESIGN HANDBOOK**. MCGRAW-HILL: 619 p. 2004.

ROTHMANN, G. *Berechnung der Kolbenbolzen von Fahrzeugdiesel-motoren*. GHH Konzern: 7 p. 1963.

RYO WAKABAYASHI, M. T., TAKAMASA SHIMADA, YASUHARU MIZUNO, TAKAHIRO YAMAUCHI. "The Effects of Crank Ratio and Crankshaft Offset on Piston Friction Losses," SAE Technical Paper 2003-01-0983. SAE 2003.

SAHOO, S.; SRIVASTAVA, D. K. Effect of compression ratio on engine knock, performance, combustion and emission characteristics of a bi-fuel CNG engine. **Energy**, 233, p. 121144, 2021/10/15/ 2021.

SANTOS, J. C. **ESTUDO E CARACTERIZAÇÃO DE UM SISTEMA DE SOBREALIMENTAÇÃO DUPLA DE MOTOR DE ALTA EFICIÊNCIA MOVIDO A**

ETANOL. Orientador: BAÊTA, P. D. J. G. C. 2018. 85 f. (Bacharelado) - Departamento de Engenharia Mecânica, UFMG, Belo Horizonte.

SANTOS, N. D. S. A. Study of a Bearing Test Bench Capable to Simulate Wear in Diesel Start-Stop Engines. Universidade Federal de Minas Gerais (UFMG): 123 p. 2019.

SCHAEFFLER. Mobility for Tomorrow. Schaeffler: 398 p. 2018.

SCHRÖN, H. Die Dynamik der Verbrennungskraftmaschine. Springer Verlag Vienna: 209 p. 1947.

SCHÄFER, F. **Handbuch Verbrennungsmotor**. 8th ed. Springer, 2017. 1409 p. 978-3-658-10901-1.

SCHÄFER, H. N. **Rotordynamics of Automotive Turbochargers**. Second Edition ed. Ludwigsburg, Germany: Springer Tracts in Mechanical Engineering, 2015. 367 p.

SEOKWON CHO, S. O., CHIHEON SONG, WOOJAE SHIN, SEJIN SONG, HAN HO; SONG, K. M., BYEONGSEOK LEE, DONGWON JUNG, SOO HYUNG WOO. Effects of Bore-to-Stroke Ratio on the Efficiency and Knock Characteristics in a Single-Cylinder GDI Engine, SAE Technical Paper 2019-01-1138. SAE 2019.

SERRANO, J. R.; PIQUERAS, P.; DE LA MORENA, J.; GÓMEZ-VILANOVA, A. *et al.* Methodological analysis of variable geometry turbine technology impact on the performance of highly downsized spark-ignition engines. **Energy**, 215, p. 119122, 2021/01/15/ 2021.

SHOBERG, R. S. Review of the Application of Design Guideline VDI 2230. PCB Load & Torque: 15 p. 2018.

SIEWERT, R. M. Engine Combustion at Large Bore-to-Stroke Ratios. SAE Technical Paper: 15 p. 1978.

SILVA, F. S. Fatigue on engine pistons – A compendium of case studies. **Engineering Failure Analysis**, 13, n. 3, p. 480-492, 2006/04/01/ 2006.

SILVA, T. R. V. **ESTUDO DE ESTRATÉGIAS DE CONTROLE DOS PROCESSOS INTERNOS DE UM MOTOR DE COMBUSTÃO INTERNA DE INJEÇÃO DIRETA DE ETANOL TURBO - ALIMENTADO PARA MAXIMIZAÇÃO DA EFICIÊNCIA GLOBAL**. Orientador: BAETA, J. G. C. 2017. 217 f. (Mestrado) - Departamento de Engenharia Mecânica, UFMG, Belo Horizonte, MG.

SILVA, T. R. V.; BAETA, J. G. C.; NETO, N. A. D.; MALAQUIAS, A. C. T. *et al.* Split-Injection in a Downsized Ethanol SIDI Engine Aiming to Mitigate Pre-Ignition, 2017a, SAE International.

SILVA, T. R. V.; BAETA, J. G. C.; NETO, N. A. D.; MALAQUIAS, A. C. T. *et al.* The Use of Split-Injection Technique and Ethanol Lean Combustion on a SIDI Engine

Operation for Reducing the Fuel Consumption and Pollutant Emissions, 2017b, SAE International.

SILVA, T. R. V.; BAËTA, J. G. C.; DINIZ, N. A.; DUTRA, W. *et al.* Effects of Continuously Variable Valve Timing (CVVT) on Ethanol Spark Ignited Direct Injection (SIDI) Downsized Engine. *In: I Congresso Internacional de Motores, Combustíveis e Combustão - CIMCCO*, 2016, Belo Horizonte, MG, Brasil. p. 7. Disponível em: www.amm.demec.ufmg.br/index.php?journal=revista&page=article&op=download&path%5B%5D=6&path%5B%5D=6.

SKF. Valve stem seals. SKF Group: 12 p. 2020.

SMITH, P. H.; MORRISON, J. C. *The Scientific Design of Exhaust and Intake Systems*. Bentley Publishers: 298 p. 1972.

SROKA, Z. J. Thermal load of tuned piston. **Archives of Civil and Mechanical Engineering**, 12, n. 3, p. 342-347, 2012/09/01/ 2012.

STEVE SHIN, A. C., FANGHUI SHI. "Offset Crankshaft Effects on SI Engine Combustion and Friction Performance," SAE Technical Paper 2004-01-0606. SAE 2004.

STROZZI, A.; BALDINI, A.; GIACOPINI, M.; BERTOCCHI, E. *et al.* A repertoire of failures in gudgeon pins for internal combustion engines, and a critical assessment of the design formulae. **Engineering Failure Analysis**, 87, p. 22-48, 2018/05/01/ 2018.

TAYMAZ, I.; ÇAKIR, K.; MIMAROGLU, A. Experimental study of effective efficiency in a ceramic coated diesel engine. **Surface and Coatings Technology**, 200, n. 1, p. 1182-1185, 2005/10/01/ 2005.

TECHNOLOGIES, G. *Engine Performance Application Manual*. Gamma Technologies: 155 p. 2020.

TRZESNIOWSKI, M. *Rennwagentechnik*. Springer Fachmedien Wiesbaden GmbH: 892 p. 2010.

UNITED NATIONS CLIMATE CHANGE, C.-. COP-26 - The Glasgow Climate Pact. 2021.

VASCONCELOS, W. D. A. METODOLOGIA DE ANÁLISE TERMO-ESTRUTURAL DE BLOCO DE MOTORES APÓS ADIÇÃO DO SISTEMA DE SOBREALIMENTAÇÃO. Universidade Federal de Pernambuco (UFPE): 158 p. 2018.

VAZ, M. G. J. VALIDAÇÃO DE MECANISMOS CINÉTICOS QUÍMICOS REDUZIDOS PARA MISTURA DE GASOLINA-ETANOL EM UM MOTOR DE COMBUSTÃO INTERNA. Universidade Federal de Minas Gerais: 208 p. 2018.

WAN, J.; ZHUANG, Y.; HUANG, Y.; QIAN, Y. *et al.* A review of water injection application on spark-ignition engines. **Fuel Processing Technology**, 221, p. 106956, 2021/10/01/ 2021.

WANG, J.-K.; LI, J.-L.; WU, M.-H.; CHEN, R.-H. Reduction of Nitric Oxide Emission From a SI Engine by Water Injection at the Intake Runner. n. 43765, p. 335-340, 2009.

WANG, Y. **Introduction to Engine Valvetrains**. First Edition ed. Warrendale, PA, USA: SAE International, 2007. 604 p.

WARNECKE W., G., P. Mobility of the Future: Integrated View of Energy and Powertrain Options. Berlin 2018.

WEBER, D.-I. C.; KRAMER, D.-I. U.; FRIEDFELDT, D.-I. R.; RUHLAND, D.-I. H. *et al.* Development of a New Combustion Engine Dedicated to Methane Operation. *In: Internationales Wiener Motorensymposium, 2018, Viena, Austria.* p. 19.

WU, X.; LIU, K.; LIU, Q.; FU, J. *et al.* Effects of direct water injection timings on knock suppression, combustion, and emission performance of high compression ratio hydrogen-enriched natural gas engine. **Energy Conversion and Management**, 250, p. 114887, 2021/12/15/ 2021.

XI-HOU FU, J.-H. W., XIAO-NAN ZHANG. "The Determination of Cylinder Centre Spacing for Vehicle Diesel Engine," SAE Technical Paper 940591. SAE 1994.

Z. S. FILIPI, D. N. A. The effect of the stroke-to-bore ratio on combustion, heat transfer and efficiency of a homogeneous charge spark ignition engine of given displacement. IMechE 2000.

ZHAO, H. **Advanced direct injection combustion engine technologies and development**. Boca Raton, FL, USA: Woodhead Publishing Limited e CRC Press LLC, 2010. 325 p.

ZHAO, J.; FU, R.; WANG, S.; XU, H. *et al.* Fuel economy improvement of a turbocharged gasoline SI engine through combining cooled EGR and high compression ratio. **Energy**, 239, p. 122353, 2022/01/15/ 2022.

ZOLDY, M.; SZALMANE CSETE, M.; KOLOZSI, P. P.; BORDAS, P. *et al.* Cognitive Sustainability. **Cognitive Sustainability**, 1, n. 1, 03/03 2022.

ÇENGEL, Y. A.; CIMBALA, J. M. **Fluid Mechanics Fundamentals and Applications**. 3° Edition ed. New York. NY, USA: McGraw Hill, 2006. 968 p.

